1-1-1979

On the structure of HII regions and their distribution in the galaxy.

Felix J. Lockman
University of Massachusetts Amherst

ON THE STRUCTURE OF HII REGIONS AND THEIR DISTRIBUTION IN THE GALAXY

A Dissertation Presented

By

FELIX JAMES LOCKMAN

Submitted to the Graduate School of the
University of Massachusetts in partial fulfillment
of the requirements for the degree of

DOCTOR OF PHILOSOPHY

MAY 1979

ASTRONOMY

This research was supported in part by NSF Grant AST 76-24610.

ON THE STRUCTURE OF HII REGIONS AND THEIR DISTRIBUTION IN THE GALAXY

A Dissertation Presented

BY

FELIX JAMES LOCKMAN

Approved as to style and content by:

Dr. G. R. Huguenin, Chairperson of Committee

Dr. M. A. Gordon, Member

Dr. N. Z. Scoville, Member

Dr. K. S. Yngvesson, Member

Dr. F. W. Byron, Department Head,
Department of Physics and Astronomy

ACKNOWLEDGMENTS

I thank my advisors, G. R. Huguenin at the University of Massachusetts and M. A. Gordon at the National Radio Astronomy Observatory, for counsel, scientific and otherwise, for encouragement and, above all, for patience (*Verti me ad aliud, et vidi sub sole, nec velocium esse cursum*). Special thanks are owed to R. L. Brown and W. B. Burton for discussion and collaboration on problems of recombination lines and galactic structure, respectively. I am grateful to B. E. Turner for providing results of his OH survey in advance of publication. Advice from T. M. Bania, W. A. Dent, M. S. Roberts, J. H. Taylor, B. E. Turner and D. Van Blerkom was helpful at various critical junctures. I am indebted to P. Jackson for preparation of the manuscript, to G. Kessler, P. Smiley and M. B. Weems for preparation of the figures, and to L. J Rickard for improvements of phrase and construction. Part of this work was done at the NRAO and part at the Department of Terrestrial Magnetism of The Carnegie Institution of Washington. I thank the director and staff of each institution for their hospitality.

This is dedicated to my parents: Felix C. and Louise C. Lockman.

ABSTRACT

ON THE STRUCTURE OF HII REGIONS AND
THEIR DISTRIBUTION IN THE GALAXY

June, 1979

Felix J. Lockman

B.S. Drexel University

Ph.D. University of Massachusetts

Directed by: Dr. G. R. Huguenin

This dissertation concerns the use of radio recombination lines to determine structure of HII regions and the distribution of HII regions in the Galaxy. The first three chapters treat the formation and transfer of radio recombination lines and examine various processes that effect our ability to deduce nebular properties from radio observations. It is shown that recombination line intensities are influenced, in a non-linear fashion, by the geometric structure of a nebula. If there are variations in the path length through even an isothermal, homogeneous HII region, the line-to-continuum ratio will vary from point to point across the nebula. When observed with an antenna beam, the measured line-to-continuum ratios may be quite different from the true values. Certain analytic shortcuts that are often used in place of a full analysis are discussed and shown to give systematically erroneous results. The behavior of a simple class of inhomogeneous models is examined in detail to show how some information on the nebular temperature, density and geometry can be determined given adequate data. Comparison of model results with observations of Orion A shows that the

nebula must have a specific radial temperature gradient. Nebular expansion is considered, and calculations suggest that this process can broaden lines sufficiently to remove discrepancies between observed and purely thermal linewidths.

In Chapter IV, the distribution of dense HII regions is derived using kinematic models based on circular rotation and density-wave theory. The HII regions are found to extend inwards to within 3 kpc of the galactic center; they have the smallest scale height of any known species. The average distance of HII regions from the galactic plane varies systematically with distance from the galactic center. Kinematic models of the observed quantities indicate that the nebulae lie in a narrow pattern like a spiral or a set of ring segments. This conclusion is independent of the precise kinematics of the Galaxy. A survey of less dense ionized gas is described in Chapter V. Moderate density ionized gas is seen at all positions observed at $b = 0°$ between $2° < \ell \lesssim 45°$. Although it may be more confined to the inner Galaxy, this medium appears to fill a larger volume of the plane than dense nebulae do. The absence of HII regions from large areas of the Galaxy that are well populated by atomic and molecular clouds indicates that the formation of massive stars does not result simply from the presence of molecular clouds, but requires an additional factor like a density wave.

TABLE OF CONTENTS

CHAPTER III, continued

LIST OF TABLES

LIST OF FIGURES

CHAPTER I

THE FORMATION AND TRANSFER OF RADIO RECOMBINATION LINES

a) The Hydrogen Atom

The hydrogen atom, excited to levels which produce recombination lines in the radio wavelength range, can have a diameter of a few microns. The low density of the interstellar medium allows such highly excited atoms to have a reasonable lifetime, but because of their large cross sections they are strongly coupled to their immediate environment through collisions with free electrons. When collisions become too frequent or too intense, the quantized character of the excited states can be destroyed. Thus the physical state of these hydrogen atoms cannot be described without a knowledge of their environment and, conversely, from a description of the state of these hydrogen atoms information about their environment is gained. Any description of excited hydrogen atoms in an astrophysical context is necessarily statistical.

The energy of a highly excited hydrogen atom is primarily related to the value of its principal quantum number, n. Electronic transitions between $n + \Delta n$ and n produce photons which, for $n \gtrsim 40$ and $\Delta n << n$, have frequencies in the radio range, $\nu \lesssim 100$ GHz. A particular electronic transition to level n in hydrogen will be designated by the symbol Hn plus a Greek letter suffix to indicate the value of Δn: α for $\Delta n = 1$, β for $\Delta n = 2$, etc. The spectral lines arising from these transitions are called recombination lines; they are commonly formed in clouds of nearly wholly ionized hydrogen called emission nebulae or HII regions. Various aspects of the formation and transfer of radio recombination lines have

been considered by Kardashev (1959), Goldberg (1966, 1968), Palmer (1968), Dupree and Goldberg (1969), Hjellming et al. (1969), Churchwell (1970), Brocklehurst and Seaton (1972), Gordon (1974), and Lockman and Brown (1976). While most of the material in this Chapter has been developed in the aforementioned references, it is important that the basic relationships be reviewed and often cast into a form particularly suited for later use. Virtually all of the effects treated in Chapters II and III follow directly from the basic formulae discussed in this Chapter.

For radio astronomical purposes the state of a hydrogen atom can be described solely in terms of its principal quantum number n. For $n \gtrsim 40$, collisions are very effective in redistributing electrons among various angular momentum states according to a statistical distribution which is simply related to n (Pengelly and Seaton, 1964; Brocklehurst, 1971). Fine structure splitting of these high levels produces frequency shifts orders of magnitude less than the spread in the lines due to Doppler motions (Palmer, 1968), and hence the energy of a transition (or the frequency) is given by the well known Rydberg relation which is a function only of n and its change Δn. Thus the rest frequency, ν_o, of a recombination line is

$$\nu_o = Z^2 R_a c\left[\frac{1}{n^2} - \frac{1}{m^2}\right] \qquad (1)$$

where Z is the effective nuclear charge, c is the velocity of light, R_a is the appropriate Rydberg constant and $m = n + \Delta n$. The Rydberg constant for an atom of mass m_a is related to the infinite mass constant R_∞

$$R_a = R_\infty (1 - m_e/m_a), \qquad (2)$$

where m_e is the mass of an electron. For $n >> 1$ and $\Delta n << n$, a useful approximation to eq. (1) is

$$\nu_o \simeq \frac{2 Z^2 R_a c \Delta n}{n^3} . \qquad (3)$$

Motion of the atom along the line of sight will produce an observed frequency ν shifted from the rest frequency ν_o by an amount given by the radio astronomical convention for the classical Doppler formula

$$\frac{\nu - \nu_o}{\nu_o} = - \frac{V}{c} . \qquad (4)$$

b) The Formation of Hydrogen Recombination Lines

The interaction of a hydrogen atom with a radiation field, either through emission or absorption of a photon, involves three processes which are schematically listed below:

Spontaneous emission: $m \rightarrow n + h\nu$: $A_{m,n}$

Absorption: $n + h\nu \rightarrow m$: $B_{n,m} I_\nu$

Stimulated emission: $n + h\nu \rightarrow n + 2h\nu$: $B_{m,n} I_\nu$.

Here m represents an atom with an electron occupying the principal quantum number $m > n$, and the rates of the processes are given by the Einstein coefficients A and B, and may also depend on the specific intensity of the radiation field I_ν at the frequency of the transition.

The total number of absorptions, N_a, per unit volume between states n and m is the difference between the absorption and the stimulated emission rates weighted by the populations, N_n and N_m, of each level:

$$N_a = (N_n B_{n,m} - N_m B_{m,n}) I_\nu. \tag{5}$$

The number of absorptions per unit frequency is given by eq. (5) multiplied by a suitable frequency profile function ϕ_ν. This function describes the frequency distribution of photons arising from a single transition, and is assumed to be the same for stimulated and spontaneous emission and for absorption. It will be discussed in §Ic. Unless there is a possibility of confusion, quantities will be written without their frequency subscripts and will, unless otherwise specified, refer to a single transition.

It is convenient to work with the line absorption coefficient κ_L, defined as

$$\kappa_L = N_a \, h\nu / I_\nu \tag{6}$$

or, from eq. (5),

$$\kappa_L = h\nu \, (N_n B_{n,m} - N_m B_{m,n}) \, \phi_\nu, \tag{7}$$

and the emission coefficient (the emissivity), j_L,

$$j_L = h\nu \, N_m A_{m,n} \, \phi_\nu \, / \, 4\pi, \tag{8}$$

where the factor 4π accounts for the isotropy of spontaneous emission. The absorption coefficient can be positive or negative; negative values occur when stimulated emission outweights absorption.

The Einstein coefficients are related in the following way:

$$g_n B_{n,m} = g_m B_{m,n} = \frac{c^2}{2h\nu^3} \frac{A_{m,n}}{4\pi} g_m, \tag{9}$$

where g_i, the statistical weight of the i^{th} level, has a value of $2i^2$ for hydrogenic atoms. Expressing κ_L in terms of eq. (9),

$$\kappa_L = \frac{c^2}{8\pi\nu^2} \left[N_n \frac{g_m}{g_n} - N_m \right] A_{m,n} \phi_\nu. \tag{10}$$

The level populations, N_n and N_m, are functions of the thermodynamic state of the atom, and depend on the number and energy of collisions between the atom and free electrons. In general the population does not depend on the value of I (Dyson, 1967; Brocklehurst and Seaton, 1972). The Boltzmann equation relates N_m and N_n:

$$\frac{N_m}{N_n} = \frac{g_m}{g_n} \exp(-h\nu/kT_{ex}) \tag{11}$$

where T_{ex}, often called the excitation temperature, is a number (in temperature units) chosen so that eq. (11) is true. The value of the excitation temperature depends on the specific transition and the thermodynamic state (i.e., the temperature and the density of the ensemble of atoms) and is a quantity of limited use given the enormous number of possible recombination line transitions. It is more convenient to work in terms of the kinetic electron temperature, T_e, which is a state variable

in an ensemble of atoms. The assumption of Local Thermodynamic Equilibrium (LTE) is that $T_{ex} = T_e$, giving

$$\frac{N_m^*}{N_n^*} = \frac{g_m}{g_n} \exp(-h\nu/kT_e), \tag{12}$$

where quantities marked with an asterisk are those derived under the assumption of LTE. A single parameter, dependent only on the principal quantum number of a level and not on the actual transition, relates N_n^* to N_n:

$$b_n \equiv \frac{N_n}{N_n^*} . \tag{13}$$

Because the level populations are virtually independent of I, the so-called departure coefficient b, which measures the departure of the population of a level from its LTE value, can be uniquely determined from the thermodynamic state of a gas. The relative population ratio is

$$\frac{N_m}{N_n} = \frac{b_m}{b_n}\frac{g_m}{g_n} \exp(-h\nu/kT_e) = \frac{b_m}{b_n}\frac{N_m^*}{N_n^*} . \tag{14}$$

Thus, when the statistical weights are evaluated,

$$\kappa_L = \frac{c^2}{8\pi\nu^2}\left(1 - \frac{b_m}{b_n}\exp(-h\nu/kT_e) \right) \frac{m^2}{n^2} N_n^* b_n A_{m,n} \phi_\nu . \tag{15}$$

The LTE population of level n, N_n^*, can be calculated from the electron and proton densities N_e and N_p by the Saha equilibrium equation:

$$N_n^* = N_e N_p \left(\frac{h^2}{2\pi k T_e m_e} \right)^{1.5} \exp(I_n/kT_e), \qquad (16)$$

where I_n is the (positive) energy required to ionize the electron out of level n. Both this equation and that of Boltzmann [eq. (12)] assume that the level populations are in equilibrium, i.e., that they vary on timescales long compared to those for spontaneous and stimulated emission.

The combined equations (15) and (16) can be separated into three parts: an LTE absorption coefficient κ_L^* which, when $b_n = b_m = 1$, is the correct expression for κ_L, a term involving the ratio b_m/b_n, and the single coefficient b_n. With this division and the substitution of eq. (16), eq. (15) becomes

$$\kappa_L = b_n \beta \kappa_L^* \qquad (17)$$

where

$$\kappa_L^* = \frac{c^2}{8\pi\nu^2} \left(\frac{h^2}{2\pi m_e k T_e} \right)^{1.5} \left(1 - e^{-h\nu/kT_e}\right) \exp(I_n/kT_e)\, A_{m,n}\, \phi_\nu, \qquad (18)$$

$$\beta = \left(1 - \frac{b_m}{b_n} \exp(-h\nu/kT_e)\right) / \left(1 - \exp(-h\nu/kT_e)\right), \qquad (19)$$

and the A coefficient is expressed in terms of the absorption oscillator strength $f_{n,m}$:

$$A_{m,n} = \frac{8\pi^2 e^2 \nu_o^2}{m_e c^3} \frac{n^2}{m^2} f_{n,m} \ . \qquad (20)$$

The quantity β in eq. (19) should not be confused with the symbol β used to designate a $\Delta n = 2$ transition.

When $h\nu/kT_e << 1$, corresponding to $\nu(\mathrm{GHz}) << 21\ T_e$, the exponential containing this quantity in eq. (18) can be expanded, and

$$\kappa_L^* = \frac{h}{kT_e} \frac{\pi e^2}{m_e c} \left(\frac{h^2}{2\pi m_e kT_e} \right)^{1.5} \exp(I_n/kT_e)\ n^2\ (\nu_o \phi_\nu)\ f_{n,m}\ N_e N_p . \qquad (21)$$

Under the same conditions the exponential term in eq. (19) can be expanded in a form first derived by Goldberg (1966),

$$\beta \simeq \frac{b_m}{b_n} \left(1 - \frac{kT_e}{h\nu} \left(\frac{b_m - b_n}{b_m} \right) \right) \ . \qquad (22)$$

Since the ratio b_m/b_n is usually very close to unity, it will be neglected in later evaluations of β. It is useful to approximate the difference between the departure coefficients by an expression of the following form:

$$\frac{b_n - b_m}{b_m} \simeq \Delta n \frac{d(\ln(b_n))}{dn} \ , \qquad (23)$$

which is acceptably accurate when $b_n \sim b_m$. A good approximation to the absorption oscillator strength, $f_{n,m}$, is given by Goldwire (1968) and

Menzel (1968):

$$\frac{f_{n,m}}{n} \simeq M(\Delta n)\ (1 + 1.5\ \frac{\Delta n}{n}), \qquad (24)$$

where M(1) = 0.19077, M(2) = 0.02633, M(3) = 0.0081056, M(4) = 0.0034917 and M(5) = 0.0018118.

These transformations give an expression for κ_L which depends only on the thermodynamic state variables (T_e, N_e and N_p), and on quantities which are a function of n and Δn: b_n, $\Delta n\, d(\ln(b_n))/dn$, $(f_{n,m})/n$ and ν. Hydrogen departure coefficients and their derivatives have been calculated by Brocklehurst (1970) for many densities and frequencies when $2500 \leq T_e \leq 20000$ K, and by Hoang-Binh and Walmsley (1974) and by Brown (1979) for lower temperatures. It is convenient to evaluate the constants in eq. (21) and to express the absorption coefficient in units of pc^{-1}:

$$\kappa_L^* = 1.62828\text{x}10^{-9}\ \exp(I_n/kT_e)\ n^3\ \frac{f_{n,m}}{n}\ (\nu_o \phi_\nu)\ \frac{N_e\ N_p}{T_e^{2.5}}, \qquad (25)$$

where some authors prefer to substitute eq. (3) for the factor n^3. The exponential term is often omitted because it is usually very close to unity.

The emission coefficient can also be separated into LTE and non-LTE parts by writing $j = b_m\ j^*$. The LTE emission coefficient is related to the LTE absorption coefficient through Kirchkoff's law:

$$\frac{j^*}{\kappa^*} = B_\nu(T_e) = \frac{2h\nu^3}{c^2}\ \frac{1}{\exp(h\nu/kT_e) - 1}, \qquad (26)$$

where $B_\nu(T_e)$, the Planck function, is given by the Rayleigh-Jeans approximation

$$B_\nu(T_e) \approx \frac{2kTe}{c^2}\,\nu^2 \qquad (27)$$

when $h\nu << kT_e$.

c) The Line Profile Function

The frequency distribution of photons from a single transition is given by the line profile function ϕ, which is the convolution of three functions:

$$\phi = \phi_n * \phi_D * \phi_I\ , \qquad (28)$$

where ϕ_n is the "natural damping profile" arising from the finite spread in the energy of any bound state, ϕ_D is the Doppler profile due to random motions of the atoms along the line of sight, and ϕ_I is the profile function resulting from perturbation of the bound states by nearby particles. The integral of the profile function over frequency is unity. Radio recombination lines have natural profiles much narrower than their Doppler profiles, so the first term will be ignored.

The profile function arising from random motion of the atoms is a normalized Gaussian function

$$\phi_D(\nu) = \frac{\alpha}{\nu_o\sqrt{\pi}}\ \exp\{-(\alpha\ (\nu-\nu_o)/\nu_o)^2\}, \qquad (29)$$

where

$$\alpha = \left(\frac{m_a c^2}{2kT_D}\right)^{0.5} = 2.32483 \times 10^6 \left(\frac{m_a(AMU)}{T_D}\right)^{0.5}, \qquad (30)$$

ν_o is the rest frequency of the transition, m_a is the mass of the atom and T_D is a characteristic "Doppler temperature". The Gaussian distribution is characterized by a full-width at half-maximum (commonly referred to as the "line width") of Δv_D in velocity units or $\Delta \nu_D$ in frequency units where

$$\Delta v_D(km/s) = 0.21471 \left(\frac{T_D}{m_a(AMU)}\right)^{0.5}, \qquad (31)$$

and for convenience the atomic mass has been expressed in AMU. In the absence of turbulent motions $T_D = T_e$. Typical hydrogen recombination lines have a width characterized by $T_D \simeq 2T_e$ indicating that microturbulence or macroturbulence contributes half of the Doppler line width. In this section we take the volume of gas to be small enough that there are no ordered motions within it. That is, macroturbulent motions such as expansion, rotation, etc., are assumed to be negligible. In real nebulae such motions may play a major role in determining the line shape. This will be discussed in later sections.

The profile function resulting from broadening of the energy levels by collisions has the general form of a Lorentzian profile

$$\phi_I(\nu) = \gamma/\{2\pi((\nu-\nu_o)^2 + (\gamma/2)^2)\}, \qquad (32)$$

with a full-width at half-maximum of γ. The convolution of Lorentzian and Gaussian profiles gives a normalized Voigt function

$$\phi_\nu = \frac{\alpha}{\nu_o\sqrt{\pi}} H(\underline{a},x) = \frac{\alpha\, a}{\nu_o \pi^{1.5}} \int_{-\infty}^{\infty} \frac{e^{-t^2}}{a^2+(t-x)^2}\, dt \qquad (33)$$

where

$$\underline{a} = \frac{\alpha\, \gamma}{2\nu_o} \qquad (34)$$

and

$$x = \alpha\, (\nu - \nu_o)/\nu_o \ . \qquad (35)$$

The quantity $\underline{a}$ gives the ratio of impact to Doppler broadening, and the parameter x is the displacement from line center in units of half-1/e-widths of the Doppler component of the function. When $\underline{a} \to 0$, eq. (33) can be reduced to the Doppler form and when $\underline{a} \to \infty$ eq. (33) can be reduced to the Lorentzian form (Hummer, 1965). The evaluation of γ, and hence $\underline{a}$, was a matter of considerable uncertainty in early studies of radio recombination lines, but since the work of Griem (1967) and the re-evaluation of the problem by Brocklehurst and Leeman (1971) and Peach (1972) it appears that the line broadening processes for highly excited electron transitions in hydrogen and hydrogen-like atoms are fairly well understood.

We will use an expression for the quantity $\underline{a}$ given by Griem (1974)

$$\underline{a} = 9.253\times10^{-16} \frac{n^7 N_e}{\Delta n Z^4} T_e^{-\frac{1}{2}} (m_a(\mathrm{AMU})/T_D)^{\frac{1}{2}} \{\tfrac{1}{2} + \ln(6.366\times10^{-6} \frac{nT_e}{Z})\} \tag{36}$$

where the mass of the atom is again given in AMU. The strong dependence of $\underline{a}$ on the principal quantum number is not unexpected since as n increases not only does the atomic cross section for collisions increase, but each collision produces a large perturbation on the less tightly bound electrons. From eq. (36) it is clear that, for a given N_e, it is theoretically possible to find an n such that $\gamma << \Delta\nu_D$ and collisional broadening is negligible. Similarly, for $\gamma >> \Delta\nu_D$ lines will noticeably depart from Gaussian shape, a circumstance that will occur in hydrogen when

$$N_e \gtrsim 7\times10^4 \, (n/100)^{-7.4} \ \mathrm{cm}^{-3} \ . \tag{37}$$

This expression was obtained by evaluating an approximation to eq. (36) given in Brocklehurst and Seaton (1972) for $T_e = 10^4$ K, $T_D = 2T_e$ and $\underline{a} = 0.83$.

The Voigt function must be evaluated numerically, although tables of its value for certain ranges of $\underline{a}$ and x are given by Hummer (1965) and by Finn and Mugglestone (1965). Approximations to the Voigt function are also available, for example that of Kielkopf (1973). An excellent critical summary of the methods available for the calculation of Voigt profiles is given by Drayson (1976).

d) The Continuum Emission

Interactions between free charged particles produce continuous thermal bremsstrahlung (free-free) radiation which is the major source of radio emission in most nebulae; emission and absorption from bound-free processes and electron-neutral atom interactions is usually negligible (e.g., Churchwell, 1970). The absorption coefficient for free-free interactions is given by Oster (1961)

$$\kappa_c = 0.0314\ T_e^{-1.5}\ Z^2\ \nu^{-2}\ \{\ln(0.0496/\nu Z) + 1.5\ \ln(T_e)\}N_e N_i, \quad (38)$$

where ν is in GHz. This formula is valid for most temperatures and densities encountered in HII regions. Altenhoff *et al*. (1960) have derived an approximation to eq. (38) which has been widely used because of its simplicity:

$$\kappa_c \simeq 0.08235\ T_e^{-1.35}\ \nu^{-2.1}\ N_e N_i \quad (39)$$

where ν is once again in GHz. Because the free electrons have a Maxwellian energy distribution, free-free radiation is always formed under conditions of LTE, and the emission and absorption coefficients are related through eq. (26):

$$j_c = \kappa_c\ B_\nu(T_e). \quad (40)$$

e) The Equation of Transfer for Radio Recombination Lines

The solution of the equation of transfer for radio recombination lines is simplified by the negligible importance of scattering into and out of the line of sight. Thus the equation of transfer can be written

$$\frac{dI}{ds} = j - \kappa I, \tag{41}$$

where ds is an increment of distance along the line of sight from source to observer. We will use the quantities

$$dt = -\kappa\, ds, \qquad t = \int_0^s \kappa\, ds,$$

$$\tau = \int_0^\ell \kappa\, ds, \tag{42}$$

where ℓ is the total path length through the object along the line of sight from observer to source, to give

$$I = I_0\, e^{-\tau} + \int_0^\ell j\, e^{-t}\, ds. \tag{43}$$

The emergent radiation is composed of the radiation incident on the far side of the object, I_0, modified by the total absorption coefficient integrated through the object, together with that radiation which is formed within the object.

Equation (43) has been solved for isothermal homogeneous nebulae with and without the LTE assumption (e.g., Kardashev, 1959; Goldberg 1966; Palmer, 1968), but Brocklehurst and Seaton (1972) have shown that homogeneous models predict line shapes which are inconsistent with those

actually observed. Brocklehurst and Seaton reduce eq. (43) to a form which is appropriate over certain frequency ranges in isothermal nebulae, but their solution is of limited use because isothermal models predict incorrect line intensities for some nebulae, e.g., Orion A (Lockman and Brown, 1975). In addition, the departure coefficients are not analytic functions of n, so even the Brocklehurst and Seaton approximations result in an equation which must be evaluated numerically for models with varying density. Because numerical integration is necessary to evaluate eq. (43) for most reasonable models, it seems preferable to deal with the entire quantity within the integral rather than to make assumptions which restrict the applicability of the results.

A useful form of the solution to the equation of transfer can be derived by considering the solution to eq. (43) for a line of sight through an homogeneous, isothermal nebula with no macroturbulent motions. For clarity I_0 is temporarily assumed to be zero, but the final equation will allow for radiation incident on the far side of the object. When the medium is homogeneous and isothermal, the emission and absorption coefficients are constants, j_1 and κ_1, and

$$I = \int_0^{\ell} j_1 \, e^{-\int_0^s \kappa_1 \, ds'} \, ds = \frac{j_1}{\kappa_1} \left(1 - e^{-\kappa_1 \ell}\right). \qquad (44)$$

Now consider a line of sight which intersects two regions, the first lying between ℓ' and ℓ, and the second between 0 and ℓ'. Within each region j and κ are constant. Under these circumstances eq. (43) can be written in two parts:

$$I = \int_0^{\ell} j_2 \; e^{-\int_0^s \kappa \, ds'} \, ds + \int_{\ell'}^{\ell} j_1 \; e^{-\int_0^s \kappa \, ds'} \, ds. \qquad (45)$$

In the first term the upper limit on the integral in the exponential will run to ℓ', over which path $\kappa = \kappa_2$. The integral in the exponent of the second term can be written

$$\int_0^s \kappa \, ds' = \int_0^{\ell'} \kappa_2 \, ds' + \int_{\ell'}^s \kappa_1 \, ds' \qquad (46)$$

and, as the first term in this expression is not a function of s, eq. (45) becomes

$$I = \int_0^{\ell'} j_2 \; e^{-\int_0^s \kappa_2 \, ds'} \, ds \; + \; e^{-\int_0^{\ell'} \kappa_2 \, ds'} \int_{\ell'}^{\ell} j_1 \; e^{-\int_{\ell'}^s \kappa_1 \, ds'} \, ds \qquad (47)$$

which, from eq. (44), is just

$$I = I_2 + I_1 \, e^{-\int_0^{\ell'} \kappa_2 \, ds'}, \qquad (48)$$

where I_1 and I_2 are evaluated using the appropriate limits on their integrals. The solution to the equation of transfer under these conditions has been reduced to a sum of homogeneous isothermal solutions with

appropriate weighting factors. This equation is easily generalized to describe the emission along any line of sight through nebulae which can be divided into an arbitrary number, r, of isothermal homogeneous cells, each with a line of sight extent Δx_i. The emergent radiation is then

$$I = \int_0^{\ell} j\, e^{-t}\, ds = \sum_{i=0}^{r} I_i\, e^{-p_i} \tag{49}$$

where

$$p_i = \sum_{ii=i+1}^{r} \kappa_{ii} \Delta x_{ii} \,. \tag{50}$$

Here region 1 is farthest from the observer, p = 0 when i = r, and the effect of background radiation is included by letting $I_i = I_0$ when i = 0. When there are ordered, large-scale motions along the line of sight, the distance increment is chosen so that a given region can be characterized by a single velocity.

The radiation in line + continuum from a single region can be evaluated in terms of the individual emission and absorption coefficients:

$$I_{L+c} = \frac{j_L + j_c}{\kappa_L + \kappa_c} \{1 - \exp(-(\tau_L + \tau_c))\} \tag{51}$$

where $\tau = \kappa \Delta x$. This can be written in terms of absorption coefficients alone using eqs. (17), (26) and (40):

$$I_{L+c} = B_\nu \frac{b\kappa_L^* + \kappa_c}{b\beta\kappa_L^* + \kappa_c} \{1 - \exp(-(\tau_L + \tau_c))\} \tag{52}$$

and the Planck function, B_ν, can be eliminated by considering the ratio of the intensity in line + continuum to that in the continuum:

$$\frac{I_{L+c}}{I_c} = \frac{b\kappa_L^* + \kappa_c}{b\beta\kappa_L^* + \kappa_c} \frac{1 - \exp(-(\tau_L + \tau_c))}{1 - \exp(-\tau_c)} \quad . \tag{53}$$

Throughout this discussion the subscripts n and ν have been suppressed, but the line absorption coefficient nonetheless refer to a particular frequency and a particular transition, and the resulting intensities are also functions of frequency.

Specific intensities can be converted into brightness temperatures through the Rayleigh-Jeans approximation to the Planck function

$$T_b = \frac{c^2}{2k\nu^2} I \tag{54}$$

for $h\nu << kTe$. For example, from eqs. (40) and (44) the emergent intensity in the continuum from a homogeneous isothermal medium is

$$I = \frac{j_c}{\kappa_c} (1 - e^{-\tau_c}) = B_\nu (1 - e^{-\tau_c}) = \frac{2kT_e}{c^2} \nu^2 (1 - e^{-\tau_c}) \tag{55}$$

and the brightness temperature in the continuum is

$$T_b = T_e (1 - e^{-\tau_c}) \quad . \tag{56}$$

When the Rayleigh-Jeans approximation is valid, brightness temperatures may be substituted for specific intensities and eq. (49) can be written

$$T_b = \sum_{i=0}^{r} T_{b_i} e^{-p_i} \quad . \tag{57}$$

Note that the Rayleigh-Jeans approximation is not valid for the 2.7 K isotropic background radiation at frequencies near 100 GHz, so in practice eq. (57) must be modified at high frequencies to take this into account.

f) Recombination Lines from Heavier Elements

The discussion of radiative transfer in the previous section is entirely general and will be valid for recombination line and free-free emission from any atomic species provided that the absorption coefficients can be specified. The absorption coefficients of elements heavier than hydrogen must contain terms to account for effects due to the larger mass and the possible difference in effective nuclear charge of these atoms. Palmer (1968) has shown that the hydrogenic approximation (i.e., the Rydberg equation) with an integral effective charge gives an excellent description of an electron's energy for $n \gtrsim 40$.

The free-free absorption coefficient was derived assuming an infinite nuclear mass (Oster, 1961), and thus heavy ions with $Z = 1$ can be included into N_i in the expression for κ_c. If there are a significant number of atoms with $Z > 1$, the absorption coefficient will have to be written $\kappa_c = \Sigma\kappa_c(Z,N_i(Z))$.

The line absorption coefficient must be modified to take into account the difference in the line shape function because of the difference in atomic mass. This function, through the quantity $\underline{a}$, involves the atomic mass, the effective nuclear charge and the Doppler temperature, T_D. A difficulty arises in evaluating T_D for each species, for this temperature includes both thermal and turbulent motions within a

nebulae. The thermal motion is related to the mass of an atom but the turbulent motion is not. For this reason the Doppler temperature can only be determined empirically through observations of Δv_D, unless one has <u>a priori</u> knowledge of both T_e and the magnitude of turbulent motions. These observations must be taken at an n where $a \sim 0$, and may then be used to predict the line shape at larger n. For these purposes it is convenient to combine eqs. (31) and (36) and write $\underline{a}$ in terms of Δv_D

$$\underline{a} = 1.9828\times10^{-16}\ T_e^{-\frac{1}{2}}\ \frac{n^7 N_e}{Z^4 \Delta n}\ \Delta v_D(m_a)^{-1}\ \{\tfrac{1}{2} + \ln(6.366\times10^{-6}\ \frac{nT_e}{Z})\}, \quad (58)$$

where $\Delta v_D(m_a)$ is the Doppler line width in km/s (full-width at half-intensity) of the species with mass m_a. The LTE absorption coefficient may then be written using this expression to determine the line shape with the appropriate ion density in place of N_p.

Dielectronic recombination can overpopulate excited levels of multi-electron atoms by factors of 10^3 relative to the LTE values. This process is most effective at temperatures $\gtrsim 10^4$ K, and departure coefficients in this temperature range are given by Shaver (1976) for magnesium and calcium, and by Dupree (1969) for carbon. Dielectronic recombination is not very effective for helium at normal nebular temperatures ($T_e \sim 10^4$ K), or for any of the more abundant elements when $T_e \lesssim 10^3$ K, so under these conditions the population of heavier elements should be given accurately by the hydrogen departure coefficients (Palmer, 1968; Churchwell, 1970; Brown 1979) as long as Z = 1. For Z > 1 Weisheit and Walmsley (1977) have shown that $b(Z,N_e,T_e) \simeq b(1,N_e/Z^6,T_e)$, and thus the departure coefficients for H_e^+, for example, are easily gotten from those for hydrogen.

With the determination of individual absorption coefficients, a total absorption coefficient over all ionized species can be constructed: $\kappa = \Sigma\kappa(m_a)$, where the parameter $x(\alpha,\nu,\nu_o)$ in the Voigt function is determined using the values of α and ν_o for each species. In practice it is often more convenient to form a complete spectrum by calculating the intensity of each species separately and adding them together shifted in frequency by amounts determined from the Rydberg equation. If this is to be accurate it requires that $|\nu_o(1)-\nu_o(2)| >> \Delta\nu_1,\Delta\nu_2$, that is, it requires that the central frequencies ν_o of the two species be separated by more than the line width of each species. This is necessary because emission from the high-frequency line wing of helium, for example, could stimulate emission in the low-frequency line wing of carbon. Even though $I_{L+c} \sim I_c$ in most HII regions at most frequencies, it is best to construct a total absorption coefficient when lines are closely spaced.

CHAPTER II

NEBULAE AND ANTENNAS

a) General Considerations

The appearance of nebulae in optical photographs suggests that, along any particular line of sight, the temperature and especially the density may change by orders of magnitude. Although it is easy to calculate the radio emission from a small element of gas, it is necessary to understand the behavior of a superposition of many such elements in order to interpret radio recombination line emission. We also observe changes in the brightness from point to point across a nebula, and when such structure is present the object must be treated as two-dimensional. This is particularly important for radio observations because the quantity measured by a radio telescope, the antenna temperature, is the product of the two-dimensional source brightness temperature and an antenna response function. For circularly symmetric antenna beams this product is equivalent to a two-dimensional convolution:

$$T_a \propto T_b * F \ . \qquad (59)$$

Here T_a is the antenna temperature, F is normalized to unit area and the constant of proportionality depends on the specific antenna. When the antenna beam is larger than the nebular structure, the observations may average lines of sight through gas of varying properties. Thus

the antenna temperature is a weighted mean, and the weighting depends on many factors, all of which vary with the detailed nebular structure and with the frequency of observation. These three aspects of the transfer of radio recombination lines, involving structure along and perpendicular to a line of sight and observation with an antenna beam, are the topics of this chapter.

The effects of the antenna beam are important only when radio lines or continuum are not uniform across a nebula, so it is easiest to begin with a discussion of the emission from plane-parallel models which have a uniform surface brightness.

b) Isothermal, Homogeneous, Plane-Parallel Models

In plane-parallel models antenna temperatures are simply proportional to brightness temperatures, and geometric effects disappear. Thus the relevant solution to the equation of transfer is given by eq. (53). If $T_0 = 0$, all characteristics of the antenna can be removed by taking the ratio of the peak line to continuum antenna temperatures:

$$\frac{T_L}{T_c} = \frac{b\kappa_L^* + \kappa_c}{b\beta\kappa_L^* + \kappa_c} \frac{1 - \exp(-(\tau_L + \tau_c))}{1 - \exp(-\tau_c)} - 1, \qquad (60)$$

where $\tau = \int_0^\ell \kappa \, ds$. (Throughout this chapter the 2.7 K isotropic background radiation will be ignored. The magnitude of its effects on a 10^4 K gas can be estimated from the discussion in §IIc and §IIIc; in a lower temperature gas it can be a major factor determining line

intensities.) By expanding the exponentials to second order, Goldberg (1968) has shown that eq. (60) can be written

$$\frac{T_L}{T_c} \simeq \frac{b\kappa_L^*}{\kappa_c} (1 - \beta\tau_c/2) \ . \qquad (61)$$

This is valid only when $\tau_c << 1$ and $|\tau_L + \tau_c| << 1$. If τ_c is very small, $\beta\tau_c/2$ might also be much less than unity and eq. (61) would reduce to the simple ratio of absorption coefficients times the departure coefficient. This latter situation would give a line-to-continuum ratio

$$\frac{T_L}{T_c} \propto \frac{b\nu_0^{1.1}}{T_e^{1.15}} \ (\nu_0\phi_\nu) \ , \qquad (62)$$

where eq. (3) has been substituted for the factor n^3 in κ_L^*, and eq. (39) has been used for κ_c. At sufficiently low n, the line shape will be dominated by Doppler broadening and $\nu_0\phi_\nu$ will be constant. The line-to-continuum ratio may vary by orders of magnitude over the observable frequency range, so it is convenient to normalize it by the quantity 100/ν (GHz) and to define a normalized line-to-continuum ratio

$$L \equiv \frac{T_L}{T_c} \frac{100}{\nu(\mathrm{GHz})} \ , \qquad (63)$$

where hereafter T_L refers to the peak ($x = 0$, $\nu = \nu_0$) line temperature unless otherwise indicated.

The variation of L with principal quantum number for Hnα lines is illustrated in Figure 1 for a region with ℓ = 1 pc and three different

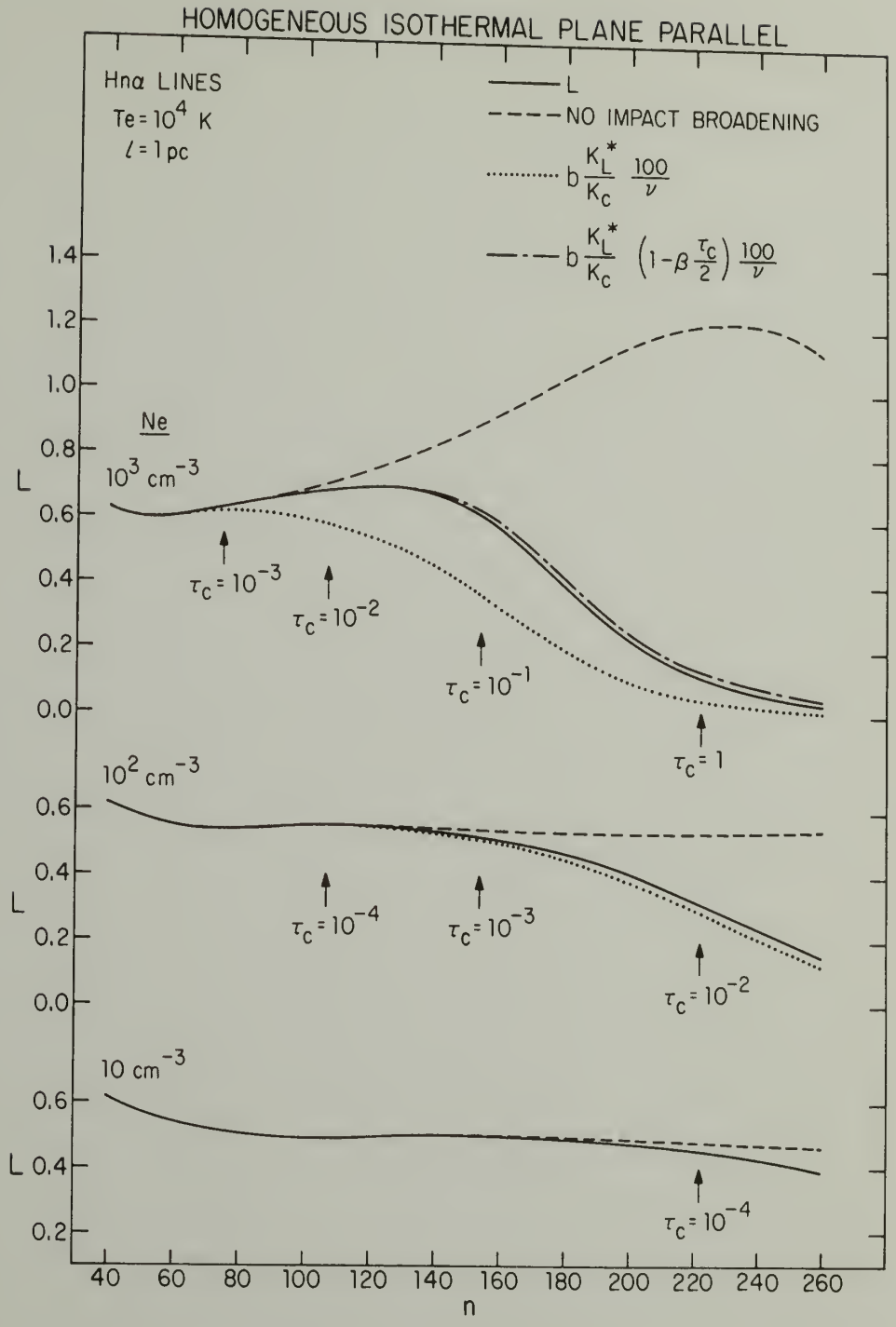

Figure 1: The normalized line-to-continuum ratio L, for three isothermal, homogeneous, plane-parallel models. Two approximations to the exact solution are also shown. Dashed curves show L in the absence of impact broadening. The optical depth in the continuum, τ_c, is indicated for each model.

values of N_e. Here $T_e = 10^4$ K, $T_D = 2T_e$, and $N_e = 1.1N_p = N_i$. Various curves show the range of validity of the approximations in eqs. (62) and (61), and also the reduction in L caused by impact broadening.

In these examples the behavior of L can be characterized by the value of τ_c which is shown beneath each curve. For $\tau_c < 10^{-3}$, L is not very sensitive to N_e; in this regime, where L can be approximated by eq. (62), the density enters only through its slight effect on b. When $\tau_c \gtrsim 10^{-3}$, stimulated emission, entering through the quantity $\beta\tau_c/2$ in eq. (61), enhances the line intensity above the value given by eq. (62), and L increases. When $\tau_c \gtrsim 10^{-1}$, the approximation used to derive eq. (61) is no longer valid and eq. (60) must be used. The effect of impact broadening on the peak line intensities is quite striking. In the densest gas it has reduced L by nearly an order of magnitude at $n \sim 200$, and even with $N_e = 10^2$ cm^{-3} it produces a noticeable effect at $n \sim 150$.

[Although it is more convenient to study the ratios of temperatures than the actual antenna or brightness temperatures, brightness temperatures depend on the optical depths [eq. (51)], and T_L will increase with $|\tau_L|$ when all other conditions are equal. Thus, for the models displayed in Figure 1, the value of T_L from the $N_e = 10^3$ cm^{-3} region at $n = 200$ will be $\sim 10^3$ times greater than the value of T_L from the region with $N_e = 10$ cm^{-3} even though at this transition $L(N_e = 10^3 \text{ cm}^{-3}) < L(N_e = 10 \text{ cm}^{-3})$].

It is worthwhile to consider the role of stimulated emission in the line formation and transfer in some detail. The magnitude of

this process depends both on the extent of the atomic population inversion and on the number of photons available to induce the transition. Even under conditions of LTE ($b_n = b_m = 1$) there is stimulated emission, but its rate is less than that for absorption and serves only to reduce the magnitude of the absorption coefficient. When the level populations depart from their thermal equilibrium values, a significant population inversion can occur and stimulated emission can be more likely than absorption. This is the case for nearly all temperatures and densities of interest; a positive κ_L is the exception rather than the rule. The population inversion is characterized by the quantity β, which contains information on relative level populations through the term $d(\ln (b_n))/dn$. Figure 2 shows the magnitude of these quantities and of κ_L for the temperature and densities of the preceding models. The departure coefficients were taken from Brocklehurst (1970). The line absorption coefficient is positive only for $N_e = 10^4$ cm^{-3} and $n > 210$.

In isothermal homogeneous models with $I_0 = 0$ the photons which stimulate emission in a volume of gas are formed within that gas. In the cases discussed here $T_L + T_c \sim T_c$, so when $|\tau_L + \tau_c|$, $\tau_c << 1$ the number of incident photons is proportional to τ_c and the emission is described by eq. (61). In terms of this equation, stimulated emission will significantly increase the line intensities when $-\beta\tau_c/2 \gtrsim 0.1$. For the models shown in Figure 2, $-\beta \lesssim 10^2$, and stimulated emission can begin to affect the line intensities when τ_c reaches a value $\sim 10^{-3}$. In a 10^4 K nebula $\tau_c \sim 10^{-3}$ when $\nu(\text{GHz})^{2.1} \sim 3\text{x}10^{-4}$ E,

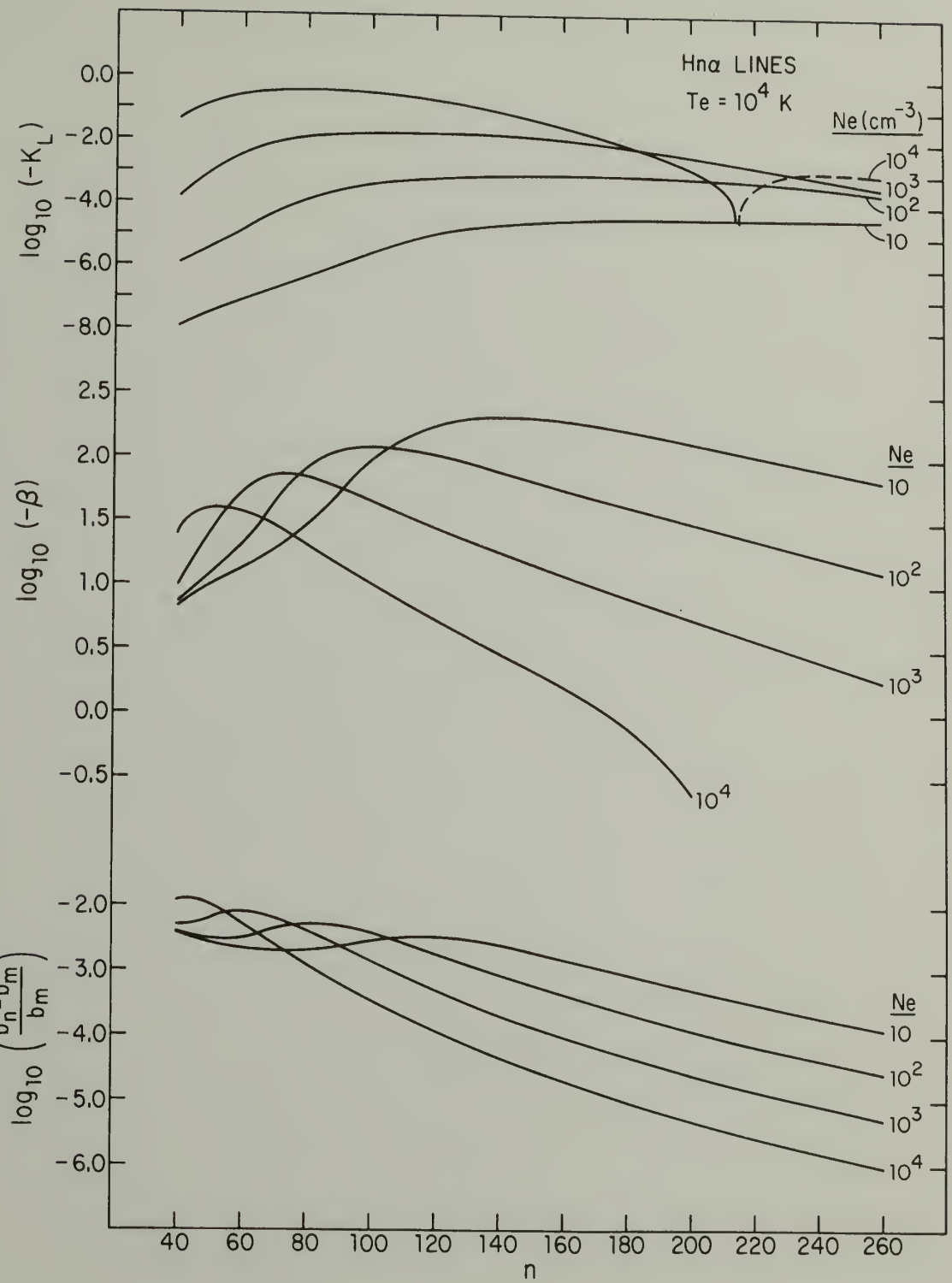

Figure 2: The quantities $(b_n-b_m)/b_m$, β, and κ_L for a few densities at $T_e=10^4$K. The quantity κ_L was calculated for a gas with $T_D=2T_e$ and $N_e=N_i=1.1N_p$. When $\kappa_L>0$ it is drawn in a dashed line.

where E, the emission measure, is $N_e N_i \ell$ in units of cm^{-6} pc.

Stimulated emission may occur in regions of even lower continuum optical depth if a nebula has structure such that one part of the nebula provides photons that stimulate line emission in another part (Brocklehurst and Seaton, 1972). In this case τ_c in a given region would no longer be necessarily related to the total number of photons in that region, and there may be significant line enhancement for very small τ_c.

c) Isothermal, Homogeneous, Plane-Parallel Models with a Background Source

When $T_0 \neq 0$ the solution to the equation of transfer for a line of sight through an isothermal homogeneous region must be written

$$T_L+T_c = (T_L+T_c)_1 + (T_c)_0 \exp(-(\tau_L + \tau_c)_1),$$
$$T_c = (T_c)_1 + (T_c)_0 \exp(-(\tau_c)_1), \qquad (64)$$

where region 0 is behind region 1, and for the moment it is assumed that $(T_L)_0 = 0$. Line enhancement occurs when $(\tau_L)_1 < 0$. The magnitude of the enhancement can be estimated by examining T_L/T_{L1}, the ratio of the total peak line temperature to that obtained in the absence of a background source. From eq. (64),

$$\frac{T_L}{(T_L)_1} = 1 + \frac{(T_c)_0}{(T_L)_1} \{\exp(-(\tau_L+\tau_c)_1) - \exp(-(\tau_c)_1)\} \qquad (65)$$

and, when $|\tau_L + \tau_c| \ll 1$ and $\tau_c \ll 1$,

$$\frac{T_L}{T_{L1}} \simeq 1 - \frac{T_{c_0}}{T_{L1}} \tau_{L1} \cdot \qquad (66)$$

The relative continuum temperature of two optically thin ($\tau_c \ll 1$) regions is a constant, $f \equiv T_{c_0}/T_{c1}$, and, using the definition of L, eq. (66) can be written

$$\frac{T_L}{T_{L1}} \simeq 1 - \frac{100\ f}{L_1\ \nu} \tau_{L1} \cdot \qquad (67)$$

Since $L \sim 1$, and in most cases $|\tau_L| < 10^{-2}$, it is clear that f must be much greater than unity for the enhancement to be significant. This is illustrated in Figure 3, where eq. (65) has been evaluated for the $N_e = 10\ cm^{-3}$ region used in the previous example at values of f between 0 and 10^3. As expected, the enhancement is important only when $f \gg 1$, indicating that in order to alter the line intensities the background source must have a much larger continuum brightness temperature than the foreground source. Depending on the magnitude of f, significant enhancement can occur at $n \sim 100$ (in contrast to the situation for the same region with $T_0 = 0$, where stimulated emission is not important for $n < 180$), and at large n line intensities may be increased by orders of magnitude. It should be emphasized that Figure 3 shows realistic situations: $f = 10^3$ corresponds to a density ratio of only $10^{1.5}$ between the same size background and foreground sources. Larger contrasts than this are often encountered along the

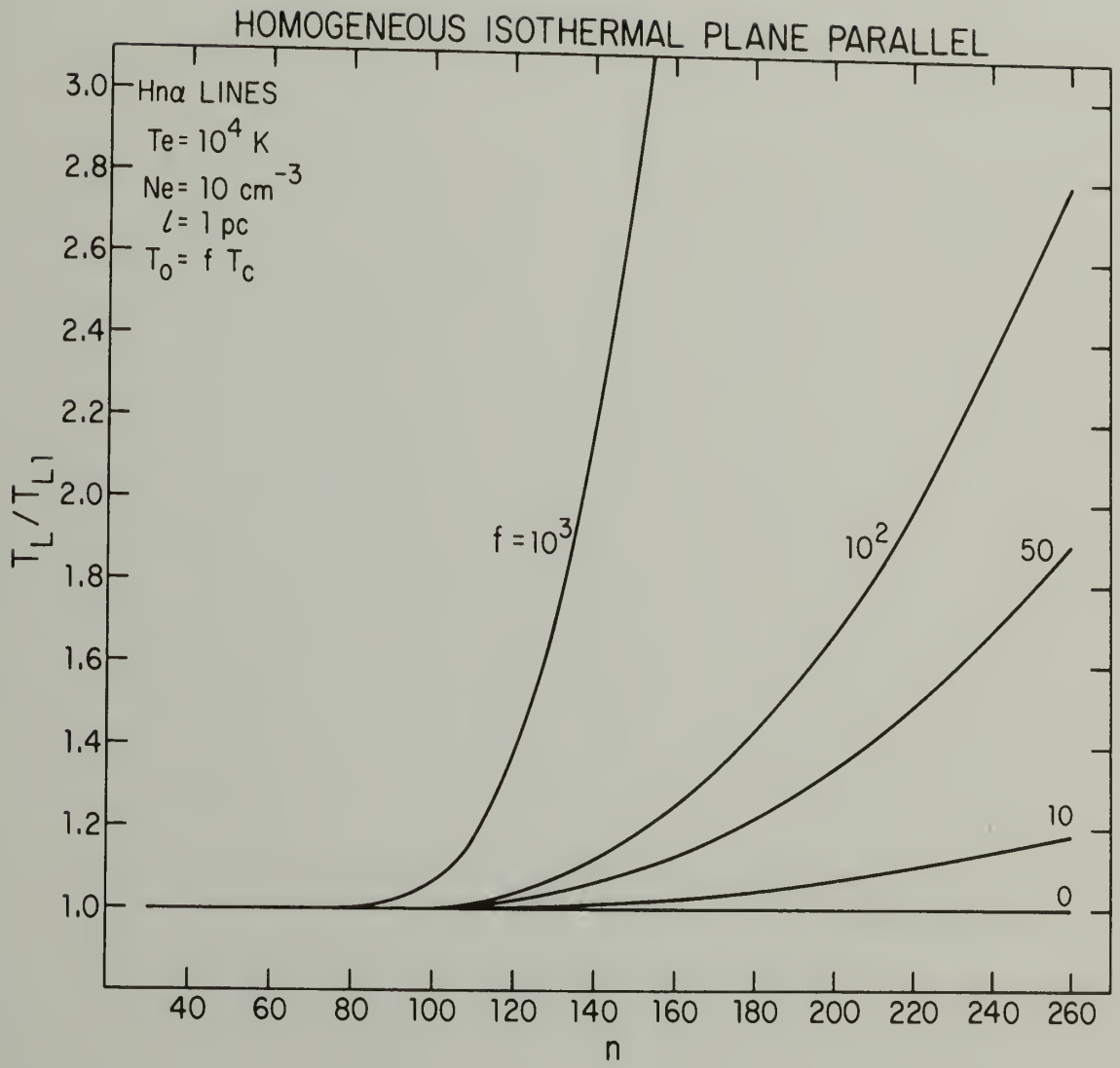

Figure 3: Line enhancement by a background continuum source. The brightness temperature T_0 of the background source is some multiple, f, of the continuum from the foreground source, T_c.

line of sight through nebulae, thus lines from foreground gas may be enhanced by orders of magnitude.

Figures 1 and 3 show that, in the simple case of a dense region behind a more tenuous one, the decrease in L from dense gas at large n (owing to impact broadening) may be somewhat compensated by line enhancement in foreground gas. This is a very interesting situation because it suggests that under some circumstances most of the continuum might come from region 0, but most of the line might be formed in region 1 through emission stimulated by region 0.

Although it is difficult to derive general rules for the behavior of line and continuum from a superposition of more than one isothermal, homogeneous region, it is possible to determine the circumstances which will make a majority of the total line arise in one region, and a majority of the continuum in another. Consider the ratio of the emergent line intensity which originates in region 1 to that which originates in region 0:

$$\frac{T_{L1}}{T_{L0}} = \frac{T_{L1}' + (T_L'+T_c')_0 \{\exp(-(\tau_L+\tau_c)_1) - \exp(-(\tau_c)_1)\}}{T_{L_0}' \exp(-(\tau_c)_1)}, \quad (68)$$

where primed quantities indicate the brightness temperature in the absence of another region. The situation is most interesting when both regions have the same electron temperature, assumed to be 10^4 K, so that the condition that most of the continuum arises in the background region requires $\tau_{c_0} > \tau_{c1}$ and $\tau_{c1} < 1$. Because we are discussing

the case of a dense region behind a more tenuous one, $N_e(0) > N_e(1)$. When $|\tau_L + \tau_c|_1 << 1$ and $\tau_{L1} << 1$, the exponential terms in eq. (68) can be expanded, and because in virtually all cases $T_{L0}' << T_{c_0}'$,

$$\frac{T_{L1}}{T_{L0}} = \frac{T_{L1}'}{T_{L0}'} - \frac{T_{c_0}'}{T_{L0}'}\tau_{L1} = \frac{T_{L1}'}{T_{L0}'} - \frac{100\ \tau_{L1}}{L_0'\ \nu}, \qquad (69)$$

where L_0' is the normalized line-to-continuum ratio from region 0 and it is assumed that $1 - \tau_{c1} \tilde{\simeq} 1$. The second term in this equation shows the relative line enhancement caused by the background source. When this term is > 1, the enhanced portion of the line from region 1 will make the largest contribution to the total line temperature. If region 0 is relatively dense ($N_e \sim 10^3$ cm^{-3}), and has a size $\sim$ 1 pc, then $L_0' \lesssim 0.5$ and the enhancement will preferentially occur at low frequencies ($\nu \lesssim 1$ GHz), and at rather large negative optical depths in the line ($|\tau_L|_1 \gtrsim 10^{-3}$). At ν = 1 GHz (n $\sim$ 185), Figure 2 shows that, for $N_e \sim 10^2$ cm^{-3} and $\ell \gtrsim 1$ pc, τ_L will have the required magnitude and sign. Also, since $\tau_c \propto N_e^2$ and $\tau_{c1} < \tau_{c_0}$, in this case most of the continuum will come from region 0 and most of the line will be formed in and reflect the conditions of the less dense gas. This effect depends strongly on frequency: when $\nu >> 1$ GHz, the total continuum and line will be dominated by region 0; when $\nu << 1$ GHz, where $\tau_{c1} \sim 1$, most of the line and continuum will arise in region 1.

In this example, the requisite optical depth in the line occurs only over a narrow range in density: for $N_{e1} << 10^2$ cm^{-3} τ_{L1} will be too small; if N_{e1} is too much larger than 10^2 cm^{-3} the optical

depth in the line will be large, but the region will also tend to dominate the continuum emission. However, because the optical depth in the line and continuum have different dependencies on T_e, a nebula with a temperature gradient in the same sense as its density gradient can produce, at some frequencies, most of its continuum in the hotter, more dense gas, and most of the line in cooler, less dense foreground gas. This is an important consideration when interpreting observations of objects which lie behind partially ionized cool clouds, e.g., the line of sight towards the galactic center (Lockman and Gordon, 1973; Brown and Balick, 1973).

Brocklehurst and Seaton (1972) and Hoang-Binh (1972) were the first to recognize that in an inhomogeneous nebula the Hnα lines and the continuum might originate in somewhat different parts of the nebula, and that different Hnα lines might also arise from different parts of the nebula. This effect explains the relatively narrow observed width of low-frequency recombination lines from nebulae which contain dense gas. However, this conclusion is not specific to α transitions. Radio recombination lines from higher order transitions may also arise in different gas than the continuum, and because the effect depends on τ_L, the major portion of the total α line intensity at a given frequency may not necessarily arise in the same gas as the major portion of the intensity of higher order lines at a nearby frequency. The fact that a given transition might reflect conditions in only one part of a nebula means that nebular properties generally cannot be <u>derived</u> from observations but instead must be inferred from

models constructed to agree with the data. The information contained in observations of a few transitions over a limited frequency range is usually not sufficient to determine the thermodynamic properties of a nebula.

Although we have only considered the superposition of two regions along the line of sight, it is clear from the series formulation of the solution to the equation of transfer (eq. 57) that this is equivalent to considering any number of isothermal homogeneous regions along the line of sight. The quantities T_{L0} and T_{c_0} are merely the brightness temperatures impinging on region 1 from behind; they could represent the emergent temperatures from any combination of thermal sources or, in the case that $T_{L0} = 0$, from non-thermal sources or the 2.7 K isotropic background radiation.

d) Geometric Effects

In plane-parallel models, all lines of sight are equivalent and the radiative transfer of recombination lines can be studied without geometric complications. Real nebulae, however, are not plane-parallel objects, and the path length through the ionized gas may differ along each line of sight. This aspect of radio recombination line emission, along with the related problem of antenna beam effects, has been discussed by Lockman and Brown (1976). In this section we will consider a more realistic geometry: the spherical nebula illustrated schematically in Figure 4.

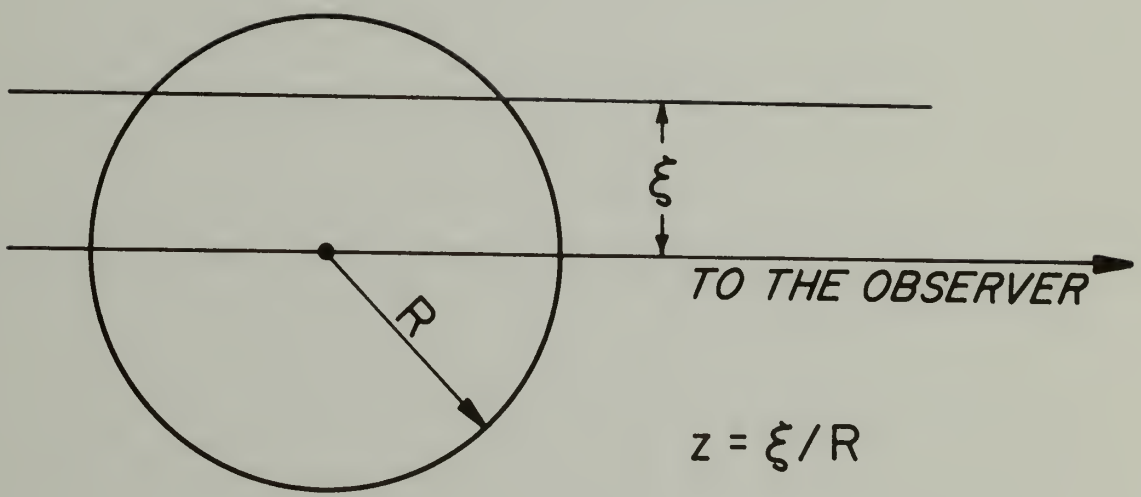

Figure 4: Schematic of a spherical nebula. A line of sight through the nebula is ξ pc distant from the line of sight through the center. In units of the nebular radius, the displacement is given by z.

Here it is assumed that all lines of sight are parallel to the one through the center. The linear displacement of any line of sight from the one through the center is ξ in pc. We define a dimensionless parameter $z \equiv \xi/R$, so that the length of any chord through the sphere is

$$\ell(z) = 2R\ (1 - z^2)^{\frac{1}{2}} \tag{70}$$

where R is the outer radius of the sphere. (Note that this definition of z differs from that used by Lockman and Brown.) In homogeneous, isothermal nebulae where $\tau_c << 1$, $T_c \propto \ell$ and the point at which the continuum brightness temperature has fallen to one-half the peak value, $T_c(z) = 0.5\ T_c(0)$, occurs at $z = \sqrt{3/4}$.

In an isothermal, homogeneous, spherical nebula where $|\tau_L + \tau_c| << 1$ and $\tau_c << 1$, eq. (61) provides a good description of the emergent line to continuum ratio, and it can be written in terms of z:

$$L(z) = \frac{100}{\nu(\mathrm{GHz})} \frac{b\kappa_L^*}{\kappa_c} (1 - \beta\kappa_c \ell(z)/2) \quad \propto \quad (1 - \beta\kappa_c R(1-z^2)^{\frac{1}{2}}). \tag{71}$$

As both line and continuum temperatures vary with z owing to the presence of the second term in eq. (71), their ratio L will also vary with z. This is illustrated in Figure 5, where the full solution to the equation of transfer has been evaluated for Hnα lines from a region with $T_e = 10^4$ K, $N_e = 10^3$ cm^{-3}, R = 0.5 pc, $T_D = 2T_e$ and $N_e = 1.1\ N_p$, for values of z between 0 and 0.96. In this model T_L and T_c have their largest values at z = 0, and the same is true

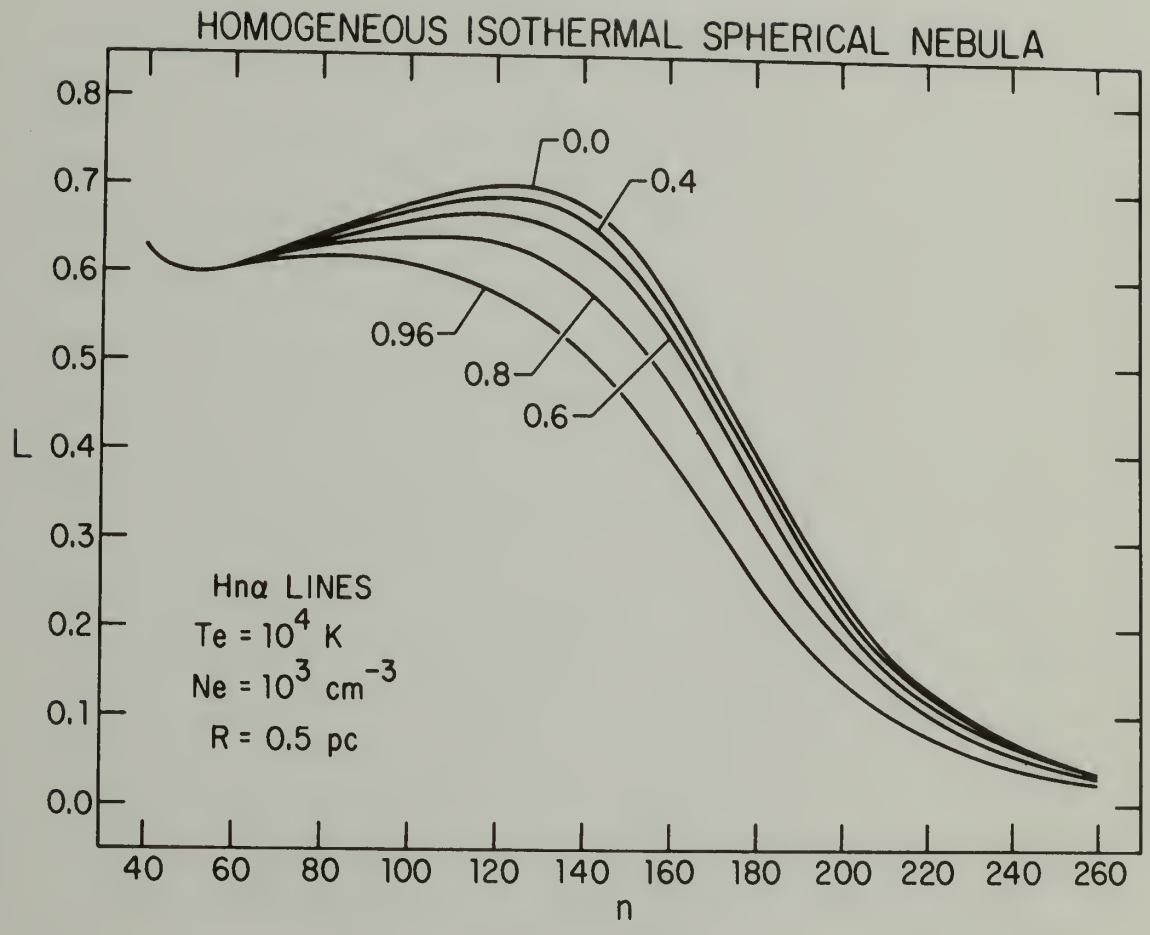

Figure 5: L(n) along a line of sight offset by z nebular radii from the center of a homogeneous, isothermal, plane-parallel, spherical nebula. Each curve is labeled by its value of z.

for their normalized ratio L. The function L(z) varies with frequency owing to the frequency dependence of β and κ_c. In this model L has its largest value at z = 0, but the exact change in L with z depends on all properties of the system.

It is clear that the nebular geometry has an important effect on the emergent lines: changes in the path length can mimic changes in <Te> or <Ne>. Thus the path length, which cannot be observed directly, is an important factor in the line formation process, and causes the shape and size of models to be almost as important as the temperature and density. A finite antenna beam averages over many lines of sight, and the path length effect enters into most observations.

e) Observation with an Antenna Beam

If the antenna beam is circularly symmetric, then observation is equivalent to the convolution of two two-dimensional functions f and g:

$$h(x,y) = g(x,y)*f(x,y) \equiv \int_{-\infty}^{\infty}\int g(x',y')\ f(x-x',y-y')\ dx'dy' \qquad (72)$$

(e.g., Bracewell 1965). The functions can be expressed in terms of a single variable r (or z), but the convolution remains two-dimensional. It can be calculated directly from its definition, through Fourier transform techniques, or, in the case of total circular symmetry,

through Hankel transforms. A radio telescope detects $T_a = \eta T_b * F$ [eq. (59)], where F is normalized to unit area and η depends on individual antenna characteristics. The exact form of F depends on the antenna structure and illumination: for a single parabolic reflector the main portion of F is often close to a circular Gaussian function characterized by a standard deviation σ_a and a half-power beam width $\Gamma = 2.355\ \sigma_a$, both of which increase linearly with wavelength over almost the entire operating range of the instrument. For this reason the antenna response function is taken to be

$$F(z) = \frac{1}{2\pi\sigma_a^2} \exp(-z^2/2\sigma_a^2). \qquad (73)$$

When $\sigma_a \to 0$ $F(z) \to \delta(z)$ giving $T_a \propto T_b$; when $\sigma_a \to \infty$, F(z) becomes constant and $T_a \propto \int T_b$.

Some characteristics of convolution are illustrated by considering a circularly symmetric source with a normalized Gaussian brightness distribution characterized by σ_s. The antenna temperature is then

$$T_a(z) \propto \frac{1}{2\pi(\sigma_a^2+\sigma_s^2)} \exp(-z^2/2(\sigma_a^2+\sigma_s^2)), \qquad (74)$$

where, in order to use the parameter z, the source brightness temperature is assumed to be negligible beyond some finite R. Consider the case when $\sigma_a = \sigma_s$. Here F and T_b have the same dependence on z, and

an antenna directed toward z' will receive equal emission from a unit area at z' and a unit area at the nebular center (z = 0). But, to obtain a Gaussian surface brightness distribution, either T_e, N_e or ℓ must vary with z; and if any of these vary, L(z) will generally not be constant. Thus the observed L(z) will usually differ from the true L(z).

This can be discussed a bit more quantitatively by assuming circular Gaussian brightness temperature distributions in both line and continuum, but with $\sigma_L \neq \sigma_c$. For an antenna beam at z,

$$L \propto \frac{\sigma_c^2+\sigma_a^2}{\sigma_L^2+\sigma_a^2} \exp\left(-\frac{z^2}{2}\left(\frac{1}{\sigma_L^2+\sigma_a^2}-\frac{1}{\sigma_c^2+\sigma_a^2}\right)\right), \qquad (75)$$

and even when z = 0 the observed L differs from the true L by an amount which depends on σ_a. Because σ_a, σ_L and σ_c all vary with frequency, it is clear that the effect of beam convolution must be considered separately for each transition and each antenna.

Models with Gaussian surface brightness distributions are very artificial. To show how beam convolution effects manifest themselves in a simpler model, the surface brightness for the spherically symmetric, isothermal, homogeneous 10^4 K 10^3 cm^{-3} region discussed in the previous section was convolved with a circular Gaussian antenna response function having half-power beam widths $\Gamma << R$, $\Gamma = R$ and $\Gamma >> R$, where again R is the radius of the nebula. In the first case Γ was chosen to be so small that T_a was linearly proportional to T_b. In the last case the beam was so large that the response was constant

over the entire source. Results of the convolution are shown in Figure 6 for n = 100, 150, and 200. Even in this extremely simple model, it would be difficult to derive the true L(z) from observations taken with $\Gamma \geq R$. Of course the observed antenna temperatures in line and continuum do decrease with increasing z. It is only because T_L and T_c do not generally have the same dependence on z that beam convolution has such an important effect.

To summarize, a given brightness temperature T' will appear to an observer using a telescope of finite beam width as an antenna temperature weighted by the surface area over which the brightness temperature is equal to T' and by the antenna response to that surface area. In general, the convolution will be different for line and continuum.

As we explore more and more complications in the transfer of radiation from atom to observer, it appears that the quantity L depends, to some degree, on every phase of the transfer. This is true. Nonetheless, the use of the ratio L is the simplest and most accurate way to describe radio recombination line emission. The antenna only enters into the ratio through the normalized antenna response function; if antenna temperatures in the line and continuum were treated separately, an additional factor would be needed to account for the telescope efficiency. Also, in a properly designed experiment, L can be determined more accurately than the individual line and continuum antenna temperatures because the calibration of the antenna temperature scale does not enter L.

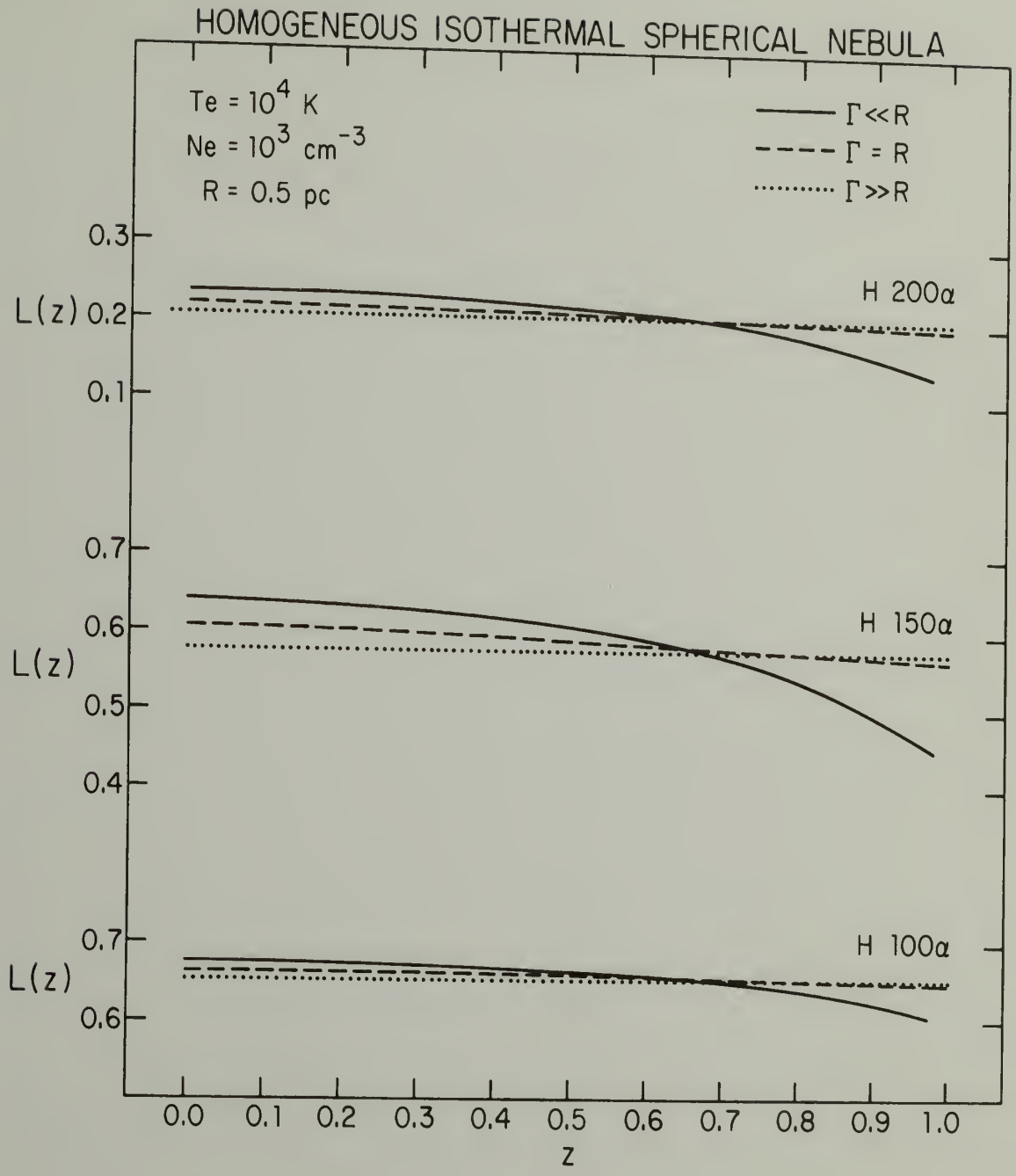

Figure 6: The normalized line-to-continuum ratio of a homogeneous, isothermal, spherical nebula, observed with a circular Gaussian antenna beam, as a function of z for three transitions. The antenna beam's full-width at half maximum, Γ, is either very small, very large, or of a size equal to the nebular radius.

f) A Varying Density Model

In this section we examine a model which illustrates most of the major factors in the formation and transfer of radio recombination lines. The model is spherically symmetric, isothermal, and consists of three regions numbered in order of their distance from the center of the nebula. The regions have outer radii R(I) = 0.05 pc, R(II) = 0.50 pc and R(III) = 1.50 pc, with densities $N_e(I) = 10^{4.5}\ cm^{-3}$, $N_e(II) = 10^{3.5}\ cm^{-3}$ and $N_e(III) = 10^{2.5}\ cm^{-3}$. Throughout the model $T_D = 2T_e$, $T_e = 10^4$ K and $N_e = N_i = 1.1\ N_p$.

The surface brightness is convolved with three different circular Gaussian antenna beams having $\Gamma << R$, $\Gamma >> R$ and $\Gamma(n = 150) = R$, all centered at z = 0 (i.e., the nebular center). The first beam reproduces true brightness temperatures, the second averages the brightness temperatures weighted by their surface area, and the last, where $\Gamma(150) = R$ and Γ varies inversely with frequency, simulates observations with a real antenna.

Figure 7 shows the peak L(n) (i.e., the value of L at x = 0) for Hnα lines and the three antenna beams. Dashed curves are the ratios of the lines formed in each region to the total continuum, showing the fraction of the total line intensity that originates in each region at a given n.

With the smallest beam, we observe the ratio of the brightness temperatures along a line of sight through the center of the nebula. Over a large range in n the densest gas dominates the emission, and from n = 40 to n = 80, as τ_c in Region I increases, stimulated

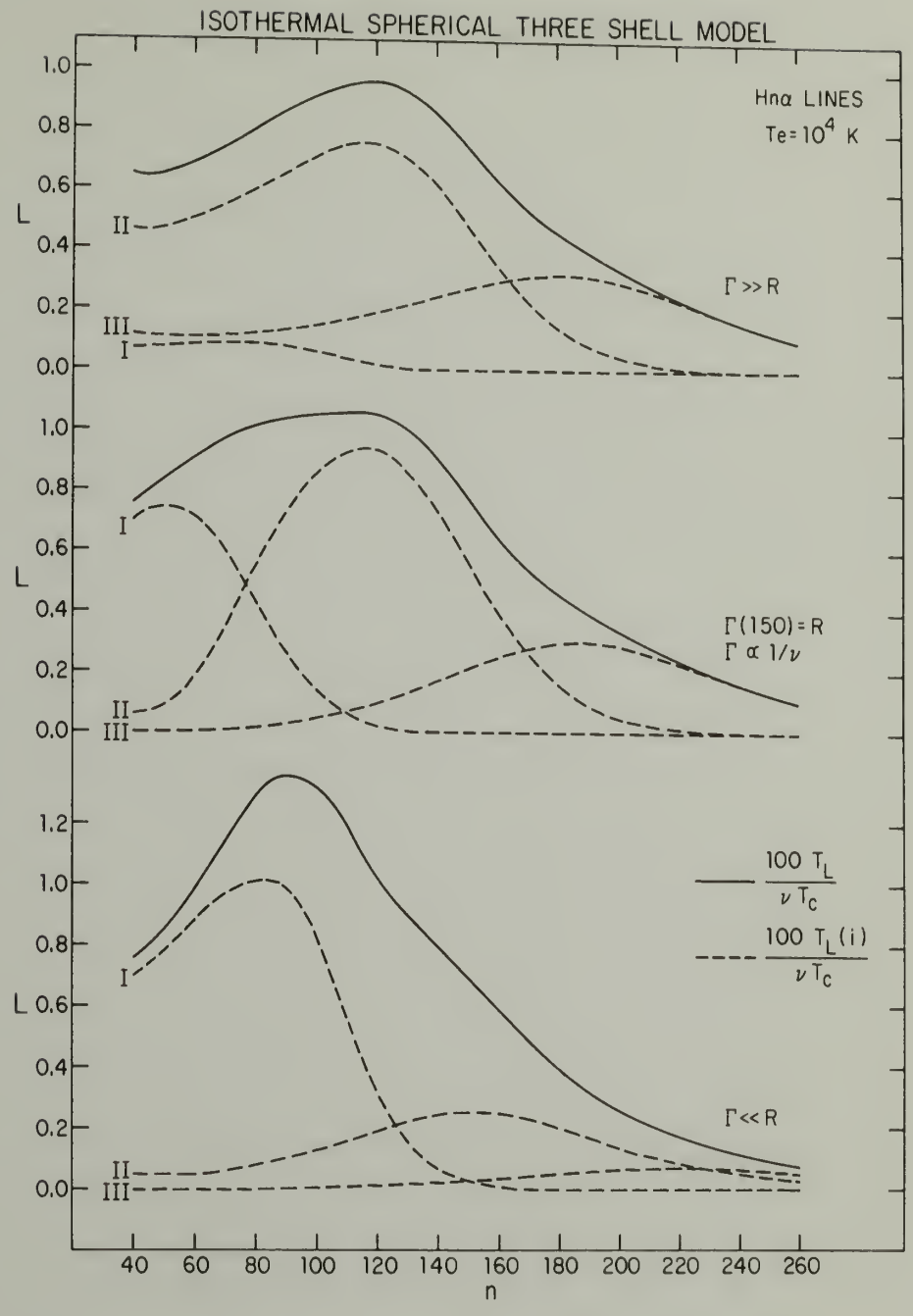

Figure 7: L(n) from an inhomogeneous isothermal nebula. The lower set of curves is for a narrow line of sight through the model at z=0, the upper set shows L for a beam much larger than the nebula, and the middle set shows L when the beam-width varies inversely with frequency and $\Gamma(n=150) = R$. The dashed lines show the contribution to the total T_L of each region in the model. Region I is the most dense and the smallest; Region III is the least dense and the largest.

emission in that region causes the total L to rise. Beyond n = 80, $|\tau_L(I)|$ decreases with increasing n owing to the combination of a decrease in the value of β, impact broadening, and eventually, large optical depths in the continuum. For n > 130 most of the peak line intensity comes from Region II, first through emission stimulated by the continuum radiation from Region I, then increasingly through emission stimulated by its own continuum. The total L, however, continues to fall because the extra line emission is not enough to compensate for the large amount of continuum radiation from Region I. In addition, Region I is optically thick for n > 110 and the parts of Regions II and III which lie behind it no longer contribute to the surface brightness. At very large n, Region III begins to contribute to the peak line emission, and for n > 230 it produces most of the brightness temperature at the line peak. The quantity L has its largest value at an n close to the peak in the Region I emission because Region I dominates this line of sight at most frequencies.

When $\Gamma >> R$, most of the observed line originates in Regions II or III simply because Region I has a small surface area compared with the others. For the same reason, the point at which Region III begins to contribute most of the line is shifted to lower n; with a large antenna beam it is not just the value of the brightness temperatures in line and continuum that determines the balance of emission between the regions, but the temperatures weighted by their surface area. In this case the maximum value of L occurs at an n near the peak in the Region II curve.

When the antenna beam width varies inversely with frequency, being sometimes larger and sometimes smaller than the nebula, the quantity L will approach the true brightness temperature ratio at low n (high ν) and will reproduce the $\Gamma >> R$ results at high n. The contribution of Region I decreases more rapidly with n than in the previous examples because of progressively increasing beam dilution, yet since the beam is relatively small at the higher frequencies, Region I dominates at low n. The peak in L is broadened by the changing beam size, and in this example it shows the influence of the peaks in both Regions I and II.

It is interesting to make a more detailed examination of the fraction that each Region contributes to the line and continuum. For this illustration the intensities of the Hnβ lines were also calculated. Figure 8 shows the ratios $T_L(i)/T_L(\text{Total})$ for both α and β lines and the ratio $T_c(i)/T_c(\text{Total})$ for the continuum as a function of frequency. The ordinate is drawn so that n increases to the right; the H40α and H50β lines are near 100 GHz and the H185α and H235β lines are near 1 GHz. These quantities were calculated for the antenna beam that varies inversely with frequency. When the α and β lines and the continuum from one region contribute equal fractions to the total at any frequency, the solid, dashed and dotted lines coincide. This is not generally the case. For example, at $\nu \sim 1.5$ GHz more than half of the continuum and the α line come from Region II, but a majority of the β line comes from Region III. At $\nu \sim 1$ GHz, most of the α and β lines come from Region III, but most of the continuum

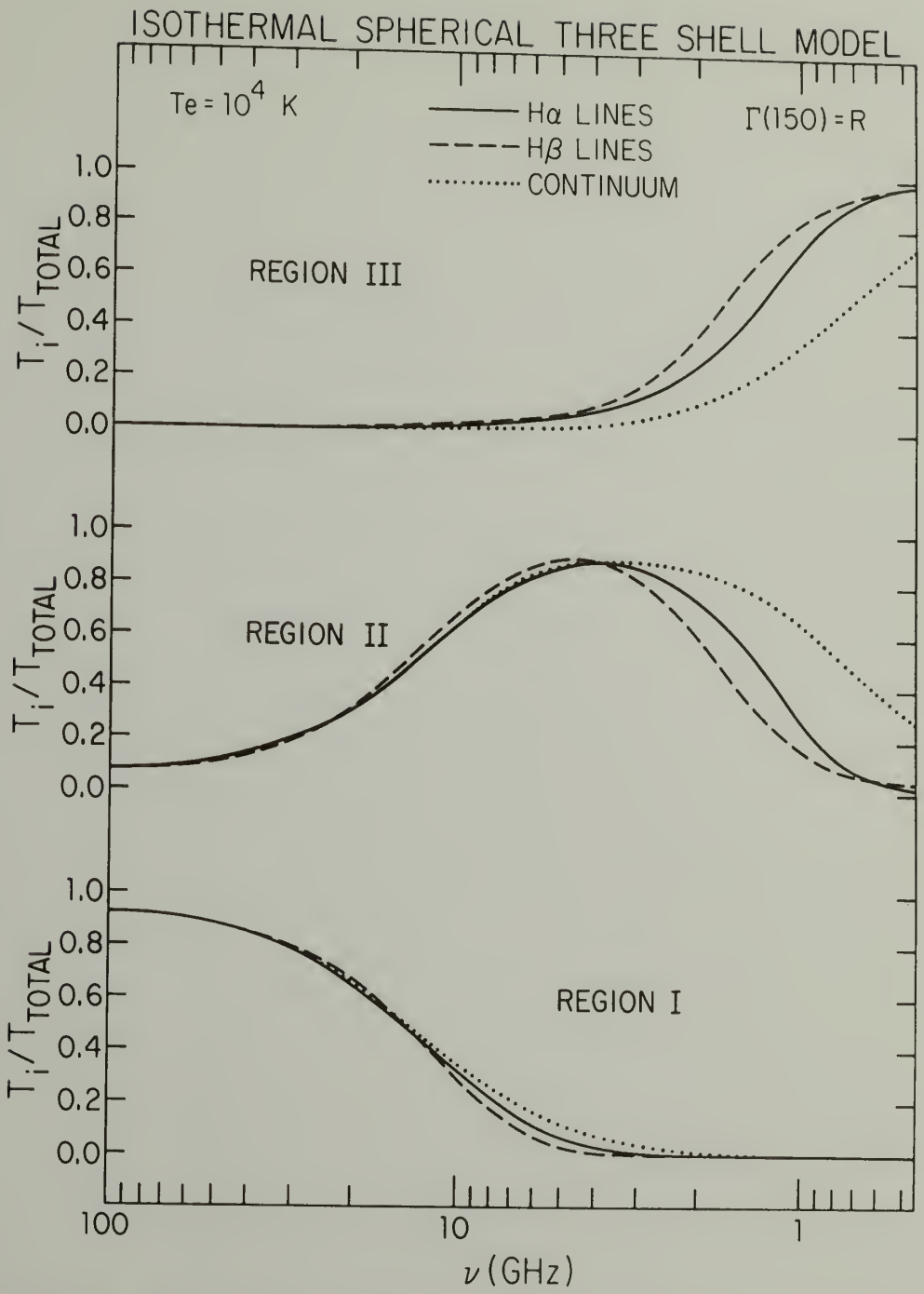

Figure 8: The fraction of the total Hnα line (solid curve), Hnβ line (dashed curve) and continuum (dotted curve) as a function of frequency for the three Regions. When the lines and continuum at a given frequency come equally from the same nebular gas, the solid, dashed and dotted lines coincide. These calculations were made for an antenna beam that varied inversely with frequency and that had Γ(n=150) = R.

still arises in Region II. At higher frequencies, the effect is reduced somewhat, but is still present.

This model illustrates a general rule for isothermal nebulae: lines emitted at high frequencies will tend to be formed in the more dense nebular gas, and lines emitted at lower frequencies in less dense nebular gas. The exact weighting depends somewhat on the size of the regions relative to the antenna beam as well as on the densities, but even when $\Gamma >> R$ the trend is evident.

A radio recombination line is a superposition of Voigt profiles, sometimes appearing as nearly Gaussian, other times showing broad wings. (If the optical depth at the line peak approaches -1, lines may be "narrowed" through maser amplification and they will have neither a Gaussian nor a Voigt profile. This is evident in some of the models discussed in Chapter III.) Representative line shapes for the spherical model are shown in Figure 9. Each curve has been normalized to its own peak value. Lines from the densest gas are the broadest, and the smaller the beam, the more this gas contributes to the overall line shape at $z = 0$. This is the source of the change in line shape with antenna beam width. The strong dependence of impact broadening on principal quantum number results in a progressive broadening of the profiles with increasing n. The line shape also depends on z. Toward the edge of this model, dense gas contributes a smaller fraction to the total line, and, as one goes from $z = 0$ to $z = 1$, there is a narrowing of the lines at some frequencies.

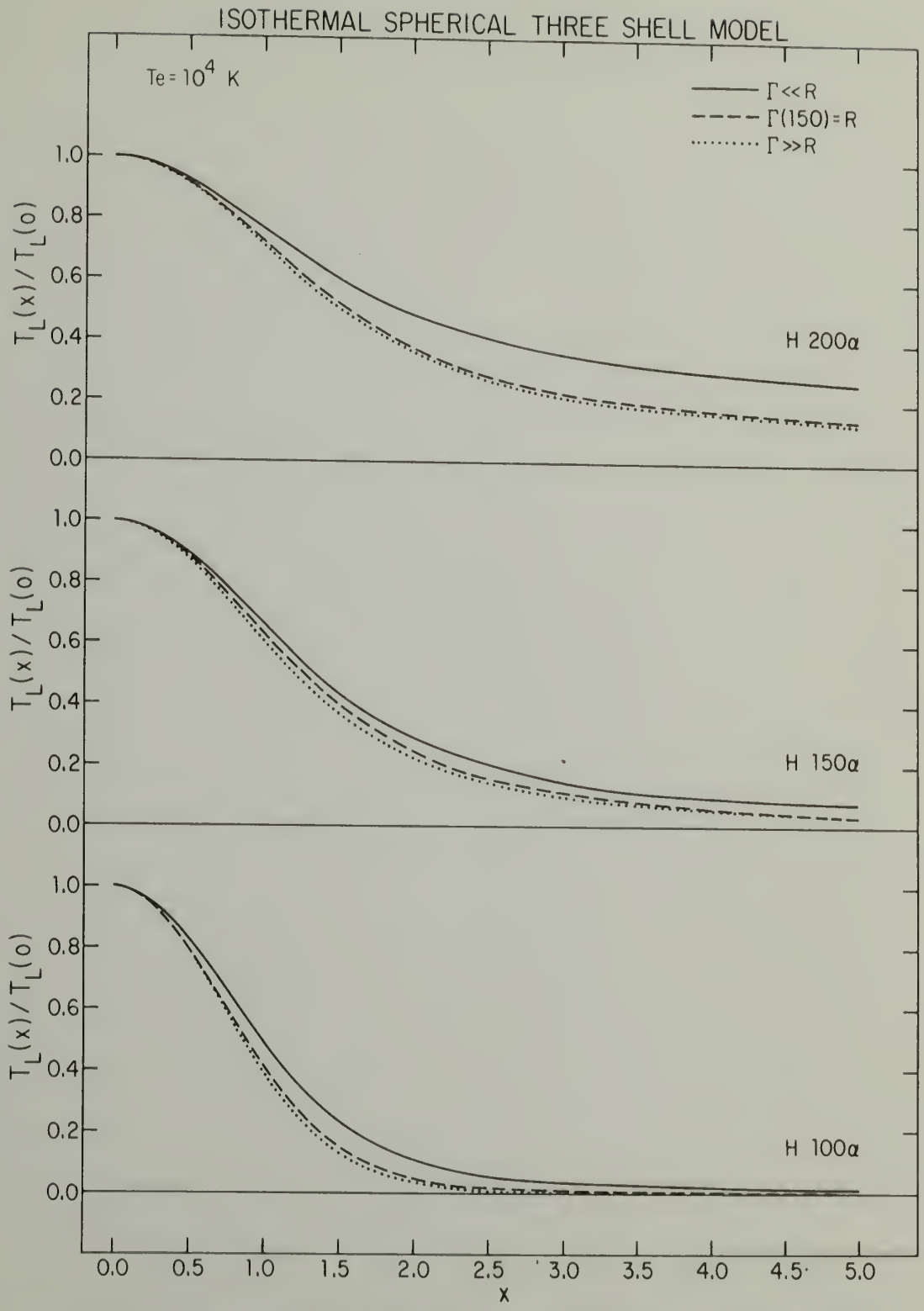

Figure 9: The shapes of Hnα recombination lines from the three shell model for antenna beams at z=0.

Finally, it is worthwhile to examine L(z) at a few transitions. This quantity is plotted in Figure 10, where the solid line shows the true brightness temperature ratio and the dashed line the ratio "observed" with the $\Gamma(150) = R$ antenna beam offset z radii from the center of the nebula. Because this beam varies with frequency, the actual full-width at half-maximum was 0.3 R, R and 2.4 R at n = 100, 150 and 200, respectively.

Positions where the line of sight intersects the edge of a region stand out quite clearly. Lines of sight with $z > 0.33$ do not intersect Region I, and those with $z > 0.33$ do not intersect Region II. The discontinuities in L(z) illustrate the importance of the competing processes of stimulated emission and impact broadening. Stimulated emission, which tends to increase L, is a function of T_e, N_e, n and ℓ: impact broadening, which decreases the peak line intensity, depends almost solely on N_e and n. At n = 100 impact broadening in Region I reduces the peak line intensity by a negligible factor considering the substantial line enhancement. Because Region I dominates the low z lines of sight at this transition, as z increases and the path length through this region becomes smaller, there is less line enhancement and L decreases. The ratio shows the same general behavior when Region II dominates the line of sight, as can be seen in the decrease in L from z = 0.04 to z = 0.35. There is not much enhancement in Region III at this frequency, so for large z, where this is the only region along a line of sight, L is nearly independent of the total path length and thus is independent of z.

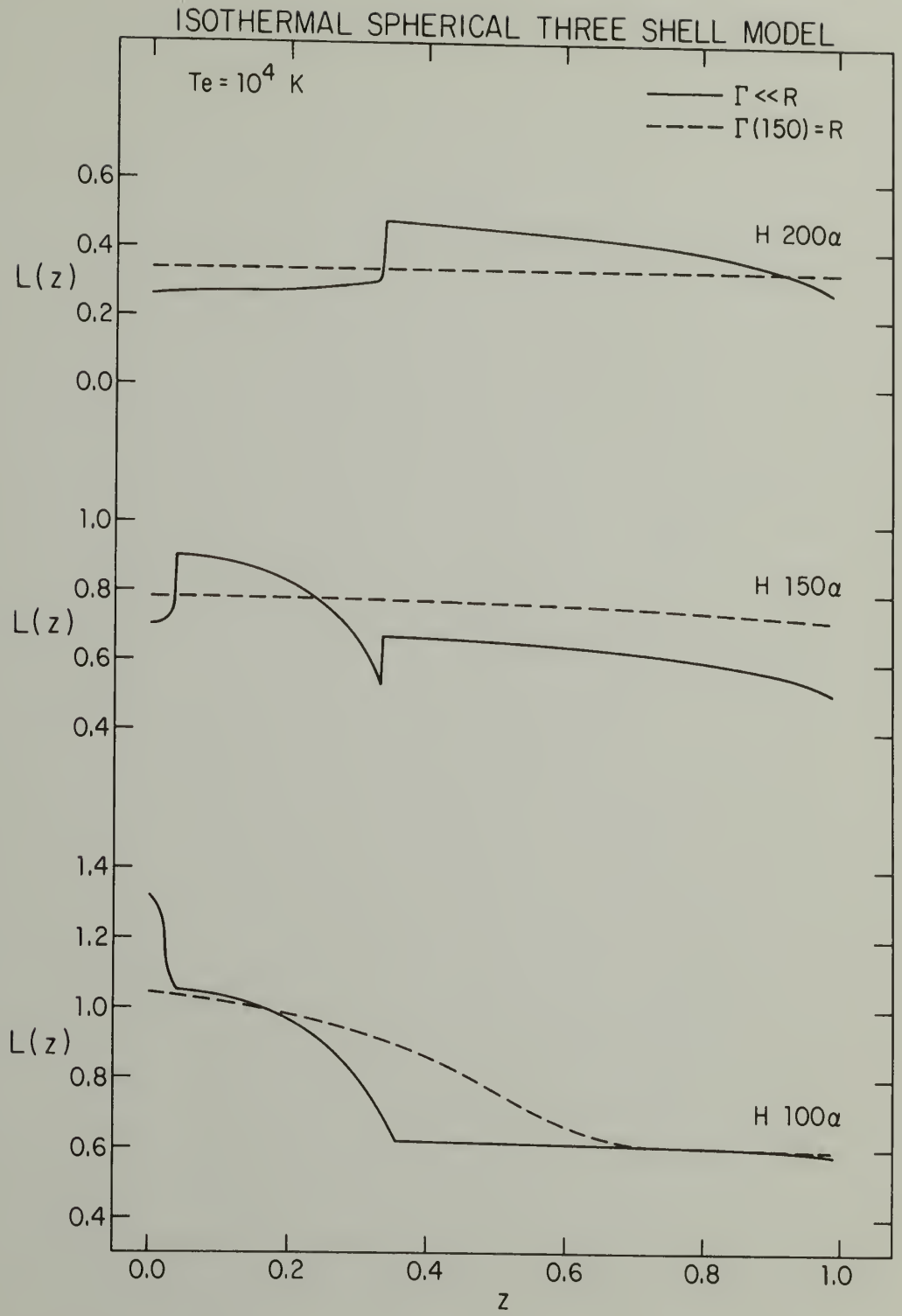

Figure 10: The dependence of L on z for Hnα lines from the three shell model. Also shown (dashed curve) is L(z) after convolution with an antenna beam whose width varies inversely with frequency and is equal to R at n=150.

The situation if quite different at n = 150. Here impact broadening reduces the peak line temperature from Region I by more than an order of magnitude. Also, the population inversion in this gas, at this frequency, is rather small. The net result is that the line to continuum ratio from Region I is rather small. The continuum emission from Region I does stimulate some line emission in the foreground Regions II and III, but this is insufficient to keep the total L from being low.

The behavior of L between z = 0.04 and z = 0.4, positions where Region II dominates the emission, is a perfect example of the independence of stimulated emission and impact broadening. At n = 150 the peak line temperature from Region II has been reduced by $\sim$ 2 owing to impact broadening. However, stimulated emission is still rather effective in enhancing the line and L remains high as long as there is a sufficiently long line of sight through the region. When $z > 0.3$, the line of sight through Region II is too small to enable stimulated emission to compensate for the broadening and L continues to fall with increasing z until the lines of sight intersect Region III alone. There is only a modest amount of stimulated emission in Region III at n = 150, but impact broadening is also not very important, and as a result L jumps sharply at the boundary between Regions II and III.

At the frequency of the n = 200 transition, Region II is optically thick in the continuum and therefore Region I is not visible. For $z < 0.35$ a substantial portion of the line originates in Region III, but not enough to compensate for the very low value of L from Region

II. For $z > 0.35$ L gradually decreases as the path length through Region III becomes smaller, and stimulated emission becomes less important.

When the source is convolved with even the rather narrow antenna beam used at $n = 100$, most details of the change in L with z are lost. Unless $\Gamma << R$, a map of this nebula would give a very deceptive picture of its true structure. At $n = 100$, for example, a big beam at $z = 0$ seems to reflect only the Region II emission, but as can be seen from Figure 7, about 15% of the total line is formed in Region I. In addition, brightness temperatures towards the center of the model are so large in comparison with those towards the edge, that even with the antenna centered at $z = 0.3$, where its response to Region I is down by a factor ~ 15, the fraction of the observed line formed in Region I has decreased by a factor of only ~ 5.

g) Summary

Any attempt to interpret radio recombination lines must take into account the various aspects of radiative transfer which have been examined in this chapter. Unless nebulae are homogeneous, isothermal plane-parallel objects, their emission will have the following general properties: 1) Lines may be enhanced through stimulated emission in a manner that depends on almost all parameters of the system. 2) The relationship between the enhancement and the path length through a region causes the line-to-continuum ratio to be very sensitive to the nebular geometry. 3) The combination of impact broadening and line

enchancement may cause lines of differing frequency to be formed in different gas within the nebula--the general trend is for high frequency lines to be dominated by emission from the more dense gas, and low frequency lines, by the less dense gas. 4) At a given frequency most of the lines may not originate in the same gas as the continuum, and lines from different Δn transitions do not necessarily arise in the same gas even though they are emitted at similar frequencies. 5) When an antenna beam observes the nebula, it averages over different lines of sight which may, depending on the geometry, have differing line-to-continuum and line-to-line ratios and different line shapes. The observed quantities should be considered as weighted averages, the weighting being dependent on structure that is not necessarily apparent in low resolution maps of a region.

These considerations make it virtually impossible to <u>derive</u> the thermodynamic structure of an HII region from observations of its recombination line and continuum emission, but by the same token, they indicate the wealth of information contained in radio recombination lines. The following chapter describes methods by which at least some nebular properties can be inferred from the behavior of radio recombination lines.

CHAPTER III

THE INTERPRETATION OF RADIO RECOMBINATION LINE OBSERVATIONS

a) Introduction

It should be apparent from Chapter II that the derivation of T_e, N_e, ℓ, N(He), etc., from recombination line measurements is not straightforward. Although the physical processes are all well understood, an enormous amount of data is necessary to discriminate between models of somewhat differing temperature or density structure, or differing geometry. At this time there are probably not enough observations to determine a unique model even for the well-studied nebula Orion A. Thus, only a few specific problems in the interpretation of thermal radio emission are considered in this chapter. First, to emphasize the necessity of taking all relevant physical processes into account, we examine ways in which certain approximations, commonly used in lieu of the full solution to the equation of transfer, give not only erroneous, but systematically misleading results. After this warning against analytic shortcuts, the behavior of a set of very general isothermal models will be discussed. These models can be used to infer the expected form of L(n) for simple nebulae. When these expectations are compared with the observations of Orion A, it becomes apparent that this nebula cannot be isothermal but must have a rather specific radial temperature gradient. Finally, the shape of recombination lines from expanding nebulae is discussed in the context of theoretical models of nebular evolution.

b) Shortcuts Lead to Pitfalls

The complexity of a full analysis of radio recombination line observations has led many investigators to use simplifying approximations in an effort to derive at least some information, however qualitative, from limited data. While attempts at simplification are laudable in the early phases of any field, it is regrettable that the current literature is still full of plane-parallel approximations to the nebular geometry, isothermal and homogeneous approximations to the nebular temperature and density structure, and the occasional assumption that recombination lines are formed and transferred under conditions of LTE. It may be tacitly understood that quantities derived from certain approximations are not precise, but it is not fully appreciated that the use of some approximations will cause systematic and to some extent predictable trends in derived properties. Such trends have been observed, but too often have been given physical or astronomical significance, instead of being recognized as likely consequences of an approximation.

The continuum flux density.

First consider the information which can be derived from the least complex observable quantity, the continuum flux density. In an isothermal nebula the emergent brightness temperature in the continuum at one point on an object's surface is given by eq. (56)

$$T_b = T_e \, (1 - \exp(-\tau_c)), \tag{76}$$

and the flux density is

$$S = \frac{2k\nu^2}{c^2} \int T_b \, d\Omega \qquad (77)$$

where Ω is the solid angle subtended by the nebula. Analyses of the flux density are of two types: those which use the magnitude of S at high frequencies where $\tau_c << 1$ along all lines of sight, and those which use the spectrum $S(\nu)$ with emphasis on the lowest frequency measurements.

At sufficiently high frequencies the exponential in eq. (76) can be expanded to first order, and, using eq. (39) for τ_c,

$$S \propto \nu^{-0.1} T_e^{-0.35} r^{-2} \int N_e^2 \, dV \qquad (78)$$

where r is the distance to the nebula and the integration is performed over the volume of ionized gas V. Equation (78) is often used to define an average electron density (e.g., Mezger and Henderson, 1967)

$$N_e^* \equiv \langle N_e^2 \rangle^{\frac{1}{2}} \propto \left(\frac{Sr^2}{V}\right)^{\frac{1}{2}} \propto \left(\frac{S}{\theta^3 r}\right)^{\frac{1}{2}} \qquad (79)$$

where N_e^* denotes the density estimated by this method and θ is the observed angular size of the nebula.

Because the kinetic temperature enters into the expression for the optically thin flux density rather weakly, an analysis of S is most useful for estimating the density of a nebula, and this is reflected in the form of eq. (79). Note, however, that S is independent of the actual density structure of a nebula and depends only on the total N_e^2. Thus two nebulae, with totally different mass distributions, can have

the same flux density if their volume and $\langle N_e^2 \rangle$ are equal. Nonetheless, it would be useful if an accurate $\langle N_e^2 \rangle$ could be estimated from S, and for this reason various forms of eq. (79) are frequently used.

To determine N_e^* it is necessary to estimate V, and this requires knowledge of both the geometry and distance of the nebula. In this chapter distances are assumed to be known; Chapter IV treats the distance question in more detail. A major difficulty in determining the volume of a nebula is that the continuum emission carries no information about a nebula's extent along the line of sight. Thus the path length must be inferred from considerations of symmetry and one's own favorite nebular geometry. Equation (79) was derived by assuming that nebulae are symmetric. Thus the path length is proportional to $r\theta$ and the volume is derived from $(r\theta)^3$ times some scaling factor. This is a reasonable choice, and even if it is not exactly correct the errors it produces in N_e^* will be moderate and random, unless all nebulae are very asymmetric. Of more importance is the fact that N_e^* depends critically on the poorly defined quantity θ. Because θ is measured from the variation of T_b across a source, it is a function of the density structure and line of sight extent of the source, and also depends on details of the antenna beam convolution. Typically, the measured value of θ is proportional to the antenna beam width (cf. the Reifenstein et al. 1970 and the Wilson et al. 1970 measurements of the angular size of Orion A). Conversely, antenna beam smearing will tend to make distant sources appear larger than nearby identical sources, making the N_e^* from a group of identical nebulae be, to some extent, inversely proportional to the square root of the distance. It is

therefore important to consider the extent of instrumental effects (which enter through θ), and systematic errors in the determination of V (which enter through the r or θ dependence of N_e^*), on estimates of the density derived from N_e^*.

Figure 11 shows $\langle N_e^* \rangle$ vs. intervals in distance from the sun, r, for those nebulae from the surveys of Reifenstein et al. (1970, made at NRAO with a 6' HPBW) and of Wilson et al. (1970, made at CSIRO with a 4' HPBW) which are included in the kinematic sample discussed in Chapter IV. Distances were taken from the circular motion analysis in Chapter IV, and the widths of the intervals in r were chosen so that each interval contains approximately the same number of objects: 8 to 10 for NRAO data and 11 to 15 for CSIRO data. Note the strong dependence of $\langle N_e^* \rangle$ on r: nearby nebulae appear to be more dense, on the average, than distant nebulae. Note also the systematic difference between the two surveys in the $\langle N_e^* \rangle$ at any r. Although there is a large scatter about the mean values, as would be expected when nebulae of fundamentally different size and flux density are averaged together, the trends are real. Ten of the nebulae in this sample have been observed at both NRAO and CSIRO; nine of them show $N_e^*(\text{CSIRO}) > N_e^*(\text{NRAO})$, and the average over all ten gives $\langle N_e^*(\text{CSIRO}) \rangle = 1.6 \langle N_e^*(\text{NRAO}) \rangle$.

The trends in Figure 11 have the same sense as systematic effects do, but would be hard to understand (especially the variation of N_e^* with HPBW) in physical terms. It is therefore likely that N_e^*, and any other parameter derived from the combination of S, r and θ, has little physical significance.

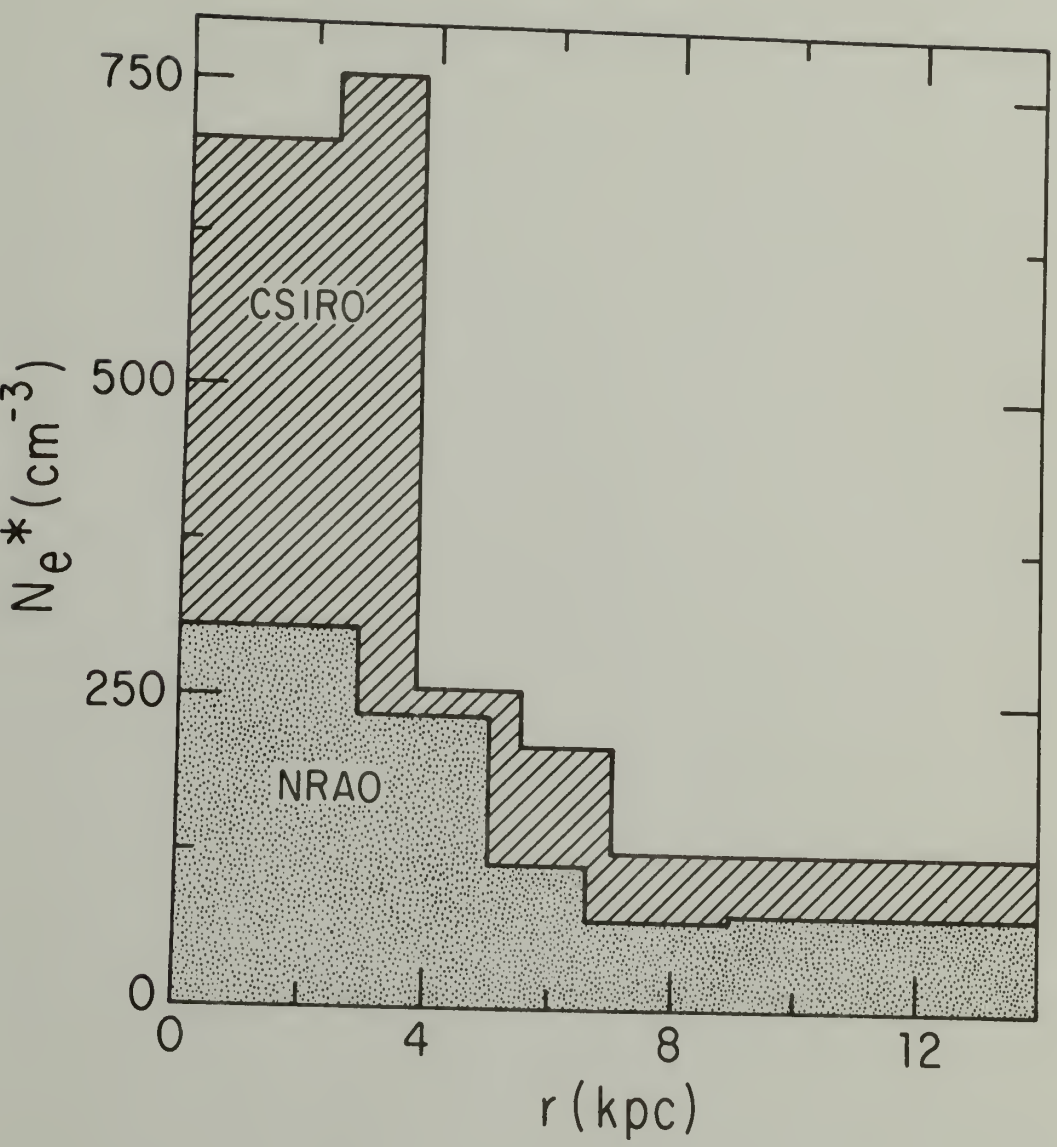

Figure 11: The average electron density N_e^* (as defined in eq. 79) for nebulae from the surveys of Reifenstein et al. (1970, made at NRAO with a 6' HPBW) and Wilson et al. (1970, made at CSIRO with a 4' HPBW) plotted against distance from the sun, r. Each interval in r contains about the same number of objects: 8-10 for the NRAO data and 11-15 for the CSIRO data.

It is not worthwhile to give a detailed description of the various methods which have been used to derive nebular properties from $S(\nu)$. At high frequencies the flux density spectrum is virtually independent of the nebular structure, so any model which fits a single measurement of S will fit all measurements of S as long as the nebula remains optically thin in the continuum. In contrast, the low frequency spectrum of a spherical nebula is a sensitive function of its density structure (Olnon, 1975), and eq. (76) shows that it will also be a function of any temperature structure. Moreover, because continuum measurements cannot distinguish between N_e^2 and ℓ, the geometry can also influence the low frequency flux density spectrum. Unfortunately, this implies that there are always a number of reasonable models which can be constructed to fit the rather limited information contained in the low frequency flux density measurements of any object. For instance, the spectrum of Orion A below 1 GHz is fit by models with properties as diverse as: the isothermal 5000 K model of Terzian and Parrish (1970); the isothermal 11000 K, two-density-component model of Hjellming and Churchwell (1969); the isothermal 9500 K and 9000 K, spherical varying-density models of Brocklehurst and Seaton (1972) and Cato (1973), respectively; the model proposed by Pyatunina and Soglasnova (1973) wherein T_e <u>decreases</u> with distance from the center of the nebula; and the varying-density, varying-temperature model of Lockman and Brown (1975) wherein T_e <u>increases</u> with distance from the center of the nebula.

As this example shows, the continuum flux density does not contain enough information to be used to determine unique nebular properties,

although any successful model must certainly give values of S in agreement with those observed, especially at the low frequencies where the distributions of T_e and N_e enter S rather directly. Only when there are compelling reasons for adopting a specific geometry and density structure, and where thermal structure is ignored (e.g., the case of mass outflow from stars; see Olnon, 1975; Panagia and Felli, 1975; Wright and Barlow, 1975) can the continuum spectrum be interpreted with any hope of deriving meaningful results.

The definition of T_e^*

The line intensity and the line shape should be discussed separately, for though they are not fully independent, they are affected somewhat differently by various atomic processes (Brocklehurst and Seaton, 1972). Although it seems obvious, it is worth noting that models must reproduce not only the product $T_L \Delta v$, but the individual quantities themselves. As usual, to reduce the influence of the specific antenna on the derived nebular properties, we will work with a normalized line-to-continuum ratio.

As seen in Chapter I, the solution to the equation of transfer for the emergent T_L/T_c along any line of sight (with no background continuum) can be written

$$\frac{T_L(\nu)}{T_c} = \frac{\int j_{L+c} \exp(-t_{L+c})\, ds}{\int j_c \exp(-t_c)\, ds} - 1 \qquad (80)$$

where $t = \int_0^s \kappa\, ds'$. This equation cannot be inverted and used to derive unique nebular properties, so observations must either be compared

with model calculations, or eq. (80) must be reduced to a simpler form by approximation. The following chain of reduction has been widely used in recombination line analyses (specific references are given in the following section).

Approximation 1: The lines and continuum at a given frequency can be treated as if they are formed in an isothermal, homogeneous plane-parallel medium. All lines of sight through a plane-parallel medium are equivalent, thus eq. (80) can be used for the observed T_L and T_c. With the homogeneous and isothermal assumptions,

$$\frac{T_L(\nu)}{T_c} = \frac{\kappa_L/\beta + \kappa_c}{\kappa_L + \kappa_c} \frac{1 - \exp(-(\tau_L+\tau_c))}{1 - \exp(-\tau_c)} - 1. \qquad (81)$$

This equation, which was discussed in Chapter II, is correct for a uniform plane-parallel medium, but like eq. (80), it cannot be inverted and used to derive unique nebular properties. Thus a second approximation is required.

Approximation 2: $\tau_c \ll 1$ and $|\tau_L + \tau_c| \ll 1$. It is necessary to take the absolute value of $\tau_L + \tau_c$ because τ_L is generally negative, and may have a larger magnitude than τ_c. With this approximation the exponential in eq. (81) can be expanded (Goldberg, 1968) to give an equation that was discussed in Chapter II:

$$\frac{T_L(\nu)}{T_c} = \frac{b\kappa_L^*}{\kappa_c} (1 - \beta\tau_c/2). \qquad (82)$$

For Hnα lines from a gas containing 10% singly ionized He by number, eq. (82) becomes

$$\frac{T_L(\nu)}{T_c} = 2.24\text{x}10^{-2}\ \frac{b\ \nu^{1.1}}{T_e^{1.15}}\ (\nu\phi_\nu)\ (1 - \beta\tau_c/2). \quad (83)$$

The level populations enter into eqs. (82) and (83) in two ways: The first way, directly through the departure coefficient b, will be called the non-LTE line formation effect because it is governed solely by the atomic level populations. The second way, through the term $-\beta\tau_c/2$, will be called the non-LTE transfer effect because its magnitude depends not only on the extent of the population inversion (contained in β) but also on the number of photons available to stimulate line emission. Neither b nor β are analytic functions of T_e, N_e and n, so eq. (83) cannot be used directly to derive the thermodynamic state of a nebula.

Approximation 3. Recombination lines are formed and transferred under conditions of LTE, i.e., b = 1 and β = 1. Thus, since $\tau_c \ll 1$ from approximation 2, eq. (83) becomes

$$\frac{T_L(\nu)}{T_c} \simeq 2.24\text{x}10^{-2}\ \frac{\nu^{1.1}}{T_e^{1.15}}\ (\nu\phi_\nu). \quad (84)$$

This equation can be integrated over frequency and, with the measurement of the power in a given recombination line, can be used to solve for a T_e. [There is, of course, the problem raised by Brocklehurst and Seaton (1972) of whether an accurate $\int T_L d\nu$ can even be measured. The difficulty is that weak wings of pressure broadened lines, such as those shown in Figure 9, might be difficult to distinguish from instrumental spectral response, and thus be removed routinely during data reduction. Lockman and Brown (1975) and Brown et al. (1978) have discussed this problem and conclude that while $\int T_L d\nu$ may be unobservable,

the individual quantities T_L and Δv are likely to be acceptably accurate. Unfortunately, this does not imply that the power in a pressure broadened line is measurable, but only that there are methods of analysis which avoid this particular difficulty.]

The line profile function ϕ_ν is the sum of Voigt functions and its form is related to the density structure of a nebula through the density dependence of impact broadening. While some aspects of the profile shape are specified by T_L and Δv, knowledge of these quantities is not generally sufficient to determine either the overall profile shape or $\int T_L d\nu$. Equation (84) can be rewritten in terms of T_L and Δv only when ϕ is a Gaussian function, i.e., when the Lorentzian line component caused by impact broadening is negligible.

Approximation 4: Impact broadening is negligible. With this approximation the line profile function is a Gaussian and

$$\frac{T_L}{T_c} \simeq 6.35\text{x}10^3 \ \frac{\nu^{1.1}}{T_e^{1.15}\Delta v} \tag{85a}$$

or, solving for a T_e

$$T_e^* \equiv \left(6.35\text{x}10^3 \ \nu^{1.1} \ \frac{T_c}{T_L \Delta v}\right)^{0.87}, \tag{85b}$$

where Δv is the line width in km/s. Equation (85), or some variant of it, is frequently used to derive an electron temperature from radio observations of T_L/T_c and Δv. We denote this temperature as T_e^*, and while it is commonly called the LTE electron temperature, it includes three approximations besides that of LTE. If all four approximations

are good, T_e^* is the actual kinetic temperature; if one or another approximation is bad then T_e^* will not be a kinetic temperature but will be a quantity which contains information on the density and geometry, and it will differ from the true temperature in ways which are not at all obvious from eq. (85).

The cumulative effect of the approximations has been to remove the density and the nebular geometry from the problem. Equation (85) implies that radio recombination lines can be understood as arising from plane-parallel objects of indeterminate line of sight extent and electron density. The path length and density did not vanish from the expressions because they were explicitly assumed to be unimportant, but because they only enter into the complicating terms in the solution to the equation of transfer, and as the complications were removed, so were the density and path length. When the approximations are valid, all information on nebular density and geometry must be derived from continuum measurements.

The first approximation, that nebulae are isothermal and homogeneous, is certainly least accurate. Optical observations show that HII regions have internal density variations of orders of magnitude, and temperature variations of thousands of kelvins (e.g., Pottasch, 1965), and every nebula that has been mapped at radio wavelengths shows variations in T_L and T_c across its surface, suggesting that these objects are not plane-parallel. Attempts to model the radio emission from nebulae indicate that there must be substantial variations in N_e along the line of sight in order to account for the shape of low frequency radio recombination lines (Brocklehurst and Seaton, 1972), and

to account for the form of the continuum spectrum (e.g., Hjellming and Churchwell, 1969). In addition, the run of T_L/T_c with principal quantum number n in some nebulae suggests that they have significant variations in their electron temperature (Lockman and Brown, 1975). Thus the first approximation seems poor, and only in exceptional circumstances (i.e., when the other three approximations are good) will a T_e derived using approximation 1 be even a weighted average kinetic temperature over the volume of gas sampled by the antenna beam (see the discussion below).

Because dense, high optical depth components are found in many HII regions (e.g., Balick, 1972), the second approximation is generally valid only at frequencies above 10 GHz, and even at 10 GHz κ_L may have values of order -0.5/pc (see Fig. 2).

As a result of these first two approximations, the subsequent expressions for T_L/T_c do not directly depend on N_e, although the density still enters through its effect on the level populations b, through the non-LTE transfer term $\beta\tau_c/2$, and may enter into the line profile function through impact broadening. The nebular geometry likewise appears only indirectly, through τ_c in eqs. (82) and (83), and since $\tau_c \propto N_e^2 \ell$, the geometry is to some extent indistinguishable from the density. Thus it is very difficult to derive the density and geometry from recombination line observations of a uniform optically thin nebula, because its line emission is described by eq. (82).

The first part of the third approximation, that lines are formed under conditions of LTE, has been known to be incorrect for many years; in general $b \neq 1$ (Seaton, 1964; Brocklehurst, 1970). It is more difficult to determine <u>a priori</u> if lines are transferred under conditions

approximated by LTE. Although β is rarely unity (Fig. 2), the extent of the non-LTE transfer effect also depends on τ_c, which itself is a function of the structure of the nebula. For the simple models discussed in Chapter II, non-LTE transfer effects became important when $\tau_c \gtrsim 10^{-3}$.

The fourth approximation, that impact broadening is negligible, removes the last influence of N_e on the simplified expressions for T_L/T_c. Impact broadening changes a radio recombination line in two ways: it reduces T_L as power is transferred from the line core into the wings, and, to a lesser extent, it increases the line width Δv. Because the amount of impact broadening is related to the magnitude of the quantity $\underline{a}$ in eq. (33), approximation 3 is that $\underline{a} = 0$. The range of validity of this approximation may be determined by examining $H(\underline{a},0)/H(0,0)$: the ratio of the actual peak line intensity to that of the purely Doppler broadened line. It is reasonable to consider that impact broadening is important if $H(\underline{a},0)/H(0,0) < 0.9$, that is, if it reduces T_L by at least 10%. This occurs for $\underline{a} = 0.1$. Figure 12 shows the density which will give $\underline{a} = 0.1$ for Hnα lines from an isothermal homogeneous 10^4 K gas with an unbroadened Δv of 26 km/s. In the rather moderate density $10^{3.5}$ cm^{-3} gas T_L is reduced by more than 10% for all $n > 110$. At this value of $\underline{a}$, Δv is only increased by about 6.5%, and thus the quantity $T_L \Delta v$ is also reduced by impact broadening, though to a lesser extent than T_L is reduced. Clearly impact broadening must be taken into account, even in LTE models, except for the lowest density nebulae.

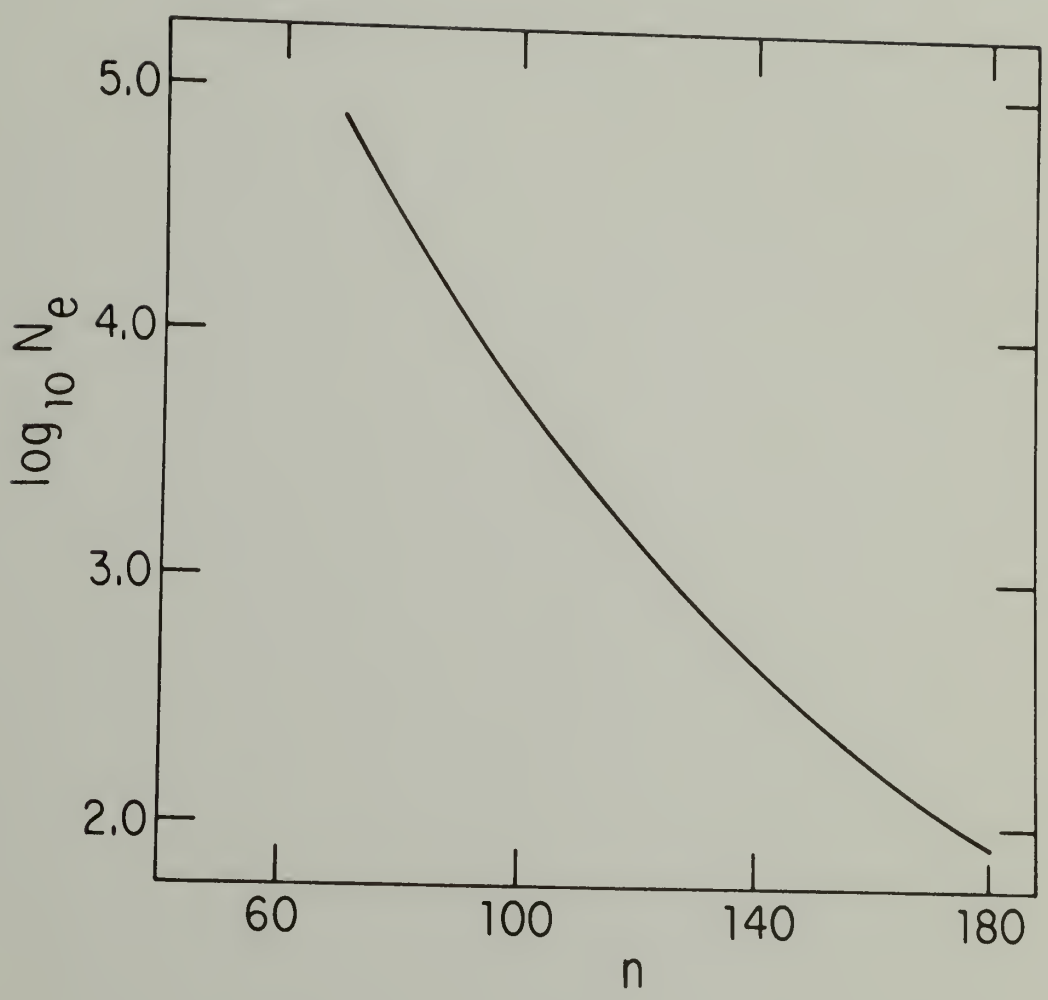

Figure 12: The electron density at which impact broadening reduces peak recombination line intensities by 10%, plotted against principal quantum number n, for Hnα lines from a 10^4 K gas.

A comparison of the exact solution to the equation of transfer with the approximate eq. (85) illustrates the extent of the approximations: the nebular geometry, density, and of course, the density structure are assumed to have no effect on T_L/T_c. Because all these quantities enter into the correct expressions, it is clear that the approximations have the effect of "aliasing" information on the density and geometry into the "LTE" electron temperature--variations in N_e and ℓ will appear as variations in T_e^*. If this is not appreciated, observed changes in T_e^* might be equated with real changes in the electron temperature rather than being recognized as natural consequences of the definition of T_e^*.

Systematic effects in T_e^*.

To understand some peculiarities of T_e^*, consider an isothermal homogeneous plane-parallel nebula observed at a frequency so high that $\underline{a} = 0$. In this case the true value of T_L/T_c is given by eq. (83), and T_e^* is related to T_e by

$$\frac{T_e^*}{T_e} = (b(1-\beta\tau_c/2))^{-1}. \qquad (86)$$

When the frequency is so high that $\beta\tau_c/2 \sim 0$ because $\tau_c \sim 0$, then $T_e^* > T_e$ because $b < 1$. Moreover, because $b(\nu)$ increases monotonically with decreasing frequency, $T_e^*(\nu_1) > T_e^*(\nu_2)$ when $\nu_1 > \nu_2$. At lower frequencies where $\beta\tau_c/2 \neq 0$ the situation is more complex, but for $\nu \gtrsim 3$ GHz and $N_e \lesssim 10^4$ cm^{-3}, $-\beta > 10$ and $\beta\tau_c \propto \nu^{-3.1}$, approximately, in a 10^4 K gas. Thus once again we expect $T_e^*(\nu_1) > T_e^*(\nu_2)$ when $\nu_1 > \nu_2$.

This dependence of T_e^* on frequency has been noted previously (e.g., Dupree and Goldberg, 1970) and has been observed in a number of objects. For instance, Viner et al. (1976) have measured the H85α (ν = 10.5 GHz) recombination line and continuum emission from a number of HII regions previously observed in the H109α line at 5.0 GHz; they find that in most HII regions T_e^* (10.5 GHz) > T_e^* (5.0 GHz). Although Viner et al. conclude that the 10.5 GHz observations are sampling hotter nebular material than the 5.0 GHz observations (implying that there are temperature variations within each nebula and that approximation 1, and hence their entire analysis, is invalid), their result does not necessarily have physical significance, but merely confirms an expected trend in T_e^*.

Another effect arises because the quantity $-\beta\tau_c/2$ in eq. (86) is generally positive; any decrease in τ_c will make T_e^* increase, even if T_e and N_e remain constant. This implies, of course, that T_e^* will vary with position over all but plane-parallel nebulae. If a homogeneous isothermal nebula has a spherical shape, then ℓ will vary as $(1-z^2)^{1/2}$ and since nebulae are as likely to be spherical as plane-parallel, T_e^* should increase towards the edge of many nebulae. Such a trend has been observed in Orion A (Mezger and Ellis, 1968; Perrenod, Shields and Chaisson, 1977), in the Carina nebula (Gardner et al., 1970a), in NGC 7538 (Lada and Chaisson, 1973), in M20 (Chaisson and Willson, 1975) and in other HII regions. The usual interpretation given to this observation is that there is a "hardening" of the radiation field at the nebular edge and hence an increased temperature at these positions. While this may well be true, it cannot be proven by interpreting the

observations with the four "LTE" approximations. In fact, eq. (86) suggests that these results have no physical significance other than to indicate that nebulae have a geometric structure more spherical than planar, and that T_e^* is not a reliable measure of nebular temperatures or differential temperatures.

If approximation 4 is used when it should not be used, it can have an interesting effect on T_e^*. Assume that the first three approximations are valid, but that the lines are somewhat broadened. We have seen that with $\underline{a} = 0.1\ T_L$ is reduced by 10% while Δv is only increased by about 6.5% and thus the power in the line, if calculated from the peak intensity and the width, is underestimated by about 4%. This will cause T_e^* to be greater than T_e by about 4%. For larger values of $\underline{a}$ this effect will be more severe, even if nebulae are isothermal, homogeneous, plane-parallel objects whose lines are formed and transferred under conditions of LTE.

A few other examples of the misbehavior of T_e^* (resulting, e.g., from "Malmquist bias" in a survey) are given by Lockman and Brown (1978) and need not be repeated here.

Non-LTE shortcuts.

A few non-LTE analytic shortcuts have been proposed (these are discussed in Dupree and Goldberg, 1970), all of which are based on eq. (82). One of these methods is to compare an α transition with a β transition at a similar frequency. The antenna beam width, T_c and τ_c will be identical for the two measurements, and one should be able to estimate the relative degree of enhancement of each line. Another

method compares an Hnα transition and its corresponding Hnβ transition. Because b and $d(\ln(b_n))/dn$ are both smoothly varying functions of n (Fig. 2), relative non-LTE effects between the two transitions can be evaluated and removed. Unfortunately, neither of these methods is valid when applied to an inhomogeneous nebula. As shown in Fig. 8, α and β lines from inhomogeneous nebulae do not necessarily arise in exactly the same gas, even if the frequencies or principal quantum numbers of the transitions are identical. Thus direct comparison of different lines can give meaningless results. It is worthwhile to reemphasize that the line and continuum emission at a given frequency may not arise in precisely the same nebular gas (Fig. 8). This implies that any technique which relies on just a few measurements cannot, in general, give reliable results, for one measurement may be carrying information about a part of the nebula which in some sense is not "seen" in another measurement.

c) The Canonical Isothermal Nebula

The proper procedure for determining nebular structure from radio recombination line observations is to construct a model, calculate its emission, and compare it with the observations. This is a difficult task, and it is generally not worth the effort unless an object has been mapped at many frequencies in both the line and the continuum. It is instructive, however, to consider the properties of a very general class of model nebulae, for radio recombination line emission from simple models has characteristics which give insight into the behavior of a much larger class of models. Although only Hnα lines will be discussed,

the results apply, in a qualitative way, to other transitions, and to lines from species like He as well.

All models discussed in this section are spherically symmetric and have a density structure.

$$N_e(r) = N_0 / (1 + tr^2) \qquad 0 \le r \le R \qquad (87)$$

where, for the rest of this chapter, r is a radial parameter in pc, N_0 is the density at r = 0, and the value of t controls the rate of change of N_e with r. The radius of the model is R. Unless otherwise noted, all models are isothermal ($T_e = 10^4$ K), have a uniform unbroadened line width of 30.2 km/s (this width gives $T_D = 2T_e$), and contain 10% singly ionized He. A model is completely described by specifying the values of N_0, R and t.

A convenient way to calculate the emission from a varying density model is to divide it into ns shells, each of which has a single N_e. In such a shell model, eq. (49) is the exact solution to the equation of transfer for the emission along a single line of sight. To account for geometric effects the emission is calculated for nz lines of sight equally spaced from the center (z = 0) to the edge (z = 1) of each model. In the calculations presented here, typical values for ns and nz were 25 and 200, respectively. The brightness distribution across the model is multiplied by a two-dimensional Gaussian function to account for the finite resolution of antennas. The computer program used to evaluate these models is described in Appendix A.

It is worth mentioning a few general properties of models whose $N_e(r)$ is given by eq. (87). For large positive t (i.e., a centrally

peaked density structure) $N_e(r_i) \propto r_i^{-2}$, approximately, and since the differential volume dV_i of a shell is approximately proportional to r_i^2, the mass of any model increases linearly with r. However, the optically thin continuum flux density S, being proportional to N_e^2, converges to a finite number as R and the mass increase indefinitely.

The emission measure along a line of sight at z = 0 through these models is

$$E = N_0^2 \left[\frac{R}{1+tR^2} + \frac{1}{\sqrt{t}} \tan^{-1}(R\sqrt{t}) \right]. \qquad (88)$$

For $t > 0$, E converges rapidly with increasing r, and material at $r > 1.5/\sqrt{t}$ contributes less than 10% to E. All models discussed here have $t > 10$, so gas at $r > 0.5$ pc contributes little to the total emission measure along central lines of sight.

Continuum properties.

The flux density spectrum of inhomogeneous isothermal nebulae has been thoroughly discussed by Olnon (1975) and his results cover the models considered here. Briefly, $S(\nu) \propto \nu^{-0.1}$ at high frequencies (typically $\gtrsim$ 10 GHz), while at progressively lower frequencies $S(\nu)$ turns over, gradually approaching the spectral form of an optically thick nebula. But, because of the varying density structure, each model has some optically thin gas at very low frequencies, and the transition between thin and thick spectral indices can be gradual. Typically, $S(\nu)$ for these models does not have the optically thick spectral index of +2 until $\nu \lesssim$ 100 MHz.

L(n,R).

Let us take $N_0 = 10^4$ cm^{-3} and t = 100 pc^{-2}. The two-parameter function L(n,R) then shows how a change in the radius of a model effects the emergent line-to-continuum ratio. Since t > 0, an increase in R adds progressively lower density gas to the dense inner regions of a model. Results for a series of values of R are shown in Figure 13. With $N_0 = 10^4$ cm^{-3} and t = 100 pc^{-2}, the density structure is such that $N_e > 500$ cm^{-3} for r < 0.5 pc, $500 \geq N_e \geq 25$ cm^{-3} for 0.5 > r > 2 pc, and $25 > N_e > 4$ cm^{-3} for 2 > r > 5 pc. Each model is evaluated for very large and very small antenna beams (centered at z = 0) and the curves are labeled with the value of R.

The increase in R from 0.5 to 5.0 pc increases the mass of the model by a factor $\sim$ 10, and increases the flux density by about 25%. Most of the added flux density comes from the relatively low brightness outer parts of the models; there is little actual change in T_b along the bright central lines of sight because, for t = 100 pc^{-2}, the emission measure at z = 0 is virtually independent of R for R > 0.2 pc.

Figure 13 shows that the exact value of R has little effect on L(n < 120). This is true for all R > 0.2 pc. Thus, in this set of models, the highest frequency lines carry little information about the existence or extent of low density gas surrounding the dense nebular cores. Of course high resolution mapping would show that the larger models are larger, but at high frequencies the integral properties of the models, and characteristics of the emission from the brightest parts of the models (lines of sight near z = 0), are determined entirely by the most dense, high emission measure regions.

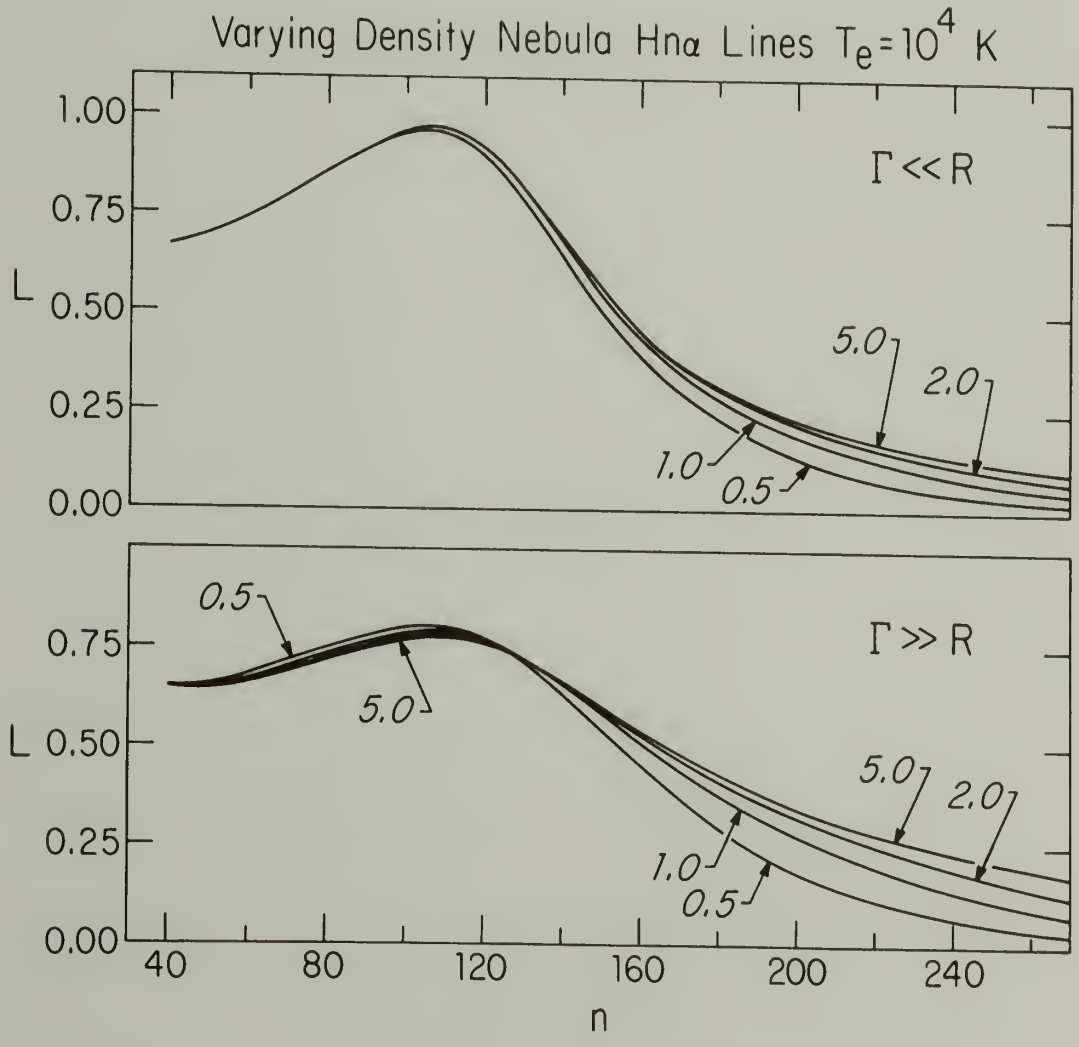

Figure 13: The normalized line-to-continuum ratio L, for Hnα lines from spherical isothermal nebulae that have a density structure given by eq. (87). Here, $N_0 = 10^4$ cm^{-3} and t = 100 pc^{-2}. Individual curves are labeled with the value of the nebular radius. Models were evaluated for extremely large (upper panel) and extremely small (lower panel) antenna beams centered at z=0.

At lower frequencies ($n > 120$), where the lines from dense gas are reduced by impact broadening and the increasing continuum opacity, much of the line originates in moderate density foreground material. Because the amount of foreground material is proportional to R, $L(n > 150)$ increases with increasing R. It is interesting that the low frequency lines at $z = 0$ arise almost entirely from gas which makes a negligible contribution to the total emission measure, and which produces little of the continuum brightness temperature, of the flux density, or of the high frequency lines. For example, the $R = 5.0$ pc model has an emission measure at $z = 0$ only 0.3% greater than the $R = 0.5$ pc model, yet its $L(200)$ is more than 70% larger than $L(200)$ of the $R = 0.5$ pc model.

These trends are also evident in the $\Delta v(n,R)$ curves shown in Figure 14. At frequencies where it is important, impact broadening increases with the density, and because dense gas produces most of the line emission from $n = 40$ to $n = 120$, the line width increases from $n = 40$ to $n = 120$. For $n > 120$ however, the line width is inversely proportional to R, since lines from less dense foreground gas (if such gas is present) are less broadened than lines from the dense regions. Thus the presence of low density gas moderates the increase in Δv with n. The upper panel of this figure gives a beautiful illustration of the gradual transference of the region of line formation from high to low density gas. At $n < 130$ a majority of the line comes from the inner 0.5 pc of the model, even in the larger models, and thus the individual $\Delta v(n)$ curves merge with the $R = 0.5$ pc curve. Gas in the annulus $0.5 < r < 1.0$ pc does not produce much of the line until $n = 130$, but at that transition the width from the $R = 1.0$ pc model starts to fall below

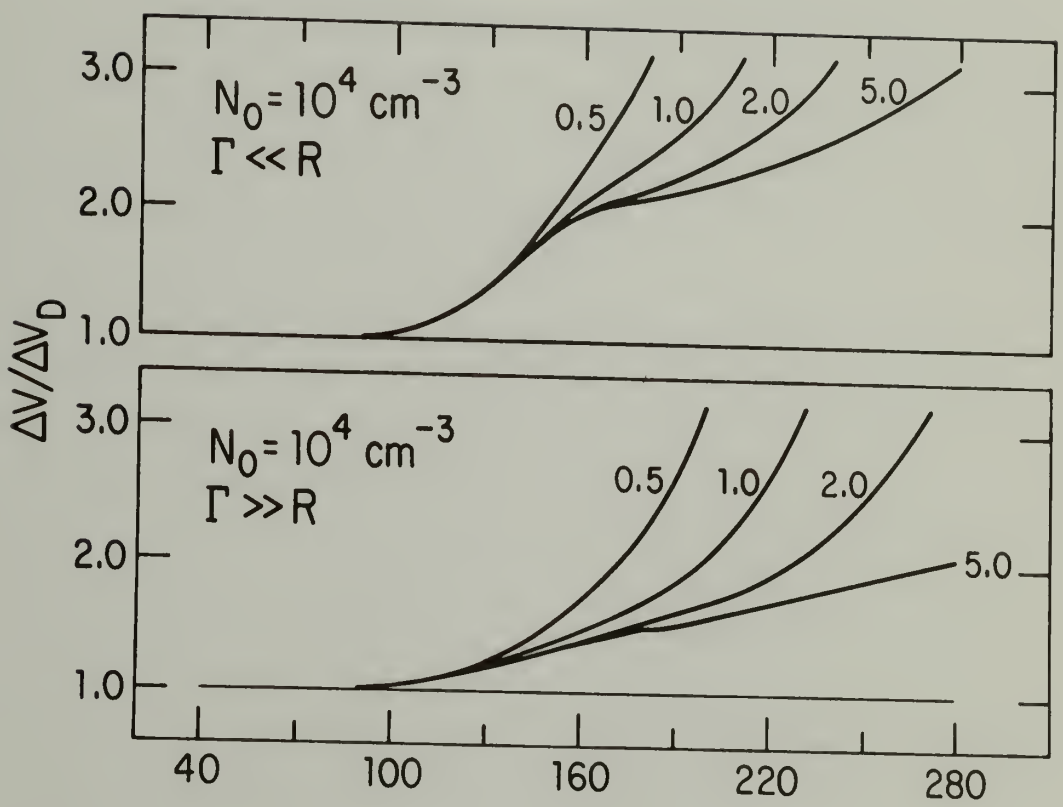

Figure 14: The full-width at half-maximum of recombination lines from the varying-radius model. Line widths are normalized to the intrinsic Doppler width of 30.2 km/s.

the width from the smaller model. Similarly, the lower density gas in the $1.0 < r < 2.0$ pc annulus does not contribute to the line shape until $n = 150$, and the least dense gas, that at $2.0 < r < 5.0$ pc, does not effect the line shape until $n = 170$.

This qualitative behavior is not specific to any particular geometry or density structure, but simply follows from the principles discussed in Chapter II. Low density gas in isothermal heterogeneous nebulae is essentially invisible at high frequencies, but determines the character of the line emission (though not necessarily the continuum) at low frequencies.

$L(n,N_0)$.

Let us set $t = 100$ pc^{-2} and $R = 2.0$ pc. The function $L(n,N_0)$ shows the normalized line-to-continuum ratio as the central density, and thus the density at any point in the model, is changed. Figure 15 shows $L(n)$ for $10^{4.5} \leq N_0 \leq 10^3$ cm^{-3}. The curves are labeled with the value of $\log_{10}(N_0)$ and, again, the upper panel is for an extremely small antenna beam and the lower panel is for an extremely large beam.

The differences in these $L(n,N_0)$ curves result from differences in the relative importance of stimulated emission and impact broadening in the models. It was noted above that nebulae with continuum optical depths of order 10^{-3} have lines enhanced by stimulated emission; in a 10^4 K nebula the condition that $\tau_c \sim 10^{-3}$ requires that $E \sim 10^{3.5}\ \nu^{2.1}$; with ν in GHz. Stimulated emission will occur at 100 GHz ($n = 40$) only in a gas with an extremely high emission measure. In the $N_0 = 10^{4.5}$ cm^{-3} model there are such high emission measure lines of sight, and at low z, recombination lines are enhanced even at the highest frequencies.

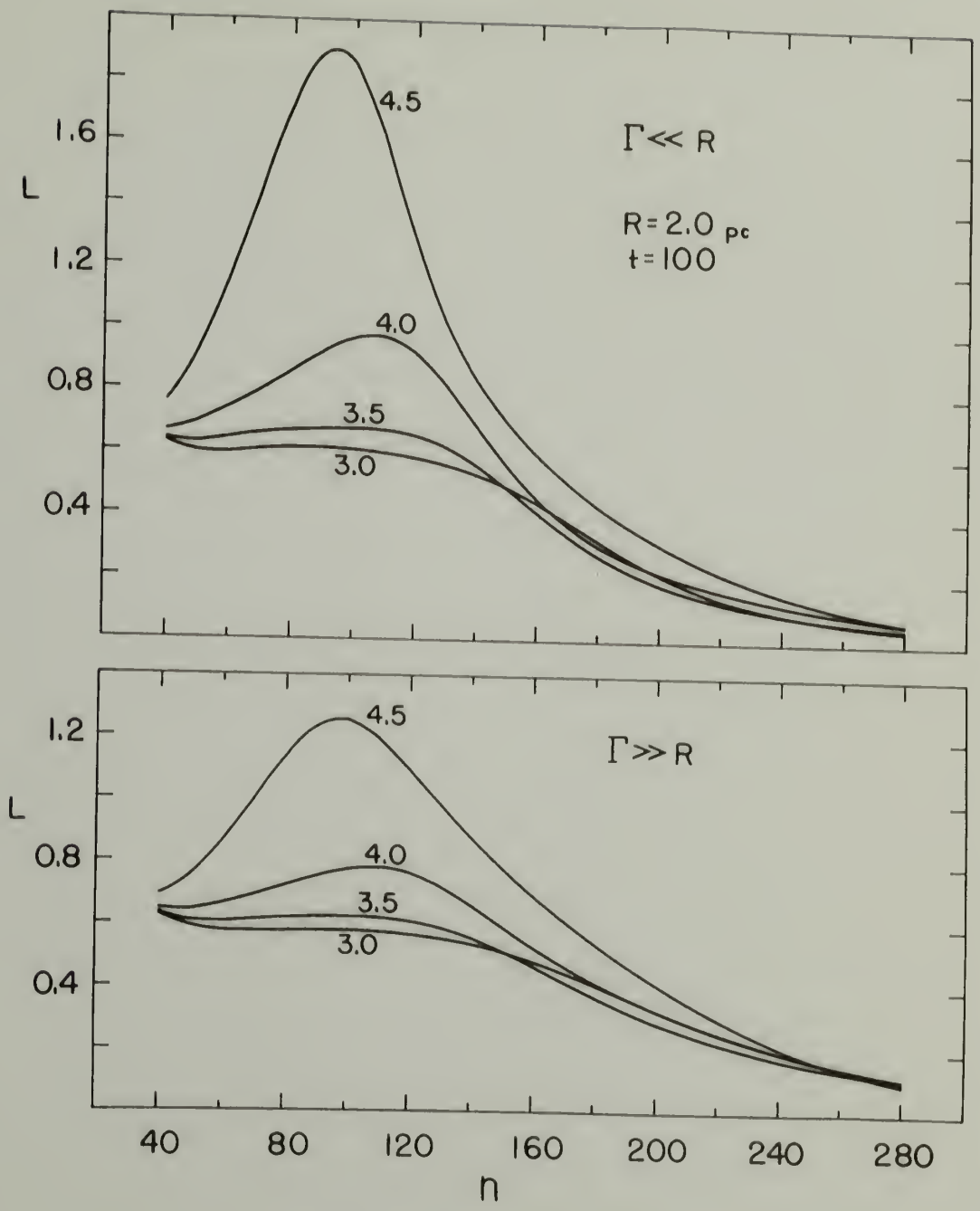

Figure 15: L(n) for models with R=2.0 pc, t=100 pc^{-2}, and various values of N_0. Curves are labeled with the value of $\log_{10}(N_0)$.

Stimulated emission is not a very important factor in determining the value of L(40) for the less dense models. Instead, the change in L(40) with N_0 results mainly from the slight density dependence of the departure coefficient.

Impact broadening is the main cause of the turnover in L(n). Impact broadening has a much stronger frequency dependence than stimulated emission, and below some frequency it will always reduce T_L despite stimulated emission. The turnover occurs at $n \sim 100$ for the dense models and at higher n for the less dense models. In fact, impact broadening in the 10^3 cm^{-3} model begins to reduce L at the frequency where stimulated emission is just beginning to enhance L, and a peak never forms. This is a common feature of low emission measure models. Qualitatively, the height of the peak in L is proportional to E and the location of the peak is proportional to N_0.

Figure 16 shows $\Delta v(n,N_0)$ for this set of models. An infinitely large antenna beam (lower panel) sees $\Delta v(n) \propto N_0$, as would be expected from the simple density dependence of impact broadening. The small beam however shows no clear relationship between $\Delta v(n)$ and the density of the gas along the line of sight. For example, $\Delta v(180, 10^4) = \Delta v(180, 10^{3.5})$, and both are larger than $\Delta v(180,10^{4.5})$ even though at every point along the line of sight the $10^{4.5}$ cm^{-3} model is denser than the other models. This unexpected behavior can be understood by recalling that the amount of the line which is stimulated in foreground gas is proportional to the brightness temperature of the background continuum source. The denser models, with large continuum brightness temperatures at z = 0, can stimulate a larger percentage of their total line in

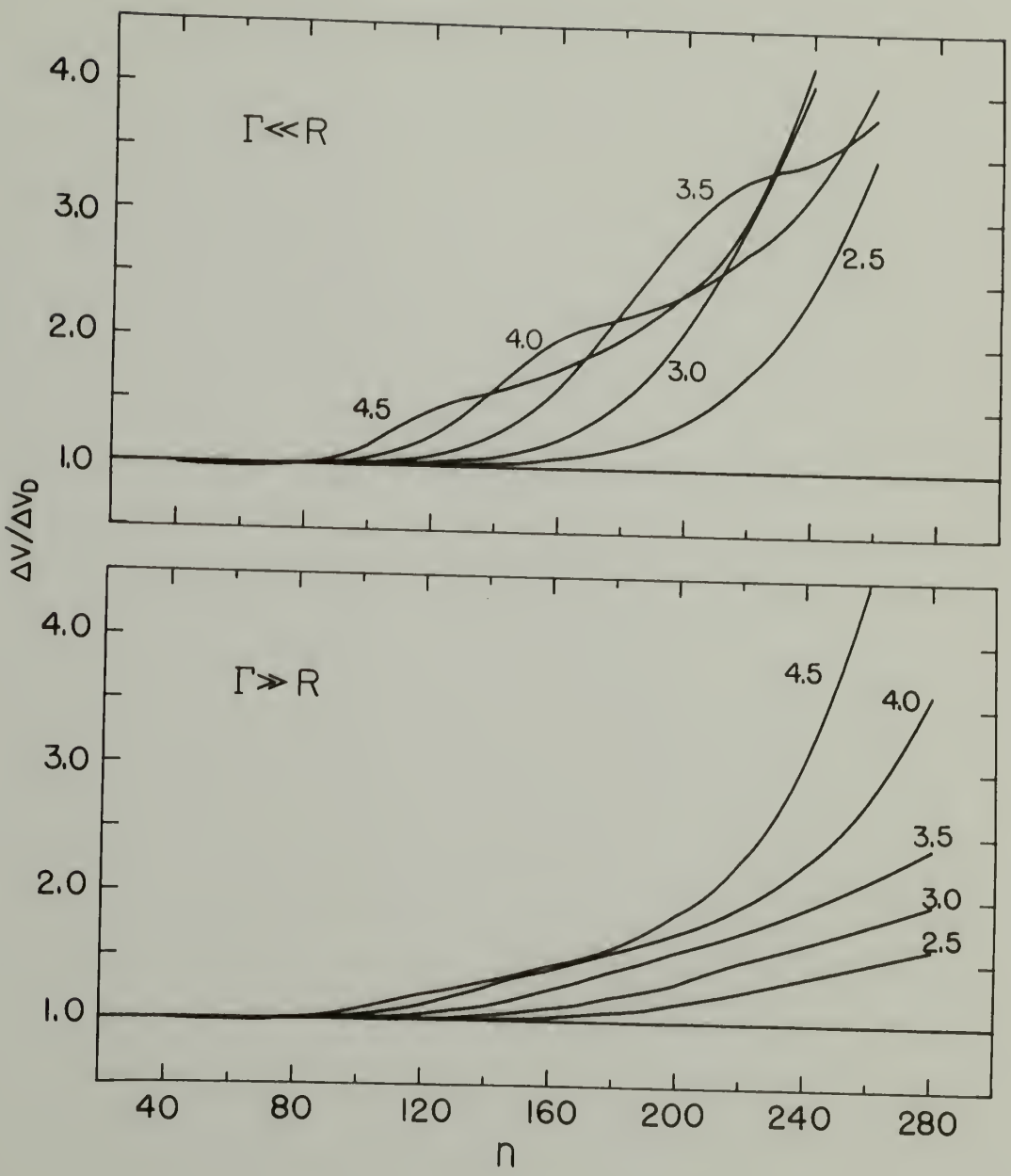

Figure 16: Line widths, normalized by the Doppler width, for models with R=2.0 pc, t=100 pc^{-2}, and various values of N_0. Curves are labeled with the value of $\log_{10}(N_0)$.

foreground gas than the less dense models can. Thus at some frequencies the lines from the $N_0 = 10^{4.5}$ cm^{-3} model are coming from gas less dense than that producing the line in the $N_0 = 10^4$ and $N_0 = 10^{3.5}$ cm^{-3} models. Of course, because the models have finite size (and hence a lower limit to their density), at sufficiently low frequencies Δv will always be proportional to N_0. (We are approaching this situation at n = 240 in the current models.) These effects can be washed out by a large antenna beam (lower panel), but at intermediate frequencies it is not generally safe to assume that denser nebulae will have broader recombination lines than less dense nebulae, because, as we see here, the line shape is a complicated function of both the peak density and the density structure of a nebula.

There is a correlation between the onset of line broadening, as indicated by an increase in Δv, and the location of the turnover in L. The correlation is quite good for these models, and both the n of the peak in L and the n of the onset of broadening give information about the peak density.

Some of the models show line "narrowing" near n = 60. This results from non-linear amplification of the 2.7 K microwave background, and it can reduce Δv by about 1 km/s below the Doppler width. This effect requires rather large values of τ_L. In this case, $\tau_L = -0.2$ for the densest model at n = 60, but as τ_L decreases at either higher or lower n (Fig. 2), line narrowing is only seen over a small portion of the spectrum. For $n >> 60$, impact broadening becomes the dominant source of the line shape. However, in cooler nebulae, or in nebulae with

substantial temperature gradients, line narrowing can occur in less dense gas and over a wider range of frequency.

In summary, the height of the peak in L, being related to the amount of stimulated emission in the gas, is proportional to the emission measure and thus increases with increasing N_0. The turnover in L, caused mostly by impact broadening, moves to lower n as N_0 increases. In contrast to the behavior of the L(n,R) models, which differed only in the amount of low density gas they contained, the high frequency lines of these L(N_0) models vary considerably from model to model. The value of L(n) at low n carries information on the maximum emission measure of an HII region, while the value of L at high n contains information on the amount of low density foreground gas.

L(n,t).

The sequence of curves in Figure 17 for a model with $N_0 = 10^4$ cm^{-3} and R = 2.0 pc, shows L(n) when the rate of decrease of N_e with r is varied. Note first that the curves all peak at about the same principal quantum number. This is a consequence of two factors: 1) at high frequencies most of the line comes from the densest gas, and 2) impact broadening, which causes the turnover in L(n), is proportional to N_e. Because all these models have identical values of N_0, their lines begin to be broadened at almost identical values of n, and they have nearly identical locations of their peak L. The height of the peak however, being dependent on the emission measure, is the greatest in those models where the density falls least rapidly with increasing r, i.e., in the models with small values of t. This behavior again indicates that the

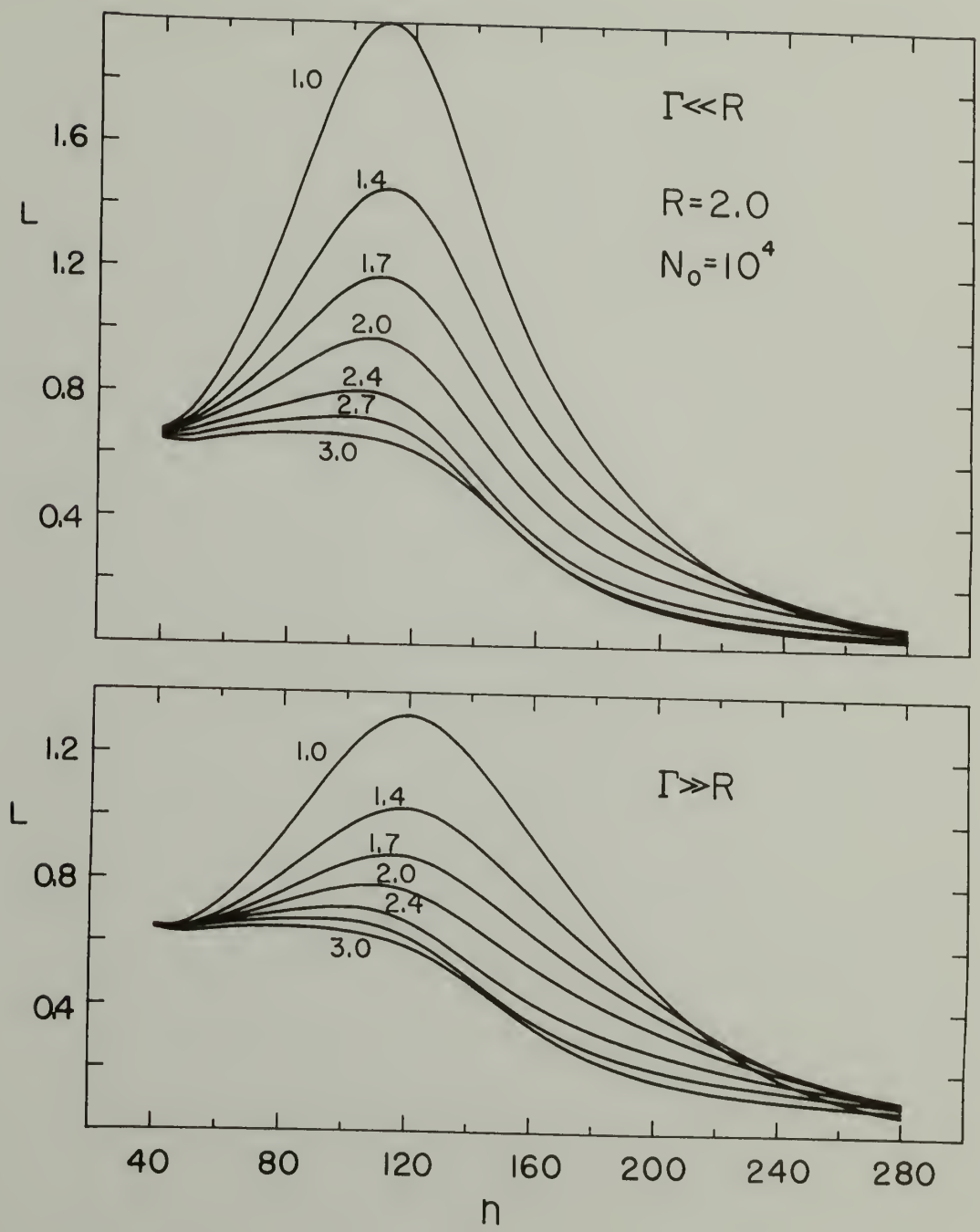

Figure 17: L(n) for models with $N_0=10^4$ cm^{-3}, R=2.0 pc, and various values of t. Curves are labeled with the value of $\log_{10}(t)$.

height of the peak in the L(n) function in isothermal models carries information on the emission measure somewhat independent of the actual peak density; the location of the peak is more related to the maximum density of the nebula. Models that are very centrally condensed, e.g., those with $t > 500\ pc^{-2}$, have lines that are reduced by impact broadening at frequencies where stimulated emission is not yet important. The converse situation--a nebula with high emission measure yet low density, thus having a very broad peak in its L(n) function--is not likely to be encountered.

The line widths shown in Figure 18 have all the characteristics discussed previously: There is slight line narrowing at $n = 60$, and at intermediate values of n there is no monotonic relationship between Δv and t. Also, the broadening begins at essentially identical n in all models, consistent with the identical locations of the peak L.

The upper panel of Figure 18 shows that $\Delta v(n)$ does not always increase monotonically with n; lines from heterogeneous nebulae may either broaden, remain constant, or narrow with increasing n, depending on the detailed density structure of the object. This effect appears quite clearly in the models of southern nebulae constructed by Batty (1979), because those models contain large discontinuities in their density structure. One general feature of spherical, centrally condensed static models is that $\Delta v(n)$ decreases with increasing antenna beam width as more of the low density outer parts of the model are added to the observation. (The exception occurs when there is significant line narrowing.) This suggests that if observations are made at a frequency where impact

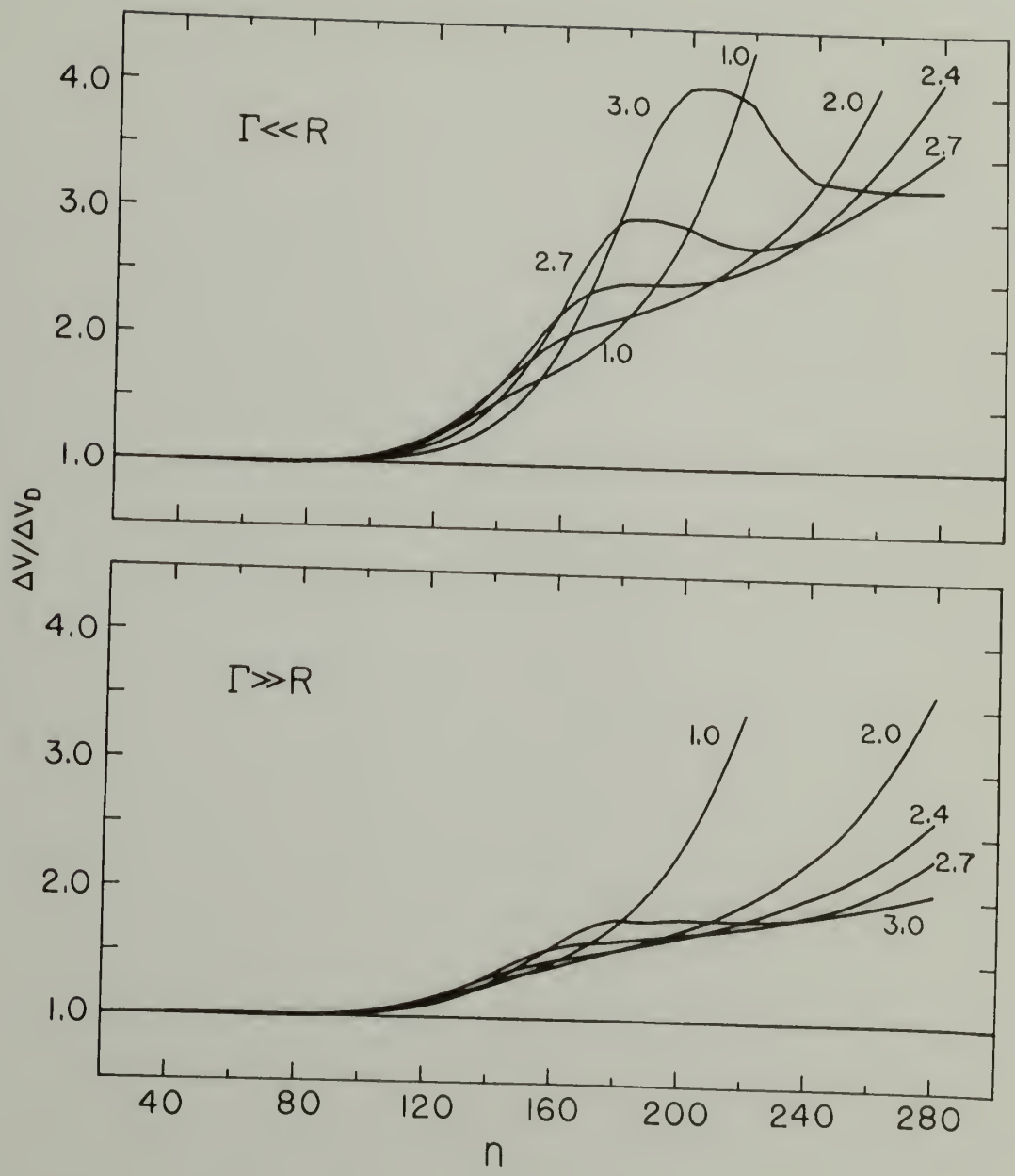

Figure 18: Line widths normalized by the Doppler width for models with $N_0=10^4$ cm^{-3}, R=2.0 pc, and various values of t. Curves are labeled with the value of $\log_{10}(t)$.

broadening is important, the brighter parts of a spherical static nebula should have a larger Δv than the fainter parts.

Summary: L(n) from hot, isothermal models.

Perhaps the most remarkable property of the 41 different L(n) functions which have been examined so far is the most obvious one: all the curves look alike. This is not a trivial statement, nor is it a consequence of the specific density structure (see, e.g., Fig. 1), or of the geometry. Hemispherical models have the same characteristic L(n) shape as the models discussed in this chapter, and the L(n) functions from even simple homogeneous isothermal plane-parallel models are, at first glance, indistinguishable from the L(n) functions of spherical heterogeneous models. All the models presented here have an $L(40) \sim 0.6$, show either a monotonic increase in L(n) or a flat L(n) to $n \sim 100$, and then have a monotonic decrease in L(n) with increasing n until $L(n > 180) < L(40)$.

There are two reasons for the essential similarity of all the L(n) curves: 1) there are only a few physical processes which govern the line emission and though some of these are not linear, they are all rather straightforward (e.g., they are independent of the radiation field except along the line of sight); and 2) the models discussed in this chapter have been simple, but more important, they have been reasonable. By reasonable, I mean that the models try to approximate real nebulae and therefore are not low density yet high emission measure objects (which would have to be kiloparsecs in size), nor extremely dense, nor dense yet low emission measure (like pancakes viewed face-on).

The symmetry of the models, though unavoidable in a preliminary treatment like this, has remarkably little to do with the form of the L(n) function as long as we evaluate the models for either large or small antenna beams. (Questions of asymmetry become very important when comparing models with observations of complex nebulae because the data, typically, are taken with HPBW's that change by more than an order of magnitude over the radio frequency range.) Any circular antenna beam centered at z = 0 will measure an L lying between the small and large beam cases. Thus it is not possible for significant deviations from the canonical L(n) shape to arise solely from the size of the antenna beam (or its variation) as long as both the nebula and the antenna beam are circularly symmetric.

The role of the atomic processes in determining the canonical L(n) curve for isothermal nebulae is quite straightforward. Remember first that, in the absence of stimulated emission, impact broadening and optical depth effects, L(n) is approximately constant. Thus at n = 40 (100 GHz), where $\tau_c \sim 0$ and $\underline{a} \sim 0$ in most models, L depends on T_e and, weakly, on the density through its influence on the departure coefficient b. Since we have dealt exclusively with isothermal 10^4 K nebulae, it is not surprising that L(40) varies so little among the different models.

All models with sufficiently high emission measure show a peak in L at some n. We can establish that such a peak <u>should</u> occur by considering, once again, a simple homogeneous, isothermal, 10^4 K model. In this case the standard, crude criterion for line enhancement, i.e., $\tau_c \sim 10^{-3}$, can be used to determine the frequency at which L will be

enhanced by 10% for a region of given emission measure. The competing process, impact broadening, will tend to reduce L by about 10% when the quantity $\underline{a} = 0.10$. But because $\underline{a}$ is a function of N_e while τ_c is a function of $N_e^2 \ell$, we can determine the value of the path length ℓ which, for a given density and at a given frequency, will give $\tau_c \gtrsim 10^{-3}$ yet $\underline{a} < 0.1$. That is, we can determine how large an isothermal, homogeneous 10^4 K nebula must be to have stimulated emission occurring at a higher frequency than impact broadening. Using eq. (39) for τ_c and the approximation given by Brocklehurst and Seaton (1972) with $T_D = 2 \times 10^4$ K for $\underline{a}$, stimulated emission will enhance a relatively unbroadened line when

$$N_e < 10^{3.9} \left(\frac{100}{n}\right)^{7.4} \quad cm^{-3} \tag{89a}$$

and

$$E > 1.7 \times 10^5 \left(\frac{100}{n}\right)^{6.3} \quad cm^{-6} \text{ pc.} \tag{89b}$$

These relationships imply that at $n = 100$, a $10^{3.5}$ cm^{-3} HII region need only be 0.02 pc in size for the effects of stimulated emission to outweigh the effects of impact broadening and for L to be enhanced. This restriction on ℓ is easily met: even Orion A (a rather modest nebula in all respects) is thought to have a region of this density with a size of about 0.5 pc (Lockman and Brown, 1975). Despite that fact that this discussion is extremely simplistic [as are the criteria of eq. (89)], the implications are correct for all the models seen so far: for $N_e > 10^3$ cm^{-3} and for reasonable nebula sizes, line intensities are enhanced at relatively high frequencies, and are not reduced by impact

broadening until somewhat lower frequencies. Thus L(n) has a peak. Low emission measure objects are the exceptions; in these, impact broadening can always reduce L more than stimulated emission can enhance it, and there is no peak.

That L for some large n is always smaller than L(40) is a consequence of the strong frequency dependence of impact broadening and of the fact that stimulated emission in foreground gas, though it enhances L, does not enhance it enough to compensate for the reduced line intensity from the dense regions.

For all these reasons we expect the L(n) function for isothermal nebulae to have a well defined shape. Qualitatively, the height of the peak will be related to the emission measure and the location of the turnover will be related to the maximum density of the nebula. The low frequency value of L will depend on the amount of low density foreground gas.

From this discussion we can formulate a general strategy for analyzing radio recombination line observations. First, the highest frequency measurement ($n < 60$), because they are least likely to be enhanced by stimulated emission (except in highest emission measure nebulae), will give the most information about the temperature of the densest gas. Millimeter wave measurements of L are therefore critical, although they are of use only in determining the properties of the most dense components of a nebula.

Secondly, there must be enough measurements in the range $80 < n < 140$ to establish the existence and properties of the peak in L. These,

together with continuum observations, place rather strict limits on the maximum beam-averaged emission measure in the nebula. Finally, observations at n > 180, together with the lowest frequency flux density measurements, can establish the properties of low density foreground gas. The line widths, together with the location of the turnover in L, allow us to distinguish between E and N_e, and thus to a certain extent they carry information on the density structure and geometry of the nebula.

Because the isothermal L(n) function is so well behaved, we can learn a lot about any object whose recombination line spectrum does not have the canonical shape just by considering what is necessary to produce the deviation. This will be discussed further in §IIIe, after we examine the effects of modest, smooth variations in T_e on the shape of the L(n) function.

d) Variations in T_e

To first order, changing the temperature of an isothermal model is equivalent to multiplying the canonical 10^4 K L(n) function by a constant factor: > 1 if $T_e < 10^4$ K, and < 1 if $T_e > 10^4$ K. The shape of the L(n) function does not change very much as the overall temperature is raised or lowered.

The effect of smooth temperature variations within a model is shown in Figure 19. Here T_e is varied linearly with r, from 7500 to 12500 K and from 12500 to 7500 K, where $N_0 = 10^4$ cm^{-3}, R = 2.0 pc and t = 100 pc^{-2}. For comparison, the isothermal 10^4 K model is also shown. Because the highest frequency values of L are most sensitive to the

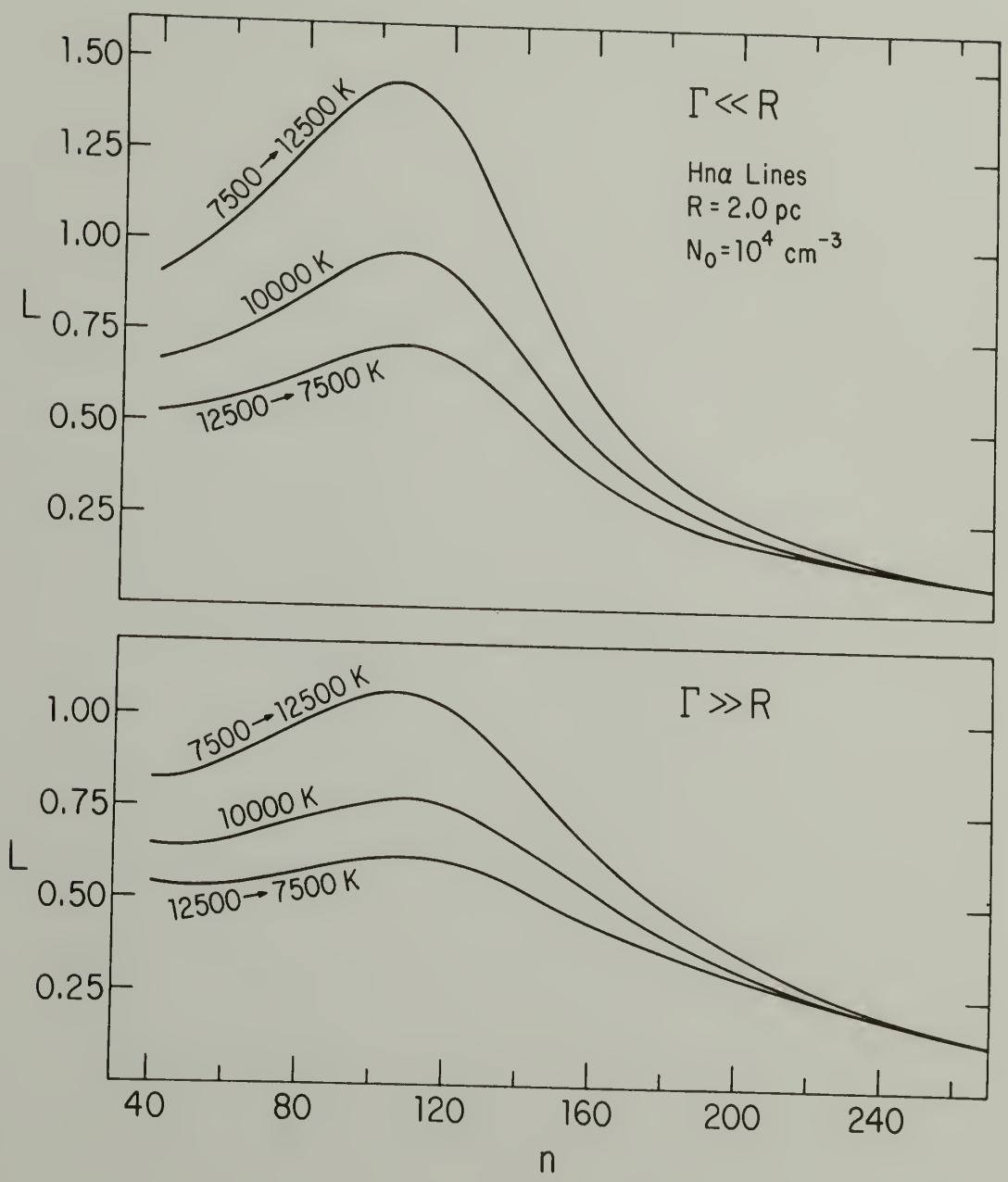

Figure 19: L(n) for models with $N_0=10^4$ cm^{-3}, R=2.0 pc, and t=100 pc^{-2}, with a constant T_e (10^4 K), or a T_e that varies linearly with r from 7500→12500 K, and from 12500→7500 K.

temperature of the densest gas, the models with the coolest central regions have the highest L(40). At larger n, where most of the emission comes from moderate density gas, the curves merge because all models have substantial regions of moderate density gas with $T_e \sim 10^4$ K. At still larger n ($\sim$ 290, not shown on this figure), the curves cross and the model with the coolest outer regions has the largest L.

This figure shows 1) that L(40) is related to the temperature of the densest nebular gas, again showing the importance of accurate high frequency measurements; 2) that it may be rather hard to determine the temperature of the outer parts of a nebula if it is not too different (less than a factor of two) from the temperature of the dense inner parts; and 3) that smooth $\pm$ 25% temperature variations do not greatly alter the canonical shape of the L(n) function.

e) The Recombination Lines from Orion A

Observations show that many nebulae have L(n) curves which look like the canonical L(n) function (e.g., M17 and the brightest component of W51), but there are prominent exceptions. Figure 20, adapted from Lockman and Brown (1975), shows L(n) (at z = 0) for Orion A. It is unlike the canonical L(n) function: L(40) is nearly twice the value expected from a 10^4 K object, and there is no well defined peak--within the uncertainties, L decreases monotonically with increasing n for all n > 40. These data cannot be matched by simply lowering the temperature of one of the standard isothermal models because, as mentioned above, changing the T_e of an isothermal region only raises or lowers the canonical 10^4 K L(n) curve, it does not remove or displace the "peak".

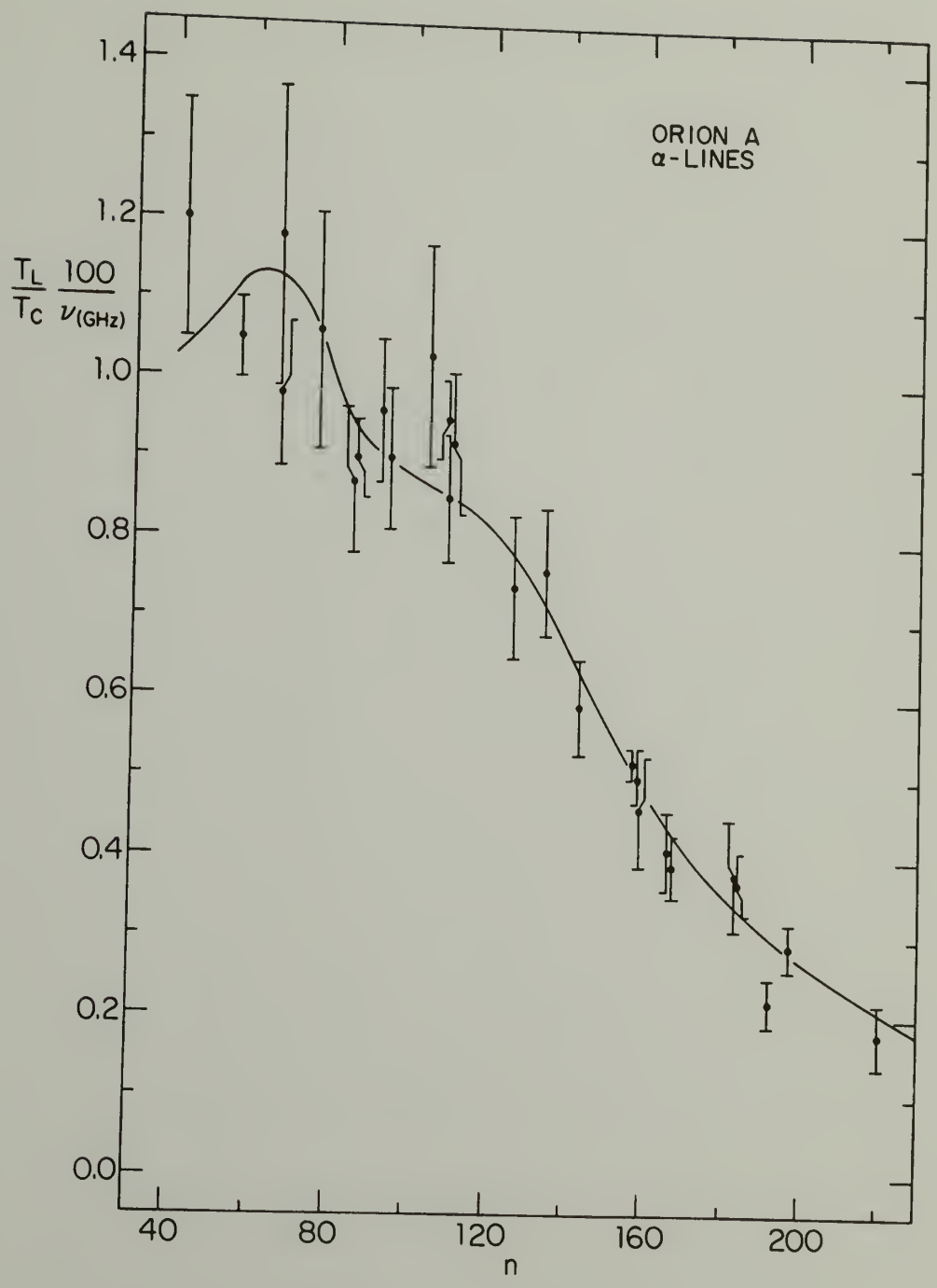

Figure 20: L(n) for Orion A. Data are taken from the compilation of Lockman and Brown (1975), and the solid line shows L(n) for the Lockman and Brown model.

Unlike the line intensities, the line widths from Orion A show no unexpected behavior. Within the errors Δv is constant for $n < 100$ and increases monotonically at larger n.

The study of the canonical L(n) function and its relationship to nebular structure suggests two alternative ways of modeling the Orion A data: 1) construct a model with such a high emission measure that lines are enhanced by a factor of two at 100 GHz through stimulated emission, and with such a high density that impact broadening becomes important near 100 GHz causing L to decrease for $n > 40$: or 2) construct a model with a temperature gradient so that the gas producing the lines near 100 GHz (which must be the densest nebular gas) has a T_e near 5000 K, and that producing the lines near 5-10 GHz has a T_e near 10000 K. The first alternative has the effect of shifting the peak in L to low principal quantum numbers. It requires $E \gtrsim 10^9$ cm^{-6} pc, $N_e \gtrsim 10^{6.5}$ cm^{-3} and gives $T_b > 20$ K at $n = 40$. This model would be somewhat brighter than Orion is, but, more important, in this model all recombination lines with $n > 40$ are impact broadened. This is not observed, as Δr remains constant from $n = 40$ to $n = 100$, and thus Orion A is unlikely to be just a denser, higher emission measure version of one of the standard isothermal models.

The second alternative is to make the gas seen at 100 GHz be cooler than the rest of the nebula. There is no inherent difficulty in this approach, as long as one can construct a model whose cooler gas dominates the line emission at mm-wavelengths but does not produce much of the line at centimetric wavelengths.

Lockman and Brown (1975) have found one model that fits these data (the solid line in Fig. 20) by making the densest gas 7500 K and of small angular size, and the moderate density gas 10^4 K and an order of magnitude larger in size. At centimetric wavelengths the combination of beam dilution, impact broadening and optical thickness in the densest gas reduces the intensity of the lines it emits and the nebula appears to be a 10^4 K object. The Lockman and Brown model is only one of a set of models which will fit the L(n) spectrum of Orion A at z = 0. All the models have a temperature gradient in the opposite sense as the density gradient (i.e., low T_e in regions of high N_e). But more important, the temperature gradient in the densest gas must be so steep that it approaches a discontinuity (though it does not necessarily have to be accompanied by a discontinuity in the density as in the Lockman and Brown model). Otherwise Orion would have a L(N) curve like that of the smoothly varying T_e models of Figure 19.

The nebular structure required by the recombination line observations is quite consistent with the structure inferred from other evidence. Orion A appears to be located on the edge of a massive molecular cloud (Zuckerman, 1973, and references therein) and is probably density bound on the side facing the sun and ionization bound on the side away from the sun. Thus the nebula is not symmetric and its densest portions are contiguous with the neutral molecular cloud. The structure of ionization fronts is quite complicated, but in general, as one moves from the fully ionized to the neutral regions the temperature decreases faster than the fractional ionization (see, e.g., Hill, 1977). At some point

there is probably ionized gas which has not yet been heated to 10^4 K, and it is likely that this gas will be very dense (approximately the density of the molecular cloud). Furthermore, this cooler gas is being continually replenished, maintaining the non-equilibrium temperature and density configuration at the back of the nebula.

Thus the sharp temperature gradient in the densest nebular gas implied by the recombination line observations is entirely consistent with theoretical estimates of the thermal structure of ionization fronts given the accepted geometric structure of Orion A. But this is far from the sort of structure one would build into "reasonable" standard models such as those discussed earlier; these do not contain temperature discontinuities and thus do not give L(n) functions like that of Orion A. However, the discussion of recombination line emission from reasonable models gave enough insight that the "peculiarities" of Orion A, and ways to model them, were obvious.

The state of the Orion A data does not warrant a complete modeling of the objects at this time. Better L($n < 60$) measurements, preferably maps, are needed in order to pin down the properties of the densest gas. But this brief discussion has illustrated how the understanding gained by examining standard models can be applied to a real object. Deviations from the canonical L(n) curve point to interesting aspects of an object and provide indications of the most important data that need to be obtained.

f) The Shape of Recombination Lines from Expanding Nebulae

When a cloud of neutral gas is ionized, the pressure within the gas rises by roughly two orders of magnitude--the ionized cloud must expand. The "macroturbulent" motion of expansion will alter the shape of recombination lines in ways that depend on the details of the temperature, density, geometry and velocity field of the cloud.

The most simple case is the homologous expansion of a uniform spherical nebula, i.e., $V(r) \propto r$, where the velocity is entirely radial and is taken to be positive for expansion. The observed velocity, V_{obs}, along a line of sight z radii from the nebular center is

$$V_{obs} = -V(R)\ (1 - z^2)^{\frac{1}{2}} + V(R)s/R, \qquad (90)$$

where s is the distance along the line of sight measured from the near side of the nebula so that $0 \leq s \leq 2R(1-z^2)^{1/2}$, and V(R) is the radial velocity at the edge of the nebula (at r = R). The amount of material in a given observed velocity interval is $N(s)\ |ds/dV|$ which, in a uniform, homologously expanding nebula, is $N_e V(R)/R$--a constant. Thus this simple model has a line profile function which is the convolution of a "boxcar" function arising from the nebular expansion (i.e., ϕ = constant for $-V(R)(1-z^2)^{1/2} \leq V_{obs} \leq V(R)(1-z^2)^{1/2}$), with Gaussian functions from the thermal and microturbulent motions, possibly convolved with a Lorentzian function if the lines are pressure broadened. In general, the total line profile function from even this simplest of models cannot be described by an analytic function, but, if $T_e = 10^4$ K, small expansion velocities (V << 10 km/s) will hardly affect the profile

shapes, while large expansion velocities (V >> 10 km/s) will cause profiles to resemble the boxcar function.

In this first-order model, the component of expansion is greatest at z = 0, so recombination lines will "narrow" away from central lines of sight, just as lines from centrally condensed models do when impact broadening is important. When expansion dominates the line shape, the width will vary as $(1-z^2)^{1/2}$. In more complex HII regions, the line shape and its variation can be more complicated: When $V(r) \propto r$, high frequency lines from centrally condensed nebulae, being formed at small radii, may show few effects of expansion. On the other hand, some nebulae seem to consist of dense components embedded in a more tenuous ionized medium (e.g., DR 21; Pankonin et al., 1977). In this case the extended medium may be in pressure equilibrium with its surroundings while the dense gas is not. At high frequencies the lines could be quite broad (coming from the dense, rapidly expanding condensations), while at low frequencies, where the lines are formed in the more tenuous gas, they would be narrower owing to the lack of systematic velocity gradients in the tenuous gas.

It is clear that the importance of systematic motions in a nebula depends on the entire structure of the nebula, and thus few general rules can be formulated. However, once again it is worthwhile to consider the properties of the line shape from a few idealized models in order to understand what effects might occur, and how these might change our understanding of the properties of dense nebulae.

Mathews (1969) has followed the evolution of a uniform $10^{4.5}$ cm^{-3} cloud of gas with an initial radius R = 0.1 pc excited by a central star.

The cloud is allowed to expand into a vacuum. He finds that after 8850 years the cloud is completely ionized and is expanding nearly isothermally. Some 13000 years after turn-on of the central star the velocity field is nearly linear in r, and since the outer parts are expanding more rapidly than the inner parts, the density structure becomes centrally peaked: after 13000 years N_e^2 is decreasing by 10^8 cm^{-6}/pc at low r. This central density peak is smoothed out as the expansion continues until after 23000 years dN_e^2/dr is -10^5 cm^{-6}/pc at low r. Compared to the model at 13000 years, the model at this later time has a central density which has decreased from $10^{3.8}$ to $10^{2.5}$ cm^{-3}, and has a maximum velocity of expansion which has increased by a few km/s to 80 km/s. (Note that gas freely expanding into a vacuum can reach a velocity many times greater than the local sound speed without developing shocks.)

A modified version of the program used to calculate the static line profiles was used to calculate the line profiles from the expanding model (the code is more fully described in Appendix A). In short, each model nebula is divided into 15 shells, within which the density and radial velocity are taken to be constant. The temperature was fixed at 10^4 K. Each line of sight through the model is divided up into small intervals in order to account for the changing projection of the radial velocity field. Thus there are three forms of "gridding" in the macroturbulent models: the assumed shell structure of the nebula, the finite number of lines of sight along which the equation of transfer is evaluated (the calculations were performed over 100 lines of sight equally spaced between z = 0 and z = 1), and, finally, the division

of each line of sight into cells, each of which has a single temperature, density, and projected velocity. However, the gridding is the only approximation; the results are exact for a model divided as these are.

In all these calculations the Doppler width of the lines is the width due to thermal motion alone, i.e., there is no microturbulence in these models. The reason for this omission will become apparent.

Figures 21 and 22 show the recombination line profiles, normalized by their peak value, as observed by large and small antenna beams, for the model 13000 and 23000 years after the turn-on of the exciting star. The normalized line temperatures are plotted against x, the half-1/e-width of the thermally broadened line component. In these figures velocity increases from left to right, and $x = +1$ is equivalent to a velocity of + 12.9 km/s. The line drawn at a normalized T of 0.5 shows the thermal Δv, i.e., the width that the lines would have in the absence of expansion and pressure broadening. It is clear that expansion has significantly broadened all the lines.

After 13000 years the high frequency (n = 40) line width is 24.1 and 26.2 km/s for the $\Gamma << R$ and $\Gamma >> R$ beams, respectively, and after 23000 years is 33.8 and 38.8 km/s. These values roughly span the range of observed recombination line widths (see, e.g., Reifenstein et al., 1970; Wilson et al., 1970) and, coincidentally, the 13000 year $\Gamma >> R$ model has a high frequency line width exactly that observed from Orion A. Since these models contain no microturbulence and have only the intrinsic 21.5 km/s thermal line width appropriate to hydrogen recombination lines from a 10^4 K gas, we conclude that if nebulae are expanding like these

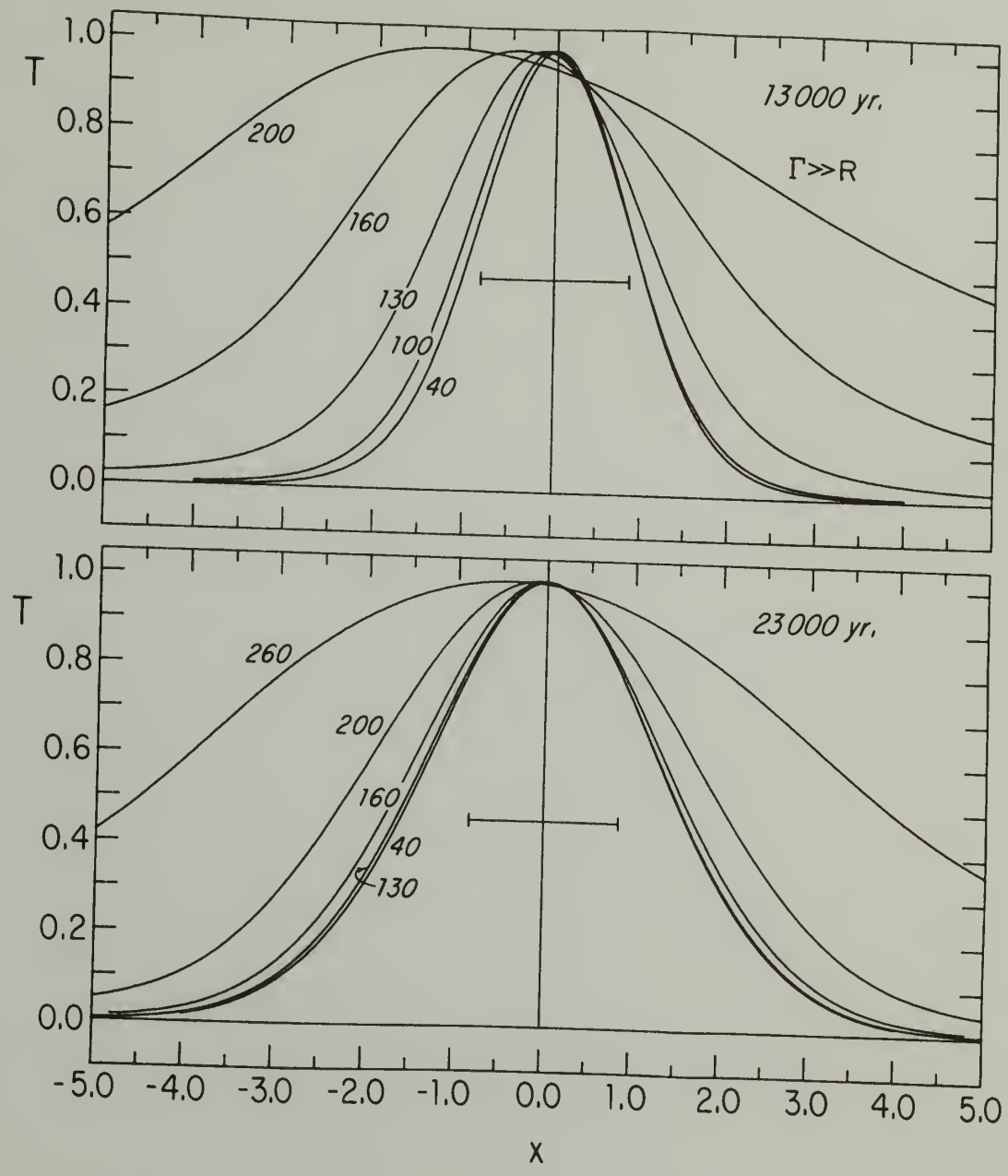

Figure 21: Recombination line profiles, normalized by their peak value, for Mathews' model HII region 13000 and 23000 years after the start of its ionization. The abscissa is in units of half the 1/e-width of the Doppler line component which, for this model, is 12.9 km/s. Velocity increases from left to right. The solid line at T=0.5 shows the line width in the absence of expansion and impact broadening. These models are observed with a very large antenna beam.

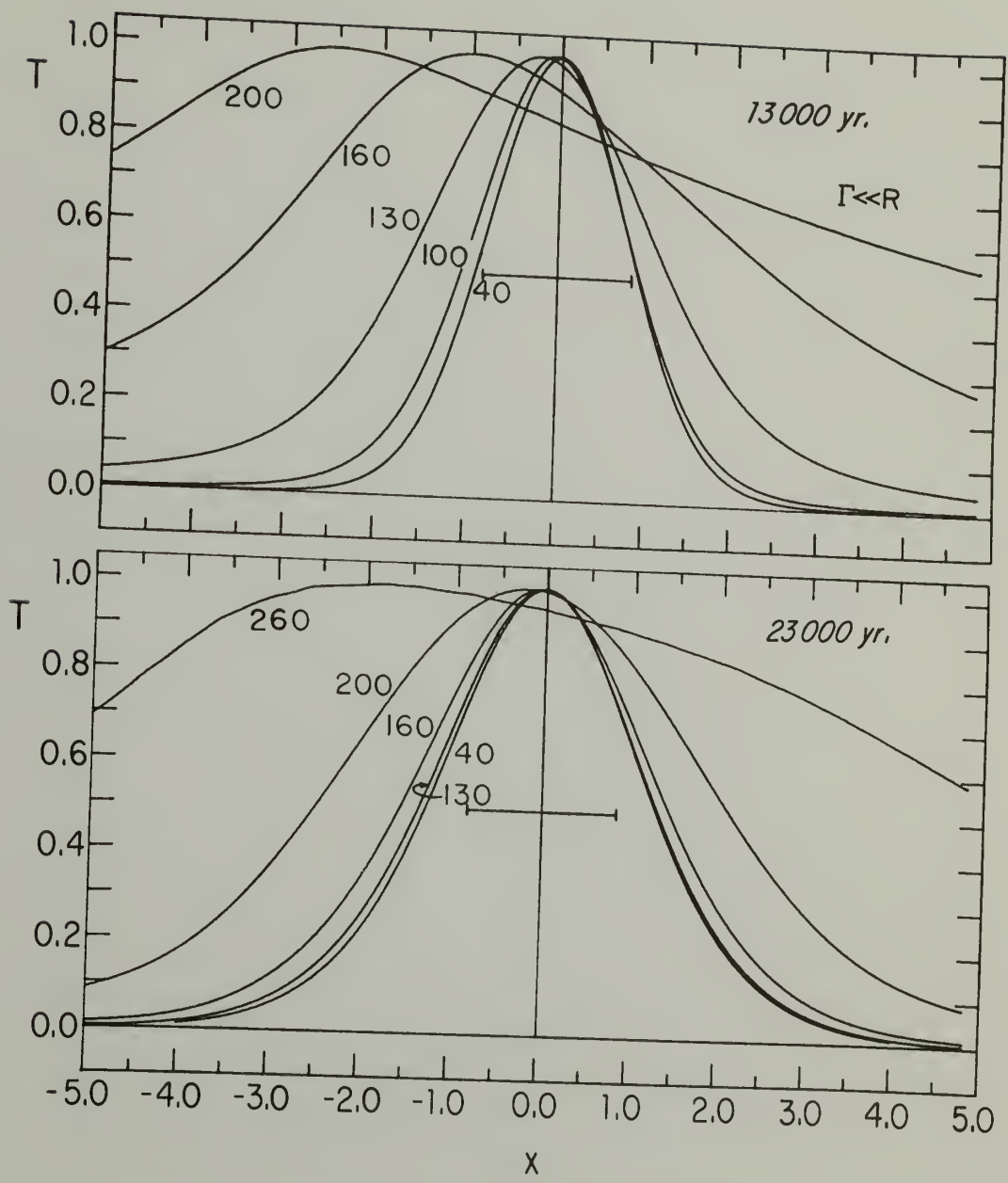

Figure 22: Mathews' model observed with a very small antenna beam centered at z=0.

models are then there is no need to invoke microturbulence to explain the difference between thermal and observe line widths--the extra width can arise entirely from expansion.

As n increases the line width increases because of impact broadening and because more and more of the line is formed through stimulated emission in foreground, higher velocity gas. At the highest frequencies the line shapes are generally indistinguishable from Gaussian profiles but, at low frequencies ($n > 160$), where continuum opacity in the dense gas cuts off the line emission from the back of the models while lines from foreground gas are enhanced, the lines become somewhat asymmetric and, at some frequencies, have few of the characteristics of simple Gaussian or Voigt profiles. Lines from expanding nebulae broaden more rapidly with increasing n than lines from their static counterparts, so in general, $\Delta v(\text{expanding}) > \Delta v(\text{static})$ at all n. Because impact broadening is the only frequency dependent broadening mechanism other than expansion, if there is significant expansion in an object we ignore it at the risk of overestimating the extent of impact broadening.

The increase in Δv with increasing age of the model is due less to any change in the velocity field than to the overall evolution of the density structure. After 13000 years, the model is so centrally condensed that most of the line to quite low frequencies arises at small r where V(r) is rather small. However, as the central density peak is smoothed out, after 23000 years even the highest frequency lines come from a much larger volume than previously, and thus come from gas with a larger range in velocity.

This same effect causes $\Delta v(40)$ to <u>increase</u> with increasing z in the 13000 year model despite the fact that as z increases the expansion is projected more and more across the line of sight. At 13000 years the model is so centrally condensed that over 75% of the emission measure at $z = 0$ comes from material within $\pm$ 5 km/s of $V = 0$, while at $z = 0.5$, 75% of the emission measure comes from material within a projected velocity range of $\pm$ 11 km/s about $V = 0$. Thus the naive expectation that Δv will be inversely proportional to z (because of simple projection effects in uniform models) does not necessarily hold for nonuniform models, especially those which have large central density peaks. This trend of line narrowing at low z has almost disappeared by the time the model has the 23000 year density structure, when at $z = 0$, 75% of the emission measure comes from gas with $|V(r)| \leq 19$ km/s.

Table 1 summarizes the line shapes from this expanding model. A gradual blueshift in the line peak accompanies the distortion of line profiles at large n. While the blueshift can be quite large in the case of the 13000 year model, after another 10000 years it has become so small that it lies within the measurement errors of present low frequency observations. In this respect the 23000 year model is probably more characteristic of observed nebulae than the 13000 year model is, for blueshifts are rarely observed and then only at a level of a few km/s (e.g., Batchelor and Brocklehurst, 1973; see also Chapter IV). Because different transitions form in somewhat different parts of a heterogeneous nebula, α, β and γ lines emitted at nearby frequencies do not have the same peak velocity, although their velocities differ by only a few km/s in this model.

TABLE 1

LINE SHAPES FOR MATHEWS' MODEL NEBULA

	13000 Years				23000 Years			
	$\Gamma \ll R$		$\Gamma \gg R$		$\Gamma \ll R$		$\Gamma \gg R$	
n	V (km/s)	Δv (km/s)	V (km/s)	Δv (km/s)	V (km/s)	Δv (km/s)	V (km/s)	Δv (km/s)
40	0	24.1	0	26.2	0	33.8	0	38.8
80	- 0.2	26.3	- 0.4	26.2	0	33.8	0	38.8
100	- 0.6	39.2	- 0.8	27.8	0	33.8	0	38.8
130	- 2.8	80.8	- 2.1	36.1	0	34.5	- 0.3	40.2
160	-13.0	127	- 5.7	61.9	- 0.5	35.0	- 0.6	42.6
180	-22.0	182	-10.0	90.5	- 1.4	46.5	- 0.9	47.1
200	-32.7	--	-16.3	131	- 2.7	60.3	- 1.2	54.9
220	-40.2	--	-24.3	180	- 5.7	83.2	- 1.9	67.1
240	-46.9	--	-30.9	--	-12.3	113	- 2.8	85.1

No entry is made for $\Delta v > 200$ km s^{-1}

While Mathews' model is the best published calculation of expansion in a dense HII region, it is not clear that real nebulae behave in a similar way. Perhaps surprisingly, it is not the neglect of a surrounding interstellar medium and the resultant high velocities of expansion that is the major inadequacy, for the highest velocity gas is so tenuous that its influence on most lines is negligible. The major inadequacy of Mathews' model is its symmetry. In symmetric models the high density gas relaxes so rapidly that we would never expect to observe ionized gas with $N_e > 10^4$ cm^{-3}, but many nebulae do contain such components [see, e.g., Israel's (1976) study of the unassuming W58 region]. The solution of this difficulty undoubtedly lies in the relationship between the nebular gas and the molecular cloud from which it formed.

If the exciting stars are not located at the center of the molecular cloud, there may be a dense neutral gas contiguous to the HII region which, as it is ionized, continually renews the high density component of the nebula (as in Orion A). After some initial expansion, the overall nebular motion becomes more like flow of gas away from a dense slab than spherically symmetric expansion, and it is difficult to generalize about a velocity and density structure.

A few model calculations for ad hoc combinations of density and velocity indicate that the general results for uniform expanding models still hold in these non-uniform cases. In particular, because of the correlation between high density and low velocity of expansion, gross blue (or red) shifts of the high frequency lines will be unlikely, although an overall broadening of all lines is still evident.

One interesting property of asymmetric expanding models is that they can appear to be rotating when no such rotation exists. Consider a one-dimensional geometry in which gas expands along a line in the direction of increasing r with $V(r) \propto r$. Viewing this linear nebula from an arbitrary angle θ, we observe a velocity $V_{obs} \propto r \cos(\theta)$, and V_{obs} will vary linearly across the object. Similarly, a hemispherical, uniform, homologously expanding nebula viewed from an arbitrary angle will be expanding across the line of sight at one projected edge, but the expansion will not be tangent to the line of sight at the other projected edge (because the object is not a full sphere), and again there may be the appearance of rotation. In general, a regular asymmetry in either geometry or velocity field can give the appearance of rotation in a nebula. It is thus possible that observation of apparent nebular rotation (e.g., as in Sgr B2 by Chaisson, 1973, or in NGC 7538 by Lada and Chaisson, 1973) is only the result of asymmetric structure and projection effects (Israel, 1977, has alluded to this possibility in his discussion of NGC 7538).

In sum, nebular expansion is an interesting but poorly understood phenomenon which needs much more theoretical and observational study. At the least, the microturbulent contribution of HII regions to the interstellar medium is probably less than has been previously assumed, and it may be the case that gas flows in nebulae are more regular (i.e., less microturbulent) than is immediately apparent from the line widths.

CHAPTER IV

THE DISTRIBUTION OF DENSE RADIO HII REGIONS

a) Introduction

HII regions, besides being objects of interest due to their coincidence with early phases of star formation, are useful probes of galactic structure and evolution. The lifetime of a typical nebular exciting star is only $\sim 10^6$ years, so HII regions are only found near sites of recent star formation. The amount of ionized gas contained in an HII region can be used to derive information on the number and type of exciting stars, and the kinematics of the regions may provide insight into the global mechanism which triggers star formation.

Westerhout's (1958) continuum survey of the northern sky showed that nebulae, and presumably the youngest stars in the Galaxy, were most abundant ~ 5 kpc from the galactic center, and were less abundant at both larger and smaller galactocentric radii. This distribution is now known to be characteristic of many galactic constituents, including supernova remnants, molecular clouds, γ-rays, and OH stars (Burton, 1976 and references therein; Bowers, 1978). The H109α radio recombination line surveys of Reifenstein et al. (1970) and Wilson et al. (1970) provided new information on individual dense nebulae but, with minor exceptions, these data did not alter the view of the Galaxy given by Westerhout's continuum survey. In particular, straightforward kinematic analyses of the H109α velocities did not reveal a distinct pattern, spiral or otherwise, in the locations of the nebulae.

Wilson et al. (1970) offered two possibilities: 1) the inability to resolve the twofold distance ambiguity of sources within the solar circle made the pattern indistinct; 2) the kinematic distances were not sufficiently accurate.

The first difficulty has since been removed, for there is now a substantial body of atomic and molecular absorption measurements towards radio HII regions, and most distance ambiguities can be resolved. The problem of determining the transformation from the measured velocity into a position in the Galaxy remains serious. However, because of recent advances in our understanding of galactic dynamics, we can now analyze observations using more sophisticated, and possibly more appropriate, kinematic models than simple circular rotation. It thus seems worthwhile to reconsider the distribution of known radio nebulae, and to examine their kinematics using models based on aspects of the density wave theory and the modelling techniques which have been successfully applied to HI and CO emission (Burton, 1971; Burton and Gordon, 1978).

There are three basic limitations on the analysis in this chapter. The first arises because an accurate derivation of kinematic distances not only requires a good knowledge of galactic motions, but also requires that the projected component of motion along any line of sight be large enough so that objects at different distances have significantly different LSR velocities. These considerations limit the useful range of purely kinematic analyses to the portion of the galactic plane within $\sim 55°$ of $\ell = 0°$ (§IIIc). Second, the investigation in this chapter is limited to objects which have been detected

in the H109α recombination line (this transition having been more completely and uniformly surveyed than any other) so there is a strong thermodynamic selection effect which must be kept in mind when evaluating the results. This will be discussed further in Chapter V. Finally, there are numerous observational selection effects which combine to underrepresent distant parts of the Galaxy while overrepresenting the local area. Throughout this chapter there is no attempt to correct, except by elimination of intrinsically faint objects, for distance selection effects, and the only results which will be discussed at length are those which appear to be independent of selection effects and which do not depend on the exact form of large-scale galactic motion.

The emphasis will be on certain observed quantities: the position of a region (ℓ,b), the velocity of the peak of the recombination line V(HII), assumed to be the velocity of the ionized gas, and the continuum flux density S. The actual shape and intensity of the recombination lines are of secondary importance.

When a large number of HII regions are being examined for their overall distribution, the exact distance to any individual region is not a critical quantity, but it is important that the distances be known fairly well in order to estimate a luminosity function and a scale height, and to examine selection effects. Fairly accurate nebular distance estimates can be obtained from spectroscopic measurements of the exciting stars (see, e.g., Georgelin and Georgelin, 1970), but unfortunately most radio HII regions have not been detected at

optical wavelengths and the portion of the Galaxy which is accessible to optical studies remains small. Thus, in this chapter distances are derived solely from V(HII). Kinematically derived distances are subject to systematic errors because some aspects of galactic motions are poorly understood. However, one can always invert the procedure and, by calculating kinematic models based on derived quantities, test many of the assumptions that entered the original analysis. This is done in §IVg. An alternative approach to the study of the nebular distribution has been taken by Georgelin and Georgelin (1976). They combine spectroscopic and kinematic distance estimates (the latter determined from pure circular rotation heavily weighted, and occasionally altered, by arguments based on the "continuity" and "alignment" of the pattern they are deriving), and do not test their results against their assumptions.

A quantity of immediate interest, but one difficult to determine, is the number of HII regions in the Galaxy. The difficulties are several: 1) small nebulae are only detected when they are nearby; 2) surveys of different transitions preferentially detect gas of different density (Chapters II and III), and to some extent the thermodynamic structure of nebula may make it prominent in one survey and obscure in another; and 3) there is no adequate definition of a discrete HII region. Effects of the first two problems are reduced by restricting the investigation to HII regions that have been detected in surveys of the H109α line and which have an absolute flux density greater than some value. The last difficulty is more serious.

Although HII regions have been previously treated as isolated discrete objects, they often appear to be complex structures containing components which may have formed and evolved quite independently of one another. High resolution mapping often shows that what appeared to be a single source is comprised of two or more concentrations of gas. Even when the velocity of each continuum feature is known there is often no clear way to decide if the object should be counted as one large region or many small ones. This problem will be discussed in a later section, but it is brought up here to illustrate a fundamental difficulty which is not likely to be resolved with existing data. Although the distribution of dense concentrations of ionized gas can be studied without a strict definition of an HII region, this weakness in the analysis should be kept in mind.

b) Motions in the Galaxy

In order to describe the motion of a particle in the Galaxy several coordinate systems have been adopted (Figure 23). The galactocentric coordinate system identifies a point by its radius R and azimuthal angle θ, measured from the sun-center line and increasing in the direction of galactic rotation (clockwise), and its distance from the plane, z. The local coordinate system identifies a point by its distance from the sun r, and by its galactic longitude ℓ and latitude b. Because all nebulae discussed in this chapter lie close to the galactic plane, kinematic consequences of their z-displacement are ignored. The velocity of material at (R,θ) is its galactocentric

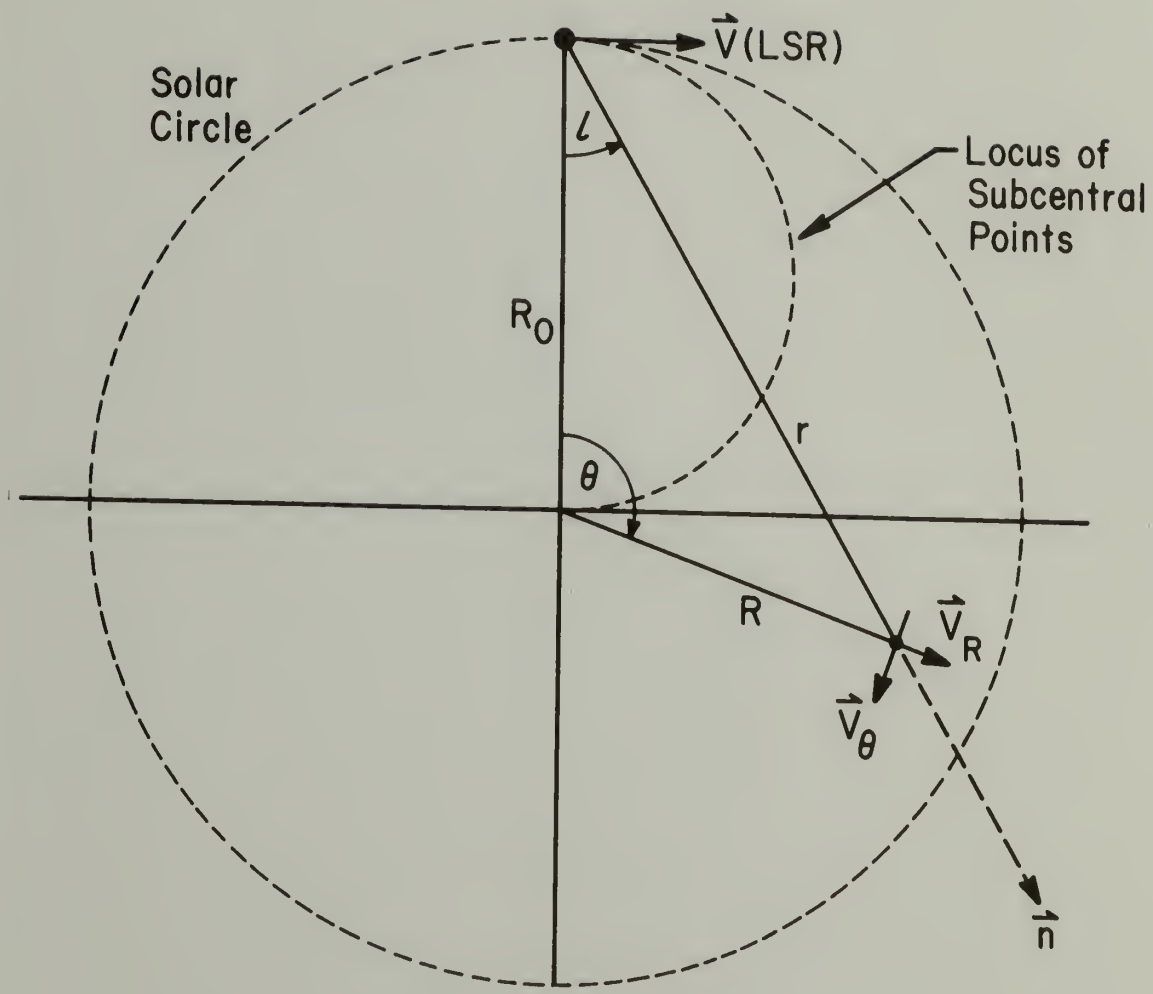

Figure 23: Definitions of coordinate systems used in this chapter. In the local coordinate system a point in the direction $\vec{n}$ is identified by its longitude and latitude (ℓ,b) and by its distance r. In the galactocentric coordinate system a point has a radius R, aximuthal angle θ, and distance from the plane z. Velocities in the plane can be resolved into galactocentric radial and azimuthal components.

radial and azimuthal velocities $\vec{V}_R$ and $\vec{V}_\theta$. The observed quantity is the projected velocity (with respect to the local standard of rest) along a line of sight from the sun in the direction of the unit vector $\vec{n}$. This projected velocity, V, is

$$V = \vec{V}_\theta \cdot \vec{n} + \vec{V}_R \cdot \vec{n} - \vec{V}_{LSR} \cdot \vec{n} \qquad (91)$$

or

$$V = V_\theta \left(\frac{R_0}{R} \sin\ell \right) - V_R \cos(\ell+\theta) - V_{LSR} \sin\ell \quad , \qquad (92)$$

where V_θ is the magnitude of $\vec{V}_\theta$, etc., $R_0 \equiv 10$ kpc is the distance to the galactic center, and it is assumed that there is no galactocentric radial velocity of the local standard of rest. Note that azimuthal motions are not observed when θ or ℓ are integral multiples of π. Similarly, for $\theta + \ell = \pm (n+1/2)\pi$ radial motions are not observed. This latter condition is met when $R = R_0 \sin \ell$, i.e., at the point along the line of sight where R is a minimum. This is called the subcentral point; the locus of these points in the first quadrant of longitude is drawn in Figure 23. Outside of the solar circle ($R > 10$ kpc) R increases monotonically with r and there is no subcentral point.

The azimuthal component of motion can be treated as the sum of an axisymmetric velocity V_c which arises from galactic differential rotation, and a velocity V_c' which may be a function of R and θ. Because the angular velocity V_c/R within the solar circle is inversely proportional to R, the highest velocity along a line of sight occurs at the minimum R, or at the subcentral point. Thus the highest

positive (negative) velocity material observed along a line of sight through the first (fourth) quadrant of longitude can be used to derive a suitably defined terminal or cutoff velocity that, if the effects of V_c' can be neglected and if the material being observed is present at the subcentral point, is a measure of V_c at the radius of the subcentral point. The function $V_c(R)$ (the rotation curve) will be approximated by

$$
\begin{aligned}
V_c &= (228574\ R - 190470.5\ R^2)^{\frac{1}{2}} && R \leq 0.7 \text{ kpc}, \\
V_c &= (60433/R - 80051 + 111370.6\ R \\
&\quad -43804.96\ R^2 + 7558.87\ R^3 - 459.645\ R^4)^{\frac{1}{2}} && 0.7 < R \leq R' \text{ kpc}, \\
V_c &= 250 + 4.05(10 - R) - 1.62(10 - R)^2 && R' < R \leq 10 \text{ kpc}, \\
V_c &= 885.44\ R^{-\frac{1}{2}} - 30000\ R^{-3} && R > 10 \text{ kpc},
\end{aligned}
\qquad (93)
$$

(Burton, 1971; Simonson and Mader, 1973), where R_0 = 10 kpc, R' = 5.5 kpc, and V(LSR) = 250 km/s. The rotation curve is not well determined, especially for R > 10 kpc where its form in eq. (93) results from the extrapolation of a model mass distribution (Schmidt, 1965), but even interior to the solar circle there are well known non-circular motions and suggestions of velocity asymmetries between the North and South (e.g., Kerr, 1969).

The velocities V_R and V_c', while uncertain, are much smaller than V_c except, perhaps, in the galactic nucleus. These "non-circular" motions are functions of θ as well as R, and there is convincing evidence of their existence and importance in the Galaxy (e.g., Burton, 1966, 1971). Systematic motions of this type are expected from

density-wave models. In the linear density-wave (LDW) theory (e.g., Lin et. al., 1969) V_R and V_c' should vary as

$$V_R = -A_R \cos(\chi(R,\theta))$$

$$V_c' = A_\theta \sin(\chi(R,\theta)), \qquad (94)$$

where A is the amplitude of the streaming motions and χ is the phase at (R,θ) relative to the potential minimum $\phi(R)$:

$$\chi(R,\theta) = 2(\theta-\theta_0) - \phi(R) \qquad (95)$$

where $\phi = 0$ at some initial R and θ_0. In the linear theory the amplitude of the streaming motions depends on the gas density and its variation with R and θ as well as on details of the spiral wave pattern. The pattern and the streaming motions it excites are presumed to terminate at some inner radius, usually placed near 4 kpc. In this chapter we take $A_R = A_\theta = 0$ for $R < 3$ kpc, although the results are not very sensitive to this boundary as long as it occurs at $R \leq 4$ kpc.

Burton (1971) has analyzed HI spectra from the first and second longitude quadrants and gives values of A_R and A_θ which provide the best fit between the observations and linear density-wave models. His streaming amplitudes between $3 < R < 10$ kpc are well fit by

$$A_R = -1.735 + 2.776\ R - 0.1944\ R^2$$

$$A_\theta = -3.435 + 3.033\ R - 0.2103\ R^2. \qquad (96)$$

These functions, together with those that describe the spiral pattern,

constitute a self-consistent linear density-wave (LDW) model of galactic kinematics.

There are two problems with the Burton pattern: First, it is not accurate in the solar neighborhood (e.g., Burton and Bania, 1974a, b). Thus linear density-wave distances to nearby objects may have a large percentage error. However, only a few nebulae, all intrinsically faint, are close enough to the sun to be seriously affected, so this is not a major concern here. Second, the pattern does not exactly fit HI observations from the fourth longitude quadrant in the sense that the spiral crosses the locus of subcentral points $\sim 5°$ in longitude away from where it should (Burton, 1971). This was not a problem for Burton, who constructed his model primarily to fit first quadrant observations, but here it causes difficulties, particularly in model calculations based on the pattern (see §IVf). Despite its shortcomings, the Burton (1971) pattern appears to be the most accurate, complete, mathematical description of the loci of LDW potential minima that is available.

More recent discussions of density waves emphasize that the gas response to the spiral wave is expected to be nonlinear, and shocks may dominate the kinematics near the potential minimum (e.g., Roberts, 1972; Shu et al., 1972). Under these circumstances the streaming motions depend on the shock strength and the detailed thermodynamic structure of the gas. This problem has been treated only in the most general way and there has been no systematic attempt to derive the required parameters from comparison with observations. For this reason

nonlinear density-wave models will not be emphasized in this discussion; where they are considered, the radial and azimuthal velocities will be those derived by Shu et al. (1972) for the intercloud medium (strong shock case) in the solar neighborhood; the location of the potential minima will remain that of Burton (1971).

Two additional components of motion must be considered: a random motion which applies to all clouds of the type likely to become HII regions, and a possible macroturbulent motion of ionized gas relative to the neutral gas in its vicinity. A recent estimate is that HI clouds have velocity dispersions of 6.5 km/s (Falgarone and Lequeux, 1973), but it may not be valid to compare the dense radio HII regions to the relatively low density HI clouds. It is probably more meaningful to compare HII regions with the molecular clouds observed in CO emission. These objects have a random velocity dispersion of 4 km/s along the line of sight (Burton and Gordon, 1978), and this is adopted as the velocity dispersion of the material from which HII regions are formed.

Macroturbulent motions of HII regions would arise from a preferential expansion of the ionized gas. A specific example is thought to be Orion A (Zuckerman, 1973; Balick et al., 1974), where the ionized gas is located on the edge of a dense molecular cloud and is flowing away from the neutral material at roughly the speed of sound (10 km/s). If this occurs in many HII regions, and if they are aligned randomly to the line of sight, the effect is that of an additional significant random motion not present in neutral gas. (An HII region evolving

entirely within a uniform molecular cloud would have no net center of mass motion with respect to the cloud.

Because it is by no means certain that all nebulae have evolved like Orion A, the H109α velocities of the HII regions considered here were compared with the CO velocities from the discrete source surveys of W. J. Wilson et al. (1974) and Gillespie et al. (1977). The 54 nebulae common to both samples have a $\langle\Delta V(CO)\rangle \equiv \langle\Delta V(H109\alpha)-V(CO)\rangle$ of -0.0 km s^{-1} with a dispersion of 2.8 km s^{-1}, and none of the nebulae considered here has as large a difference between ionized and molecular velocities as Orion A. There is an apparent difference between the southern nebulae measured by Gillespie et al., which have $\Delta V(CO) = 1.1$ km s^{-1} for 28 objects in the range $305° \leq \ell \leq 355°$, and the 26 northern nebulae measured by W. J. Wilson et al. in the range $5° \leq \ell \leq 55°$ which have $\Delta V(CO) = -1.0$ km s^{-1}. However, the CO velocities of the 5 nebulae common to both surveys differ, on the average, by 1.3 km s^{-1} in the sense that the Wilson et al. velocities are more positive than the Gillespie et al. velocities, so the apparent difference in $\Delta V(CO)$ between northern and southern nebulae may not be intrinsic to the objects, but may result from systematic differences between the two surveys. Thus the random line of sight velocity of any HII region is assumed to have no systematic component, and is taken to be drawn from a Gaussian distribution with a combined dispersion of 5 km/s.

As a final note, a model of cloud collapse by Woodward (1976) suggests that the orientation of an HII region with respect to the

cloud from which it formed will not be random, but will be related to the direction of a cloud's passage through a density-wave shock. If this is correct it offers the possibility of estimating and perhaps removing macroturbulent velocity components, but an evaluation of the model will require more detailed observational and theoretical study.

c) The Determination and Limitations of Kinematic Distance Estimates

The kinematic distance to an HII region is derived by determining the function V(r) at the longitude of the nebula, measuring the velocity of the recombination line V(HII), and identifying the r at which V(r) = V(HII). Several examples of V(r) for pure circular rotation are shown in Figure 24.

Within the solar circle (at $R < R_0 \equiv 10$ kpc) there are generally two points with V(r) = V(HII). The exception occurs for nebulae which have the largest possible positive (negative) velocity along their particular line of sight through the first (fourth) quadrant of longitude. Because these objects have the terminal velocity, V_t, they must be located quite near the subcentral point where $r = R_0 \cos \ell$. The distance ambiguity of other nebulae can be resolved by examining atomic and molecular absorption spectra seen against the nebular continuum: if the absorption extends to V_t and $|V(HII)| < |V_t|$ then the nebula is placed at the far distance. If $|V(abs)| \lesssim |V(HII)|$ then the nebula is placed at the near distance. There is no distance ambiguity for nebulae outside the solar circle, and the distance ambiguity has little effect on the determination of R [if

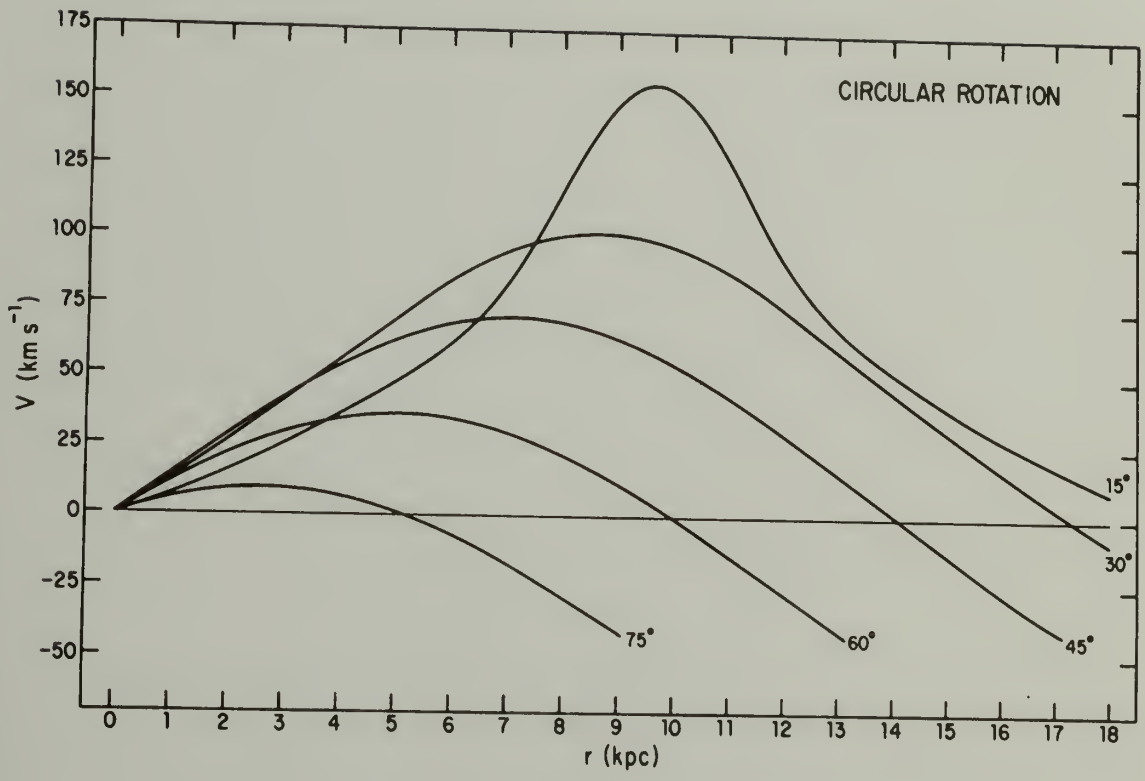

Figure 24: Velocity with respect to the local standard of rest, vs. distance from the sun at a few longitudes in the first quadrant. The velocities were derived from a circular rotation model.

the Galaxy is in pure circular rotation, R can be determined directly from V(HII)].

If the recombination line velocity is known exactly and all distance ambiguities are resolved, kinematic distance estimates will still have errors that arise from uncertainties in the value of the projected galactic velocity field and from the effects of a nebula's random motion. The galactic rotation curve is not well known outside of the solar circle (i.e., for all objects in the longitude interval $90° \leq \ell \leq 270°$), and in this part of the Galaxy kinematic distances may differ from true distance by large systematic amounts. To minimize errors caused by this uncertainty, nebulae located between 90° and 270° longitude were not included in this analysis. Within the solar circle it is reasonable to expect that our estimate of galactic motion at any point is in error by $\sim \pm 8$ km s^{-1}, a value which is the approximate magnitude of streaming motions in linear density-wave models. These errors are, however, more likely to be systematic than random.

The accuracy of kinematic distances is proportional to the magnitude of the quantity $|dV(r)/dr|$ at the velocity of the nebula. Where $|dV(r)/dr|$ is small, projected galactic motions give poor velocity discrimination between objects at different r, and conversely, objects at similar r whose recombination line velocities differ slightly because of random motions may be assigned quite different kinematic distances. In particular, $|dV(r)/dr|$ is always small near the subcentral point (the location of the peak velocity in Figure 24) and we must assume that distance estimates to HII regions located there have larger errors

than average. For pure circular rotation, small values of $|dV(r)/dr|$ result from the smallness of $|dR/dr|$, indicating that the galactocentric radius will always be known more accurately than the distance.

A crude estimate of the accuracy of kinematic distances is shown in Figure 25, where the $|dV(r)/dr|$ for pure circular rotation, averaged over the line of sight interior to the solar circle, is plotted against ℓ. At $\ell \sim 70°$ (or 290°) the kinematic distance to an HII region having a random motion ~ 5 km s^{-1} will be uncertain by ~ 1 kpc on the average, even if both galactic motions and the nebular velocity are known exactly. To avoid excessive uncertainty in the analysis, it will be restricted to directions having fairly good kinematic distance discrimination: $5° \leq \ell \leq 55°$ and $305° \leq \ell \leq 355°$. A kinematic analysis of nebulae at these longitudes (which will be called the northern and southern longitude intervals, respectively) largely avoids the uncertain V(r) at R > 10 kpc and the low average $|dV(r)/dr|$ at $90° \leq |\ell| \leq 55°$, and the omission of the innermost 10° of the plane minimizes the influence of possible non-circular motions associated with the galactic nucleus.

Even with these restrictions the average accuracy of kinematic distances is not good, because some parts of the Galaxy with rather high values of $|dV(r)/dr|$ do not contain any dense radio HII regions. When the empty areas (specifically the portion of the Galaxy at R < 3 kpc, see §IVf) are excluded, projected differential rotation averaged over $5° \leq \ell \leq 55°$ gives an average kinematic distance discrimination ~ 100 pc/(km/s). Since the combined uncertainty in galactic

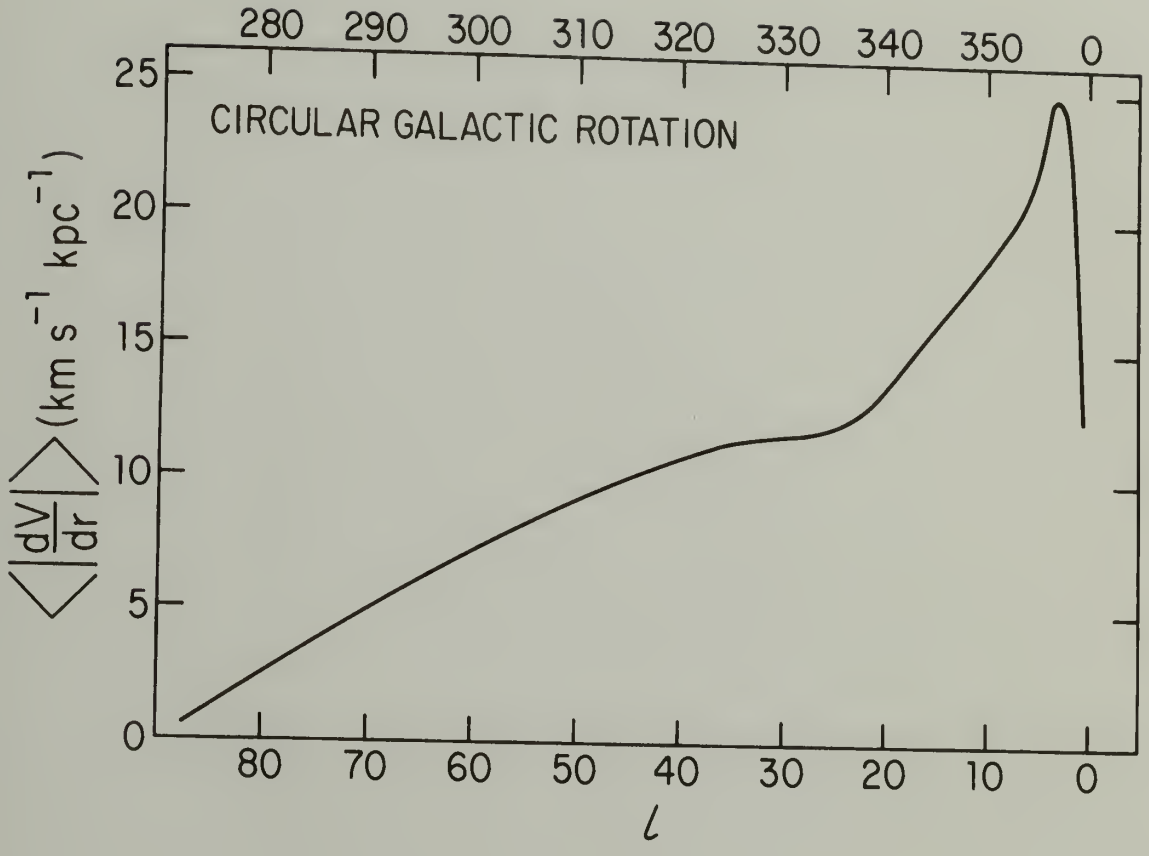

Figure 25: The absolute value of dV(r)/dr for circular rotation, averaged over the line of sight interior to the solar circle, vs. longitude. This quantity is inversely proportional to the average uncertainty in derived distances to objects along a line of sight.

and nebular motions is $\sim$ 10 km s^{-1}, we expect an average uncertainty $\sim$ 1 kpc in the distance to any individual HII region.

Ordered linear density-wave type motions perturb the circular V(r) relationship with results illustrated in Figure 26. These small but systematic motions can have a profound effect on kinematic distance estimates of HII regions. At some longitudes and velocities there might be more than two possible distances (e.g., a nebula at $\ell = 15°$, V(HII) = 20 km/s can be located at 1.6, 2.6, 3.3 or 17.0 kpc). Furthermore, V(r) is no longer necessarily monotonic on either side of the subcentral point, and it might be the case that $|V(abs)| > |V(HII)|$ even for "near" regions. (The difference must still be relatively small: at most longitudes the projected amplitude of the streaming motions given by eq. (96) requires $|V(abs)|-|V(HII)| \leq$ 8 km/s, neglecting random motions.)

Streaming motions alter V(r) so that both it and $|dV(r)/dr|$ are no longer simple functions of R at a given longitude. Thus, there is not necessarily a unique R for each nebula, although the differences between the possible values of R are usually small. Finally, the streaming motions can make $|dV(r)/dr|$ at any point either much smaller or larger than in the case of pure circular rotation. The average $|dV(r)/dr|$ within the solar circle for the linear density-wave velocity field oscillates around the average for circular rotation (Figure 25) but has the same approximate variation with longitude.

If a model velocity field incorporates nonlinear density-wave shocks, there will be discontinuities in V(r) where the line of sight

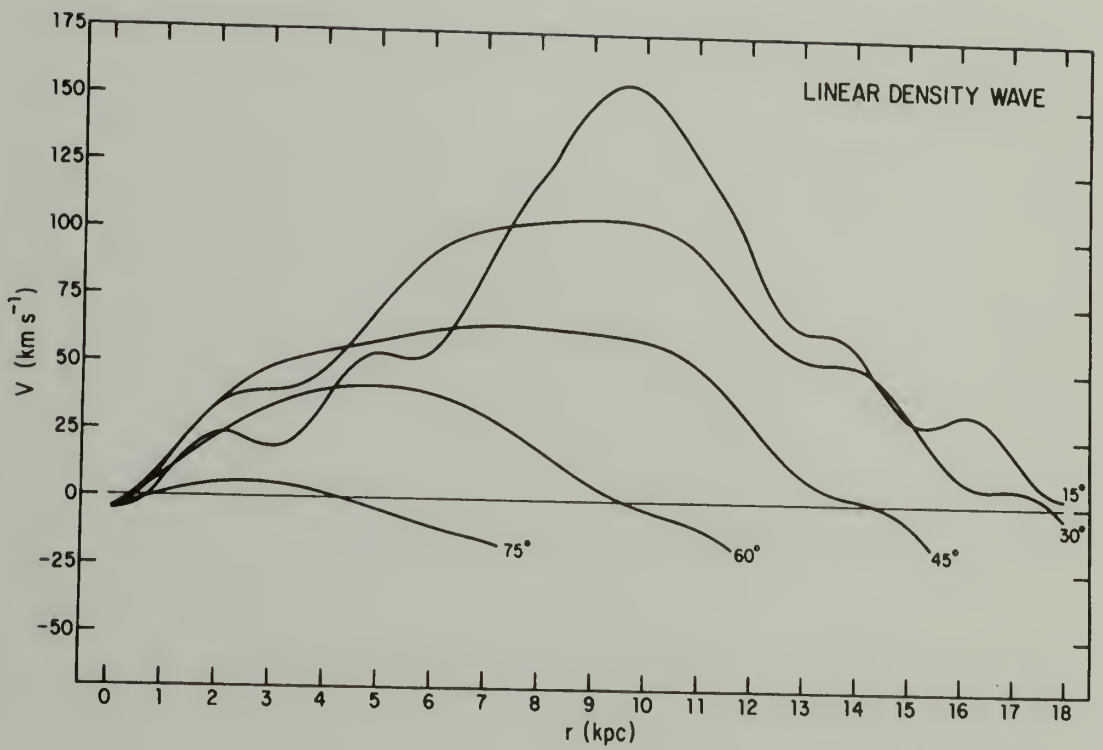

Figure 26: Velocity with respect to the local standard of rest vs. distance from the sun, at a few longitudes in the first quadrant. The velocities were derived for a linear density-wave model.

intersects a shock. The major discontinuities in the Shu et al. (1972) nonlinear density-wave model occur in V_R. Thus jumps in V(r) in the first and fourth longitude quadrant will be largest at low longitudes and will be small near the subcentral point.

d) The Set of Discrete Radio HII Regions

The complete sample.

The most complete and uniform surveys of discrete radio HII regions have been made in the H109α line, so the analysis will be restricted to nebulae observed in this transition. There are 166 continuum peaks within the longitude intervals 5-55° and 305-355° that have been detected in this line. These 166 sources comprise ∿ 65% of the total number of discrete galactic HII regions detected in radio recombination lines. The HII regions, identified by their longitude and latitude, are listed in Table 2 together with their continuum flux density (measured at 5 GHz unless otherwise noted) and the velocity of the H109α recombination line. Objects with optical counterparts are identified by their Messier, NGC, IC, Sharpless or RCW number, or by the designation "opt". Uncertain optical identifications are indicated by a question mark. Use of the W number for sources from the Westerhout (1958) survey is so common that it is included in column 5 for some regions.

The flux densities are somewhat sensitive to the resolution of the specific antenna used for the observation [cf. the Mezger and Henderson (1967) measurements of W51 with those of Goss and Shaver

TABLE 2

Dense Radio HII Regions $5° \leq \ell \leq 55°$, $305° \leq \ell \leq 355°$

ℓ	b	S(Jy)	V(km/s)	Name	Notes	Ref.
5°.89	-0°.42	23.3	+ 10.5	W28		1
5.97	-1.18	85.1	+ 3.8	M8,N6523		1,2
6.08	-0.12	***	+ 11.5	W28,opt(?)	a	3
6.57	-0.08	***	+ 14.7	W28,opt(?)	a	3
6.64	-0.27	12.0	+ 14.2	W28,opt(?)	a	1
6.99	-0.25	13.3	+ 16.4	M20,N6514,S30		1
8.14	+0.23	5.8	+ 19.3	W30		1
8.49	-0.32	7.7	+ 34.1	W30		1,4,5
10.16	-0.35	51.8	+ 13.9	W31		1
10.31	-0.15	13.6	+ 9.7	W31		1
10.63	-0.39	10.2	+ 0.3	W31		1
12.79	-0.19	44.9	+ 36.3	W33		1
13.19	+0.05	4.7	+ 57.0	W33		1
13.38	+0.13	4.0	+ 28.0		b	5,6,7
14.60	+0.06	24.3	+ 37.2	W33		1
15.05	-0.69	534.6	+ 17.3	M17,N6618		1,8
16.98	+0.82	107.8	+ 24.5	M16,N6611,S49		1
18.47	+1.93	102.6	+ 32.9	N6604,S54,W35		1
19.05	-0.27	17.0	+ 67.8	W39		1
19.67	-0.18	12.4	+ 43.4			1
19.98	-0.17	10.4	+ 33.0		c	9
20.74	-0.09	14.5	+ 57.4			1
22.78	-0.28	45.5	+ 82.5	W41		1
23.26	-0.27	4.3	+ 79.7		d	4,10
23.43	-0.20	13.2	+101.5			1
23.55	-0.04	7.7	+ 91.8		d	4,10
23.95	+0.15	2.5	+108.7		d	4,10
24.48	+0.23	12.0	+116.0			6,11
24.64	-0.18	8.2	+109.2			1
24.81	+0.10	11.5	+114.1			1
25.39	-0.17	23.8	+ 60.4	W42		1
25.78	+0.21	9.5	+110.0			1
27.29	-0.16	7.7	+ 97.6			1
28.62	+0.02	14.4	+ 96.2			1
28.79	+3.49	35.1	+ 0.7	R174,S64,W40		1

TABLE 2 (continued)

ℓ	b	S(Jy)	V(km/s)	Name	Notes	Ref.
29°.93	-0°.04	21.1	+ 96.4			1
30.23	-0.15	9.2	+101.0			1
30.39	-0.24	4.6	+103.0		d	4,10
30.51	-0.28	6.1	+103.0		d	4,10
30.70	-0.26	4.0	+ 97.0		d	4,10
30.76	-0.03	97.4	+ 92.1	W43		1,8
31.06	+0.04	8.0	+ 99.2	W43		1
32.81	+0.18	4.4	+ 15.3		d	1,4
33.12	-0.08	7.5	+ 97.0			9
34.26	+0.15	15.0	+ 53.9	W44		1
35.20	-1.74	15.3	+ 46.5	W48,opt		1
35.59	-0.03	15.6	+ 52.0			5,9
37.56	-0.11	7.9	+ 55.8	W47		1
37.88	-0.37	24.4	+ 60.2	W47		1
43.17	-0.00	49.8	+ 9.6	W49A		1,8
45.45	+0.06	12.4	+ 55.0			1,12
46.50	-0.25	6.0	+ 55.0		e	9,13
48.59	+0.04	10.6	+ 17.0			1
48.93	-0.28	34.2	+ 66.4	W51		14
49.02	-0.28	111.3	+ 63.2	W51,opt		1
49.07	-0.37	12.6	+ 72.4	W51		14
49.25	-0.32	12.0	+ 67.2	W51		1
49.38	-0.30	37.2	+ 52.8	W51		14
49.48	-0.38	117.4	+ 58.7	W51,opt		1,8
51.20	+0.07	37.0	+ 55.3			1
54.09	-0.07	5.1	+ 37.4		e	11,13
305.10	+0.15	14.2	- 37.9		b	14
305.20	+0.03	28.0	- 40.0			14
305.25	+0.22	52.0	- 39.1			14
305.36	+0.19	39.4	- 38.0			8,14
305.53	+0.35	3.3	- 38.7		d	4,10
305.55	+0.01	17.8	- 44.7			14
307.62	-0.29	10.5	- 38.7			11
308.65	+0.59	9.1	- 51.8	R79	b	14
308.73	+0.57	5.1	- 46.4	R79	b	14
310.83	-0.44	9.0	+ 18.5			5,9
311.49	+0.39	5.1	- 64.8			14
311.62	+0.29	2.8	- 63.5			14
311.89	+0.09	7.1	- 47.3			14
311.92	+0.21	7.8	- 45.5			14

TABLE 2 (continued)

ℓ	b	S(Jy)	V(km/s)	Name	Notes	Ref.
314°.24	+0°.42	5.2	- 50.5			
316.80	-0.06	28.7	- 36.0	opt(?)	b	14
316.99	+0.28	14.7	- 47.4			8,10
317.31	+0.23	6.7	- 46.8			14
319.16	-0.40	8.2	- 22.8			14
						14
319.39	-0.01	8.2	- 14.1			
320.17	+0.80	7.7	- 36.0	R87		14
320.26	-0.31	7.2	- 67.7			14
320.33	-0.18	5.8	- 7.7			4,14
321.04	-0.50	7.8	- 61.6	R91		14
						14
321.13	-0.53	7.8	- 55.5	R91		
322.16	+0.62	12.2	- 51.8	R92		14
324.20	+0.12	3.3	- 86.6			14
326.46	+0.90	7.2	- 39.0	R94	b	14
326.65	+0.58	35.7	- 43.0	opt		14
						8,10
327.30	-0.55	44.9	- 48.8	R97-98		
327.62	-0.36	5.7	- 69.8			14
327.99	-0.10	4.4	- 44.7		b	14
328.28	-0.58	5.0	- 42.9	opt	b	10,14
328.31	+0.43	10.0	- 96.2		e	11,13
						14
330.68	-0.40	2.8	- 59.6			
330.87	-0.37	9.5	- 56.1		e	4,10
331.04	-0.15	8.3	- 89.2			14
331.12	-0.53	3.2	- 67.7			14
331.27	-0.19	4.2	- 84.4			14
					b	14
331.33	-0.35	7.8	- 64.4			
331.36	-0.02	6.6	- 79.0			14
331.53	-0.08	31.1	- 89.0			14
332.15	-0.45	13.2	- 55.0	opt		8,10
332.54	-0.14	2.2	- 55.9	opt		14
					b	14
332.66	-0.62	20.1	- 47.0	R106		
332.81	-0.57	18.7	- 57.2	R106		14
332.98	+0.77	5.0	- 52.1			14
333.03	-0.45	39.7	- 53.8	opt	e	11,15
333.04	+0.03	3.5	- 46.3			14
					d	4,10
333.12	-0.45	42.1	- 52.0	opt		
333.17	-0.10	12.3	- 90.8			8,10
333.29	-0.38	34.2	- 50.0	opt		14
333.60	-0.09	15.0	- 53.7			8,10
333.61	-0.22	84.4	- 48.3		b	14
						14

TABLE 2 (continued)

ℓ	b	S(Jy)	V(km/s)	Name	Notes	Ref.
333.70	-0.48	3.2	- 49.9			
335.77	-0.16	7.6	- 52.1		b	14
336.37	-0.14	7.6	- 68.5	N6164	b	14
336.43	-0.25	10.0	- 93.1	N6165(?)	b	14
336.47	+0.02	3.3	- 63.4			14
					b	10,14
336.50	-1.49	8.6	- 24.9	N6193,R108		
336.53	-0.17	14.6	- 88.6			10,14
336.81	+0.04	57.5	- 75.3		b	14
336.93	-0.15	14.4	- 73.1			4,10,14
337.12	-0.17	15.1	- 72.7			14
						14
337.28	-0.13	7.4	- 53.5			
337.63	-0.05	6.1	- 54.8		b	14
337.80	-0.09	7.2	- 52.0			14
337.92	-0.47	17.3	- 40.4			5,10
337.98	-0.13	11.1	- 52.5			14
					b	14
338.06	+0.01	7.3	- 41.7			
338.11	-0.18	6.3	- 47.7			14
338.40	-0.20	3.9	- 4.3		b	14
338.43	+0.05	46.6	- 36.9		b	14
338.92	+0.60	9.9	- 63.0			14
						14
338.92	-0.07	3.4	- 40.0			
340.06	-0.22	5.0	- 51.8			14
340.29	-0.21	4.9	- 43.3		e	10,11,16
340.79	-1.02	9.4	- 24.8	R110-111		14
342.07	+0.42	3.1	- 65.0			10,14
						9,17
342.27	+0.31	6.0	-122.0			
343.48	-0.04	12.6	- 30.3		e	9,16
345.01	+1.53	14.8	- 17.4	opt		14
345.21	+1.02	10.4	- 9.4	opt		14
345.29	+1.45	12.6	- 15.5	opt		14
						14
345.39	+1.40	13.1	- 14.6	opt		
345.42	-0.96	34.0	- 21.1	R117,H2-3		14
345.49	+0.32	4.0	- 21.6			11
347.61	+0.20	23.4	- 96.2		d,e	4,18
348.22	+0.46	7.6	- 14.0	R120	f	1,14
						1,5
348.23	-0.98	8.4	- 18.9	R121,H2-6		
348.72	-1.04	33.4	- 12.0	R122	g	19,20
349.09	+0.10	12.0	- 74.0			8,10
349.82	-0.56	9.2	- 25.8	opt	e	11,18
350.11	+0.08	6.5	- 69.8			1
						1

TABLE 2 (continued)

ℓ	b	S(Jy)	V(km/s)	Name	Notes	Ref.
351°.04	+0°.66	47.9	- 5.3	N6334,R127,S8	d	4,10
351.16	+0.69	22.5	- 3.6	N6334,R127,S8	d	4,21
351.19	+0.48	20.9	- 7.8	N6334,R127,S8	d	4,10
351.35	+0.63	171.4	- 3.8	N6334,R127,S8		1,2
351.59	+0.18	15.7	- 42.5			
351.63	-1.25	36.8	- 12.2			1
353.06	+0.34	31.3	- 3.8	N6357,S11,W22		1
353.12	+0.64	111.3	- 4.0	N6357,S11,W22		8,10
353.19	+0.89	87.1	- 4.0	N6357,S11,W22		8,10
353.41	-0.37	8.8	- 12.8			1
353.52	-0.04	7.0	- 51.0			1,6

Notes

a) Radio flux may have a substantial non-thermal component. Source was removed from the kinematic sample (see text).
b) Velocity may be very uncertain. Source was removed from the kinematic sample (see text).
c) Line measurements were not made at continuum peak. Source was removed from the kinematic sample (see text).
d) No published measurements of recombination line intensity or width.
e) Flux density from 2.7 GHz measurements.
f) Flux density not given in Goss and Shaver (1970); quoted value is from Wilson et al. (1970).
g) Flux density from 10 GHz measurements.

References

1. Reifenstein et al. (1970).
2. Churchwell (1970).
3. Milne and Wilson (1971).
4. Whiteoak and Gardner (1974).
5. Dickel and Milne (1972).
6. Altenhoff et al. (1970).
7. Goss and Day (1970).
8. Churchwell et al. (1974).
9. Caswell and Clark (1975).
10. Goss and Shaver (1970).
11. Caswell (1972).
12. Wilson and Altenhoff (1972).
13. Day et al. (1969).
14. Wilson et al. (1970).
15. Beard (1966).
16. Thomas and Day (1969).
17. Caswell, Haynes and Clark (1975).
18. Beard, Thomas and Day (1969).
19. Rubin and Turner (1971).
20. Rubin (1970).
21. Shaver and Goss (1970).

(1970)]. All the observations used were made with either the CSIRO 210-foot diameter telescope (4' HPBW) or the NRAO 140-foot telescope (6' HPBW). In general, flux densities from Reifenstein et al. (1970) are listed for nebulae observed with the 140-foot telescope and flux densities from Goss and Shaver (1970) for those observed with the 210-foot telescope. The continuum measurements given in Wilson et al. (1970) were taken, for the most part, from Goss and Shaver, and unless there is a conflict, reference is made only to Wilson et al. (1970). Some nebulae have not been measured in the 5 GHz continuum, so flux densities were taken from 2.7 or 10 GHz measurements.

The number of HII regions represented by the entries in Table 2 is not well known. Maps with the CSIRO telescope tend to show more continuum peaks than maps with the NRAO telescope, and occasionally different parts of a large complex have different recombination line velocities, suggesting that the complex results from the projection of many sources spread out along the line of sight. In addition, a relatively nearby complex region of ionized gas may be resolved into a number of continuum peaks which, if they have somewhat different velocities, will be counted as several HII regions. More distant sources will be counted either once or not at all, depending on the confusion and sensitivity limits of the survey. Thus the number of objects and hence any derived property which depends on the number of objects is in some way a function of the antenna and the sensitivity of a survey. In contrast, the total flux density is always conserved no matter how a region is divided up, but it decreases with the

inverse square of the distance to the nebula. The absolute flux density, $S_0 \equiv Sr^2$ Jy - kpc^2, has a number of advantages as a measure of the distribution of ionized gas, but it is extremely sensitive to the distance of an object and must be used with caution.

Despite the fact that most of the HII regions in the southern part of the sample have been observed only by the 210-foot telescope and most regions in the North only by the 140-foot telescope, there is sufficient overlap to prevent gross instrumental selection effects. Fully one-third of the HII regions in the North have been detected by the 210-foot telescope in surveys subsequent to that of Reifenstein et al. (1970).

Several other initial comments may be made about the sample of nebulae. The restriction to H109α observations implies a selection based on thermodynamic properties. Observations of this transition are most sensitive to relatively dense gas and will discriminate against low and moderate density regions, i.e., those with $N_e \lesssim 10^2$ cm^{-3}. In addition, there is a serious effect arising from the manner in which the surveys are conducted: positions to be observed are chosen on the basis of the continuum intensity, but an HII region is detected only if that direction shows a certain line intensity. Because the line and continuum strengths have very different dependencies on the thermodynamic properties of a nebula, this procedure introduces a selection effect of undetermined extent and importance. It is clear that out of a sample of HII regions with the same continuum intensity, recombination lines will be detected more

often from those with lower electron temperatures than from those with higher electron temperatures, but because non-LTE processes are so important in determining the line intensity, it is not possible to estimate thermodynamic selection effects until multiple frequency surveys are available.

The kinematic sample.

Not all of the numbers in Table 2 are accurate enough to be used in a kinematic analysis. The H109α line from most sources has been observed only once, so the data must be examined for internal evidence of possible systematic errors in V. In this regard, Figure 27 shows a disquieting relationship between the H109α line width Δv and the peak line temperature T_L in the data from the Wilson et al. (1970) survey: many of the weak lines are extremely broad. No such lines have been observed by other groups using the same telescope (their data are shown as different symbols in this figure) and, with two possible exceptions, no similar lines have been detected with the NRAO telescope. Broad lines will tend to have a smaller peak antenna temperature than narrow lines, but it is surprising that this effect would be found in only one survey, and we would expect some broad lines from stronger sources. An effect of this type, however, could arise from instrumental problems in the spectra of sources with weak lines. In this respect it is interesting to note that, in the standard procedure of fitting polynomials to the observed spectra to remove instrumental baseline, Wilson et al. used polynomials whose degree depended on the continuum temperature of the nebula (Wilson, 1970).

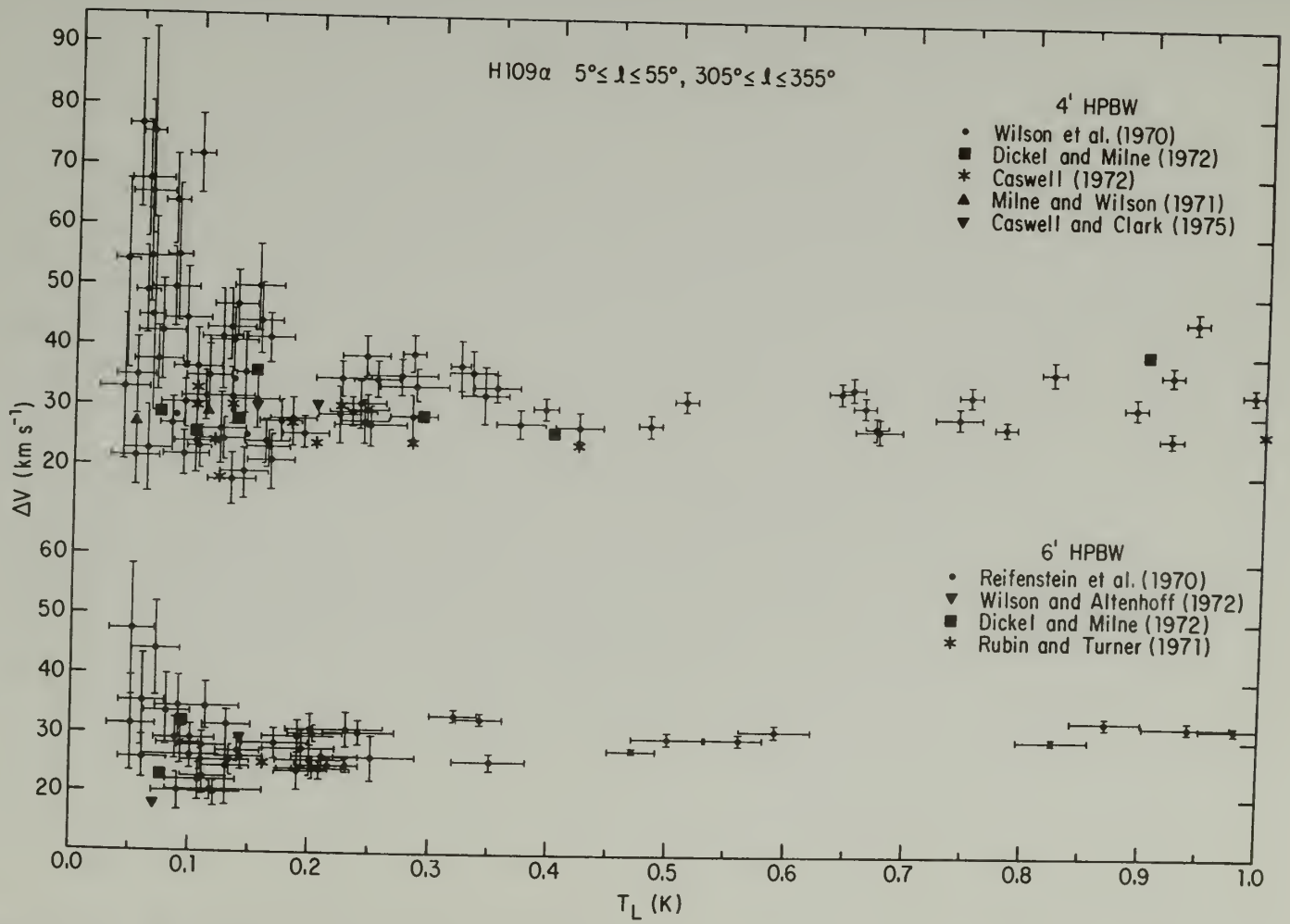

Figure 27: The full-width at half-maximum (Δv) vs. the peak line temperature (T_L) for the weaker sources in the H109α recombination line surveys. The upper set of measurements was made with the CSIRO telescope, and the lower set with the NRAO telescope. Measurements from different authors are marked with different symbols.

For our purposes it does not matter if the trend in Figure 27 is real or instrumental; broad lines will have a less well determined velocity than narrow lines, and if the broadening is spurious then the line velocity will be very uncertain. Since a kinematic analysis requires that source velocities be fairly well known, all HII regions with $T_L \leq 0.10$ K observed only by Wilson et al. (1970) were eliminated from the kinematic sample unless: 1) the width of the line was less than 40 km/s and 2) there was a molecular absorption line within a few km/s of the quoted radio recombination line velocity. In addition, all nebulae from that survey with peak line temperatures between 0.11 K and 0.15 K and line widths greater than 40 km/s were eliminated unless a molecular absorption line had been detected within a few km/s of the quoted recombination line velocity. The source 13.38+0.13 from Dickel and Milne (1972) has a peak line temperature so small and a line width so large that its velocity cannot be known very accurately, and it was not used. The nebulae 311.49+0.39 and 311.62+0.29 were retained in the kinematic sample because their positions are very close and their recombination lines show similar velocities.

A total of 20 nebulae were removed from the kinematic sample for having potentially erroneous velocities; all but one of these are located in the southern longitude interval. These objects are still used for some statistical purposes, but are considered as HII regions with unknown velocities.

One nebula was removed from the kinematic sample because of uncertainty in its position: the direction of the continuum peak 19.98-0.17 shows no H109α line, although a line is observed some 5' away (Caswell and Clark, 1975). Thus, while there is an HII region in the general direction of 19.98-0.17, its association with the continuum source is uncertain and it was not used in the kinematic analysis.

The only objects removed from the kinematic sample because of uncertainties in the flux density were parts of W28. This radio source appears to be composed of one or more HII regions and a supernova remnant (Milne and Wilson, 1971). The superposition of thermal and non-thermal radiation makes it difficult to estimate a 5 GHz thermal continuum flux density for individual components, and three sources in W28 were therefore not in the kinematic sample.

Column 6 of Table 2 identifies all nebulae which have been removed from the kinematic sample, and also identifies those sources from Whiteoak and Gardner (1974) for which only the H109α velocity, and not T_L or Δv, has been published. Almost all of the 24 sources removed from the kinematic sample have very weak line and continuum emission, and thus the kinematic sample can be considered as resulting from a less sensitive but more accurate survey of radio nebulae.

e) The Observed Distribution

Although the information contained in Table 2 is weighted by observational and distance selection effects, it is worthwhile to work with the observed quantities as long as possible before making assumptions about the nature or spatial distribution of the nebulae, or about the kinematics of the Galaxy. Figure 28 shows both the number of HII regions and the thermal continuum flux associated with them plotted against longitude in 3° intervals. There is a general increase in the numbers and flux densities toward low longitudes, although both distributions show the effects of clustering of sources or the presence of single bright objects. The dashed lines between longitudes 304° and 301° show the number of nebulae and their flux density in the 3° longitude interval just outside of the sample region: no radio HII regions have been detected in the corresponding interval between 56° and 59° in the North. Of the 166 nebulae in the sample, 37% are in the North and 63% in the South; but, as can be seen from the upper panel of Figure 28, the total thermal continuum flux density from the two longitude intervals is comparable. The nature of this difference can be understood from the number versus flux density distribution shown in Figure 29. There are similar numbers of nebulae with $S > 10$ Jy in both North and South, but there are many more low flux density sources in the South. While this might be attributed to the better angular resolution of southern observations, other differences between the North and South suggest that this cannot be the only explanation, and it is likely that there are actually

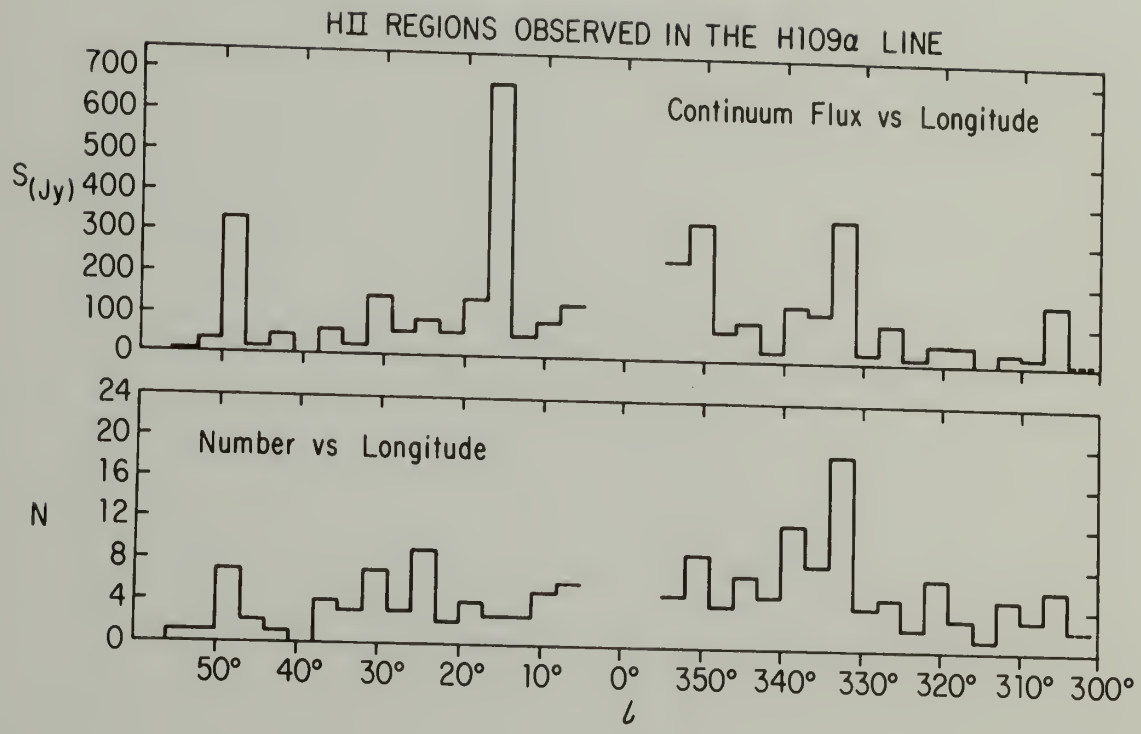

Figure 28: The numbers and continuum flux densities of dense radio HII regions vs. longitude. Data are integrated over 3^{o} bins. The dashed lines between longitudes 305^{o} and 302^{o} show the number and flux density in the 3^{o} interval just outside of the sample cutoff in the South. No nebulae have been detected in H109α from the corresponding interval in the North.

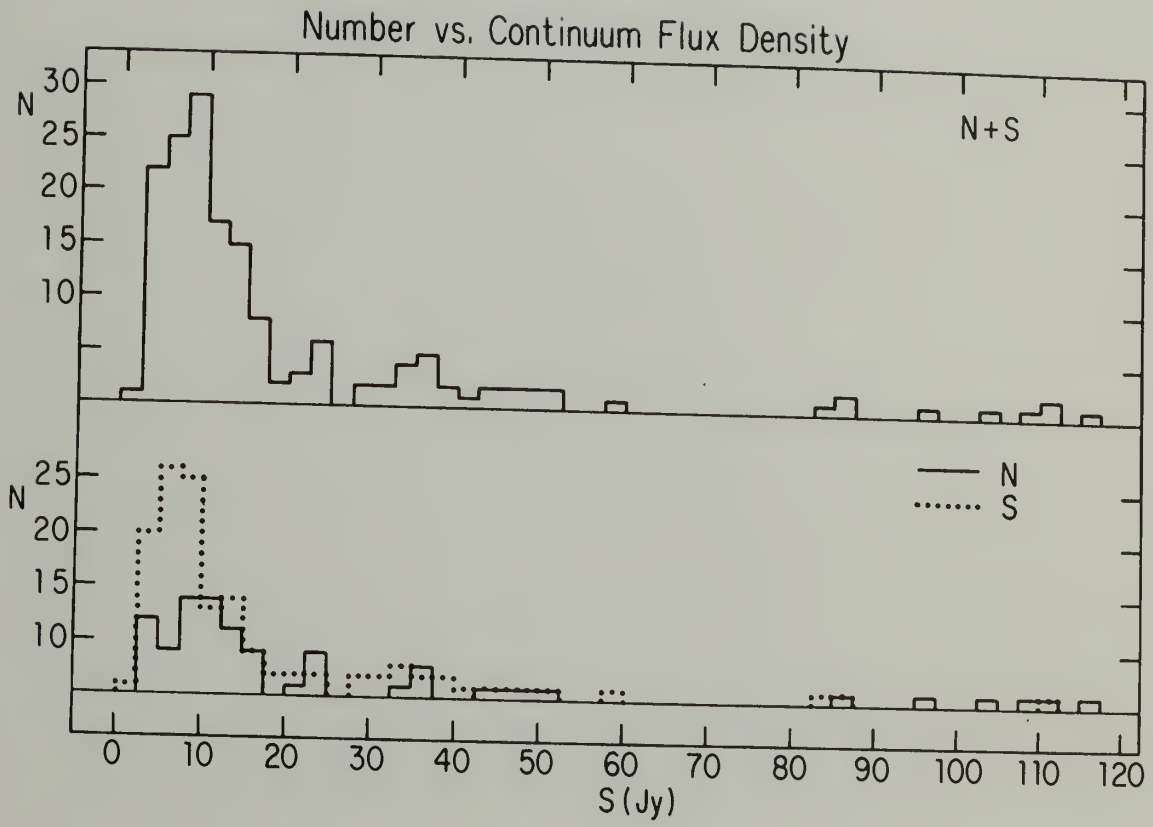

Figure 29: The distribution of continuum flux densities of nebulae in the full sample. Most measurements were made at 5 GHz. Lower panel shows the distributions for the two individual longitude intervals.

more small nebulae in the South than in the North. The cutoff in the number of sources at low flux densities (virtually none with $S < 2.5$ Jy) is a selection effect, and reflects the lower flux density limit of the surveys.

The total number and flux density of nebulae increases by a factor of about two between 50° and 10° from $\ell = 0°$. The longitudinal distribution of species like molecular clouds (Burton and Gordon, 1978), OH/IR stars (Johansson et al. 1977; Bowers, 1978), and pulsars (Taylor and Manchester, 1977) increases more steeply towards low longitudes, suggesting that the radial distribution of dense nebulae in the inner Galaxy may be somewhat broader than that of other early-type objects.

Figure 30 shows the distribution of the sources in latitude. The nebulae are all located quite close to the galactic plane with southern sources having a slightly broader distribution than northern sources. In the North, 90% of the nebulae lie within $b \leq 0.^{\circ}50$, while only 70% of the nebulae in the South are located in the same latitude interval. The mean source position is very close to $b = 0°$, being $-0.^{\circ}07$ in the North and $0.^{\circ}00$ in the South, but the median of the distribution, a measure less easily skewed by a few high latitude objects, is $-0.^{\circ}16$ and $-0.^{\circ}06$ in the North and South, respectively.

The thermal flux is less concentrated, and only 56% of the total flux is located within $0.^{\circ}5$ of the plane in either North or South. The overall mean and median latitude of the thermal flux is similar to that of the number of nebulae: both lie at slightly negative latitudes.

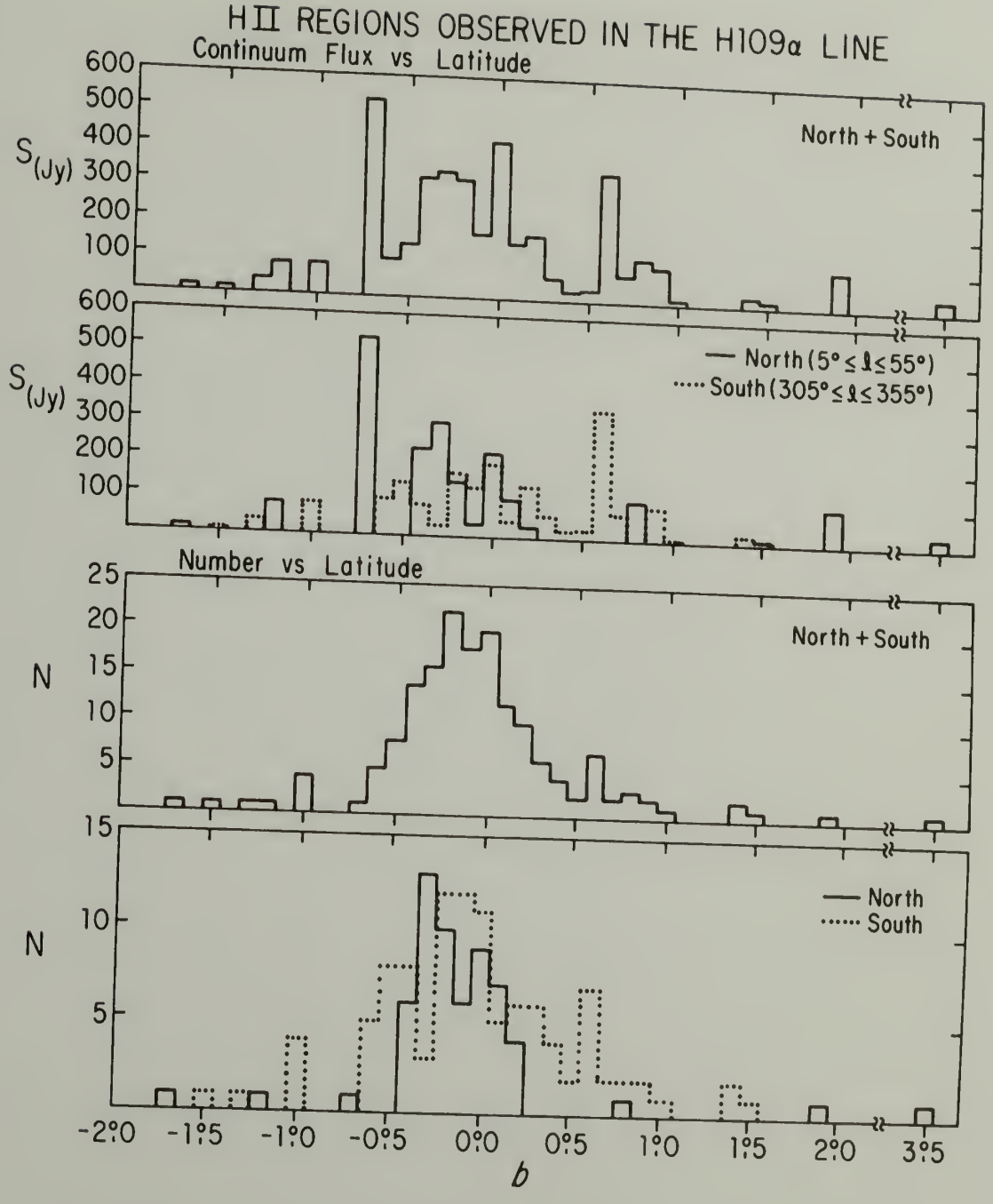

Figure 30: The numbers and continuum flux densities of dense radio HII regions vs. latitude, displayed for each longitude interval, and for the entire sample.

These trends indicate that one possible selection effect, the preferential detection of faint nebulae when they are at high latitudes where there is less confusion with the galactic background and other thermal and nonthermal sources, is unimportant. This selection effect should tend to broaden the latitude extent of the number of nebulae while having a negligible effect on the latitude extent of the flux. Since the distribution has the reverse property, it is probable that higher latitude weak sources are not being significantly overcounted with respect to nebulae at lower latitudes.

Some of the nebulae in Table 2 have been detected in optical Hα surveys. Without knowledge of the Hα velocity, it is often difficult to determine if optical and radio emission come from the same object, especially since optical nebulae are often somewhat displaced from their radio counterparts (e.g., M17). In Table 2, sources are listed as optical objects if there is reasonably good coincidence between radio and optical positions, and if the Hα velocity (where available) is in reasonable agreement with the H109α velocity. The criterion for reasonable velocity agreement depended somewhat on the complexity of the field in which the source is located, but in all cases it was required that $|V(H109\alpha)-V(H\alpha)| \leq 10$ km/s. The Hα velocities were taken from Georgelin and Georgelin (1970, 1976) and Georgelin et al. (1973). W48 and two components of W51 are listed as having optical counterparts based on the report of Georgelin and Georgelin (1976) and Crampton et al. (1978), but these detections required effort which has not been applied to other radio HII regions,

and these sources are a potential source of bias in comparisons of the two longitude intervals. Despite this, there is a striking difference between the North and the South in the percentage of radio HII regions with optical counterparts: only 15-20% of the radio nebulae in the North are seen optically (including W48 and W51), while 34-36% of the southern nebulae have optical counterparts. Given the difference in the number of radio HII regions between the two longitude intervals this means that $\sim$ 75% of the optical/radio nebulae are located in the South. The visual extinction toward radio HII regions, on the average, must be significantly less in the South than in the North. The average difference between radio recombination line and Hα velocities, $\langle\Delta V(H\alpha)\rangle \equiv \langle V(H109\alpha)-V(H\alpha)\rangle$, is identical in the two longitude intervals, and is 0.3 km/s with a dispersion of 2.8 km/s. This dispersion is smaller than the 4 km/s found for 30 radio/optical objects by Georgelin (1970), perhaps because of the stricter sample selection and improved velocities used here.

Many HII regions are associated with cool molecular clouds which may be detected in absorption lines of OH or H_2CO against the thermal continuum. The quantities $\Delta V(OH)$ and $\Delta V(H_2CO)$, defined analogously to $\Delta V(H\alpha)$, give a measure of the velocity of these absorption lines compared to the velocity of the ionized gas, and hence an estimate of the velocity difference between foreground molecular and background ionized regions. An association is defined as a velocity difference less than or equal to 10 km/s. When absorption spectra contain multiple lines, the feature closest to the velocity of the recombination

line is used for this calculation. Quite often the absorption lines have complex non-Gaussian shapes with no clearly defined peak, and there is some subjectivity in the choice of the absorption velocity. This is particularly true for HI absorption spectra, which is why the quantity $\Delta V(HI)$ was not calculated.

From the surveys of Goss et al. (1970), Caswell and Robinson (1974) and Turner (1979), main line OH absorption is found to be associated with $\sim$ 50% of the HII regions in the sample. Of the remaining 50%, some regions were not observed, others are quite weak and would have absorption features below the sensitivity limits of some of the surveys, and some nebulae have strong main line emission which could mask weak absorption. A reasonable estimate is that $\sim$ 15% of the nebulae do not have associated OH features, or have them at a weaker level than the average. The velocity difference between H109α and OH, $\langle\Delta H(OH)\rangle$, is -0.1 km/s with a dispersion of 2.8 km/s, similar to the dispersion between the CO and H109α velocities. There can be no meaningful comparison of the percentage of sources showing OH absorption in the North vs. the South, owing to strong differences in sensitivity between the various OH surveys.

The formaldehyde measurements [taken from Wilson (1972) and Whiteoak and Gardner (1974)] provide a more uniform coverage of the North and South and have the advantage of being made with an antenna beam width similar to that used in the H109α measurements, but in turn suffer from the presence of lines seen in absorption against the 2.7 K background radiation. Here $\sim$ 65% of the nebulae have associated H_2CO

absorption lines with $<\Delta V(H_2CO)> \simeq -0.1$ km/s with a dispersion of 3.6 km/s, while $\sim$ 10% of the observed nebulae do not appear to have associated H_2CO absorption. There is no significant difference in this latter figure between the North and the South. The somewhat larger velocity dispersion of H_2CO could easily arise from the presence of a few clouds which coincidentally lie within 10 km/s of the recombination line velocity, but which are being seen against the blackbody background.

The absorption line measurements are summarized in Figure 31, where the number of objects is plotted against $|\Delta V|$. (Nebulae associated with both OH and H_2CO appear twice in this figure.) The majority of the nebulae in the sample have either OH or H_2CO absorption lines within a few km/s of their recombination line velocity. It is interesting to note that there is a strong correlation (at a confidence level > 99.9%) between $\Delta V(OH)$ and $\Delta V(H_2CO)$, suggesting that the molecular lines associated with a given source arise within the same cloud. This conclusion only applies to molecular clouds with a velocity near that of the nebula; the correlation between the velocities of <u>all</u> OH and H_2CO lines is less good (Turner, 1972).

The disposition of the kinematic sample in velocity and longitude is shown in Figure 32, along with the model terminal velocities for circular and linear density wave velocity fields, the circular velocity at R = 15 kpc, and the circular velocity at R = 3 kpc (dashed line). Note that the terminal velocities from the linear density-wave model do not differ from those of circular rotation until the onset

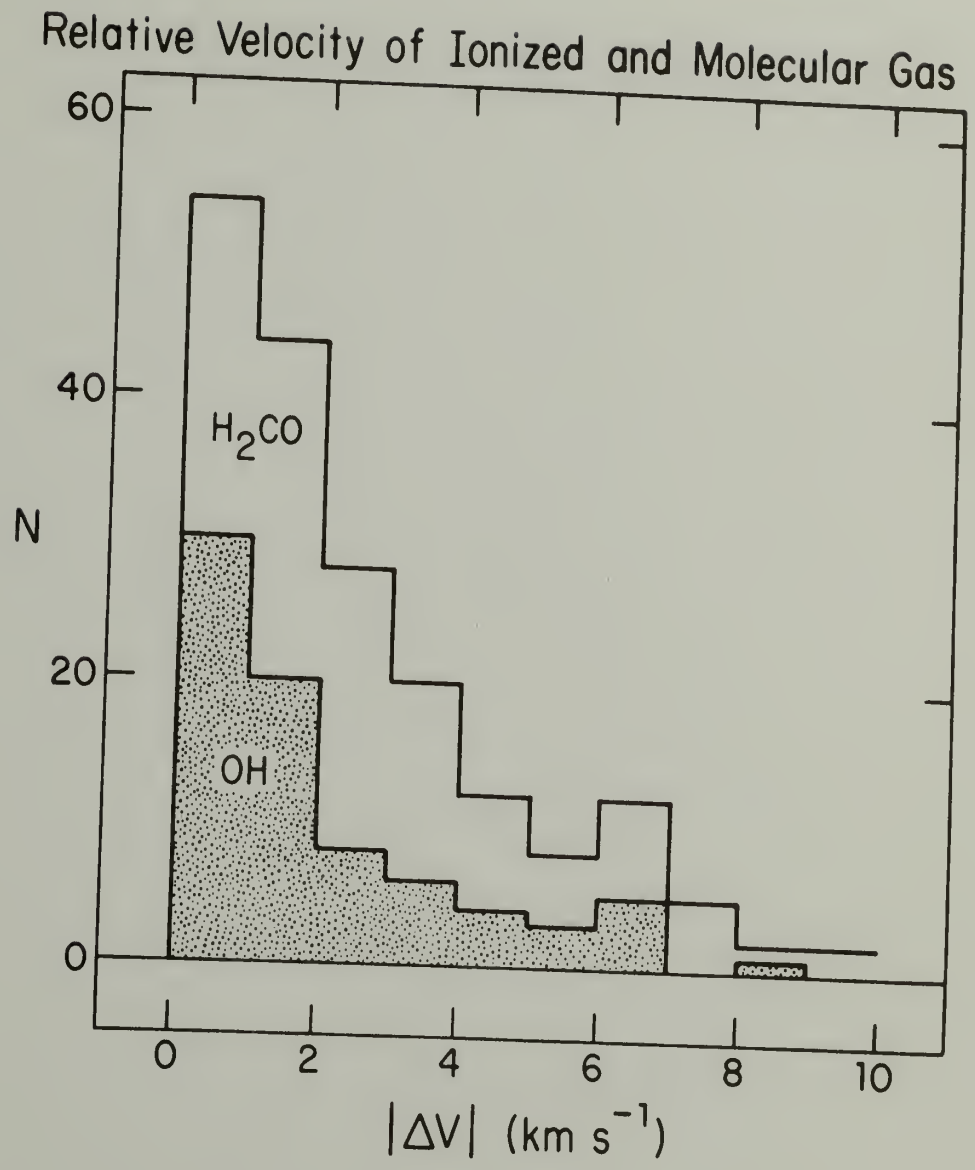

Figure 31: The number of nebulae associated with molecular absorption lines vs. the absolute value of the velocity difference between ionized and molecular species. Nebulae having associated OH and H_2CO lines appear twice in this figure.

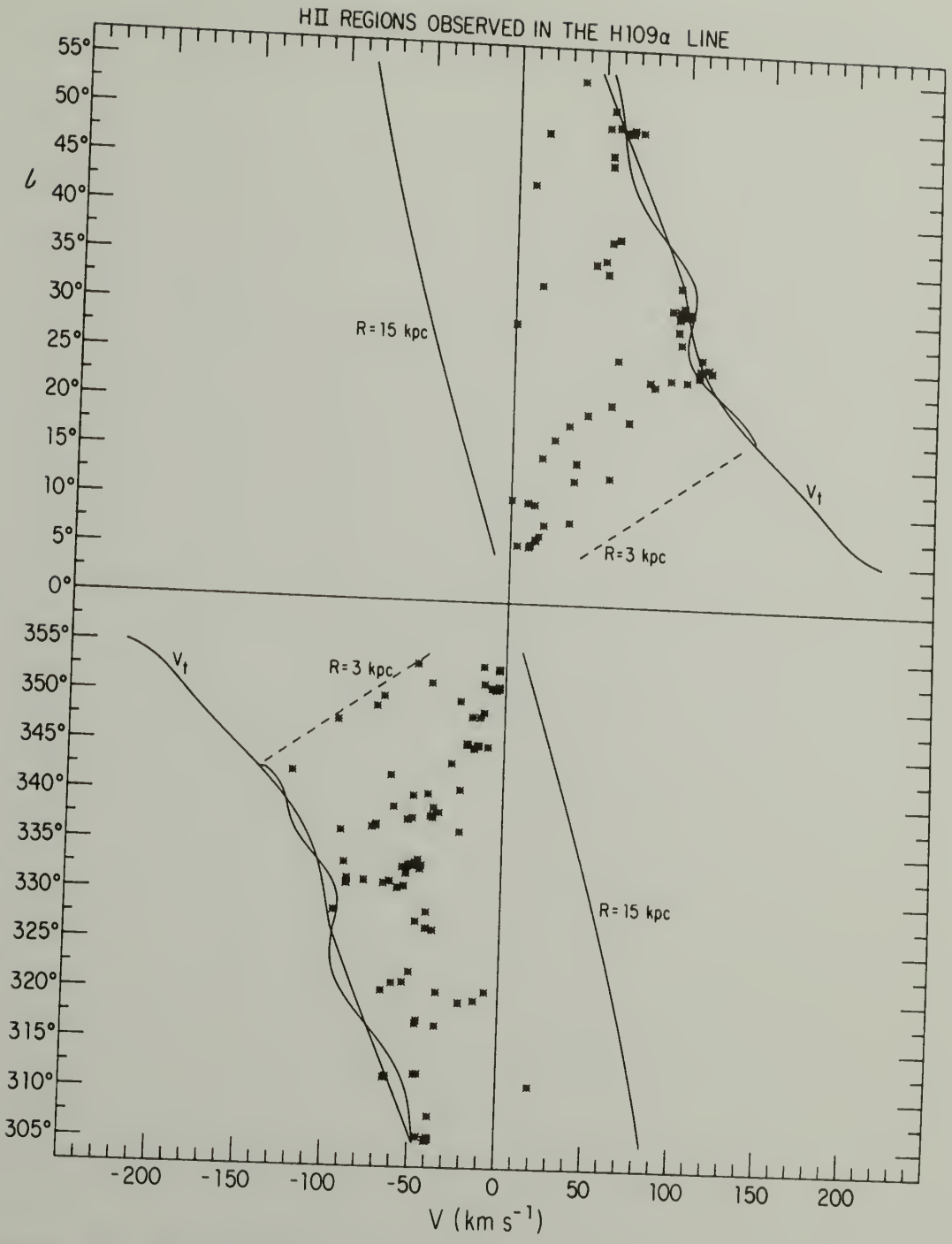

Figure 32: The kinematic sample of dense HII regions in velocity-longitude coordinates. Solid lines mark the model terminal velocities in the case of circular and linear density-wave motions, and show the expected location of material at R=15 kpc (circular motion only). The dashed lines show the expected locations of material at R=3 kpc assuming circular rotation.

of streaming at longitudes where the subcentral point corresponds to $R > 3$ kpc. The area between V_t and the line at $R = 15$ kpc (roughly the outer boundary of the Galaxy as determined from HI observations) defines the region of "permitted" velocities over this longitude range. It is clear that HII regions are not distributed uniformly in velocity-longitude space. They are confined largely to velocities between 0 and V_t, and are not found at the high velocities and low longitudes characteristic of material at $R < 3$ kpc. A detailed discussion of the sample in V-ℓ space will be the topic of §IVg, but here it is worthwhile to note that there is a certain symmetry between the North and the South. Both longitude intervals show HII regions scattered along a line extending from $V \sim 0$ km/s to the terminal velocity between 5° and 25-30° from the galactic center. In both intervals the nebulae are displaced some 20 to 60 km/s from the terminal velocity in the area roughly spanning positions 35° to 50° from the center, and in both North and South a few nebulae are found at the terminal velocity approximately 50° from $\ell = 0°$. Furthermore, there is an absence in both North and South of nebulae near zero velocity between 15° and 35° from the center. These similarities imply that the nebulae are distributed in a fairly symmetrical fashion about the line of sight to the galactic center.

The observed properties of the sample of HII regions are summarized in Table 3. The nebulae and the continuum flux densities are highly confined to the galactic plane. The major differences between North and South are found in the total number of objects in each

TABLE 3

Observed Properties of Radio HII Regions

Property	North ($55° \geq \ell \geq 5°$)	South ($355° \geq \ell \geq 305°$)	All
Number of Nebula	61	105	166
Total Thermal Flux (Jy)	1.98×10^3	1.87×10^3	3.85×10^3
Optical Counterparts:			
Number	9-12	36-38	45-50
Percentage	15-20%	34-36%	27-30%
$\langle V(H109\alpha)-V(H\alpha)\rangle \pm 1\sigma$ km/s	0.2 ± 3.9	0.4 ± 2.6	0.3 ± 2.8
Latitude:			
$\langle b \rangle \pm 1\sigma$	$-0°.07 \pm 0°.63$	$-0°.00 \pm 0°.53$	$-0°.02 \pm 0°.57$
Median b	$-0°.16$	$-0°.06$	$-0°.10$
$\langle b \rangle$ of flux $\pm 1\sigma$	$-0°.14 \pm 0°.82$	$+0°.09 \pm 0°.57$	$-0°.03 \pm 0°.72$
Median b of flux	$-0°.28$	$+0°.04$	$-0°.16$
Percentage with $\lvert b \rvert \leq 0°.5$:			
Number	90%	70%	78%
Flux	56%	56%	56%
Molecular Lines:			
$\langle V(H109\alpha)-V(CO)\rangle \pm 1\sigma$ km/s	-1.0 ± 3.1	$+1.1 \pm 2.1$	-0.0 ± 2.8
$\langle V(H109\alpha)-V(OH)\rangle \pm 1\sigma$ km/s	0.1 ± 2.4	-0.2 ± 3.1	-0.1 ± 2.8
$\langle V(H109\alpha)-V(H_2CO)\rangle \pm 1\sigma$ km/s	0.1 ± 4.2	-0.2 ± 3.3	-0.1 ± 3.6
$\langle V(H109\alpha)$ $-V(OH+H_2CO)\rangle \pm 1\sigma$ km/s			-0.1 ± 3.3

interval, in the relationship between the number and flux density of nebulae in each interval (Fig. 29), in the percentage of radio nebulae with optical counterparts, and at a less significant level, in the concentration of the objects towards the galactic plane. The total thermal continuum flux density from the two longitude intervals is essentially equal, and the nebulae are fairly symmetric about the line of sight to galactic center in their longitude and velocity. Most nebulae have either OH or H_2CO absorption within a few km/s of the recombination line velocity, and where optical velocity measurements are available, they tend to confirm the radio velocities.

f) Kinematic Distances and Derived Properties

At the longitude of each HII region the function V(r) was calculated for both circular and linear density-wave velocity fields, and the distances and radii where V(H109α) = V(r) were identified. Most nebulae have two (or, with linear density-wave velocity fields, more than two) possible distances; exceptions include the source 310.83-0.44, the only HII region in the sample that appears to lie outside of the solar circle, and a few nebulae with velocities larger than the terminal velocity. When the spectroscopic distance to the exciting star of a nebula was known, the kinematic distance closest to the spectroscopic distance was chosen. Optical identification of an HII region was not considered sufficient to exclude the far distance unless it was more than 10 kpc from the sun. Regions with forbidden velocities were assumed to be located at the distance and galactocentric radius of the subcentral point.

In most cases, single dish absorption spectra of OH and H_2CO and interferometric spectra of HI were used to discriminate between the near and far distances. There are absorption measurements available for all but one of the nebulae in the sample, and most have been observed in at least two species. Of particular value is the Turner (1979) OH survey which covers virtually each galactic continuum source north of declination -47°, and the Whiteoak and Gardner (1974) survey of H_2CO which includes most of the nebulae in the sample.

When the velocity of the HII region is much less than V_t and absorption lines extend to, or nearly to V_t, the nebula is placed at the

far distance. If the absorption lines do not have a velocity much greater than V(H109α) then the nebula is placed at the near distance. When V(H109α) is close to V_t, the dispersion of molecular velocities could give some absorption at V_t even if the nebula is at the near distance, and conversely, could displace absorption lines away from V_t for nebulae at the far distance. Also, distance estimates for nebulae near V_t have intrinsically large errors owing to the low value of $|dV(r)/dr|$ near the subcentral point. Therefore, to minimize the average percentage error in r, whenever $|V(H109\alpha)-V_t| < 7.5$ km/s the nebula was assumed to be at the distance of the subcentral point. The velocity difference of 7.5 km/s was chosen because it is roughly twice the dispersion of molecular absorption velocities (§IVe), and is 1.5 times the adopted dispersion of HII region velocities. These difficulties do not affect estimates of R, because even in linear density-wave models there is a difference of only $\sim$ 0.1 kpc between near and far galactocentric radii near the subcentral point (the difference is zero for circular rotation), and an averaged value is sufficiently accurate. Therefore, the distance given to a nebula within 7.5 km/s of V_t is the distance to the subcentral point, but the radius of the nebula remains the kinematic radius. Note that this makes the distance and the radius incompatible with the longitude of these HII regions.

Of the three absorption measurements, the interferometric HI observations are potentially the most sensitive, but are currently limited to the brighter, more compact sources and occasionally suffer when partially resolved emission appears as spurious absorption in the

spectra (see, e.g., the discussion in Caswell et al. 1975, and Greisen and Lockman, 1979). Absorption in the 18-cm lines of OH provides an unambiguous measurement of the velocity of cool, dense gas towards a nebula, however, the fairly large beam width of most telescopes at the OH frequency can occasionally cause confusion when two continuum sources, possibly at very different distances, lie within the same beam. Formaldehyde has the advantages of abundance and the frequency of its transition (it can be observed with the same antenna beam width used for the recombination line observations), but this molecule may have an excitation temperature < 2.7 K and appear in absorption against the isotropic background radiation; it is often not easy to distinguish between absorption against the 2.7 background and the absorption against an HII region. Comparison with OH and HI spectra (where available) can eliminate some obvious background H_2CO features, and, because the velocities of OH and H_2CO near HII regions are strongly correlated, the absence of OH absorption at an H_2CO feature velocity suggests, but does not require, that the H_2CO feature is absorbing background radiation. In some cases, an H_2CO feature has roughly the same antenna temperature in the direction of several adjacent sources with quite different continuum temperatures. This suggests that the H_2CO lies behind all the objects (for a discussion of this problem see Whiteoak and Gardner, 1974).

It is clear that the absorption spectra cannot be used uncritically. In general, the highest weight was given to strong HI absorption or any OH absorption. Despite the uncertainties, it was usually easy to decide between the near and far distance.

There are two nebulae with unresolved distance ambiguities. The absorption measurements, and the detection of optical emission, indicate that the source 349.82-0.56 is at the near kinematic distance, but there are three "near" linear density-wave distances all compatible with the absorption data to within the dispersion of the absorption line velocities. This source will not be used in any analysis which involves linear density-wave distances. The nebula 342.07+0.42 has not been observed in any absorption lines. The only property of this source that will be used is the radius derived from circular rotation.

Finally, there are HII regions which show absorption lines at velocities significantly greater than V(H109α), but far less than V_t. It is possible that the motion of some of these objects cannot be described by either pure circular rotation or linear density-wave models, and therefore no kinematic distances were derived. These sources will be discussed in §IVh.

The absolute flux density S_0, defined as the 5 GHz continuum flux density times the square of the distance to the source in kpc, was calculated for each nebula. This quantity provides a measure of the luminosity of a region and is proportional to the total number of UV photons necessary to ionize the gas. Note that each nebula has two absolute flux densities, one based on the distance derived from circular rotation, and one based on the distance derived from the linear density wave model.

The average agreement between kinematic and optically determined distances is good. For 25 HII regions in this sample with known

exciting stars, $\langle r(\text{cir.})-r(\text{star})\rangle = 0.07 \pm 0.53$ kpc, and $\langle r(\text{LDW})-r(\text{star})\rangle = 0.14 \pm 0.64$ kpc, where error estimates are one standard deviation about the mean.

Figure 33 shows the absolute flux density of objects in the kinematic sample plotted against the average of their circular rotation and linear density-wave distance estimates; error bars extend from one distance estimate to the other and cover the corresponding range in S_0. A curve drawn at $S_0 = 3\ r^2$ Jy-kpc^2 marks the approximate sensitivity limit of the surveys, although in the North the limit might be as high as 5 Jy-kpc^2. There are no large differences between the two sets of distance estimates: the average difference over all nebulae $\langle r(\text{cir.})-r(\text{LDW})\rangle$ is -0.01 kpc with a dispersion of 0.44 kpc. Similar values are obtained from the North and South separately.

There are more nebulae with $S_0 < 100$ Jy-kpc^2 in the South than in the North (these lie below the horizontal line in Fig. 33), and it is these intrinsically faint objects that give the South more total nebulae than the North. Although they are <u>intrinsically</u> faint, their <u>observed</u> flux densities span a large range, from 2.8 to 47.9 Jy, with a median of 8 Jy, and at least half of them probably would have been detected had they been located in the North. The excess of faint southern nebulae cannot be ascribed to simple sensitivity differences between various surveys, although it is possible that a few faint southern sources are resolved components of objects which would have been counted only once in the northern surveys. There are nearly equal numbers of HII regions with $S_0 \geq 100$ Jy-kpc^2 in the two longitude intervals.

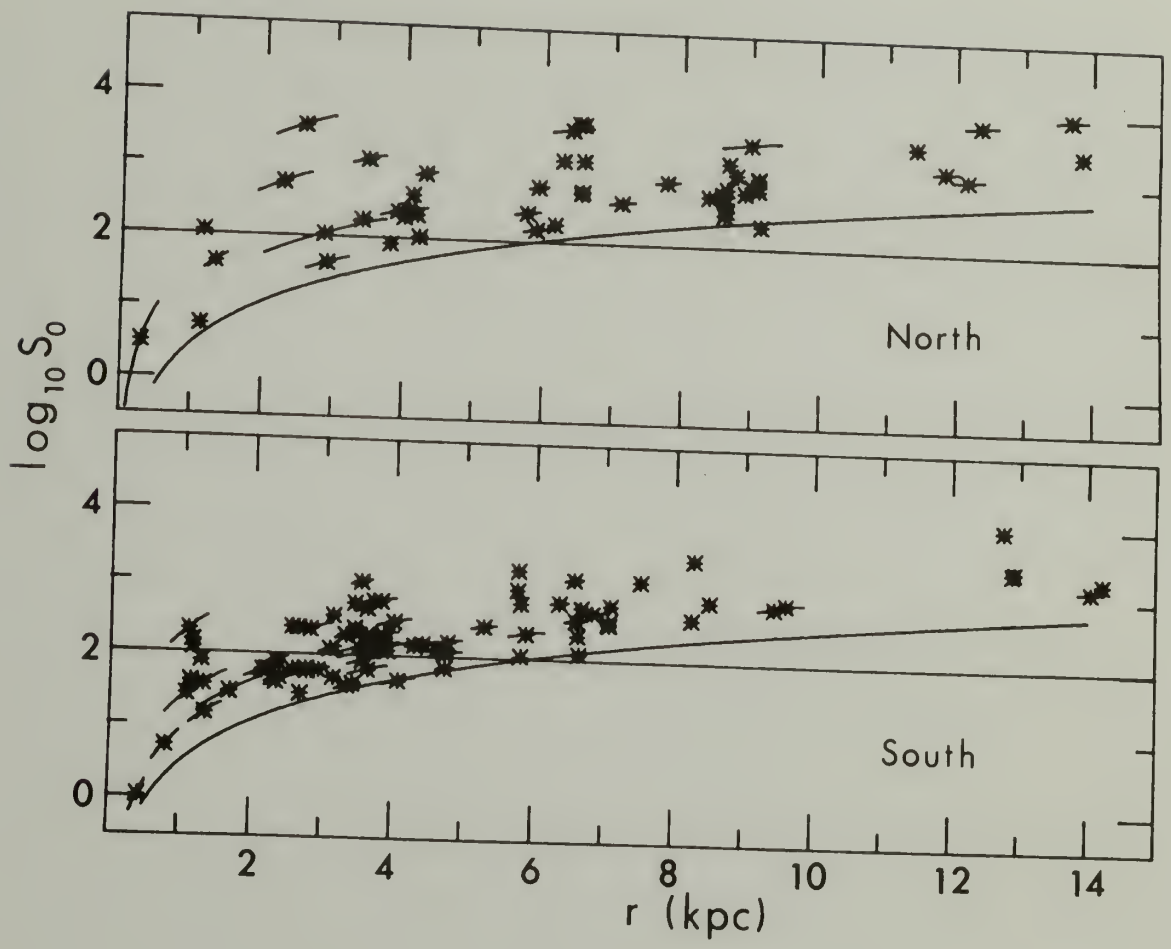

Figure 33: The absolute flux density of nebulae in the kinematic sample vs. distance from the sun. Distances are averages of circular and linear density-wave estimates; error bars extend from one estimated distance to the other and cover the corresponding range in S_0.

A luminosity function for radio HII regions may be derived by counting the number of nebulae in a given absolute flux density range over a representative volume of the Galaxy. It is most convenient to express this function as a surface density--the number of nebulae per kpc^2 with a given S_0. In order to avoid severely underrepresenting weak sources, the function has been constructed using nebulae within 5 kpc of the sun. However, the surveys are probably not complete below the 4 or 5 Jy level, and thus a number of HII regions with $S_0 < 100$ Jy-kpc^2 will be missed at r = 5 kpc. Furthermore, the distribution of HII regions is certainly not uniform and it is not clear that any volume of the Galaxy can be considered "representative".

Figure 34 shows the surface density of radio HII regions within 5 kpc of the sun plotted against the base 10 logarithm of the absolute continuum flux density derived from the circular motion and linear density-wave analyses. The decrease in the surface density with decreasing S_0 below 100 Jy-kpc^2 probably results from the incompleteness of the surveys at low flux levels. The decrease in the surface density with increasing S_0 above 100 Jy kpc^2 more likely reflects the true shape of the luminosity function. If each nebula is ionized by a single star, then, roughly speaking, an absolute flux density of 100 Jy-kpc^2 or greater requires that the star be of type O, while $S_0 < 100$ Jy-kpc^2 can be maintained by an early B star (Rubin, 1969; Panagia, 1973). The median of both functions is 100 Jy-kpc^2, indicating that at least half the nebulae in the sample require one or more O stars to maintain their ionization.

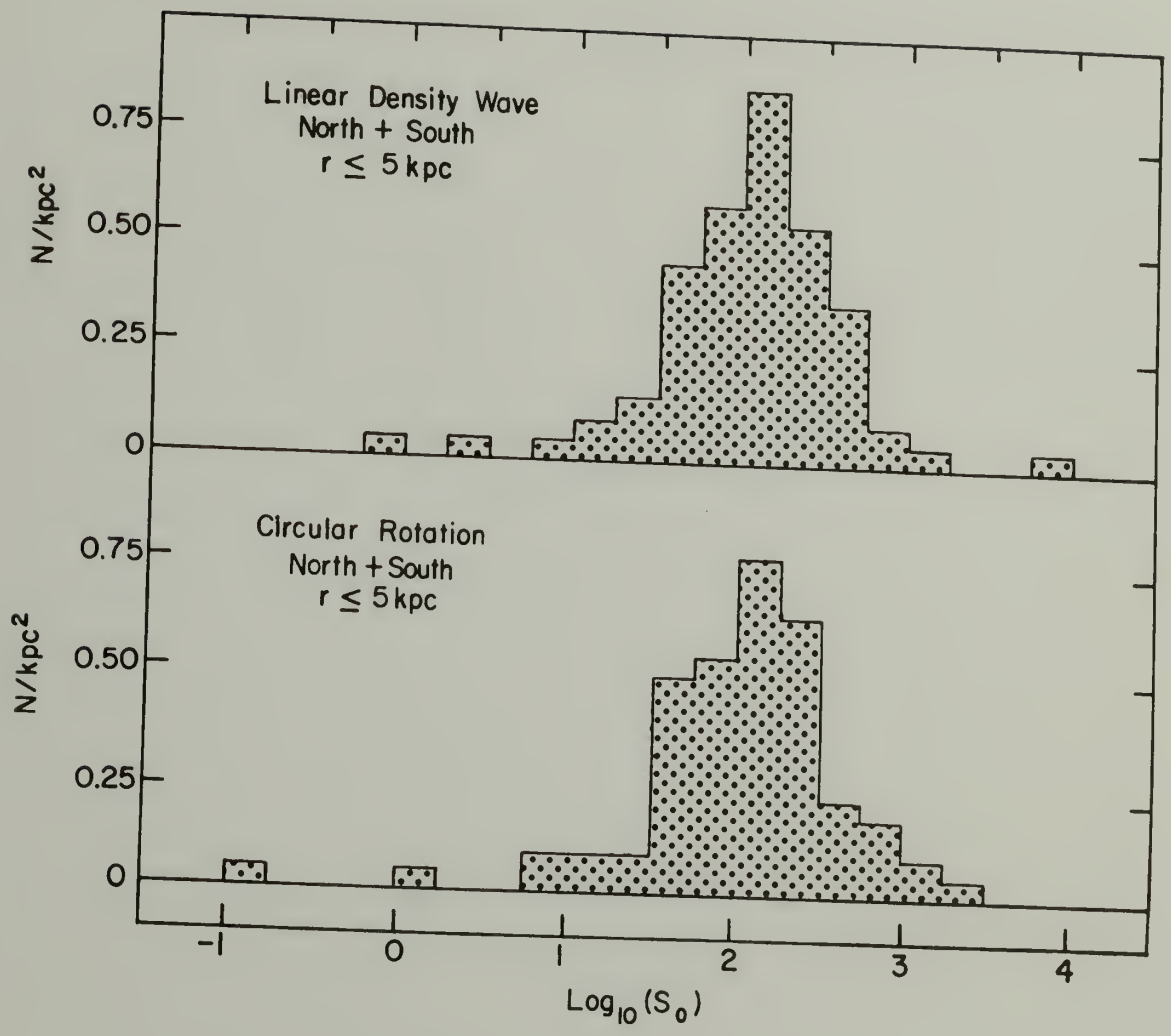

Figure 34: Luminosity functions for dense HII regions located within 5 kpc of the sun. The surface density is drawn vs. the $\log_{10}$ absolute flux density. Nebulae from both longitude intervals are included in each figure.

Within the present observational limits, only the most luminous nebulae, those which require one or more O stars to ionize the observed volume of gas, can be detected at significant distances from the sun. Because it is important to minimize observational effects when comparing different parts of the Galaxy, even at the risk of ignoring a majority of galactic HII regions, further analysis will emphasize objects with an absolute flux density $\geq$ 100 Jy-kpc^2, as derived from either circular or linear density-wave kinematic distances. Table 4 gives a list of these HII regions, with their kinematic distances, galactocentric radii and absolute flux densities. The bases for resolution of the distance ambiguity are listed under "other measurements". Asterisks indicate that the object may have an anomalous velocity with respect to the absorption data. Objects with small anomalies between absorption and recombination line velocities are indicated by a footnote but are otherwise retained in the sample. In some cases, there is uncertainty as to the exact distance, so the possible distances and radii are listed along with a note of preference. The linear density-wave model occasionally has small values of $|dV(r)/dr|$, and hence larger than normal distance uncertainties, at positions away from the subcentral point. The few nebulae affected by this are identified by an appropriate note. The objects in this list are seen out to r $\sim$ 14 kpc, and provide the sample that will be used in all further analysis.

In the South, 31-33% of the nebulae have optical counterparts as compared with 15% of those in the North. Thus the difference in average visual extinction towards radio HII regions, which was prominent in the

TABLE 4

Kinematic Distances to Luminous HII Regions

Source	Circular Motion R	Circular Motion r	Circular Motion $\log_{10}S_0$	Linear Density Wave R	Linear Density Wave r	Linear Density Wave $\log_{10}S_0$	Other Measurements	Reference	Notes
5.89-0.42	7.0	3.0	2.3	7.7	2.4	2.1	OH, H_2CO	1,2,3	a
				6.4	3.7	2.5			
5.97-1.18	8.8	1.2	2.1	8.9	1.1	2.0	Opt,HI,OH,H_2O	1,3,4,5	
6.99-0.25	6.3	3.7	2.3	8.0	2.0	1.7	Opt,OH,H_2CO	1,2,3,4	
8.49-0.32	4.6	5.6	2.4	5.4	4.7	2.3	OH,H_2CO	1,2,3	b
10.16-0.35	*	*	*	4.2	6.0	2.4			
				*	*	*	HI,OH,H_2CO	1,2,3,5	c
10.31-0.15	*	*	*	*	*	*	OH,H_2CO	1,2,3	c
10.63-0.39	*	*	*	*	*	*	HI,OH,H_2CO	1,2,6	c
12.79-0.19	5.8	4.4	3.0	6.0	4.1	2.9	HI,OH,H_2CO	1,2,3,5	
13.19+0.05	4.3	6.0	2.2	4.2	6.3	2.3	OH,H_2CO	1,2	
14.60+0.06	6.1	4.2	2.6	6.2	4.1	2.6	OH,H_2CO		
15.05-0.69	7.9	2.2	3.4	7.2	3.0	3.7	Opt,HI,OH,H_2CO	1,2,4,5	
16.98+0.82	7.5	2.7	2.9	8.2	1.9	2.6	Opt,HI,OH,H_2CO	1,3,4,5	a
				7.7	2.4	2.8			
18.47+1.93	7.0	3.2	3.0	6.6	3.7	3.2	Opt,OH,H_2CO	1,2,3	
19.05-0.27	4.9	5.8	2.8	4.7	6.1	2.8	OH,H_2CO	1,2,3	d
19.67-0.18	6.4	3.9	2.3	6.3	4.1	2.3	OH,H_2CO	1,2,3	
20.74-0.09	5.8	13.9	3.4	5.7	13.8	3.4	OH,H_2CO	1,2,3	
22.78-0.28	4.8	12.1	3.8	5.1	12.6	3.9	OH,H_2CO	1,2,3	
23.26-0.27	5.0	6.1	2.2	5.3	5.7	2.1	H_2CO	3	
23.43-0.20	4.3	7.6	2.9	4.2	8.0	2.9	OH,H_2CO	1,2,3	
23.55-0.04	4.6	6.9	2.6	4.4	7.3	2.6	OH,H_2CO	1,3	

TABLE 4 (continued)

Source	Circular Motion R	Circular Motion r	Circular Motion $\log_{10}S_0$	Linear Density Wave R	Linear Density Wave r	Linear Density Wave $\log_{10}S_0$	Other Measurements	Reference	Notes
23.95+0.15	4.2	9.1	2.3	4.1	9.1	2.3	OH,H_2CO	1,3	e
24.48+0.23	4.1	9.1	3.0	4.1	9.1	3.0	OH	1	f
24.64-0.18	4.2	9.1	2.8	4.2	9.1	2.8	OH	1	f
24.81+0.10	4.2	9.1	3.0	4.2	9.1	3.0	OH,H_2CO	1,2	f
25.39-0.17	6.2	13.5	3.6	6.0	13.2	3.6	HI,OH,H_2CO	1,2,3,5	
25.78+0.21	4.4	9.0	2.9	4.4	9.0	2.9	OH,H_2CO	1,3	f
27.29-0.16	4.8	8.9	2.8	4.9	8.9	2.8	OH	1	e
28.62+0.02	5.0	8.8	3.0	5.3	8.8	3.0	OH,H_2CO	1,2,3	e
29.93-0.04	5.2	8.7	3.2	5.5	8.7	3.2	HI,OH,H_2CO	1,2,3,5	e
30.23-0.15	5.0	8.6	2.8	5.3	8.6	2.8	OH,H_2CO	1,3	e
30.39-0.24	5.1	8.6	2.5	5.1	8.6	2.5	H_2CO	3	f
30.51-0.28	5.1	8.6	2.7	5.1	8.6	2.7	OH,H_2CO	1,3	f
30.70-0.26	5.2	8.6	2.5	5.5	8.6	2.5	OH,H_2CO	1,3	e
30.76-0.03	5.4	6.7	3.6	5.7	6.1	3.6	HI,OH,H_2CO	1,3,5	
31.06+0.04	5.2	8.6	2.8	5.5	8.6	2.8	OH,H_2CO	1,3	e
33.12-0.08	5.5	8.4	2.7	5.7	8.4	2.7	OH	1	e
34.26+0.15	7.2	3.8	2.3	6.9	4.3	2.4	HI,OH,H_2CO	1,2,3,6	
35.20-1.74	7.6	3.3	2.2	7.4	3.5	2.3	HI,OH,H_2CO	1,2,3,5	
35.59-0.03	7.4	3.6	2.3	7.0	4.2	2.4	OH	1	
37.56-0.11	7.3	11.9	3.0	7.6	12.4	3.1	OH,H_2CO	1,2,3	
37.88-0.37	7.1	11.5	3.5	7.0	11.3	3.5	OH,H_2CO	1,2,3	
43.17-0.00	9.5	13.9	4.0	9.2	13.4	4.0	HI,OH,H_2CO	1,2,3,5	
45.45+0.06	7.7	4.2	2.3	7.7	4.2	2.3	HI,OH,H_2CO	1,2,3,5	
46.50-0.25	7.7	4.3	2.0	7.8	4.1	2.0	OH	1	
48.59+0.04	9.2	12.0	3.2	9.0	11.6	3.2	HI,OH,H_2CO	1,2,3,6	

TABLE 4 (continued)

Source	Circular Motion R	Circular Motion r	Circular Motion $\log_{10}S_0$	Linear Density Wave R	Linear Density Wave r	Linear Density Wave $\log_{10}S_0$	Other Measurements	Reference	Notes
48.93-0.28	7.5	6.6	3.2	7.5	6.6	3.2	OH,H_2CO	1,3	f
49.02-0.28	7.6	6.6	3.7	7.6	6.6	3.7	OH,H_2CO	1,2	f
49.07-0.37	7.6	6.6	2.7	7.6	6.6	2.7	HI,OH,H_2CO	1,3,5	f
49.25-0.32	7.6	6.5	2.7	7.6	6.5	2.7	OH,H_2CO	1,3	f
49.38-0.30	7.9	8.6	3.4	8.1	9.4	3.5	OH,H_2CO	1,3	e
49.48-0.38	7.7	6.5	3.7	7.8	6.5	3.7	HI,OH,H_2CO	1,3,5	e
51.20+0.07	7.8	6.3	3.2	8.0	6.3	3.2	OH	1	e
305.20+0.03	8.4	5.8	3.0	8.2	5.8	3.0	OH,H_2CO	3,7	e
305.25+0.22	8.5	5.8	3.2	8.3	5.8	3.2	H_2CO	3	e
305.36+0.19	8.5	5.8	3.1	8.3	5.8	3.1	HI,OH,H_2CO	3,5,6,8	e
305.55+0.01	8.1	5.8	2.8	8.1	5.8	2.8	OH,H_2CO	3,7	f
307.62-0.29	8.4	3.2	2.0	8.2	3.8	2.2	OH,H_2CO	3,7	a
310.83-0.44	8.4	9.0	2.9	8.2	8.1	2.8			
311.49+0.39	10.8	14.3	3.3	10.7	14.1	3.2	H_2CO	3	g
311.62+0.29	7.5	6.6	2.4	7.5	6.6	2.4	H_2CO	3	f
311.89+0.09	7.5	6.6	2.1	7.5	6.6	2.1	OH,H_2CO	3,8	f
311.92+0.21	8.0	9.7	2.8	7.9	9.2	2.8	HI,OH,H_2CO	3,6,7	
316.80-0.06	8.1	9.9	2.9	7.9	9.4	2.8	HI,H_2CO	3,6	
316.99+0.28	8.3	2.5	2.3	8.0	3.1	2.4	Opt,HI,OH,H_2CO	3,5,7	
320.26-0.31	7.9	3.4	2.2	7.7	3.8	2.3	OH,H_2CO	3,7	
	7.0	5.0	2.2	7.1	4.6	2.2	H_2CO	3	
321.04-0.50	7.1	4.4	2.2	7.2	4.2	2.1	Opt,OH,H_2CO	3,7	
321.13-0.53	7.4	3.9	2.1	7.4	3.9	2.1	Opt,OH	7	
322.16+0.62	7.5	3.6	2.2	7.4	3.7	2.2	Opt,OH,H_2CO	3,7	
326.65+0.58	7.6	3.1	2.5	7.5	3.2	2.6	Opt,HI,OH,H_2CO	3,5,8	
327.30-0.55	7.3	3.5	2.7	7.4	3.4	2.7	Opt,HI,OH,H_2CO	3,4,5,7	

TABLE 4 (continued)

Source	Circular Motion R	Circular Motion r	Circular Motion $\log_{10}S_0$	Linear Density Wave R	Linear Density Wave r	Linear Density Wave $\log_{10}S_0$	Other Measurements	Reference	Notes
328.31+0.43	5.4	8.5	2.9	5.3	8.5	2.9	OH,H_2CO	3,7	e
330.87-0.37	6.7	4.1	2.2	7.0	3.7	2.1	HI,H_2CO	3,6	
331.04-0.15	5.4	6.4	2.5	5.2	6.8	2.6	H_2CO	3	
331.33-0.35	6.3	4.6	2.2	6.6	4.2	2.1	HI,OH,H_2CO	3,6,7	
331.36-0.02	5.7	5.6	2.3	5.5	6.1	2.4	H_2CO	3	
331.53-0.08	5.3	6.4	3.1	5.2	6.7	3.1	HI,H_2CO	3,5,6	
332.15-0.45	6.7	4.1	2.3	7.0	3.6	2.2	Opt,HI,OH,H_2CO	3,6,7	
332.66-0.62	7.0	3.6	2.4	7.2	3.3	2.4	Opt,OH,H_2CO	3,4,7	
332.81-0.57	6.5	4.2	2.5	6.9	3.8	2.4	Opt,H_2CO	3	
333.03-0.45	6.7	4.0	2.8	7.0	3.6	2.7	Opt,HI,H_2CO	3,5	
333.12-0.45	6.7	3.9	2.8	7.0	3.5	2.7	Opt,OH,H_2CO	3,7,8	
333.17-0.10	5.0	6.7	2.7	5.0	6.6	2.7	H_2CO	3	
333.29-0.38	6.8	3.8	2.7	7.1	3.4	2.6	Opt,H_2CO	3	
333.61-0.22	6.9	3.7	3.1	7.1	3.4	3.0	HI,OH,H_2CO	3,5,6,8	c
336.43-0.25	4.5	7.0	2.7	4.7	6.6	2.6	OH,H_2CO	3,7	
336.81+0.04	5.2	12.6	4.0	5.4	12.9	4.0	OH,H_2CO	3,7	
336.93-0.15	5.3	12.8	3.4	5.4	13.0	3.4	H_2CO	3	
337.12-0.17	5.3	12.8	3.4	5.4	13.0	3.4	HI,OH,H_2CO	1,3,6,7	
337.63-0.05	6.1	4.4	2.1	5.8	4.8	2.2	H_2CO	3	d
337.80-0.09	6.2	14.2	3.2	6.0	13.8	3.1	HI,OH,H_2CO	1,3,6,7	
337.92-0.47	6.9	3.5	2.3	7.2	3.2	2.2	HI,OH,H_2CO	1,3,6	c
338.06+0.01	*	*	*	*	*	*	OH,H_2CO	1,3,7	c
338.43+0.05	*	*	*	*	*	*	HI,OH,H_2CO	1,3,5,7	c
338.92+0.60	5.6	5.1	2.4	5.3	5.5	2.5	OH,H_2CO	1,3,7	
340.06-0.22	6.0	4.5	2.0	5.6	5.0	7.1	OH,H_2CO	1,3	

TABLE 4 (continued)

Source	Circular Motion R	Circular Motion r	Circular Motion $\log_{10}S_0$	Linear Density Wave R	Linear Density Wave r	Linear Density Wave $\log_{10}S_0$	Other Measurements	Reference	Notes
342.07+0.42	4.9	5.8	2.0	5.0	5.6	2.0			
	4.9	13.3	2.7	5.3	13.8	2.8			h
342.27+0.31	3.3	8.3	2.6	3.3	8.3	2.6			
	3.3	10.8	2.8	3.3	10.8	2.8	OH	1	a
343.48-0.04	6.9	3.3	2.1	7.2	2.9	2.0			
345.42-0.96	7.5	2.6	2.4	7.4	2.7	2.4	OH,H_2CO	1,3,7	
347.61+0.20	3.1	7.6	3.1	3.1	7.5	3.1	Opt,HI,OH,H_2CO	1,3,5,7	
							OH,H_2CO	1,3	
348.72-1.04	*	*	*	*	*	*			
349.09+0.10	3.3	7.1	2.8	3.3	7.1	2.8	HI,OH,H_2CO	1,2,3,5,7	c
349.82-0.56	6.1	4.0	2.2	7.0	3.1	1.9	OH,H_2CO	1,3	
				6.2	3.8	2.1	Opt,OH,H_2CO	1,3	i
				5.4	4.7	2.3			
350.11+0.08	3.3	7.1	2.5	3.2	7.1	2.5	OH,H_2CO	1,3	
351.35+0.63	9.2	0.8	2.1	8.7	1.4	2.5	Opt,HI,OH,H_2CO	1,2,3,4,5	
351.59+0.18	4.0	6.2	2.8	3.7	6.5	2.8	OH,H_2CO	1,3	
351.63-1.25	7.5	2.6	2.4	7.5	2.6	2.4	OH,H_2CO	1,2,3,7	
353.12+0.64	8.9	1.1	2.1	8.8	1.2	2.2	Opt,OH,H_2CO	1,3,4	
353.19+0.89	8.9	1.1	2.0	8.8	1.2	2.1	Opt,OH,H_2CO	1,3,4	
353.52-0.04	3.1	7.1	2.6	3.1	7.0	2.5	OH,H_2CO	1,3	

R is distance from the galactic center in kpc, r is distance from the sun in kpc, S_0 is absolute flux density in Jy-kpc^2.

Notes

a) Nearer distance preferred.
b) Farther distance preferred.
c) Object may have an anomalous velocity. See text.

TABLE 4 (continued)

Notes (continued)

d) Linear density wave distance uncertain by about 1 kpc.
e) HII region is virtually at the tangent point. Tangent point distance adopted.
f) HII region is at a forbidden velocity, tangent point distance and radius adopted.
g) HII region is beyond the solar circle.
h) No absorption measurements have been made towards this source.
i) All three linear density wave distances seem equally probable.

References

1) Turner (1979).
2) Wilson (1972).
3) Whiteoak and Gardner (1974).
4) Georgelin and Georgelin (1970,1976); Georgelin, Georgelin and Roux (1973).
5) Radhakrishnan et al. (1972); Goss et al. (1972).
6) Caswell et al. (1975).
7) Caswell and Robinson (1974).
8) Goss et al. (1970).

overall sample, persists for the most luminous nebulae. This effect is independent of the relative overabundance of small nebulae in the South, and by comparing the percentage of optical detections vs. distance, it can be shown that it does not arise from a coincidental proximity of large southern nebulae to the sun. Thus there must be less obscuring material along the line of sight to radio HII regions in the South than would be estimated from the northern data.

The intrinsically luminous nebulae in this final sample, comprising 110 of the original 166 objects, are distributed about equally between the North and the South. Their numbers vs. distance are shown in Figure 35 for both circular and linear density-wave velocity fields. Also shown is the total continuum flux density, including contributions from faint nebulae. The similarity between the number counts and the fluxes indicates that most of the observed thermal continuum flux comes from the most intrinsically luminous nebulae.

It is obvious that the ionized gas is not distributed uniformly with distance from the sun. Sources tend to be found near r = 1, 3.5, 6.5, 9.0 and 13 kpc, and are less common at other distances. These peaks are also evident when the two longitude intervals are considered separately. The clustering of sources makes it difficult to estimate the magnitude of any distance selection effect since, to first order, most of the structure in Figure 35 must arise from the galactic distribution of nebulae, $N(R,\theta)$. However, there is a definite decrease in the number of luminous nebulae for r > 8 kpc, and selection effects probably become severe near this point. If we assume that the local luminosity function

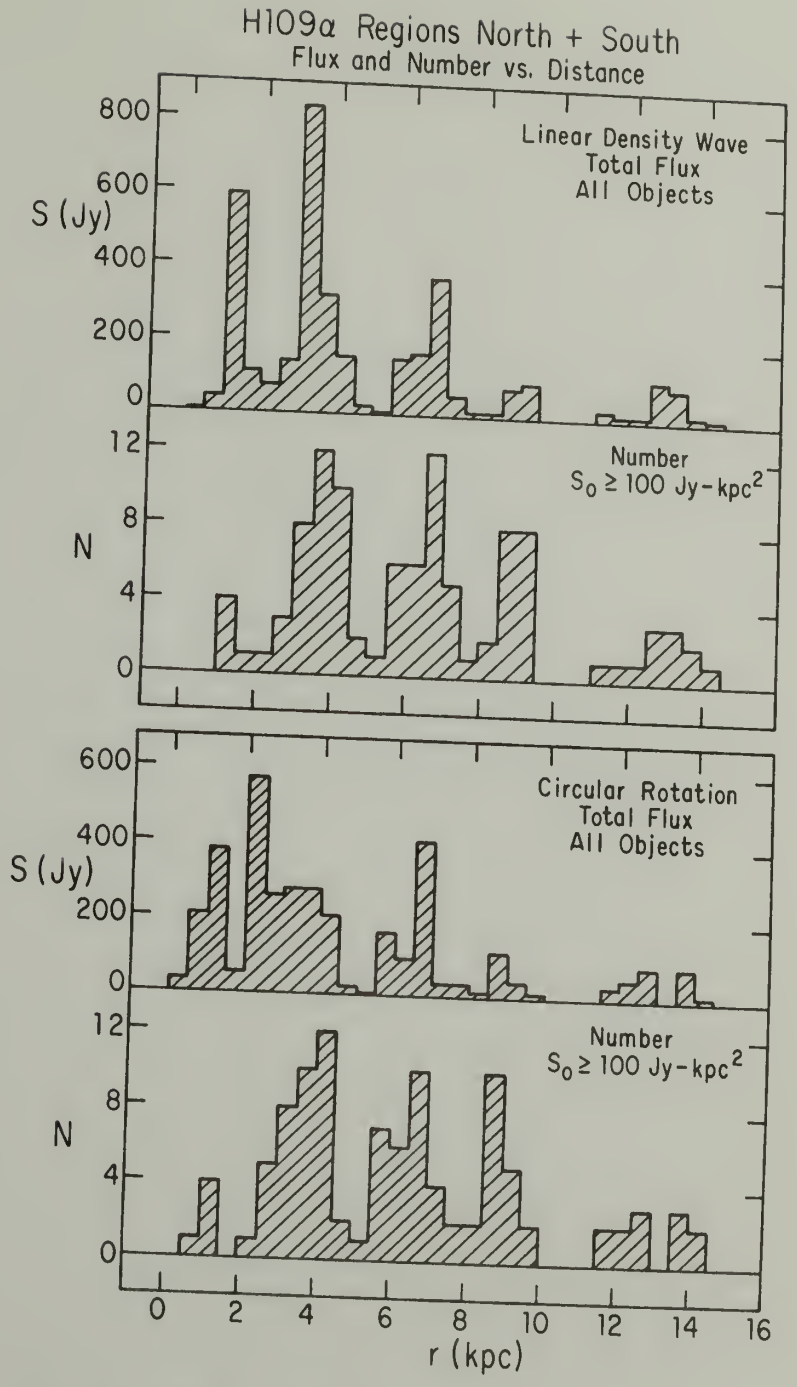

Figure 35: The number of nebulae and observed continuum flux densities as a function of distance from the sun for the two different galactic velocity fields. Number counts include only objects with an absolute flux density greater than or equal to 100 Jy-kpc^2, while the observed flux density counts contain contributions from all nebulae in the kinematic sample. The figures are averages over both longitude intervals.

is representative of distant parts of the Galaxy, and that the minimum observed flux density is 3 Jy, then only 60% of the nebulae with $S_0 \geq$ 100 Jy-kpc^2 will be detected at a distance of 8 kpc from the sun. It would be wrong to construe the structure in N(r) and S(r) as evidence of any "grand design" in the distribution of HII regions. But, the fact that the major peaks in numbers and flux appear in both longitude intervals indicates that the structure is not fortuitous and does contain some information on the large-scale distribution of nebulae.

A more direct approach is to examine quantities as functions of galactocentric coordinates. Figure 36 shows the surface density of intrinsically luminous nebulae ($S_0 \geq 100$ Jy-kpc^2) plotted against the galactocentric radius R for both velocity fields and longitude intervals. Nebulae are found at radii between 3 and 11 kpc in the South and between 4 and 10 kpc in the North. The apparent decrease in the surface density at the solar radius and interior to 3 kpc is real (see §IVg). There is obvious structure in the radial surface density, and the distribution derived from linear density-wave motions is more ordered than that derived from circular rotation. In the linear density-wave model, the major peaks in the North occur near 4, 5.5 and 7.5 kpc, and in the South near 3, 5.5 and 7.5 kpc. Similar, though less well defined peaks, are found in the distribution derived from circular rotation. The surface density in the South is especially concentrated in certain annuli, and the differences between the two longitude intervals is suggestive of azimuthal structure in the overall distribution of nebulae. The absolute flux density shows features similar to the surface density except that the southern peak near 7 kpc is less prominent.

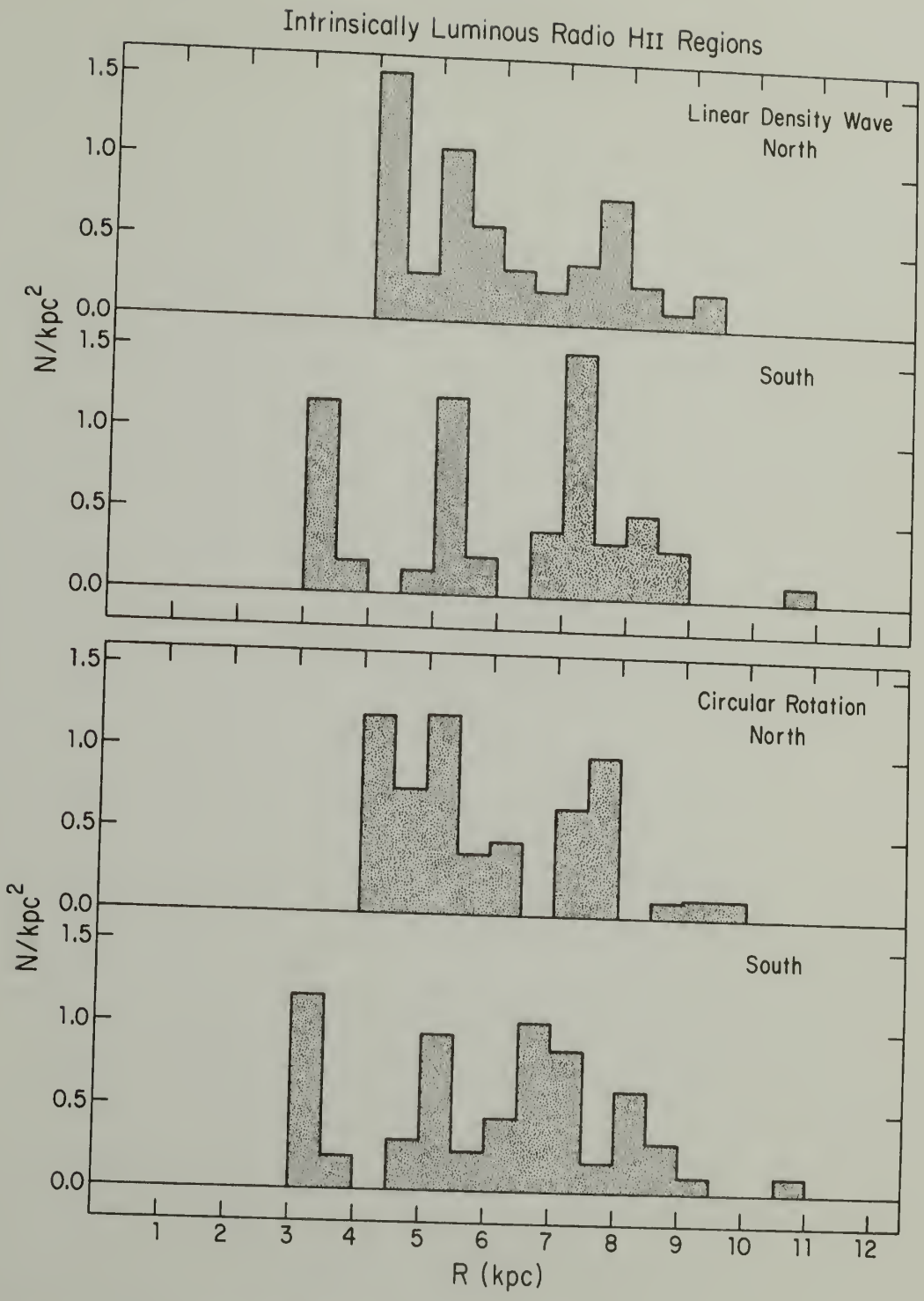

Figure 36: The observed radial surface density of intrinsically luminous radio HII regions ($S_0 \geq 100$ Jy-kpc^2) in the kinematic sample. The lower two panels use radii derived from the circular rotation model, and the upper two panels use radii derived from the linear density-wave model.

Figure 37 shows the number and absolute flux density per kpc^2 averaged over both longitude intervals. The radial structure changes somewhat according to the assumed velocity field, but the overall shape of all four curves is quite similar. The peak in the surface density of objects and absolute fluxes occurs near 5 kpc, and there is evidence for a secondary peak near 7.5 kpc. It is interesting to compare the locations of the peaks in Figure 37 with the locus of potential minima in the linear density-wave model of Burton (1971). In this model the potential minima between the sun and the galactic center are located at radii 3 to 4 kpc, 5 to 6 kpc and 7.5 to 9 kpc, where the spread in radii results from the tilt of the spiral pattern over the longitude range of the sample of nebulae. These positions qualitatively match many of the peaks in the derived radial surface density diagrams, suggesting that the data are not inconsistent with a spiral distribution of HII regions in the Galaxy.

Figures 36 and 37 show observed surface densities and, because of the longitudinal restriction on the sample, they are not complete at $R < 0.9$ kpc or at $R > 8.2$ kpc. Moreover, the values of N(R) are low by at least a factor of two because the portion of the Galaxy on the other side of the galactic center is poorly represented in this sample. However, the qualitative shape of the radial functions, the secondary peaks near 7.5 kpc and the southern extension inwards to $R = 3$ kpc, all appear to be real features of the radial distribution of dense HII regions.

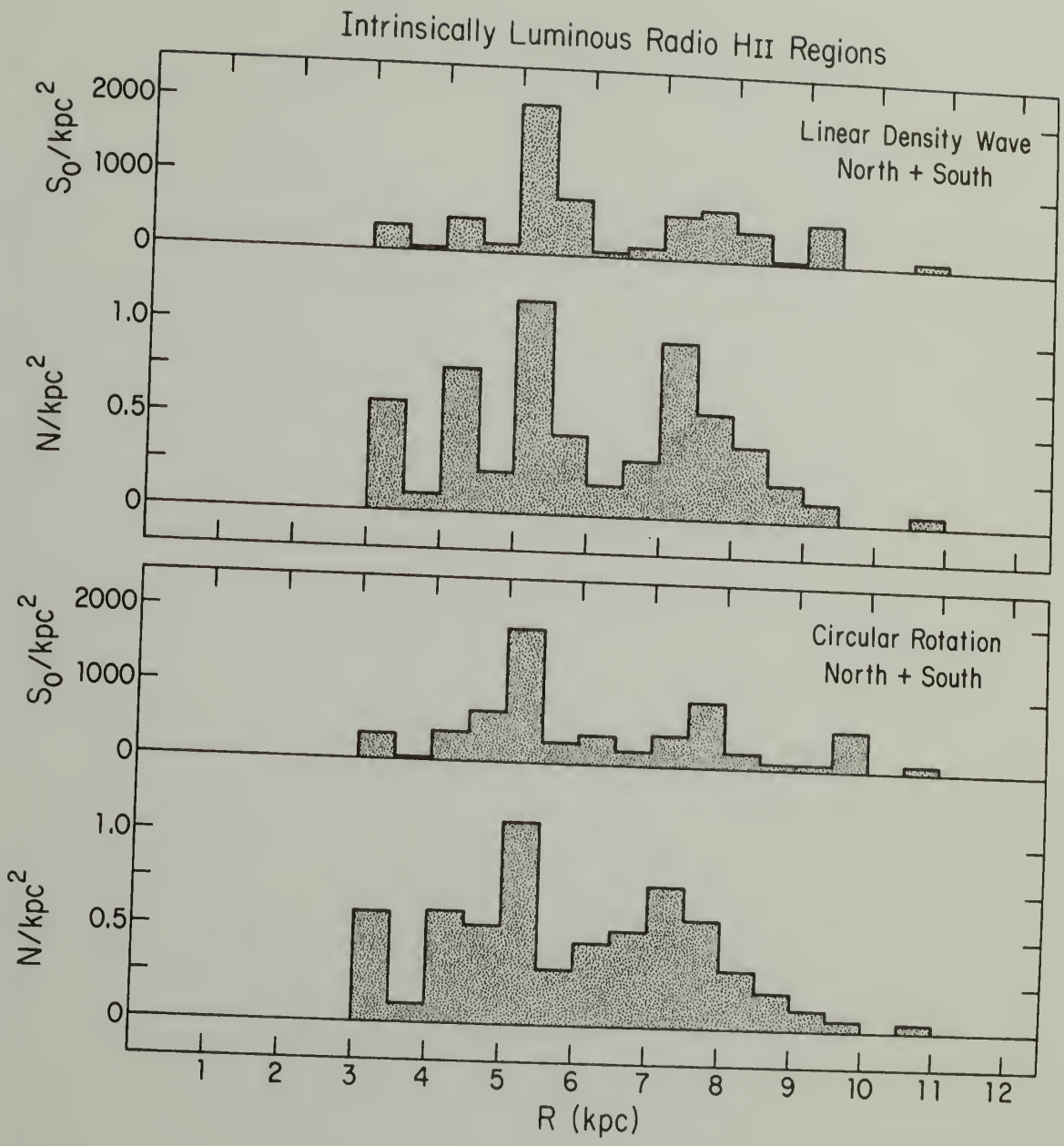

Figure 37: The radial surface density of intrinsically luminous HII regions and of their absolute flux density. Results from both the circular rotation and linear density-wave analyses are shown.

The distance of nebulae from the plane, defined as $z = r \sin(b)$, is plotted against R in Figure 38 for distances derived from the linear density-wave model. The circular rotation analysis gives a very similar distribution. The circles mark northern nebulae and the triangles mark southern nebulae. The HII regions are located quite near the galactic plane. The mean z is -10 pc with a dispersion about this mean of 30 pc. (For circular rotation the corresponding values are -10 pc and 32 pc.) One-half of the sources are found within 20 pc of the mean z. These distributions are extremely narrow, and in fact the layer of luminous HII regions has the smallest z extent of any galactic tracer. By comparison, the number of HI clouds in the z direction can be described by a Gaussian distribution which has a dispersion of 80 pc (Baker and Burton, 1975), and it has been estimated that the CO clouds have a dispersion of 50 pc about their mean z (Burton and Gordon, 1978; Scoville et al., 1977).

There is an obvious trend in z(R): nebulae at $R < 4$ kpc have $z > 0$, nebulae at $5 < R < 7$ kpc have $z < 0$ and nebulae at $R > 8$ kpc have $z > 0$ once again. A similar warping has been observed in the CO clouds, in the sense that they have an $\langle z \rangle$ of -40 pc between 4 and 8 kpc radius (Scoville et al., 1977; Cohen and Thaddeus, 1977), but the CO observations as yet are based entirely on northern longitudes, while the warping shown in Figure 38 occurs in both the North and South to a roughly equal extent. A more complete discussion of the z(R) distribution of HII regions and other Population I-type species is given in Chapter Vg.

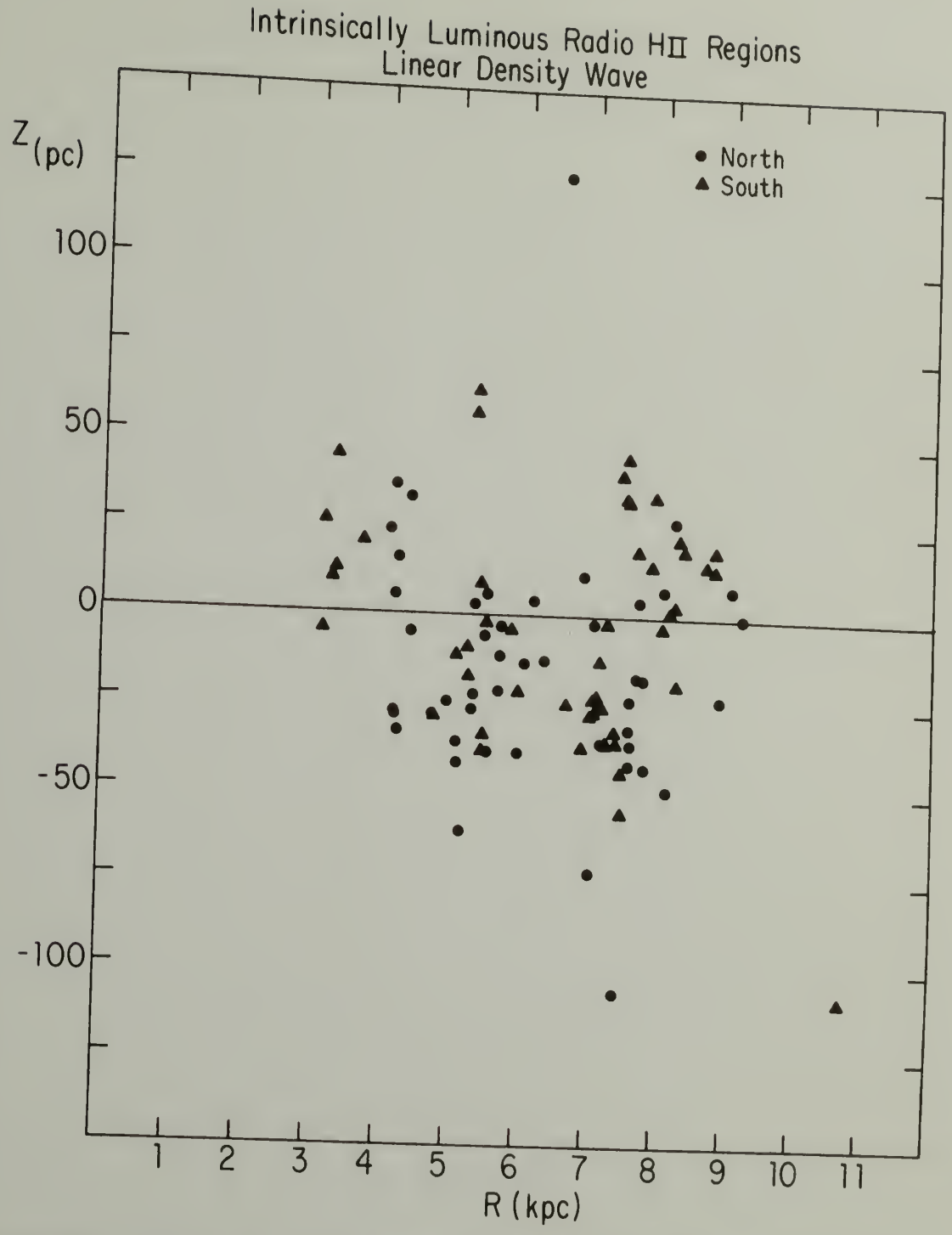

Figure 38: Distance from the galactic plane z, vs. distance from the galactic center R, for intrinsically luminous nebulae in the kinematic sample. Circles mark nebulae in the northern longitude interval; triangles mark nebulae in the southern longitude interval. These data were derived using linear density-wave distance estimates.

For completeness, the intrinsically luminous nebulae are plotted in galactocentric polar coordinates in Figure 39. The largest symbols mark nebulae with $S_0 > 800$ Jy-kpc^2, and the smallest mark those with $S_0 < 200$ Jy-kpc^2. Dashed lines drawn at longitudes 305° and 55° show the longitude extent of the sample, and a circle marks the position of the sun. While the nebulae are not located randomly, this figure shows no compelling evidence that the dense radio HII regions lie in a clear, unique pattern. It is, however, extremely unlikely that such a distribution would be visible when the data are displayed in this manner regardless of the extent to which HII regions are confined to specific locations. As seen earlier, $<|dV(r)/dr|> \sim 100$ pc/(km/s) over lines of sight interior to the solar circle. This implies that even if the magnitude of the galactic velocity field is known perfectly, random motions will give a 500 pc error, on the average, in the distance to these nebulae. Motions in the Galaxy are, of course, not perfectly known and thus one could expect a kinematically derived position to be in error by $\sim$ 1 kpc along the line of sight. This error is quite sufficient to destroy any appearance of structure in a polar diagram containing only about 100 points. A polar diagram is clearly of limited value for investigating the existence and form of any $R(\theta)$ relationship. We must rely on averaged derived quantities, and the construction of models which attempt to reproduce observed quantities, for our conclusions regarding the large-scale distribution of HII regions.

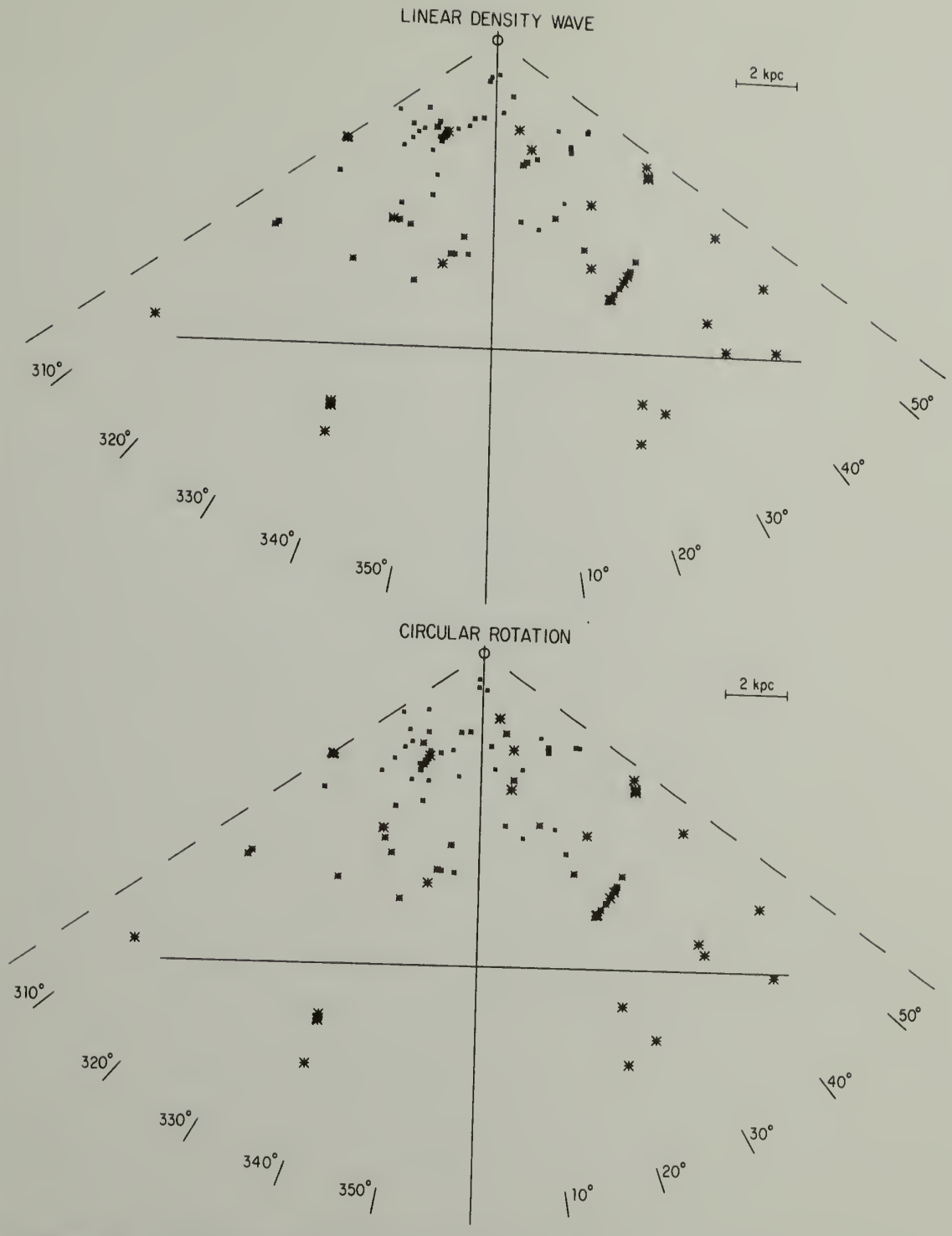

Figure 39: The distribution in galactocentric polar coordinates of the intrinsically luminous nebulae in the kinematic sample. The largest symbols mark nebulae with absolute continuum flux density >800 Jy-kpc^2; the smallest symbols mark nebulae with $100 \leq S_0 < 200$ Jy-kpc^2.

g) Kinematic Models

We construct kinematic models to determine the combinations of surface density and galactic motions that will reproduce the observed velocity-longitude distribution of nebulae. It is unrealistic to expect that any simple model will account for the placement of every nebula, but a successful model must account for the major features of the V-ℓ diagram. In particular, models should reproduce the "gaps" in the nebular distribution observed along V_t at certain longitudes. As discussed in §IVe, these gaps are triangular areas in V-ℓ space, in both the North and South, that contain no dense HII regions. The areas are well populated by species like HI and molecular clouds (CO), so their occurrence in Figure 32 is unexpected and the features should be reproduced by an adequate model.

The input to any model is a surface density of nebulae, $N(R,\theta)$, a description of the assumed kinematics, and a function $P(r)$ that accounts for distance-dependent selection effects. The observed surface density function, averaged over both longitude intervals (Fig. 37), was used in most models. This average function does not fall to zero until $R < 3$ kpc because there are six southern nebulae in the range $3 < R < 4$ kpc. However, the northern $N(R)$ is zero for all $R < 4$ kpc. None of the models discussed here reproduces this asymmetry in the location of the inner boundary of the nebular distributions, so whenever the observed surface density function was used, it was arbitrarily set equal to zero for all northern radii < 4 kpc. This only affects the

models over the longitude range $5 \leq \ell \leq 24°$. The asymmetry will be discussed in a later section.

Three forms of the distance dependence P(r) were used: 1) $P(r) = 1$. This ignores distance effects not in $N(R,\theta)$ and assures that all models give back the assumed surface density, but models with $P = 1$ have equal numbers of nebulae on the "near" and "far" sides of the Galaxy, contrary to what is observed. 2) $P(r) = r^{-2}$. This form of P was used for all ad hoc surface densities [e.g., constant $N(R,\theta)$], but when used with the observed N(R) it causes parts of the Galaxy which are poorly represented because of distance effects in the surveys to be doubly underrepresented in the models. 3) $P(r) = 1$ for $r \leq h$ and $P(r) = 0$ for $r > h$. This form of P places a horizon on the model at h kpc from the sun, while it maintains the adopted N(R) at closer distances. When an $h \sim 15$ kpc is chosen, the part of the Galaxy which has not actually been observed does not enter the models, and the models give back an N(R) function close to that observed. All model distributions which made use of the observed N(R) were calculated for each form of P(r) separately, and the results discussed here hold for all three forms of the distance dependence.

To make a model V-ℓ diagram, the line of sight at any ℓ is divided into cells of length Δr and width $r_i \Delta\ell$, where r_i is the distance to the center of a cell and $\Delta\ell$ is the angle between successive lines of sight. The product of the area of a cell times the adopted surface density function gives the probability that an HII region lies in that cell; if this probability is greater than a randomly chosen number

between 0 and 1, then a luminous HII region is assumed to occupy the cell. The absoluted flux density of the HII region (always $\geq$ 100 Jy-kpc^2) is given by another random number, chosen from a distribution like the local luminosity function. The observed flux density of a model nebula is its absolute flux density times the function P(r) which accounts for distance effects. A nebula is "detected" if its observed flux density is greater than 3 Jy. The velocity of the model nebula is the sum of the projected (model) galactic velocity field at the appropriate location, and a line of sight component randomly chosen from a distribution with zero mean and a dispersion of 5 km/s. The random numbers were generated from the method suggested by Lewis and Payne (1973). All calculations used $\Delta\ell = 1°$ and $\Delta r = 80$ pc.

The upper right and lower left panels of Figure 40 show typical V-ℓ diagrams calculated from the observed N(R) function with P = 1 for r < 14 kpc. For comparison, a uniform surface density function (i.e., N(R) = constant for <u>all</u> R) with $P(r) = r^{-2}$ was used to produce the model shown in the upper left panel. All these models are axisymmetric in that $N(R,\theta) = N(R)$. The observed luminous nebulae are shown in the lower right panel.

The uniform surface density model (upper left panel) has some nebulae at the high velocities and low longitudes characteristic of material at R < 3 kpc. Because this model contains a reasonable distance-dependent selection effect, it is likely that the lack of <u>observed</u> nebulae at R < 3 kpc is caused by a real decrease in N(R) in the inner Galaxy. We cannot conclude that there are no nebulae between

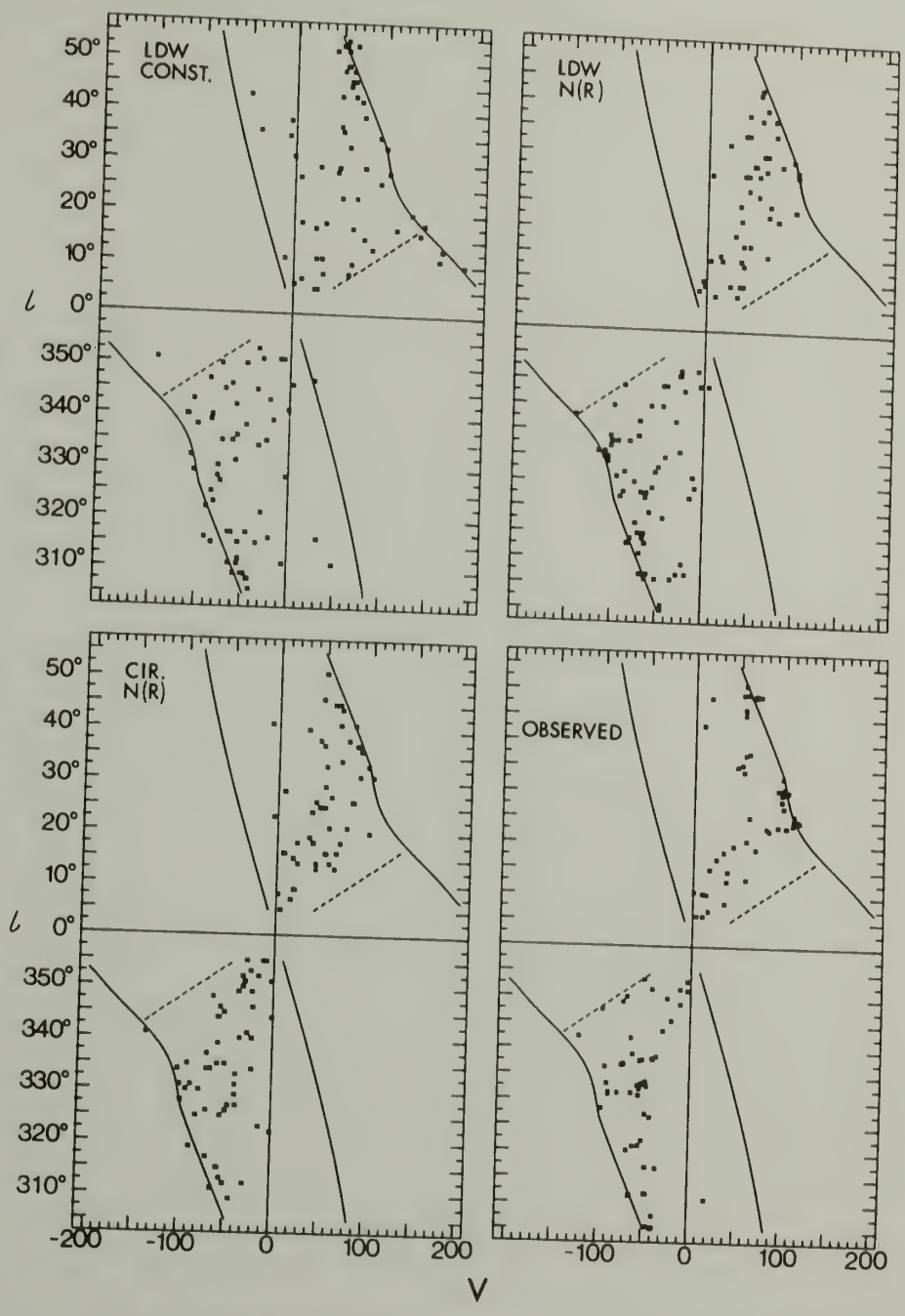

Figure 40: Three models of the distribution of luminous nebulae, and the observed distribution. Upper left panel: a constant surface density of nebulae with linear density-wave motions. Upper right and lower left panels: the observed surface density used with linear density-wave and circular motion models, respectively. Lines are drawn at longitudes and velocities corresponding to R=15 kpc, R=3 kpc (dashed line) and are drawn along the locus of terminal velocities, all as determined from the circular rotation model.

the galactic nucleus and R $\sim$ 3 kpc, but if there are any, their luminosity function must differ significantly from the local luminosity function--they cannot be bright, dense objects like those studied thus far.

Velocity crowding near the subcentral point makes the area near V_t a consistently probable location for nebulae in all models [the same phenomenon causes HI spectra to have a peak near V_t (Burton, 1971)]. Thus the observed absence of terminal-velocity nebulae at certain longitudes is not simple chance; there are no observed nebulae in just those areas of the V-ℓ diagram which have a high probability of being occupied. This conclusion holds for both the constant and the observed surface density functions. Also, there are only slight differences between model V-ℓ diagrams constructed using circular, linear density-wave and nonlinear density-wave kinematic models (the latter not shown here), and thus the gaps are not solely a consequence of nebular motions. In sum, none of the symmetric models using the observed radial surface density function reproduce the distinctive gaps along V_t. This implies that dense radio nebulae lie in an ordered pattern that is not completely described by the radial distribution function.

The left panel of Figure 41 shows a typical V-ℓ diagram produced by a model in which nebulae are confined to the spiral pattern derived from northern HI kinematics (Burton, 1971). In the specific model shown here, all nebulae are located on the outer edge of the spiral within 22°.5 azimuth of the pattern center. Thus approximately 13% of this

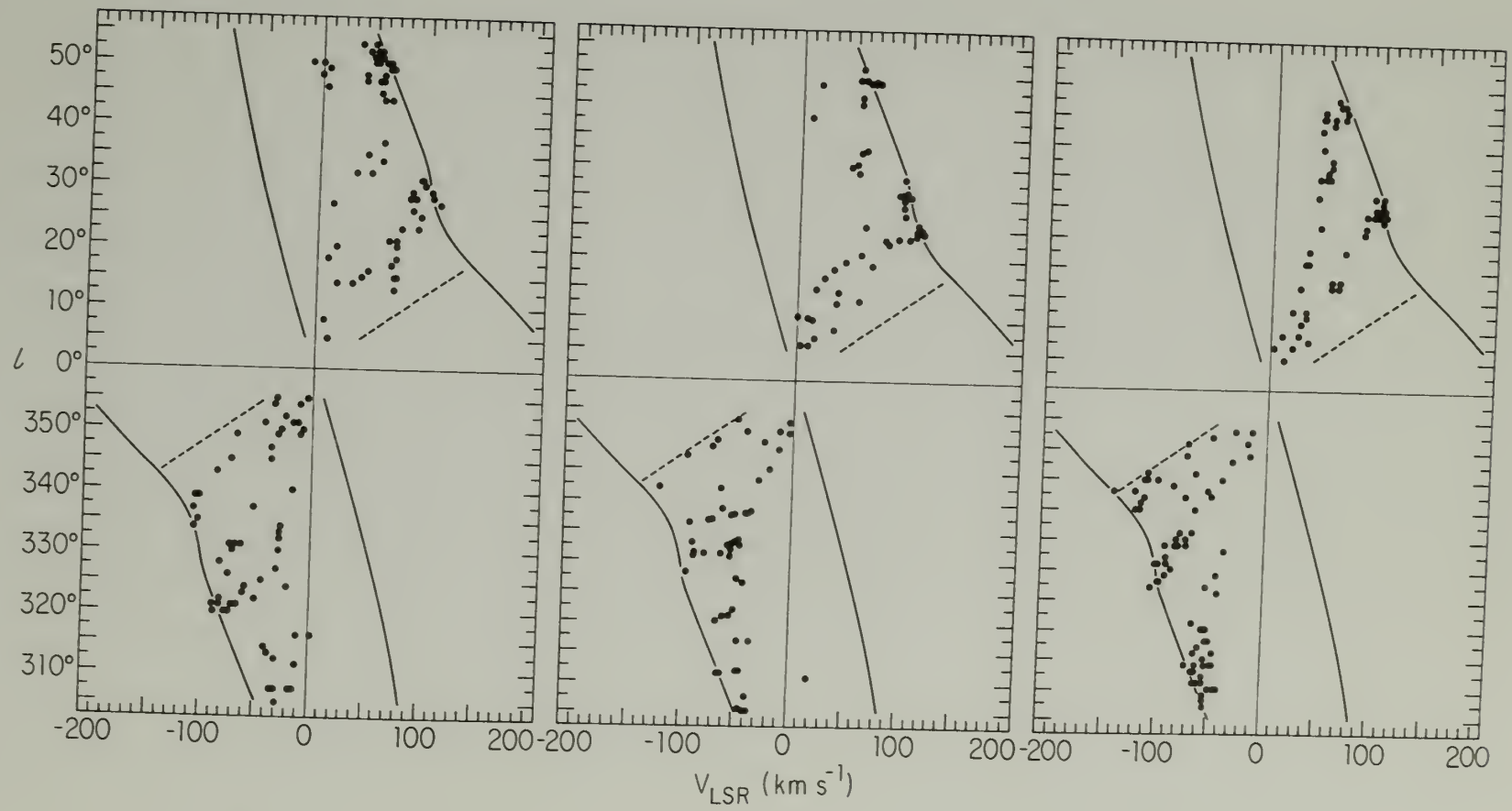

Figure 41: Left panel: model V-ℓ diagram for nebulae confined to Burton's (1971) spiral pattern. Right panel: model V-ℓ diagram for nebulae confined to a series of concentric ring segments. Center panel: Observed luminous HII regions. All models assume pure circular galactic rotation.

model galaxy contains dense HII regions (whose relative radial surface density is given by the observed value) and the remainder is empty. The actual observations are shown in the central panel of the figure.

The spiral model clearly reproduces the observed gaps along V_t in the North and produces gaps along V_t in the South. The southern model gaps do not coincide exactly with those observed, but this is not a serious problem. The adopted spiral pattern was derived entirely from northern HI observations and it itself does not fit the southern HI data very well (see §IVb). Attempts to refine the models by using a different spiral pattern were unsuccessful; there seems to be no two-armed logarithmic spiral pattern, having either a constant pitch angle or one which varies linearly in R, which fits both the northern and southern nebulae. However, a two-armed trailing pattern gives the right number of gaps along V_t and is thus sufficient to describe the observations.

The lack of an adequate pattern makes it difficult to specify a "best fit" arm width. The northern observations are matched best by models having all HII regions on the outer arm edge $< 45°$ in azimuth from the pattern center, but an extent of $< 90°$ is possible, and the models are not inconsistent with the observations if up to 25% of the nebulae are located close to the inner edge of the arms. However, there is no evidence that there are any "interarm" nebulae unconnected with the overall pattern.

A series of concentric rings is a good approximation to a small pitch-angle spiral when only one side of a galaxy is being observed.

Ring models are azimuthally symmetric and represent attempts to fit the observations by (radically) altering the radial surface density function. The right panel of Figure 41 shows a typical V-ℓ diagram that results when nebulae are confined between 3-4 kpc, 4.75-5.5 kpc and 7-8 kpc from the galactic center. The relative population of each annulus is given by the observed radial surface density function. Portions of the rings more than 14 kpc from the sun are assumed to be unobserved.

While the ring model gives gaps near the appropriate longitudes, it also gives a more regular V-ℓ pattern than is observed; and, moreover, ring models fit the observations better if the radius of the rings increases slightly from North to South, i.e., in the sense of trailing spiral arms.

The models shown in Figure 41 were generated assuming circular rotation, but adoption of linear or nonlinear density-wave kinematics does not alter the overall form of the model V-ℓ diagrams. This kinematic independence occurs because the most distinguishing feature of the various models is their behavior at the terminal velocity, i.e., near the subcentral points. There, any radial motion is projected entirely across the line of sight and does not enter the models. At the same time, the azimuthal component of density-wave "streaming" motions is rather small near the potential minimum of a spiral arm. Thus, because the best models place the HII regions near the potential minimum, projected streaming motions in even nonlinear density-wave models are comparable to the expected random motions of the nebulae.

In summary, about 300 model V-ℓ distributions have been calculated with the following results: The observed velocities and longitudes of the most luminous, dense HII regions in the inner Galaxy are not matched by axisymmetric models in which $N(R,\theta)$ is the observed $N(R)$, but are consistent with models in which nebulae are totally confined to a spiral pattern. This conclusion is independent of whether nebulae move in circular orbits or have density-wave kinematics. A spiral pattern containing two trailing arms is sufficient to describe the distribution, but the pattern does not appear to be as regular as a logarithmic spiral.

Model results are rarely unique. However, the connection between prominent kinematic features in the HII observations and large-scale galactic structure implied by the model results is supported by additional evidence. First, the adopted spiral pattern is one derived from HI kinematics and is only applied to HII regions. That the HI model fits the HII so well implies that the HII features are not selection effects, chance or local perturbations, but are connected with large-scale phenomena visible in HI. Secondly, the "gaps" in the nebular distribution along V_t begin near the "classic" tangent points of spiral arms. For example, there are distinct features in the high-energy γ-ray distribution near longitudes 310°, 330°, 345°, 35° and 55° (e.g., Stecker, 1977), very close to the positions of the "steps" in the intensity of nonthermal radiation along the plane (Mills, 1959; Wielebinski et al., 1968). These are the longitudes where nebulae are seen to the terminal velocity, and are also the approximate longitudes

of the "bumps" in the HI rotation curve (e.g., Kerr, 1969). The model results suggest that at these locations large-scale galactic features are being seen tangent to the line of sight.

Thus, there appears to be a relationship between the kinematics of the HII regions and the kinematics of HI, and between the kinematics of HII regions and changes in the emissivity of γ-rays and nonthermal radiation. These considerations suggest that the kinematics of dense ionized nebulae are, as suggested by the models, carrying information on large-scale galactic features.

h) HII Regions with Anomalous Velocity?

Approximately 20% of the luminous HII regions in the North and approximately 5% of those in the South have $|V(H109\alpha)| > |V_t|$, independent of whether V_t is derived from circular rotation or density-wave kinematics. The model calculations, using the adopted random velocity dispersion of 5 km/s, give forbidden velocities to only 8% of the objects in either longitude interval. The observations can be reconciled with the models if the northern rotation curve is raised 5 km/s relative to the southern rotation curve. This value is quite close to the observed 7 km/s difference between northern and southern HI terminal velocities (Kerr, 1969) suggesting that the discrepancies result from use of an average or otherwise incorrect rotation curve [eq. (93)] to calculate V_t. However, this explanation may not be entirely satisfactory, for some of the northern nebulae have velocities in excess of the terminal HI velocity in their vicinity. Whether this is merely a

statistical fluctuations in the random nebular motion, or is evidence of a difference in the kinematics of ionized and neutral gas, cannot be determined from the present data.

Eight nebulae have velocities that, compared with their absorption spectra, imply that the nebulae have a smaller circular velocity than given by the rotation curve at their location (or a projected component of motion which is equivalent to a reduction in circular velocity). These are listed in Table 5. The best studied is W31 (see Wilson, 1974). The components of W31 have $0 \lesssim V(HII) \lesssim 14$ km/s and $0 \lesssim V(abs) \lesssim 40$ km/s. However, $V_t \sim 150$ km/s in their direction, and thus by the criteria of §IVc these sources cannot be at their near or far kinematic distance; they are often assumed to be in the "3-kpc" expanding arm (Wilson, 1974; Caswell et al. 1975). The motion of the 3-kpc arm is so poorly understood that it is an uncritical (albeit convenient) repository for curious phenomena in the inner Galaxy. It is clear, however, that although the apparent discrepancies between recombination line and absorption velocities of northern nebulae can be removed by placing them in the 3-kpc arm, the motion of the 3-kpc arm is in the wrong sense to reconcile the measurements of southern nebulae like 338.06+0.01 and 337.92-0.47.

Recently, Greisen and Lockman (1979) have observed the 3-kpc arm in absorption against 10.16-0.35, and have argued that the W31 sources are at their far kinematic distance. They ascribe the lack of absorption near V_t to a paucity of cool clouds in the inner 4 kpc of the Galaxy and not to any anomalous motion of the nebulae. Unfortunately, if this

TABLE 5

Nebulae with Anomalous Velocity?

Source	V(H109α) (km/s)	$\lvert V(H109\alpha) - V_{max}(abs) \rvert$ (km/s)	Absorption Measurements
10.16-0.35	+ 13.9	25	HI, OH, H_2CO
10.31-0.15	+ 9.7	35	OH, H_2CO
10.63-0.39	+ 0.3	40	HI, OH, H_2CO
333.61-0.22	- 48.3	20	HI
337.92-0.47	- 40.4	20	HI
338.06+0.01	- 41.7	45	OH, H_2CO
338.43+0.05	- 36.9	40	HI, OH
348.72-1.04	- 12.0	20	HI, OH, H_2CO

hypothesis is correct, then absence of absorption at $|V| > |V(H109\alpha)|$ for any source at $\ell \lesssim 25°$ is not necessarily evidence that the source is at the near kinematic distance, for the absence could result from either the lack of clouds near the subcentral point or from the location of the nebula at its near distance.

In sum, there are no observations that unambiguously require some nebulae to have large (> 20 km/s) non-circular velocities, and if there is a single explanation for all the apparent velocity anomalies, it is not connected with the 3-kpc arm.

C H A P T E R V

THE DISTRIBUTION OF MODERATE DENSITY IONIZED GAS

a) Introduction

Dense HII regions are only one form of ionized gas found in interstellar space. The detection by Gottesman and Gordon (1970) of weak centimetric recombination lines from directions in the galactic plane apparently lacking identifiable compact continuum sources, and the subsequent work by Jackson and Kerr (1971), Gordon and Cato (1972) and Matthews et al. (1973), which established the extensive distribution of these lines over certain longitudes, indicated that there was a new species available for tracing the galactic distribution of ionized gas. The material giving rise to the lines is quite common at certain locations in the Galaxy, and thus these weak lines potentially contain more information on the detailed kinematic structure of the Galaxy than can be extracted from higher frequency lines. The source of the emission is still uncertain, although the fact that the lines are observed most easily at low frequencies, that they are found from a substantial volume of the plane and that they occur in directions where the average continuum brightness temperature is fairly low all point towards gas with an electron density of 1-100 cm^{-3}. This medium is of special interest for the study of the galactic distribution of ionized gas because to some extent it may be treated as if it were spatially continuous, and surveys can be made at positions chosen on geometric criteria rather than on the thermodynamic criteria which guided the

higher frequency surveys. (An example of a thermodynamic criterion is the existence of a discrete continuum source in a given direction.)

This chapter describes the results of a survey of distributed recombination line emission in the H166α recombination line at 1.425 GHz. The gross properties of the emission will be derived from the most straightforward analyses, and there will be some discussion regarding the origin of the emission and its relationship to the dense HII regions studied in previous sections. An independent survey of the same transition has been completed recently by Hart and Pedlar (1976) at Jodrell Bank, and their results will be used to complement the present work.

It should be emphasized that, in comparison with the dense nebulae studied in the previous chapter, our understanding of the source of H166α emission is rudimentary. There is currently no hope of deriving a distance to any element of this gas and hence the distance selection effects, the luminosity function, and other fundamental facts are unknown. The discussion in this chapter will therefore be largely restricted to a comparison of the observed properties of H166α with those of dense ionized regions and neutral gas.

b) A Description of the Survey

The main body of the survey covers galactic longitudes $358° \leq \ell \leq 50.5$ at $b = 0.0$. Over most of this range, spectra were taken every degree in longitude. Supplementary observations include four spectra taken at $b = \pm 0.5$ and eight additional spectra taken in the galactic

plane: two near $\ell = 44°$ and the remainder spaced at five degree intervals from $\ell = 100$-$125°$.

These observations provide a fairly uniform sample of the Galaxy at $b = 0.0$ over galactic radii of 2-8 kpc. The emission at $R < 2$ kpc is inadequately determined because there are only a few observations with $\ell < 10°$. The main survey does not extend beyond $\ell \sim 50°$, so the outer portion of the Galaxy ($R > 8$ kpc) is not as fully sampled as the inner portion. However, Hart and Pedlar (1976) found essentially no H166α emission between 51° and 70°; this, together with similar results from the survey by Gordon and Cato (1972) and the lack of emission at the supplementary positions over longitudes 100-125°, indicates that most H166α emission originates at $R < 9$ kpc. Thus the overall characteristics of the H166α emission can probably be determined from these observations even though longitudes greater than 50° are largely unexamined. In any case, the longitude coverage of this survey is comparable to the northern longitude interval in the sample of dense HII regions discussed in the previous chapter, and the distributions of these two species may be compared.

A fundamental limitation on the survey is the relatively coarse (approximately 1°) spacing between adjacent observations, imposed by the need for long integrations at each position. The effect of this incompleteness is examined at various stages of the analysis, and a number of tests indicate that the data are sufficient to derive reliable morphological properties of the H166α emission.

The H166α emission observed from a particular line of sight through the galactic plane will arise in different gas than, for example, the H109α emission from the same volume. From the discussion in Chapters II and III it is clear that high-frequency recombination spectra are generally dominated by emission from the most dense components of a heterogeneous medium, and lower frequency lines by less dense components. The optical depth in the continuum for ionized gas at a frequency of 1.4 GHz is greater than unity when the emission measure $E \gtrsim 25\ T_e^{1.35}\ cm^{-6}$ pc. For an electron temperature of 10^4 K and a path length of a few parsecs this condition is met when the electron density $N_e \gtrsim 10^3\ cm^{-3}$. Impact broadening, which is independent of path length and virtually independent of T_e, will significantly decrease peak H166α line temperatures when $N_e \gtrsim 1500\ cm^{-3}$. At high frequencies, where these considerations are less important, the observed spectra reflect properties of the most dense regions. At lower frequencies, the optical depth in the continuum, impact broadening, and non-LTE effects all combine to produce spectra weighted heavily by lower density gas. Furthermore, the relatively large antenna beam width of most telescopes at the H166α frequency also favors detection of extended regions more so than the H109α observations (e.g., the observations described in this chapter were made with a 21' beam in contrast to the 6' and 4' beams used for the H109α observations).

The H166α line was observed because previous studies of this and nearby transitions indicated that the recombination lines from distributed material were stronger at lower frequencies than at higher

frequencies, and the choice of a transition within the range of the NRAO 21-cm receiver gave the best combination of line strength, low system noise temperature, and overall system stability. In addition, H166α is only 5 MHz from the HI transition, so observations of both species, made with the same equipment and virtually identical antenna beam widths, could be compared. A final factor was that the galactic background emission has a fairly steep spectral index, and at frequencies much lower than 1.4 GHz it can contribute substantially to the total system temperature. The rather coarse angular resolution of most telescopes at 1.4 GHz is not a serious limitation for a survey designed to determine characteristics of the Galaxy on a large scale.

c) Equipment, Observing Procedure and Data Reduction

The main part of the survey was obtained during three observing sessions from June to August, 1975. All data were taken with the 140-ft telescope of the NRAO, which has a half-power beam width of 21 arcmin at the frequency of the H166α transition. Observations were made with two cooled parametric amplifiers located at the prime focus sampling orthogonal linear polarizations. Each amplifier had a system temperature near 55 K. Two 192-channel autocorrelation spectrometers were operated with a total bandwidth of 5 MHz each, giving a velocity resolution of 5.48 km/s and a total usable velocity coverage of > 900 km/s.

The data were taken by switching the telescope between a position in the plane and a reference position at b = $\pm$ 5-10°. To minimize the effect of ground radiation at low elevations, the reference spectra

were taken at an elevation close to that of the signal spectra. The parametric amplifiers were quite stable over time scales $\sim$ 1 hour, allowing spectra at several different signal positions to be associated with a single reference position. In general, spectra at two adjacent positions were not associated with the same reference spectrum, nor was any position in the plane always associated with the same reference position. Reference spectra compared against one another showed no evidence of line emission or instrumental features which could be mistaken for line emission.

Most directions were observed during each of the three sessions. There was no indication of variation in the spectra between June and August, and calibrations against discrete continuum sources confirmed that the properties of the telescope system remained constant to within 2% over this period.

Data were taken with the focus alternately displaced by a distance $\pm \lambda/8$ from its optimum value. While this had a negligible effect on the telescope gain, it did remove the standing waves between the receiver and the telescope structure. The final spectra showed little evidence of the sinusoidal variations associated with the standing wave phenomenon.

Every signal-reference pair (consisting typically of 10 minutes integration on signal and 15 minutes on reference) was examined before averaging, and $\sim$ 5% were rejected because of poor quality baselines of instrumental origin. The remaining data were averaged and a polynomial was fit to the extensive emission-free regions of each spectrum. In all cases the instrumental spectrum was quite smooth, and in 70% of the

spectra had a peak-to-peak deviation of $\leq$ 0.10 K from zero. This, combined with the large total velocity coverage of each receiver, insured that a minimum of uncertainty was introduced by the baseline removal process. After baseline removal the spectra were Hanning smoothed; comparison of the smoothed and unsmoothed data indicated that no statistically significant spectral features were lost as a result of the smoothing. The total integration time at each position was about 5 hours.

During the August session neutral hydrogen spectra were observed at most survey positions. These observations involved frequency switching between the HI line frequency and a reference frequency 4 MHz away. Other than frequency switching, the equipment was identical with that used in the H166α observations, and the antenna beam width was virtually the same.

The continuum temperature was measured by monitoring the change in total system temperature between signal and reference positions. While this method should be reliable, it can be somewhat sensitive to nonlinearities in the total power detectors; these nonlinearities were minimized by assuring that the input level to the detectors was identical for both signal and reference. Spectra at supplementary positions in the plane were taken during a separate observing session in November, 1974. While they could be calibrated and reduced identically to those of the main survey, during these observations reference positions were not chosen to be at elevations similar to the signal positions, and the very weak continuum temperatures were thus too uncertain to be useful.

The errors listed for the observed quantities are $\pm$ 3σ estimates and attempt to include both random and certain systematic effects where appropriate. Random noise is the major source of uncertainty in the antenna temperature of any spectral point, but the uncertainty in the total power in the line is dominated by non-random effects, principally the impossibility of determining an exact baseline level. A small systematic bias in the baseline, integrated over a typical line profile, will result in an error in the total power in the line which is orders of magnitude larger than the error formally given by the random noise. Thus the error for the total power in the line was determined by examining the sensitivity of this quantity to variations in the polynominal baseline that was removed from the observed spectrum. The resultant error estimates cover the full range of fluctuations in the line power for all reasonable baselines that could be fit to the data.

Uncertainties in the continuum measurements arise from slow variations in the system temperature between signal and reference positions and the continually changing contribution of ground radiation through spillover and sidelobes at low elevations. The latter effect can be seen most clearly in the relatively large errors for the continuum measurements around ℓ = 50°, as these longitudes were often observed at low elevation. Although these particular errors are not noise in the usual sense, the observing procedure insured that there would be no systematic bias in their magnitude or sign. Consequently these data were analyzed as if all deviations were statistical.

d) The Observed Distribution of H166α Emission

H166α emission was detected at every observed position from longitudes 4° to 44°.6. Figure 42 shows the antenna temperature vs. velocity (LSR) for some typical directions, illustrating the general characteristics and quality of the data. The observed lines are broad, weak, and often have multiple components. There is generally good agreement between the spectra obtained in this survey and those measured at the same positions and at similar transitions by other observers (Gottesman and Gordon, 1970; Gordon et al., 1972; Gordon and Cato, 1972; Matthews et al., 1973; Hart and Pedlar, 1976). The profile at $\ell = 10°$ shows emission near -120 km/s; this is identifiable as the C166α line at the velocity appropriate for carbon emission corresponding to the peak in the H166α emission. Approximately one-quarter of the spectra show possible C166α emission, usually at levels very close to the noise. The most narrow individual H166α features that could be reliably distinguished had velocity dispersions σ = 9-12 km/s. In contrast, the HI is characterized by σ = 5.5-7.5 km/s over this longitude range (e.g., Burton, 1971).

Table 6 summarizes the main body of the survey, giving the longitude, peak antenna temperature of each profile, total power in the line, and the continuum antenna temperature for each direction, as well as the integral of the antenna temperature over the positive velocity portion of the corresponding HI profile. A dash in any entry indicates that the quantity was not observed. Supplementary positions are given in Table 7.

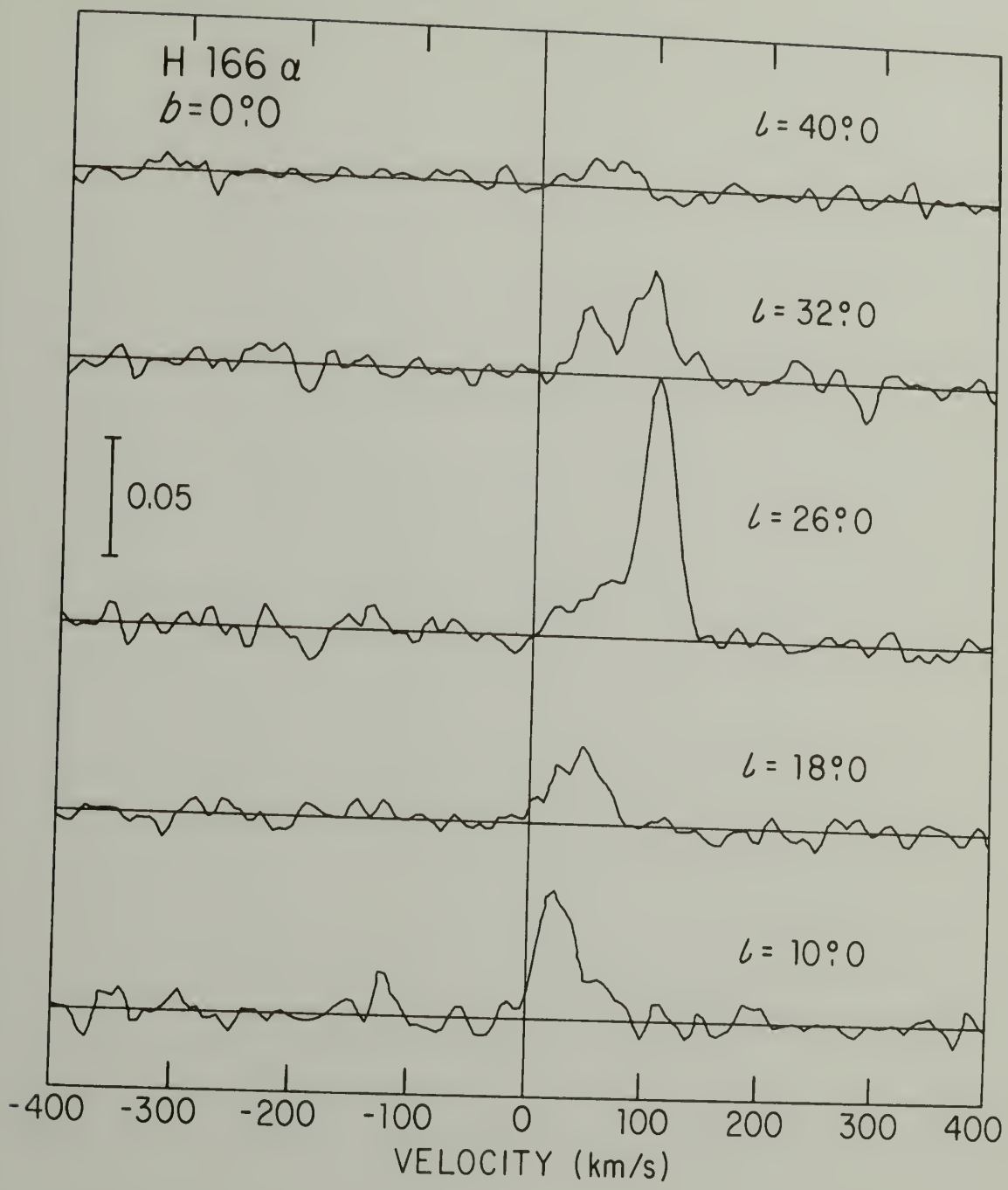

Figure 42: Examples of H166α spectra from the survey. The ordinate is antenna temperature and the abscissa is velocity with respect to the local standard of rest. The small feature at $\ell=10^{o}$, V=-120 km/s, is an example of possible C166α emission.

TABLE 6

Summary of the Main H166α Survey

ℓ	H166 T_L(peak) (mK)	H166 $\int T_L\, d\nu$ (K-kHz)	H166 T_c (K)	HI $\int_{V>0} T_L\, d\nu$ (K-MHz)
358°.0	27 ± 18	1.9 ± 0.7	13.4 ± 1.4	-
0.0	539 ± 44	210 ± 20	171.1 ±14.4	-
2.0	≤ 16	≤ 0.8	13.3 ± 1.2	15.76
4.0	45 ± 15	7.1 ± 0.6	10.0 ± 0.5	14.43
6.0	52 ± 19	9.3 ± 1.0	16.7 ± 1.2	14.75
8.0	60 ± 15	16.0 ± 0.7	13.3 ± 1.2	17.30
10.0	54 ± 14	12.3 ± 0.5	12.1 ± 0.7	20.35
12.0	58 ± 16	12.8 ± 0.4	10.9 ± 0.7	23.58
13.0	82 ± 14	20.5 ± 0.4	15.5 ± 1.2	21.68
14.0	157 ± 15	22.6 ± 0.4	14.6 ± 0.8	23.07
15.0	32 ± 13	7.9 ± 0.5	9.2 ± 0.9	24.87
16.0	51 ± 15	6.7 ± 2.4	8.9 ± 1.0	22.66
17.0	44 ± 14	13.6 ± 0.8	8.8 ± 0.8	22.47
17.5	27 ± 14	5.3 ± 0.6	8.1 ± 1.2	-
18.0	33 ± 12	6.7 ± 0.7	8.6 ± 0.6	23.22
19.0	98 ± 15	21.9 ± 0.8	12.8 ± 0.9	28.45
20.0	28 ± 14	13.0 ± 0.4	9.7 ± 0.5	28.99
21.0	43 ± 12	8.7 ± 1.4	8.3 ± 0.6	26.63
21.5	38 ± 14	9.1 ± 0.6	7.7 ± 0.6	-
22.0	38 ± 15	12.3 ± 1.5	10.4 ± 0.7	28.43
23.0	58 ± 14	15.3 ± 3.1	13.2 ± 1.0	29.66
24.0	67 ± 15	19.8 ± 1.1	11.7 ± 0.6	29.66
25.0	79 ± 14	22.2 ± 3.4	11.6 ± 1.0	24.93
26.0	112 ± 15	23.9 ± 0.5	12.0 ± 0.9	26.98
26.5	83 ± 13	22.1 ± 0.5	10.7 ± 0.7	-

Table 6 (continued)

ℓ	T_L (peak) (mK)	H166α $\int T_L \, d\nu$ (K-kHz)	T_c (K)	HI $\int_{V>0} T_L \, d\nu$ (K-MHz)
27.0	82 ± 11	18.4 ± 0.6	10.8 ± 1.3	25.64
28.0	84 ± 15	14.9 ± 0.5	8.3 ± 0.9	25.03
29.0	56 ± 13	15.9 ± 1.6	10.9 ± 0.9	28.53
30.0	228 ± 15	36.3 ± 0.4	15.2 ± 1.6	28.58
31.0	296 ± 19	69.6 ± 7.9	25.1 ± 0.9	27.87
32.0	46 ± 16	11.9 ± 0.4	9.2 ± 1.0	24.84
33.0	73 ± 13	13.5 ± 1.5	7.8 ± 1.3	24.76
34.0	50 ± 14	12.9 ± 0.4	6.7 ± 1.0	26.37
35.0	72 ± 13	13.7 ± 0.7	8.9 ± 1.0	24.36
36.0	21 ± 13	4.7 ± 2.2	5.3 ± 1.2	23.13
37.0	32 ± 12	8.9 ± 0.4	6.4 ± 0.6	24.57
38.0	72 ± 13	16.4 ± 0.7	9.0 ± 1.3	26.75
39.0	17 ± 12	5.0 ± 0.4	5.6 ± 1.5	27.04
40.0	12 ± 10	1.9 ± 1.0	4.9 ± 1.4	25.30
42.0	20 ± 13	2.7 ± 1.9	5.6 ± 2.4	22.28
44.0	23 ± 13	5.1 ± 0.6	4.5 ± 1.8	22.58
46.0	≤ 14	1.4 ± 1.4	4.1 ± 2.5	20.91
48.0	≤ 12	≤ 0.8	2.9 ± 0.8	20.11
48.5	57 ± 22	13.6 ± 0.5	6.8 ± 2.9	-
49.0	77 ± 13	15.6 ± 1.3	10.0 ± 4.2	19.96
49.5	41 ± 16	8.8 ± 2.5	6.5 ± 1.7	-
50.0	23 ± 12	1.8 ± 0.4	4.7 ± 1.4	19.24
50.5	≤ 29	≤ 0.9	3.8 ± 0.8	-
51.0	-	-	-	19.08

Errors and upper limits are ± 3σ estimates.

TABLE 7

H166α Supplementary Positions

ℓ	T_L (peak) (mK)	$\int T_L \, d\nu$ (K-kHz)
44°.2	23 ± 8	2.8 ± 1.4
44.6	11 ± 7	1.3 ± 0.4
100.0	≤ 14	≤ 1.6
105.0	≤ 16	≤ 0.4
110.0	≤ 18	≤ 0.4
115.0	≤ 16	≤ 1.8
120.0	≤ 17	≤ 1.8
125.0	≤ 17	≤ 1.3

Errors and upper limits are ± 3σ estimates.

The main body of the survey is shown in Figure 43 as contours of antenna temperature vs. velocity-longitude coordinates. Marks through the right boundary of the figure indicate the longitudes at which spectra were taken; contours are drawn every 0.01 K from 0.01 to 0.05 K, and at 0.07, 0.10, 0.15, 0.25, and 0.40 K. The lowest level contour, 0.01 K, is $\geq 2\sigma$ for 80% of the spectra.

It is apparent from this figure that H166α emission is widely distributed at positive radial velocities over this longitude range, but except for the direction of the galactic center there is no significant H166α emission at negative velocities. (Note again that some of the narrow low-level features with $V < 0$ may be attributed to C166α, specifically at longitudes 6°, 10°, 14°, 36°, and 49°). The absence of emission at negative velocities and at longitudes 100-125°, taken together with the lack of significant emission at high positive velocities for $\ell < 25°$, indicates that most H166α emission originates in the region $4 < R < 10$ kpc, that is, in the area corresponding to the location of the dense HII regions in the North.

In contrast, Figure 44 shows contours of the HI antenna temperature plotted in velocity and longitude coordinates. Marks through the right-hand border of the figure again mark the longitude of each spectrum. The relative spacing between contour levels is identical to that of Figure 43, but the intensity of the levels has been increased by a factor of 200. The HI is more extensive in both velocity and longitude than the H166α. There is a substantial amount of HI at negative velocities (corresponding to $R > 10$ kpc), and, in the lower

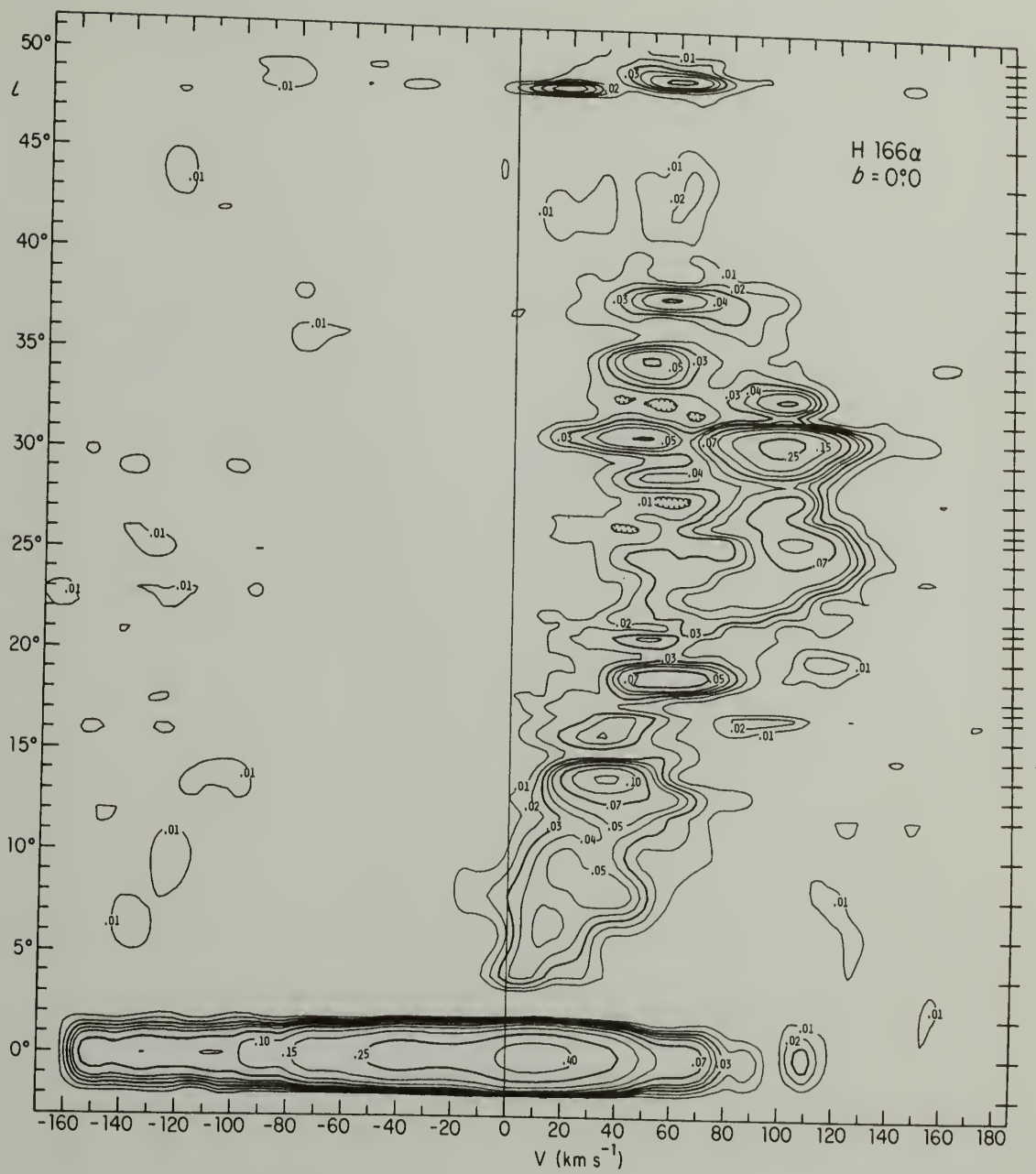

Figure 43: Distribution of H166α antenna temperature in velocity-longitude coordinates. Marks through the right hand border show the observed longitudes. The outermost contour is ≥2σ for 80% of the spectra. Some emission at V<0 km/s is attributed to the C166α line.

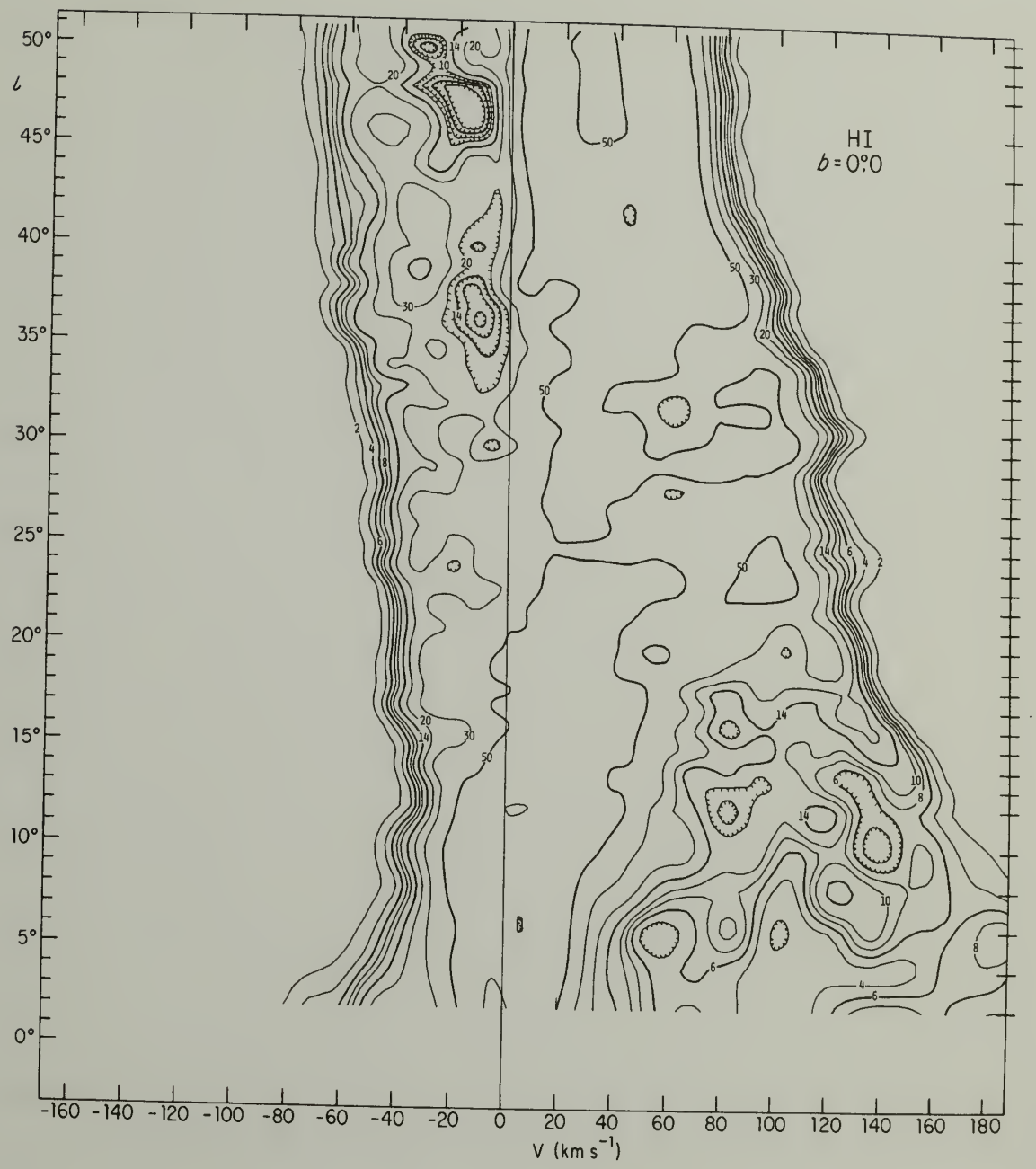

Figure 44: Distribution of HI antenna temperature. Marks through the right hand border show the observed longitudes.

longitudes, at high positive velocities. There is no obvious decrease in the intensity of HI emission at $\ell > 40°$, and the HI does not show the large changes in intensity with longitude that are evident in H166α.

Another view of the H166α emission is shown in Figure 45, where the total power in the line averaged over 3° longitude intervals is plotted against longitude. The error bars indicate the $\pm 3\sigma$ uncertainty in the average due to the uncertainty in the individual points; they do not represent the fluctuations of the points about the average. This figure clearly shows the general decrease in emission at $\ell > 35°$. The peak near $\ell = 48°$ stands out only in comparison with adjacent intervals; the power there is quite moderate. The increased power in the H166α line between longitudes 23° and 35° arises in part from a few strong lines, but also from a general increase in the level of emission at all positions. The decrease in emission at $\ell < 10°$ appears to be real, especially since there is little H166α emission at either $\ell = 358°$ or $\ell = 2°$, but these intervals are so sparsely sampled that this result should be considered tentative. If real it would be difficult to understand from purely large-scale causes, as these lines of sight cross nearly all galactic radii, and positions only 6-10° away show ample emission. Except for the peak near longitude 50°, there is little similarity between this figure and the corresponding distribution of numbers or flux densities of dense HII regions (Fig. 28). This suggests that either the selection effects involved in this survey are grossly different from the selection effects for the higher frequency surveys, or that there is no simple connection between the numbers or thermal flux

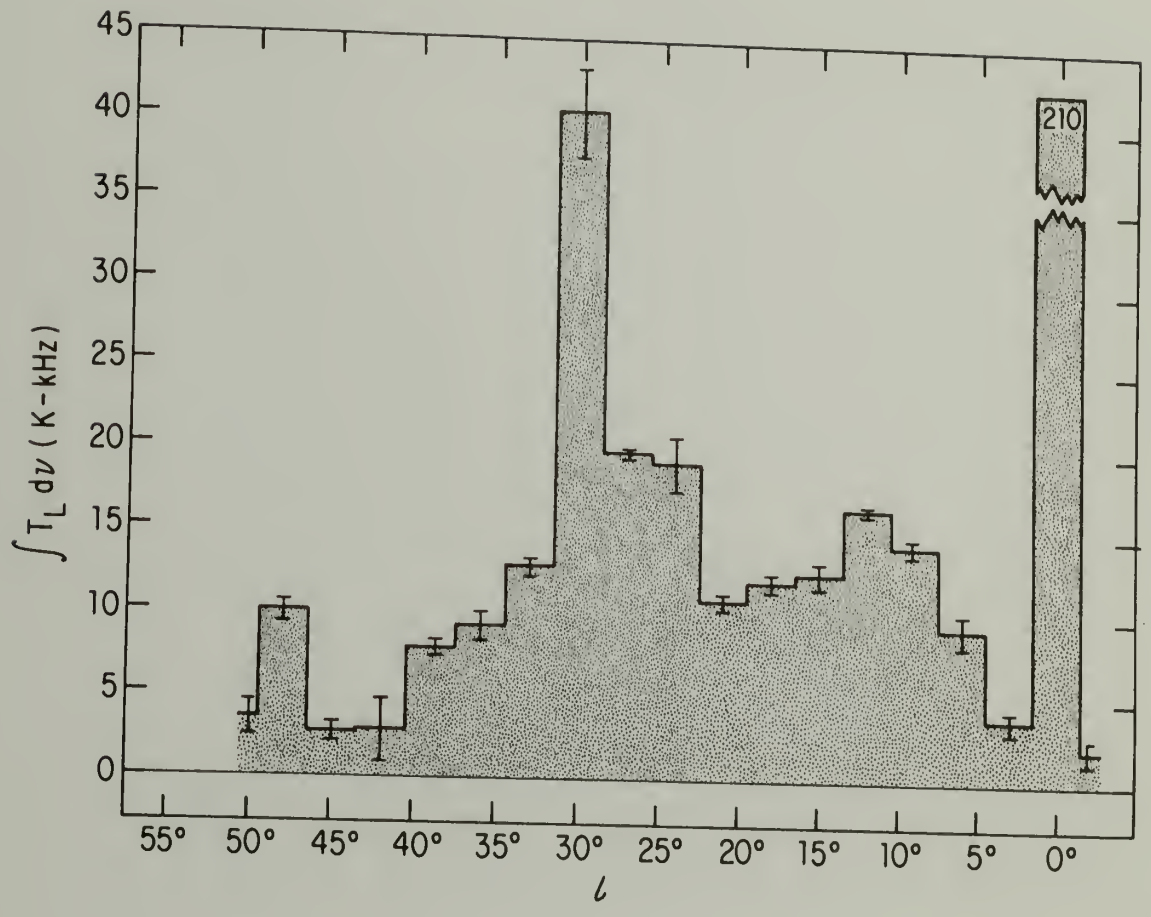

Figure 45: Total power in H166α as a function of longitude. Data are averaged over 3° intervals.

density of dense gas and the total power in the H166α emission.

Compared with H166α, the power in positive velocity HI varies much more smoothly with longitude, having maximum fluctuations of only $\sim$ 20% between adjacent positions. The general increase in the HI power from $\ell = 50°$ to $\ell \sim 20°$ and the decrease at $\ell < 20°$ result from geometric effects and the opacity of HI, and not from the details of the HI distribution (Burton, 1971; Burton et al., 1975). Unlike the H166α, the broad trend of the HI integral does not indicate large variations in abundance with position. Neutral hydrogen appears to be more widely and smoothly distributed than the ionized hydrogen sampled in the H166α observations, just as the H166α appears to be more smoothly distributed than the emission from dense HII regions.

The H166α spectrum at $\ell = 0°$, $b = 0°$, has the largest peak antenna temperature, the most power in the line, and the greatest velocity extent of any in the survey. It is all the more striking since adjacent positions at $\ell = 358°$ and $\ell = 2°$ show relatively little emission. While a discussion of the galactic nucleus is outside the scope of this work, these observations once again confirm the singular nature of this direction in the Galaxy.

Observations pertaining to the latitude structure of the H166α emission are summarized in Table 8 and shown in Figure 46. The general symmetry of the spectra about $b = 0°$ suggests that the plane defined by the H166α emission at these longitudes does not substantially deviate from the plane defined by the positive velocity HI (i.e., $b = 0°$). However, the observed mean latitude of the dense HII regions in the North

TABLE 8

H166α Observations at b = ± 0°.5

ℓ	b	T_L (mK)	$\int T_L \, d\nu$ (K-kHz)	T_c (K)
26°.5	+0°.5	43 ± 10	10.1 ± 0.6	6.3 ± 1.0
26.5	0.0*	83 ± 13	22.1 ± 0.5	10.7 ± 0.7
26.5	-0.5	52 ± 11	7.9 ± 2.0	7.0 ± 1.4
33.0	+0.5	17 ± 12	6.0 ± 1.5	4.1 ± 1.4
33.0	0.0*	73 ± 13	13.5 ± 1.5	7.8 ± 1.3
33.0	-0.5	13 ± 12	8.5 ± 2.0	4.1 ± 1.2

* Data taken from Table 6

Errors and upper limits are ± 3σ estimates.

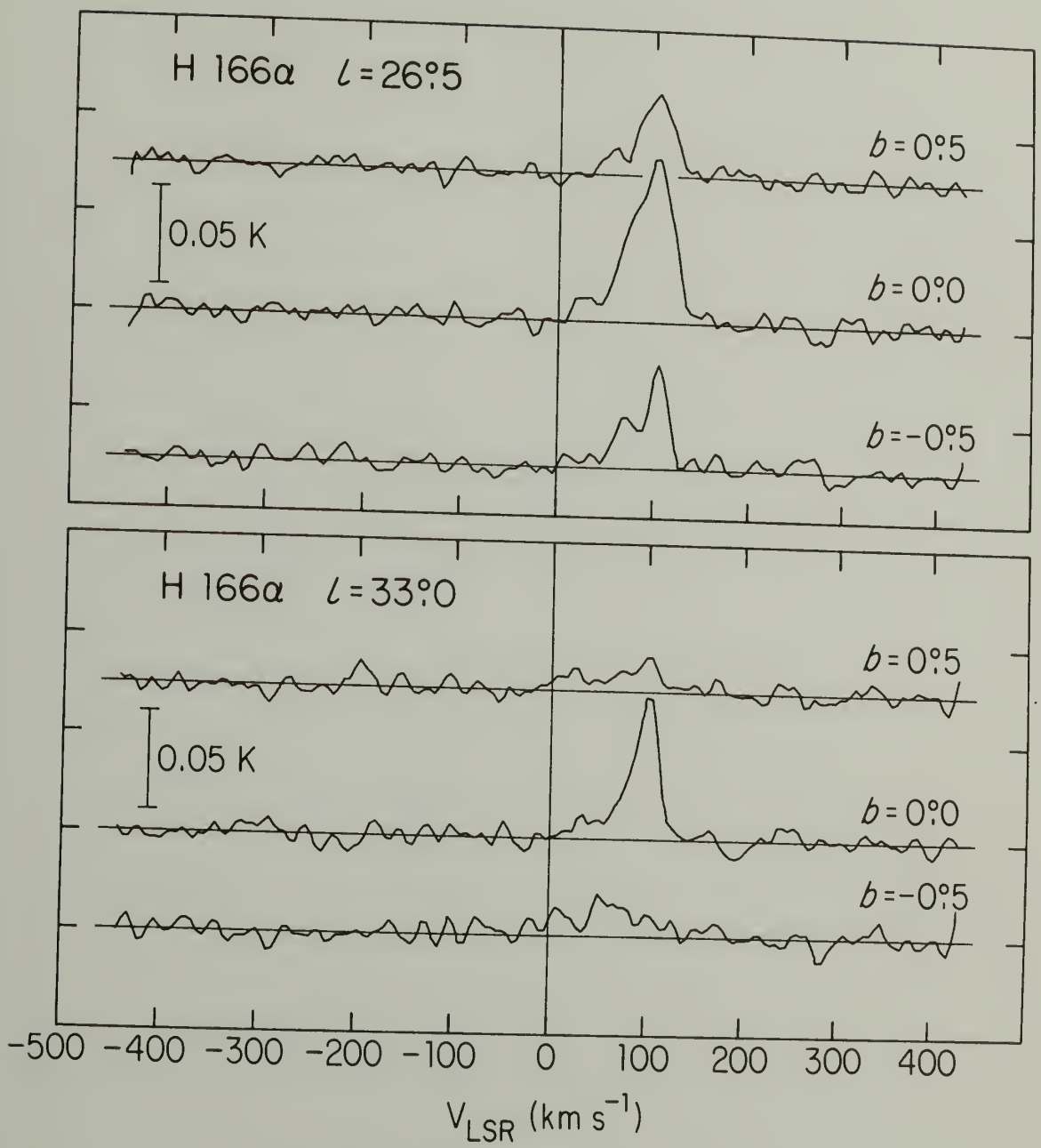

Figure 46: Variation of H166α with latitude at two longitudes.

is likewise very close to b = 0° while the HII regions themselves show a strong z(R) relationship; systematic deviations of the H166α emission, like those displayed in Figure 38 for the dense regions, would not be detectable from these few spectra.

The change in antenna temperature with latitude of the highest velocity line peak can be used to derive a scale height for the H166α emission assuming that the emission varies smoothly with latitude: at $\ell = 26.^{\circ}5$ the emission has fallen to half intensity within $\pm$ 80 pc of the plane, and at $\ell = 33°$, it has fallen to half intensity less than 40 pc from the plane. [Gordon et al. (1972) find a similar scale height at longitude 33° from measurements of H158α, and Hart and Pedlar (1976) find a value close to 80 pc at longitude 25°.] The difference in latitude structure between longitudes $26.^{\circ}5$ and 33° could be due to observation of two different types of gas. For example, if the high velocity peak at $\ell = 33°$ is formed in a relatively compact region, then the "scale height" derived for this direction will refer more to the size of that discrete region than to the overall latitude structure of the ionized gas. There is no reason to expect that all the H166α line emission arises in a smoothly distributed medium, hence it appears that a large number of measurements at many longitudes are required in order to separate local fluctuations (arising perhaps from the presence of compact dense HII regions along the line of sight) from scale height effects.

The use of terminal velocities is more appropriate for studying H166α emission than for studying dense HII regions because, to first

order, the H166α can be treated as a continuum rather than a collection of point sources. Also, because there is no reliable way to derive a distance to individual emission features, the location of the emission with respect to the subcentral point takes on special importance. Terminal velocities were calculated from the definition of Shane and Bieger-Smith (1966):

$$V_t = V_p - \frac{\Delta v}{2} + \frac{\Delta v}{T_p} \sum_{V_p}^{\infty} T_a(V), \qquad (97)$$

where V_t is the terminal velocity, V_p is the central velocity of the highest velocity peak in the profile, Δv is the width of a channel and T_p is the antenna temperature at V_p. This method gives a measure of V_t which is independent of T_p, but the resultant V_t will increase with an increased velocity dispersion of a profile. Because $\sigma(\text{H166}\alpha) > \sigma(\text{HI})$ this implies that V_t (H166α) will be greater than V_t(HI) (when both species are at the subcentral point) by an amount roughly equal to $\sigma(\text{H166}\alpha) - \sigma(\text{HI})$, or 2 to 7 km/s. The "highest velocity peak" in the H166α was required to have an antenna temperature greater than or equal to 0.015 K, a value which is $\geq 3\sigma$ for 80% of the spectra in the survey. In two directions (ℓ = 40°.0, 44°.6) the peak line temperatures were less than this amount but because these spectra had $3\sigma < 0.010$ K the requirement was relaxed. It should be mentioned that this method of determining a terminal velocity is rather insensitive to most minor problems of residual instrumental baseline in the spectra. The method's reliance on a peak in the emission deemphasizes the effects of low intensity wings of possibly instrumental origin.

Figure 47 compares the terminal velocities of the H166α lines with those of HI. The terminal velocities derived from the HI emission profiles are consistent with those derived by Burton (1970) from observations made with higher velocity resolution but lower angular resolution. The general behavior of the H166α terminal velocities resembles that of dense HII regions. At longitudes less than 23°, H166α terminal velocities are generally less than those of HI, consistent with the behavior of a medium whose abundance decreases sharply interior to a galactocentric radius of 4 kpc. Between longitudes 23° and 34° the H166α terminal velocity is generally greater than the HI terminal velocity, indicating that material is present along the entire locus of subcentral points from R = 4.1 to 5.6 kpc; this is also the qualitative behavior of the dense HII regions in this area. Finally, at longitudes greater than 35° the H166α terminal velocities generally fall below those of HI except for positions near 50° longitude. This is the area of the "gap" in the distribution of dense HII regions, and to some extent it also appears in the H166α emission, in the sense that the H166α emission seldom extends to the maximum permitted velocity. The dense HII regions never extend to the maximum permitted velocity in this longitude interval.

The maximum value of V_t (H166α) - V_t (HI) is of order 13 km/s, and occurs near longitudes 25° and 49°. This is a slightly larger velocity difference than would be expected from the difference in dispersion between the two species or from errors in the determination of V_t. Thus

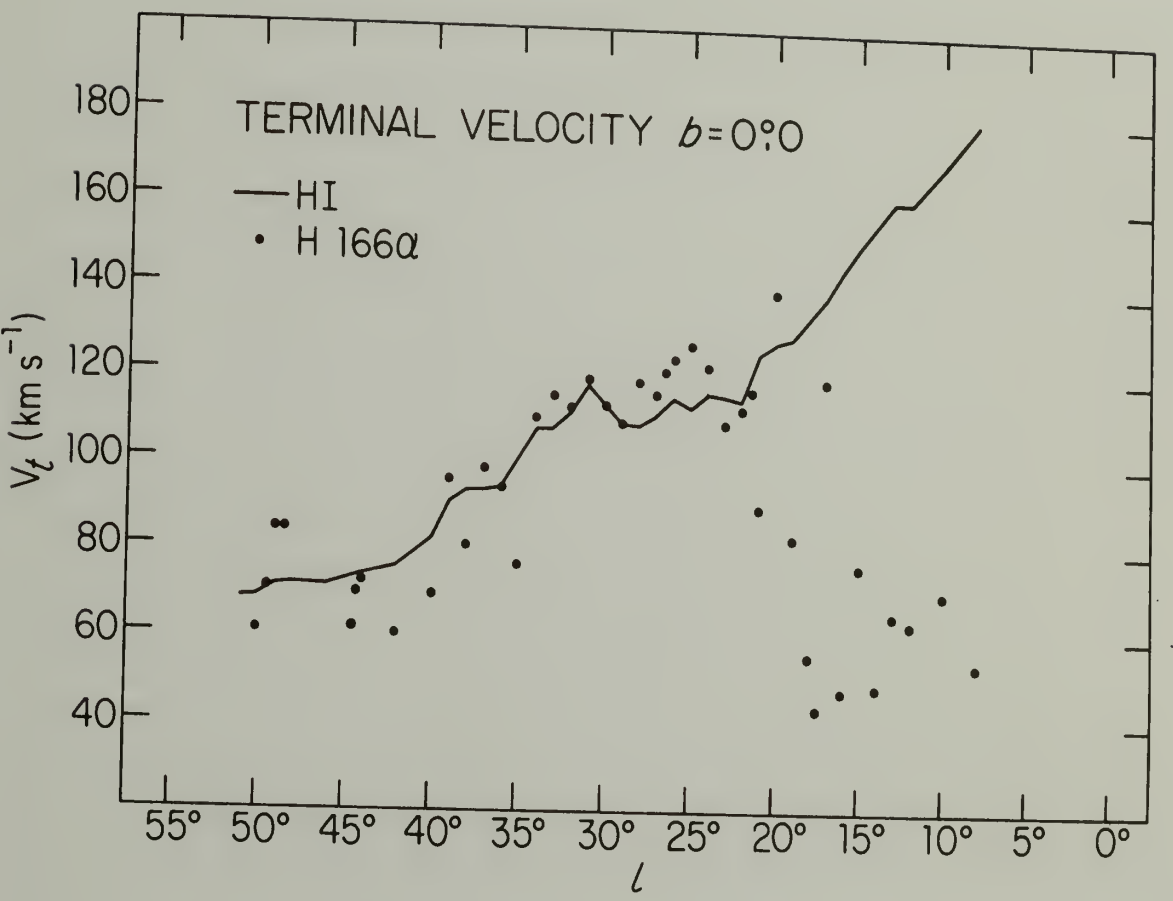

Figure 47: Terminal velocities, V_t, as a function of longitude for HI (solid line) and H166α (dots).

the H166α emission appears to show the same type of excess circular velocity found in the emission from more dense HII regions at similar longitudes, but the HI does not share this motion.

e) The Overall Distribution of H166α: Comparison with HI and H109α

The procedure for determining the radial distribution of a continuous or extended medium is not as straightforward as that used for objects that can be treated as point sources. The radial distribution of the H166α line is determined by associating the emission from each channel of velocity V_i with a galactocentric radius R_i based on a galactic rotation curve. In order to account for the projection of the galactic velocity field along a line of sight the emission must be weighted by the quantity $\Delta v/\Delta r_i$, where Δv is a channel width and Δr_i is the distance through the Galaxy which will contribute emission in the velocity range $V_i \pm \Delta v/2$. Since $\Delta v/\Delta r_i$ is the inverse of the relative probability of finding emission within $V_i \pm \Delta v/2$ in a constant surface density galaxy, multiplying T_A by this quantity effectively assigns low weight to highly probable velocities (e.g., those near V_t) and higher weight to less probable velocities. This procedure corrects for velocity crowding. The radial distribution of H166α and HI will be expressed as an average power in the line per kpc in units of K-km/s.

It is worthwhile to consider the difference between the quantity $T_A\ \Delta v/\Delta r$ and the surface density derived for dense HII regions. The implicit assumption is that the power in H166α is independent of antenna

beam width, so the only factor determining line intensities is the distance traversed through a given annulus and the power in the line produced within that annulus per unit distance. This is the most reasonable way to attempt a radial deconvolution of the data, but this method is much more sensitive to the thermodynamic properties of the gas than the method of determining radial distributions by counting objects. If there are large-scale radial changes in the temperature or density of the gas producing H166α emission, then the resultant radial distribution may be extremely misleading, and in any case the considerations of line formation and transfer discussed in the first three chapters indicate that the power in a given line may not be simply related to the amount of material present. The same comments hold for the interpretation of HI, with the exception that the radiative transfer of HI is comparatively straightforward and any thermodynamic distortions in the radial distribution will be less severe. With the exception of some preliminary work by Burton (1979), the question of thermodynamic influences on the apparent radial distributions of various species has not been treated to any depth. In this chapter, the analyses are based solely on antenna temperatures, and the results reflect actual distributions of matter only through the (perhaps unknown) relationships between density and antenna temperature. Within these uncertainties, the quantity $\langle T_A \, \Delta v/\Delta r_i \rangle$ is proportional to a surface density for emission evenly distributed across an antenna beam.

This approach to deriving a radial distribution requires the assumption of a circular galactic velocity field so that each V_i will be

associated with a unique R_i; the standard circular model described by eq. (93) was used with the quantity R' set equal to 5.0 kpc instead of 5.5 kpc in order to better match the derivatives of two expressions for the rotation curve. Longitudes less than 4°, where the analysis is very sensitive to the dispersion of the profiles because of severe velocity crowding over a substantial portion of the line of sight, were omitted from the calculation. Although there is some H166α emission at forbidden velocities, i.e., at velocities which are higher than the maximum permitted by the rotation curve, the antenna temperatures at these velocities are usually small and have been ignored.

The sensitivity of the radial distribution to the incompleteness of the survey, or to the presence of a few localized strong features was estimated by calculating the distribution for ten subsets of the data. A few of these are shown in Figure 48, where the solid line results from all data with $4° \leq \ell \leq 50.5$, the dotted line from data only at even longitudes (approximately one-half the total number of spectra), and the crosses from all spectra except those containing the strong lines at longitudes 30° and 31°.

The radial distribution can be very dependent on the exact form of the rotation curve in areas of high $\Delta v/\Delta r$. In particular, the portion of the Galaxy at R < 5 kpc (which is observed along lines of sight at $\ell < 30$) will have substantially higher values of $\Delta v/\Delta r$ than elsewhere (see Fig. 25). To examine the dependence of the derived radial distribution function on the exact form of the rotation curve an analysis was performed with the quantity R' in eq. (93) set equal to zero. This gives

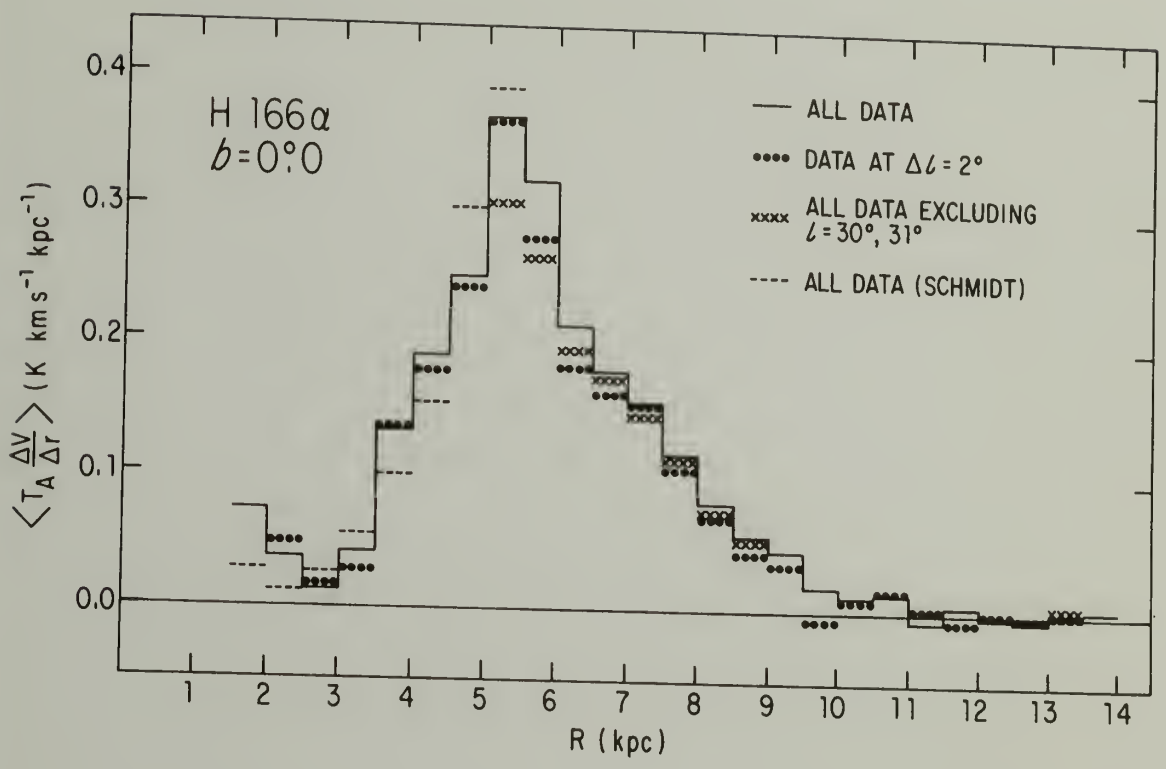

Figure 48: The power in the H166α line, per kpc, vs. galactocentric radius for various subsets of the survey. Dots show the distribution at even longitudes, crosses show the distribution when the strong features at ℓ=30° and 31° are omitted, and the dashed line shows the effect of using a rotation curve like Schmidt's at R>3 kpc, but which falls somewhat below that of Schmidt at lower radii.

a galactic rotation curve much like that of Schmidt (1965) for R > 3 kpc, and one which falls below Schmidt's at smaller radii. The difference between the solid and dashed lines gives an indication of the sensitivity of the radial distribution to the rotation curve at $R \leq 5$ kpc.

Despite the numerous small changes in the amplitude and shape of the radial distribution with the varying sample, its overall form remains constant and the peak occurs in the interval 5-5.5 kpc for all subsets of the observations.

When all the data are considered, between 50 and 75 channels contribute to each annulus with R > 2.5 kpc. This large number of measurements insures that the apparent radial distribution cannot be greatly altered by the addition of a few more observations. The modest change caused by the inclusion or exclusion of the very strong emission at $\ell = 30°$ and 31° is a specific example. In addition, the radial distribution derived from half the data is substantially the same as that derived from all the data, suggesting that the full survey is complete enough to give an accurate determination of this quantity over the observed longitude interval.

The average power in the H166α line per kiloparsec is shown in Figure 49, where the error bars cover all estimates of $\langle T_A \, \Delta v/\Delta r \rangle$ determined from variations in the total sample as well as the variation of the rotation curve at $R \leq 5$ kpc. Error bars for annuli with R > 10 kpc also cover changes caused by including observations at longitudes 100-125° in the analysis. Radii less than 1.5 kpc were inadequately

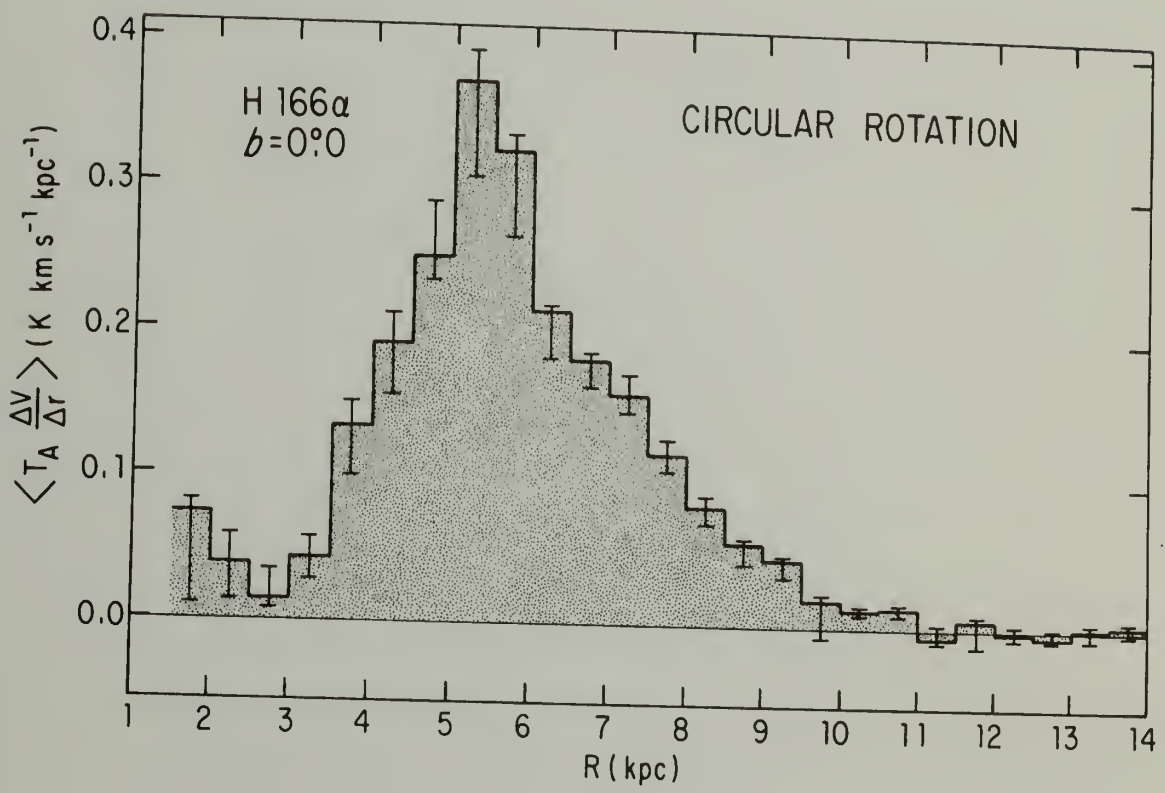

Figure 49: The power in the H166α line, per kpc, vs. galactocentric radius.

sampled and are not included in the figure, and the analysis was terminated at R = 14 kpc so that C166α emission would not be mistakenly included as negative velocity H166α emission.

The power in H166α increases sharply from 3.5-6 kpc, with the mean of the overall distribution occurring near 5.5 kpc, virtually coincident with the peak. The power falls sharply within a kiloparsec of the peak: 50% of the emission arises between 4 and 6 kpc. The actual distribution will be even more compact than suggested by Figure 49, because the dispersion of the profiles will sometimes cause emission actually arising in one annulus to be associated with another nearby annulus. Thus while Figure 49 indicates that there is no significant emission for R > 11 kpc, the actual outer boundary of H166α is probably $\sim$ 8 kpc. The lower value would also be consistent with the absence of significant H166α emission between longitudes 51° and 70° (Hart and Pedlar, 1976). The exact increase in H166α interior to 2.5 kpc depends very much on the form of the rotation curve in this region but the power is nontheless greater than zero. This is not likely to be entirely due to dispersion from lines originating at larger radii, because the extent of the "spillover" into nearby annuli due to dispersion is proportional to $(\Delta v/\Delta r)^{-1}$, a quantity which is generally small for small radii at low longitudes. Thus the decrease in H166α emission at R < 3.5 kpc is sharp, but not total.

The average power in HI per kiloparsec was derived from the HI spectra shown in Figure 44, and in Figure 50 the HI (drawn in a light line) and the H166α (drawn in a heavy line) are compared. Note that the

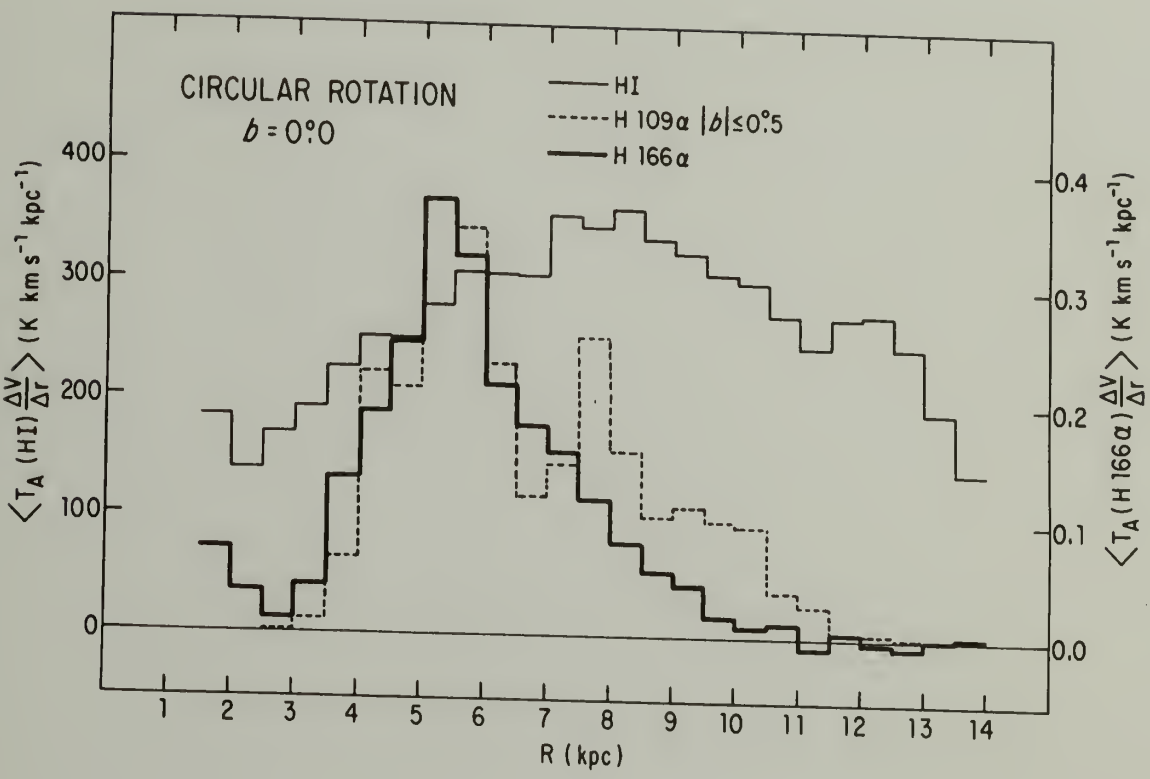

Figure 50: The abundance of H166α (heavy line), HI (light line) and H109α (dashed line) as a function of distance from the galactic center. The ordinate of H166α and HI gives the power in the line per kiloparsec. The use of composite spectra to produce the H109α curve (see text) makes its scale somewhat arbitrary, but its relative shape is accurate.

HI distribution is derived only from observations at $\ell \leq 51°$, and it differs, especially at large radii, from other such figures incorporating data from a wider longitude range. The HI power in this figure remains rather constant from radii 5-12 kpc and, compared with the H166α, decreases less abruptly interior to 5 kpc. It is apparent that the power in H166α is not related to that in HI in any simple way, implying that the source of ionization must be distributed somewhat like the H166α emission.

The distribution of dense HII regions of the type considered in the previous chapter can be displayed in velocity-longitude coordinates for comparison with HI and H166α. For this purpose the antenna temperature in H109α is a more fundamental quantity than the number or flux density of HII regions because the antenna temperature in the line is the quantity which is observed in H166α and HI, and these latter observations cannot be easily transformed into counts of objects.

For an accurate comparison the sample of HII regions was restricted to those lying within the boundaries of the H166α survey. Table 2 shows that there are 54 dense HII regions within the area ℓ = 5-51°, $|b| \leq 0.^{\circ}5$. All relevant nebulae from Table 2 have been used for this comparison, even those which for various reasons were not included in the kinematic analysis in Chapter IV. Also included are two objects from Reifenstein et al. (1970) which have $\ell < 5°$ and thus do not appear in Table 2. Whiteoak and Gardner (1974) give the continuum temperatures but not the intensities or half-widths of the lines they observed from seven of the nebulae in this sample, so it was assumed that these sources

had a Δv of 27.5 km/s and a T_L/T_c of 5%. These values are typical of H109α observations and allow this data to be incorporated into the analysis, although with some uncertainty. The results, however, depend very little on the exact properties of these nebulae as long as they do not have uncommonly large T_L/T_c ratios.

In order to display the H109α emission in a form compatible with the H166α and HI emission, the observed H109α Gaussian line profiles were added together over 1° intervals of longitude. The resulting composite spectrum at each longitude contains all the H109α emission from a one square degree area centered at that longitude. The use of composite spectra allows data to be analyzed as a series of equally spaced observations, and shows the absence as well as the presence of H109α.

Figure 51 shows the composite spectra displayed as contours of antenna temperature vs. velocity-longitude coordinates. Whereas H166α is found at all longitudes from 4 to $\sim$ 44°, there are many 1° intervals in which no dense HII regions have been detected. In addition, H109α emission is relatively more intense at the higher longitudes ($\ell > 35°$) than the H166α emission. The terminal velocities of this set of H109α observations were calculated and show much the same distribution with respect to V_t (HI) as the H166α: both recombination lines have terminal velocities in excess of the HI velocities near longitudes 25° and 49°, and there may even be a suggestion in Figure 51 of the high velocity ripple at ℓ = 25-30° seen in the HI and H166α contours.

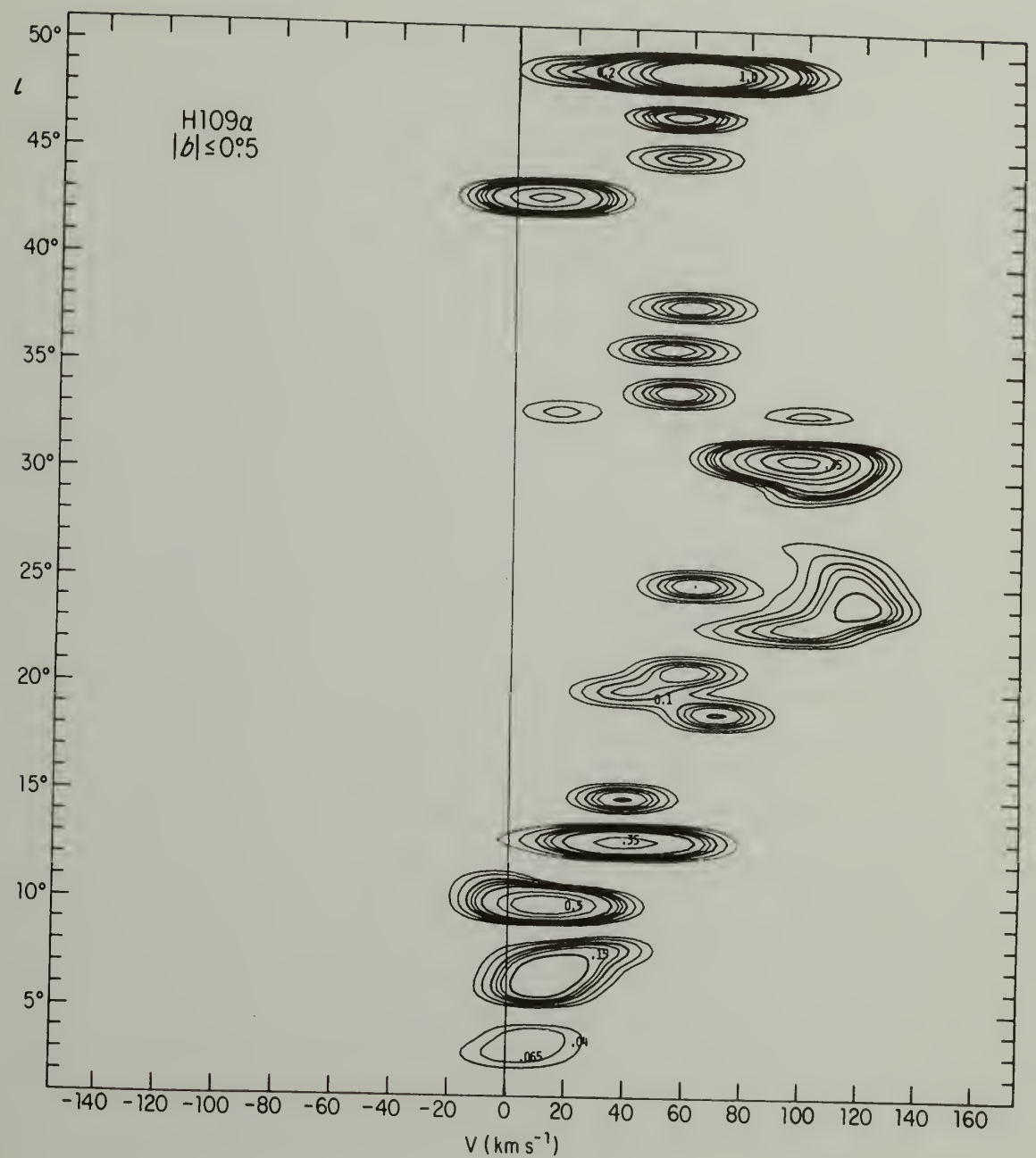

Figure 51: A velocity-longitude map in the H109α line for sources with $|b| \leq 0°.5$.

Most of the H109α emission lies within the boundaries of the H166α velocity-longitude distribution, indicating that, to first order, both species lie at similar radii in the Galaxy. This is seen in more detail in Figure 50, where the radial distribution of this sample of H109α emission derived from the composite spectra (dashed line) is compared with that of HI and H166α. The use of composite spectra makes the absolute scale assigned to the vertical axis of the H109α data somewhat arbitrary, but the relative shape of the distribution is accurate.

In the case of the H109α emission it is possible to examine the effects of velocity dispersion on the radial diagram, since all of the H109α line width arises internally in the HII region. Additional composite spectra were therefore calculated from the Gaussian profiles with the intensity appropriate to each H109α observation, but with a small uniform dispersion of σ = 3 km/s instead of the typically observed value of σ = 11-15 km/s. The "undispersed" distribution is quite similar to the "dispersed" distribution of Figure 50, the major differences being a total lack of H109α at R < 4 and R > 10 kpc, and an enhancement of the peaks at R $\sim$ 5.5, R $\sim$ 7.5 and R $\sim$ 9.5 kpc at the expense of the intervals R = 6.5-7 and R = 8-9 kpc which contained very little emission. (In this regard note that the general effect of dispersion at these longitudes is more pronounced at large radii than at small radii. This reinforces the conclusion that H166α is indeed present at R < 4 kpc but may be even less abundant at R > 8 kpc than Figure 48 suggests.) For the comparison of H109α with HI and H166α,

the "dispersed" radial distribution is sufficiently accurate, especially since there is no straightforward way to correct the latter two species for the effects of dispersion.

While the location of the peak and overall shape of the H109α radial distribution is similar to H166α, H109α is less abundant than H166α at R < 4 kpc and more abundant at R > 7 kpc. These differences are probably real. With regard to the inner parts of the Galaxy, the H109α surveys had the sensitivity to detect dense HII regions at R < 4 kpc. In the outer parts of the Galaxy, the H109α observations are biased in favor of nearby (R > 7 kpc) nebulae, but this bias should also appear in the H166α unless there is very little low density ionized gas associated with these particular HII regions. Also, to restate a previous conclusion, the number of points which determine the radial distribution of H166α is so large that a few additional H166α observations, even in directions toward known HII regions with R > 7 kpc, will scarcely change the overall shape of the curve.

It can be seen from Figure 50 that the three species change in fundamentally different fashion over the Galaxy. Their relative distribution suggests the following overall morphology of neutral atomic and ionized hydrogen in this longitude range: interior to 4 kpc (except for the galactic nucleus) there is a small amount of low to moderate density ionized gas, there is HI with an abundance roughly 2-5 times less than that at larger radii, and there are no dense HII regions. Near R $\sim$ 4 kpc, where the HI shows a modest increase, dense HII regions begin to appear and the amount of less dense ionized gas sharply rises, with

both types of ionized gas reaching a peak near 5.5 kpc. Beyond 6 kpc the amount of low to moderate density ionized gas decreases rapidly, while emission from dense regions decreases more slowly, and the amount of neutral hydrogen remains nearly constant. The ionized gas seen in H166α is confined more to the inner parts of the Galaxy than either HI or dense HII regions, and, as can be seen in the velocity-longitude diagrams, it occupies a larger surface area (and presumably volume) of the Galaxy than the dense HII regions.

A prominent feature of the distribution of dense HII regions in the North is the "gap" along V_t between longitudes 35° and 45°; this gap provides the most direct evidence of an ordered distribution of dense nebulae. Is there a similar gap in H166α? Unfortunately, there can be no conclusive answer to this question at present. In Figure 43 we can see that the velocity of the peaks in H166α does decrease from $\sim$ 100 km/s at longitude 33° to $\sim$50 km/s at longitude 35°, but there is nonetheless a low level (2-3σ) ridge of emission extending to V_t over at least longitudes 34°-39°. The investigation is hampered by the fact that the overall level of H166α emission is falling rapidly with increasing longitude at these positions, and the presence or absence of a gap must be decided from extremely weak features. The analysis of terminal velocities showed that at $\ell \geq 35°$ the H166α V_t generally fell below that of HI, although not at longitudes 36°, 37°, and 39° owing to the weak ridge of emission. At the least, the bulk of H166α emission lies at substantially lower velocities than would be expected from a medium with a smooth azimuthal distribution, whereas it is consistent

with a medium largely confined to a spiral arm. Whether the H166α emission is in fact distributed like a medium totally confined to the vicinity of a spiral arm remains to be determined through further observations of the critical longitudes. The possibility that baseline uncertainty is producing the weak (∿ 0.01 K) broad features cannot be ruled out.

f) Origin of the H166α Emission

At least two known forms of ionized hydrogen will contribute to the observed H166α profiles if they fill a significant portion of the antenna beam. These are the outer parts of dense HII regions where N_e has fallen to moderate levels, and low density HII regions such as the Rosette nebula. But a line of sight through the galactic plane may intersect a number of nebulae with possible fluctuations in T_e and N_e of many orders of magnitude. To derive the thermodynamic structure of the objects producing the H166α emission at a given velocity, a form of eq. (61) must be solved:

$$T_L(V) \simeq \sum \tau_L^*(i,V) \{T_e(i) - T_0(i)\beta(i)\} \qquad (98)$$

(Dupree and Goldberg, 1969) where τ_L^* is the LTE optical depth in the line (including the departure coefficient) for region i at velocity V, T_e is the electron temperature in the region, and β takes into account emission stimulated by the total background continuum T_0. For simplicity, the medium has been approximated by a series of optically thin, isothermal, homogeneous plane-parallel regions. The background continuum

may contain emission from unresolved dense HII regions or supernova remnants as well as a more distributed nonthermal and possibly thermal component. The approximations are certainly invalid in some directions where the optical depth in the continuum at 1.4 GHz is not negligible.

From the formulation of eq. (98) it is clear that, even when T_0 is quite small, there are a large number of variables to be considered and, in a varied environment like the interstellar medium, there is no reason to expect that the thermodynamic structure alone one line of sight is necessarily similar to that along any other line of sight. A specific observational example of this variety is given by the differing forms of the latitude scans at $\ell = 26.^{\circ}5$ and $\ell = 33°$. When effects of the background continuum become important, terms in eq. (98) that are normally negligible may dominate the expression, because $\tau_L^* T_e$ and $\tau_L^* \beta T_0$ have very different dependencies on temperature and density. An extreme example of this situation is given by the 18 and 21 cm recombination lines seen towards the intense continuum at the galactic center, where stimulated emission in a small amount of cold ionized gas dominates the line profiles to the extent that hot ionized gas is not observed (Lockman and Gordon, 1973; Brown and Balick, 1973). This is of course an extreme example, but it illustrates the possible complexity of the problem.

Multifrequency measurements are essential to provide an adequate thermodynamic description of the line emitting medium, for the lesson of Chapter III is that serious problems may result from attempts to derive meaningful physical parameters given limited data. Some preliminary

work in this direction has been carried out by Jackson and Kerr (1975) at H109α, but until there is an extensive body of data at many transitions it is not feasible to attempt to derive physical parameters for the ionized gas seen in H166α. However, some insight into the origin of the H166α emission may be gained by comparing it with the ionized gas observed in nearby galaxies.

Monnet (1971) has divided the ionized hydrogen seen in external spiral galaxies into the following four classes: I) small condensed HII regions; II) diffuse emission in the arms surrounding and connecting the HII regions; III) very faint diffuse emission extending over the entire disk of some galaxies; and IV) ionized gas in the nuclear region. Only the first two classes are relevant to the H166α observations, because emission from III would be extremely weak, and the nuclear region is not considered here.

It is important to note that the "small condensed HII regions" of Monnet's Class I are very different from the galactic HII regions seen in the H109α line. In fact, compact regions of the type seen in H109α are rarely observed in nearby galaxies. Extragalactic HII regions are relatively large, low surface-brightness objects with diameters $\sim$ 50-100 pc and emission measures of 10^{3-4} cm^{-6} pc (see, e.g., Searle, 1971; Tully, 1972; Boulestiex et al., 1974; Israel and van der Kruit, 1974). In contrast, the galactic HII regions seen in the H109α line have diameters typically < 10 pc and relatively high emission measures. [The actual H109α emission measures are uncertain, but the trend of the LTE electron temperatures derived from the H109α

lines and the generally low ratio H137β/H109α observed by Gardner et al. (1970b) indicates that there is a significant non-LTE enhancement of many H109α lines. Enhancement occurs in a gas with a typical continuum opacity $\tau_c > 10^{-3}$ or, in a 10000 K nebula, when $E > 10^5$ cm^{-3}.] The H166α emission however could arise in just the type of gas which produces the Hα observed in other galaxies: large concentrations of moderate density ionized hydrogen. A cloud of ionized gas with T_e = 10000 K, an electron density of 5 cm^{-3} and a line of sight extent of 100 pc will produce an H166α line with a peak antenna temperature of order 0.04 K, quite like that typically observed. The emission measure through this cloud would be $10^{3.4}$ cm^{-6} pc.

In addition, the average radial distribution of HII regions in a sample of galaxies shows a roughly exponential decrease in the number of HII regions outward from the peak of the distribution (Hodge, 1969). This resembles the radial distribution of H166α more than that of H109α (see also the surface density diagrams in Chapter IV and those in Mezger, 1970), but it should be noted that some individual galaxies have distributions quite different from this "characteristic" average. This is not to suggest that there is a fundamental difference between extragalactic and galactic HII regions; it is more likely that the galactic H109α emission relates to small dense concentrations that, because of their relative angular size or obscuration by dust, are not prominent in the larger regions sampled by Hα observations of nearby galaxies. Some H166α might be expected from gas in Monnet's Class II,

but this is probably very low density material ($N_e \lesssim 1$ cm^{-3}), and until its properties are better known its importance is difficult to assess.

It would be very interesting to have more information on the connection between the gas seen in H166α and that seen in H109α. Both have similar kinematics and gross radial distributions, but whether the lower density gas is the result of ionization over a large area by, for example, the proximity of many young stellar associations, or is the later stage of evolution of dense regions cannot be determined without more observations and a better understanding of the details of star formation.

g) Summary: On the Distribution of Ionized Gas and Star Formation in the Galaxy

Scale-height

In one of the series of papers that led to the redefinition of the galactic coordinate system, Gum, Kerr and Westerhout (1960) noted that the layer of HI in the inner Galaxy had a small amount of residual "waviness" with respect to the newly defined plane. The deviations were estimated to have an amplitude in the z direction of order 20 pc, and they appeared to be a phenomenon quite different from the larger-scale "hat brim" effect (a bending of the mean HI layer to $z \sim 1$ kpc at large galactic radii). The smaller-scale HI structure has been described extensively by Quiroga (1974), and Nelson (1976) has suggested that it might result from perturbations of the differentially rotating gas layer. More recently, measurements of the mean z of molecular clouds

observed in CO emission (Scoville et al., 1977; Cohen and Thaddeus, 1977) suggest that the layer of molecular clouds is also displaced from z = 0 in certain parts of the inner galaxy. Supernova remnants have a z(R) relationship that is, within the uncertainties, consistent with that of the CO (Lockman, 1977); and OH/IR stars also have a z(R) distribution like that of the other species (Bowers, 1978). Thus the pattern in $\langle z \rangle$ seen in dense HII regions is not unique, except in the facts that it is so well defined and that it was derived from northern and southern data. This last point is by no means insignificant, for the constancy of $\langle z(R) \rangle$ over the northern and southern longitude intervals allows us to estimate that the deviations from z = 0 at any R, persist for $\gtrsim$ 5 kpc around the Galaxy and are thus truly large-scale features.

A complete description of the z(R) phenomenon is given elsewhere (Lockman, 1977). Here it is discussed only in relation to questions about the galactic potential in the z-direction and about the sequence of star formation.

The galactic species that can be observed at large distances from the sun, together with their characteristic lifetimes and z-dispersions, are:

Dense HII Regions:	$t \gtrsim 10^6$ y.	σ_z = 30 pc,
Molecular Clouds:	$t \sim 3\times10^7 \rightarrow > 10^8$ y.	σ_z = 50 pc,
Supernova Remnants:	$t \sim 10^6 \rightarrow > 10^{7.7}$ y. (from formation of the original star)	σ_z = 65 pc,
HI -- clouds:	?	σ_z = 80 pc,
intercloud:	--	σ_z = 120 pc,
OH/IR stars:	$t \gtrsim 10^8$ y.	σ_z = 120 pc.

(Allen, 1973; Tinsley, 1975; Baker and Burton, 1975; Bash and Peters, 1976; Lockman, 1977 and §IV; Scoville et al., 1977; Burton and Gordon, 1978; Bowers, 1978). With the possible exception of HI, these all have similar, ordered deviations from z = 0. The characteristic lifetimes fall into two groups: the dense HII regions and the most massive progenitors of supernova remnants exist for such brief periods that they cannot move very far from their place of birth. Other species, including late O and early B stars that may be the progenitors of most supernova remnants, have lifetimes $\gtrsim 2\times10^7$ year, the period of objects oscillating about the galactic plane in the solar neighborhood (Oort, 1965); indeed, some objects have lifetimes of the order of a galactic rotation period at the radius of the Sun. It is the older objects that constrain interpretations of the z(R) phenonemon. [Although pulsars have active lifetimes of only $\sim 2\times10^6$ y. and thus belong to Population I, their distribution, at least in the z-direction, is probably determined more by "local" phenomena than by large-scale dynamical factors. They have a $\sigma_z \sim 200$ pc that results from their large ($\sim$ 200 km/s) proper motions (Taylor and Manchester, 1977).]

One explanation for the displacement of Population I-type objects from a plane is that a disturbance (perhaps that responsible for the HI warps in the outer Galaxy?) has moved the gas layer away from the potential minimum of the Galaxy. However, this proposal cannot be correct, for the most long-lived species (including molecular clouds) have stellar kinematics (Wentzel et al., 1975; Badhwar and Stephens, 1977) and will not be "blown" away from the plane like a distributed

gas can be. Unless the disturbance is sufficient to cause a distortion of the entire stellar disk, pre-existing molecular clouds, OH/IR stars, etc., cannot easily be displaced from the potential minimum of the Galaxy.

An alternative is that the cloud-forming mechanism (a density-wave?) is not planar, and thus collapses HI into molecular clouds and triggers star formation only at selected areas, not necessarily in the galactic plane. However, even if molecular clouds and stars are formed some distance from the potential minimum, their long lives assure that they will migrate a substantial distance in z and, to a large extent, information about their place of birth will be lost. It is difficult to reconcile this expected behavior with the relatively narrow scale height of the various objects, and especially with the almost identical z(R) form derived for objects whose lifetimes differ by factors of 10^2. We would at least expect some difference in $\langle z(R) \rangle$ as a function of the age of each species, but there is no such difference. Thus a simple displacement of the cloud/star forming mechanism from $z = 0$ is not sufficient to explain the observations.

The only remaining possibility is that the potential minimum (i.e., the mass distribution) of the Galaxy is not planar but has an ordered z(R) form over many kiloparsecs. (The data suggest that the $\langle z(R) \rangle$ function may be axisymmetric.) In this model the Population I-type objects are located symmetrically about the stellar distribution, and merely trace a phenomenon whose basis lies in the distribution of old stars.

HI has not been included in this discussion because it is the only galactic constituent that behaves like a gas, i.e., its kinematics depend on both gravity and pressure. The <z(R)> for HI is often similar to that of the other species (Lockman, 1977); but near R = 5 kpc the <z> of HI is 50 pc above the plane while other species are located at z = -20 pc. Such differences are not surprising, for the intercloud HI can be displaced, be blown about, develop instabilities and become tied to a magnetic field while other material cannot. The significance of the fact that the layer of molecular clouds and HII regions is not always coincident (in z) with the HI is its implication that the rate of formation of clouds, and of massive stars and HII regions, is not a simple function of the HI density.

A final consequence of the existence of an ordered z(R) pattern in all known species is that any survey conducted entirely at b = 0°0 cannot be considered complete.

There are significant differences among the thicknesses of various galactic constituents. Dense HII regions have the narrowest distribution, and are substantially more confined than even molecular clouds: in the z-direction the number of dense HII regions is related to the number of molecular clouds to the power $(\sigma_{CO}/\sigma_{HII})^2 \sim 3$. Because molecular clouds are discrete, it is unlikely that a mere increase in their numbers would cause some to collapse into massive stars. It seems more probable that an external mechanism triggers star formation in pre-existing molecular clouds over a narrow range in z (or creates new molecular clouds in a state of collapse) leaving most molecular clouds unaffected.

The objects observed in H166α have not entered this discussion because information about them is too scant to allow significant comparisons. The few measurements suggest that this medium has a σ_z less than or of order that of molecular clouds, but further observations (now in progress) are needed for accurate quantification.

The Radial Distribution

Inferences based on the derived radial distribution of dense HII regions must be made with restraint because of the possible selection effects discussed earlier. Still, some aspects appear certain: the southern distribution extends into R = 3 kpc, and the distribution is rather broad including a secondary peak near 7.5 kpc. The H166α results are more secure, if only because so many independent observations contribute to the derived surface density at any R. Comparison with other species is hampered, though, because the southern sky is largely unexplored. (Remarkably, there is no published N(R) diagram for southern HI!) Some specific conclusions can be drawn, but unless otherwise stated, they refer only to the situation in the North.

The radial surface density of CO emission, γ-radiation, supernova remnants, pulsars, H166α and OH/IR stars decreases monotonically for R > 5.5 kpc (Burton, 1976 and references therein; Lockman, 1976, Taylor and Manchester, 1977; Bowers, 1978). The radial distribution of dense HII regions is not that regular, and may well be broader than that of the other species. If this is so, then it may again signify that the rate of formation of massive stars in dense, compact clouds is not simply proportional to the number of dense clouds, just as the number of molecular

clouds is not necessarily related to the amount of HI.

Interior to R $\sim$ 5 kpc, most species show a decreased abundance, however, only dense HII regions, H166α (perhaps) and OH/IR stars are completely absent between the galactic nucleus and R $\sim$ 4 kpc. The abundance of northern molecular clouds, for example, decreases by a factor of 2 to 3 between R = 5 and R = 2 kpc, but does not fall to zero until R $\lesssim$ 2.0 kpc (Burton and Gordon, 1978; Bania, 1977). Thus, although there are many molecular clouds in the range 2 < R < 4 kpc, there is little evidence of active star formation of the kind that produces dense HII regions. Once again this leads to the conclusion that the presence of molecular clouds is a necessary but not sufficient condition for the formation of massive stars.

Lack of southern CO observations hinders an assessment of the overall significance of the extension of southern dense HII regions to R = 3 kpc. Nonetheless, the extension must be kept in mind, for it implies that the mechanism responsible for large-scale star formation operates to a smaller radius than evident in northern data alone.

Differences in the radial abundances of HII regions seen in H109α and those seen in H166α, especially at R $\gtrsim$ 7 kpc, are not inexplicable. It is plausible that near the solar radius star formation is occurring only in isolated compact areas, and not in the large complexes of ionized and molecular gas that are so plentiful in the inner Galaxy. Thus dense (and quite discrete) HII regions may be more common in the outer Galaxy than their larger, less dense counterparts.

Azimuthal Distribution

The absence of nebulae at the terminal velocity over some longitudes implies that there are areas $\sim$ 1.5 kpc in length along the subcentral points that contain no dense HII regions. As seen earlier, these gaps and other features of the nebular observations are well modelled by a spiral pattern. The exact form of the pattern is of secondary importance, and in fact it does not matter if the pattern is functionally indistinguishable from a set of ring segments. It is the confinement of HII regions to a well defined pattern, rather than the form of the pattern, that is the critical fact.

Because there are no gaps along V_t in observations of HI, CO, and OH/IR stars (Burton, 1976; Bowers, 1978) it follows that: (1) there are large areas of the inner Galaxy that contain all Population I-type species except HII regions, and (2) molecular clouds and most other young objects are not completely confined to a spiral pattern. It has been suggested that CO has periodic fluctuations in surface density that are in phase with a spiral pattern (Roberts and Burton, 1977), but these are only the dynamical consequences of "streaming" motions and, to first order, are no different from density fluctuations expected for stars moving under the influence of a spiral perturbation. In fact, the molecular data are well modeled by an axisymmetric distribution of clouds with a smooth radial surface density function (Burton and Gordon, 1978), i.e., by a model which does not have spiral arms. HI may have large azimuthal fluctuations (e.g., Visser, 1978) merely in response to the forcing potential, but HI is nonetheless present in the interarm region, unlike dense HII regions.

Thus in the azimuthal distribution, as well as in the radial and z-distributions, the ionized gas is clearly different from the netural and molecular gas. These differences have implications for the manner in which massive stars are formed.

On the Sequence of Star Formation

Because of the extremely short lifetimes of dense HII regions, their distribution gives a snapshot of the current pattern of star formation. [Throughout this section, the phrase "star formation" refers specifically to the formation of massive stars and hence dense HII regions. It is by no means certain that formation of low mass stars is accompanied by formation of more massive stars (e.g., Herbst and Racine, 1976; Brown, Lockman and Knapp, 1978).] The pattern of star formation derived in previous sections is similar, in some ways, to the distribution of molecular clouds. But it is singular in so many respects that it is clear that, although the pattern of star formation may depend on the presence of molecular clouds, it is not determined by them. Some additional factor is at work.

A likely factor is the large-scale compression which accompanies a density-wave. This model, when considered in light of the previous results, gives a scenerio for star formation in which molecular clouds are formed in the shock, or by compression of the HI by supernova remnants, HII regions, etc. The specific cloud-forming mechanism and its location in the Galaxy is not critical, except that we know it must operate over a volume defined by the CO observations. If most molecular clouds are formed in the density-wave, they must live long enough to travel between

spiral arms so that they will constitute a population that is distributed nearly axisymmetrically around the Galaxy. The actual collapse of clouds into stars occurs when a pre-existing cloud enters a density-wave induced shock (or when the shock creates a new cloud in an unstable state). Thus molecular clouds trace regions of potential but not necessarily current star formation.

Since the pattern of dense HII regions is narrow in both z and azimuth, the compression must operate most efficiently only at extremely well-defined locations.

This picture runs counter to the widely held view that, because narrow dust lanes are seen on the inner edge of arms of nearby spiral galaxies, molecular clouds should have a similar distribution. In fact, the shock accompanying a density-wave occurs only in the distributed intercloud medium--objects as massive and compact as molecular clouds will "plow through" the self-shocked intercloud gas. Although clouds may be compressed or distended, the experience of passing through a density-wave will hardly affect their center-of-mass motion (Woodward, 1978). Thus the narrow dust lanes seen in external galaxies likely consist of distributed dust that piles up, with the intercloud medium, at the shock front, together with newly formed molecular clouds. A glance at photographs of nearby spiral galaxies suggests that there is no lack of dust between the arms, and the picture described here implies that the arm-interarm difference in the surface density of extragalactic molecular clouds will not be much greater than the difference in surface density of any species that moves in a system containing a spiral perturbation. Even

including the possibility that new molecular clouds are created in the density-wave shock, the arm-interarm contrast in CO intensity should be no more than a factor of four.

CHAPTER VI

PROSPECTUS

This dissertation has been about the use of radio recombination lines to determine the structure of individual nebulae and the distribution of nebulae in the Galaxy. Here, instead of a summary, I want to discuss ideas for further work that have been prompted by the preceding chapters.

a) Nebular Structure

There are several areas where straightforward experimental or theoretical effort will make a significant, lasting contribution to the study of HII regions. At the most fundamental level, the conclusion of Brocklehurst and Seaton (1972) that "...the possible errors in these (cross-sections and other atomic) data are fairly small and hence cannot give rise to any major source of uncertainty..." is reassuring only in comparison with the uncertainties of the preceding decade; collisional cross-sections for highly excited states of hydrogen may still be in error by $\gtrsim$ 20 percent. This leads to possible errors in departure coefficients of roughly the same magnitude, and is the source of a transatlantic "difference of opinion" (in the amount of 30 percent) as to the magnitude of impact broadening (see Griem, 1974). The accuracy of some recombination line investigations may be limited more by uncertainties in the atomic data than by uncertainties in the astronomical data. Better collisional cross-sections and continued study of line broadening mechanisms are urgently needed [Griem (1974) discusses processes that

are not included in the current broadening formulae.] Until the basic atomic data are improved it may be pointless to demand exact agreement between models and data.

Nebular evolution is also in need of theoretical re-evaluation. The most recent models of nebular expansion are nearly ten years old and were made for spherically symmetric, uniform, rather low-density clouds (Lasker, 1966; Mathews, 1969). Molecular observations now suggest that it may be more appropriate to consider HII regions as forming on the edges of molecular clouds (see Chapter III) and in regions of very high density ($\gtrsim 10^7$ cm^{-3}). Thus the classic "Stromgren sphere" model for the evolution of an isolated system may no longer be relevant. It is possible that the expanding ionized gas is continually renewed from a dense neutral source, and that the geometry of expansion is away from the molecular cloud rather than away from the exciting stars. It would be very interesting to see results from an accurate two-dimensional hydrodynamic calculation of the evolution of an HII region located at the edge of a dense cloud. In particular, one would like to know the dynamics of the ionized gas and the thermodynamic structure of the interface between expanding ionized and quasi-static neutral gas.

The need for further observations is obvious: we need complete maps in both line and continuum of a number of nebulae at millimeter and centimeter wavelengths. For the observations to give information on nebular expansion they must cover the entire nebula; for the observations to aid in untangling the thermodynamic structure they must be made at many frequencies. Millimeter-wavelength observations are especially

critical. For example, the most puzzling feature of the Orion A recombination line spectrum is the high line-to-continuum ratios above 35 GHz. These data provide the clearest indication of temperature gradients in nebulae, and they should be confirmed, extended in accuracy and done on other nebulae.

Line and continuum work at frequencies below 1 GHz should not be neglected, and it is especially important that measurements be made as soon as possible because of the progressive deterioriation of the low-frequency radio environment. Surprisingly, accurate measurements of continuum flux densities below 1 GHz are still needed. Many current measurements are uncertain by 30 percent just at the frequencies where continuum spectra give critical tests of nebular models.

A very careful measurement is needed to clarify the problem of low-frequency line shapes, for I am not at all convinced that theory and experiment are consistent on this point. Models imply that 90 percent of the total power in some low-frequency lines is in broad wings that might get removed during data reduction (see Chapter IIIb). To understand the extent of this will require observation of a recombination line below 3 GHz using a very stable system (perhaps both an autocorrelator and a filter bank), covering a large velocity range (> 1000 km/s) to measure the weak signals accurately.

One can easily consume a scientific career constructing nebular models, and the art of conducting a productive investigation while avoiding such a henious fate requires more balance and insight than most investigators (perhaps myself included) possess. I think that it would

be wise to refrain from elaborate model building until there are enough new data to guarantee some semblence of uniqueness to the results, and I trust that the critiques in Chapter III of simplistic approaches are sufficiently persuasive to prevent their repetition. While it is always tempting to cap a difficult experiment with an involved interpretation of the data, a glance through the literature at the ephemeral value of most such efforts indicates that this temptation should be resisted.

b) Galactic Structure

It is sobering to realize that, after the detailed discussion of nebular structure in the first three chapters, so little is known about the objects discussed in the last two chapters that the main distinctions are "dense" and "not so dense". The needs in galactic structure are primarily observational and, to some degree, depend on results from the study of individual nebulae. It is probably most interesting to consider those aspects of the nebular distribution which differ from that of other species: (1) the nebulae between 3 and 4 kpc from the galactic center, (2) the z(R) relationship, (3) the absence of HII regions in the 3-kpc arm, and (4) the ordered (R,θ) relationship seen in HII regions and not in other species.

If young stars (and thus HII regions) are formed as a consequence of density-wave compression of some component of the interstellar medium, then at some $R < R_c$ there should be a rapid decrease in the number of HII regions (and other extreme Population I-type objects) owing to the failure of density-waves to propagate through the inner Lindblad resonance. Gordon (1978) has discussed this and, from northern CO data, has identified

R_c as 4 kpc. The northern HII regions support this figure. However, southern HII regions imply an R_c of 3 kpc and, as there are molecular clouds associated with at least some of these nebulae, it may be that R_c is not constant, or that there may be no well defined inner boundary to the Population I-type objects. I plan to extend the H166α survey to cover longitudes between 345° and 360° to see if moderate density ionized gas also extends to 3 kpc, but observations of CO and other species are clearly needed to study this problem.

One interesting implication of the displacement of nebulae from a plane (i.e., the z(R) relationship) is that no survey at b = 0° can be complete. We are, then, on shaky ground when comparing the b = 0° H166α survey with the latitudinally complete H109α surveys. Similar cautions apply to the use of CO data taken entirely in the plane. I hope to extend the latitude coverage of the H166α survey not only to better study the scale-height of the ionized gas but to check the completeness of the b = 0° survey.

A very interesting question is that of the participation of various species in the z(R) phenomenon. I have argued that the deviation from planarity is characteristic of the vertical potential distribution in the Galaxy and hence most species should show the pattern. Recent observations (Bowers, 1978) indicate that OH/IR stars have a z(R) relationship consistent with that of the HII regions, CO, and other species, indicating that the phenomenon is not restricted to gas but also involves stars. A critical test of the amount of mass involved in the displacement will come from near-IR observations of late-type stars, because these objects provide most of the mass in the Galaxy.

The 3-kpc expanding arm is conspicuously absent from the ionized gas. There is a feature at an appropriate velocity in H166α towards $\ell = 0°$, $b = 0°$; but if this is from the 3-kpc arm, then the emission is being stimulated by the enormous continuum from Sgr A and it is impossible to compare this feature with other H166α lines away from strong continuum sources. Since the 3-kpc arm is prominent in HI and CO [although it has a smaller H_2/total-mass ratio than other features at low longitudes (Bania, 1977)], the lack of young stars is rather surprising, and would again indicate that the presence of gaseous progenitors of stars is not sufficient to insure their collapse into stars. Before carrying this interpretation too far, though, better limits are needed on the ionized component of the 3-kpc arm. The easiest way to obtain these is to make long integrations at H166α in search of emission at the appropriate velocities. Unfortunately, this will require substantial amounts of telescope time, for the lines would be $\lesssim 0.01$ K at their peak, and the relevant portion of the galactic plane can only be observed for about 7 hours a day from a northern site.

Are dense HII regions the only species that lies in an ordered R,θ pattern? Type II supernova remnants, if they arise from the very massive stars, ought also to have an ordered distribution. But distance determinations to remnants are very uncertain and their kinematics are currently inaccessible to radio observation. Unfortunately, the distribution of supernova remnants in nearby galaxies (e.g., Maza and van den Berg, 1976) is less clear than one would expect (W. Herbst, private communication).

While the schema presented in this dissertation explains the broad features in the distribution of various species, it seems likely that star formation can be triggered in other ways (e.g., by supernova remnants, Herbst and Assousa, 1977). Density-wave compression alone may not be sufficient to account for phenomena like the "local arm" and isolated HII regions seen in other galaxies. It is possible that a "secondary density maximum" induced by the primary wave might be the cause of "spurs" and "feathers" on a spiral pattern, but the strength of this higher-order resonance is a matter of dispute (cf. Roberts, 1972 and Woodward, 1975).

There is need for southern hemisphere and extragalactic observations to clarify these points. A useful beginning would be to resurvey the southern plane in H109α to verify or correct the existing velocities. An H166α survey would also be useful as a check on the location of lower density ionized gas, and, of course, one always wants CO.

A prominent omission in this dissertation is that 70 percent of the galactic plane that lies more than 55° from $\ell = 0°$. This is a frustrating part of the Galaxy for radio astronomers because here kinematic distance estimates are particularly unreliable. On the other hand, it is often possible to isolate individual areas of star formation and to study them in both the radio and optical. Progress in understanding the outer portion of the Galaxy will only come from collaboration between radio and optical observers.

Our poor grasp of the structure of individual nebulae lies at the heart of our inability to quantify the properties of ionized regions on the large scale. Are most dense nebulae surrounded by extensive regions

of moderate density ionized gas? Does one type of nebula evolve into the other or are we observing two different populations with different histories? The atomic, stellar, nebular and galactic scales meet in the study of HII regions, and it often seems that we need to know everything before we can know anything.

REFERENCES

Allen, C. W. 1973, Astrophysical Quantities (London: Athlone).

Altenhoff, W. J., Mezger, P. G., Wendker, H. and Westerhout, G. 1960, Veroff. Sternwarte, Bonn, No. 59, 48.

Altenhoff, W. J., Downes, D., Goad, L., Maxwell, A. and Rinehart, R. 1970, Astr. Ap. Suppl., 1, 319.

Badhwar, G. D. and Stephens, S. A. 1977, Ap. J., 212, 494.

Baker, P. L. and Burton, W. B. 1975, Ap. J., 198, 281.

Balick, B. 1972, Ap. J., 176, 353.

Balick, B., Gammon, R. H. and Hjellming, R. M. 1974, P.A.S.P., 86, 616.

Bania, T. M. 1977, Ap. J., 216, 381.

Bash, F. N. and Peters, W. L. 1976, Ap. J., 205, 786.

Beard, M. 1966, Aust. J. Phys., 19, 141.

Beard, M., Thomas, B. M. and Day, G. A. 1969, Aust. J. Phys. Ap. Suppl., 11, 27.

Boulesteix, J., Courtes, G., Laval, A., Monnet, G. and Petit, H. 1974, Astr. Ap., 37, 33.

Bowers, P. F. 1978, Astr. Ap., 64, 307.

Bracewell, R. 1965, The Fourier Transform and its Applications (New York: McGraw-Hill).

Brocklehurst, M. 1970, M.N.R.A.S., 148, 417.

———————— 1971, M.N.R.A.S., 153, 471.

Brocklehurst, M. and Leeman, S. 1971, Ap. Lett., 9, 35.

Brocklehurst, M. and Seaton, M. J. 1972, M.N.R.A.S., 157, 179.

Brown, R. L. 1979 (in preparation).

Brown, R. L. and Balick, B. 1973, Ap. J., 185, 843.

Brown, R. L., Lockman, F. J. and Knapp, G. R. 1978, Ann. Rev. Astr. Ap., 16, 445.

Burton, W. B. 1966, B.A.N., 18, 247.

———— 1970, Astr. Ap. Suppl., 2, 261.

———— 1971, Astr. Ap., 10, 76.

———— 1976, Ann. Rev. Astr. Ap., 14, 275.

———— 1979 (in preparation).

Burton, W. B. and Bania, T. M. 1974a, Astr. Ap., 33, 425.

———— 1974b, Astr. Ap., 34, 75.

Burton, W. B., Gordon, M. A., Bania, T. M. and Lockman, F. J. 1975, Ap. J., 202, 30.

Burton, W. B. and Gordon, M. A. 1978, Astr. Ap., 63, 7.

Caswell, J. L. 1972, Aust. J. Phys., 25, 443.

Caswell, J. L. and Robinson, B. J. 1974, Aust. J. Phys., 27, 597.

Caswell, J. L. and Clark, D. H. 1975, Aust. J. Phys. Ap. Suppl., 37, 57.

Caswell, J. L., Haynes, R. F. and Clark, D. H. 1975, Aust. J. Phys., 28, 633.

Caswell, J. L., Murray, J. D., Roger, R. S., Cole, J. D. and Cooke, D. J. 1975, Astr. Ap., 45, 239.

Cato, B. T. 1973, Res. Lab. Elect., Onsala Space Obs., Chalmers Univ. Tech. (Gothenburg, Sweden) Res. Rept. No. 114.

Chaisson, E. J. 1973, Ap. J., 186, 555.

Chaisson, E. J. and Willson, R. F. 1975, Ap. J., 199, 647.

Churchwell, E. B. 1970, unpublished Ph.D. Thesis, Indiana University.

Churchwell, E., Mezger, P. G. and Huchtmeier, W. 1974, Astr. Ap., 32, 283.

Cohen, R. S. and Thaddeus, P. 1977, Ap. J., 217, L155.

Crampton, D., Georgelin, Y. M. and Georgelin, Y. P. 1978, Astr. Ap., 66, 1.

Dahl, O.-J., Dijkstra, E. W. and Hoare, C.A.R. 1972, Structured Programming (London: Academic Press).

Day, G. A., Thomas, B. M. and Goss, W. M. 1969, Aust. J. Phys. Ap. Suppl., 11, 11.

Dickel, J. R. and Milne, D. K. 1972, Aust. J. Phys., 25, 539.

Drayson, S. R. 1976, J. Quant. Spect. Rad. Transf., 16, 611.

Dupree, A. K. 1969, Ap. J., 158, 491.

Dupree, A. K. and Goldberg, L. 1969, Ap. J., 158, L49.

———————— 1970, Ann. Rev. Astr. Ap., 8, 231.

Falgarone, E. and Lequeux, J. 1973, Astr. Ap., 25, 253.

Finn, G. D. and Mugglestone, D. 1965, M.N.R.A.S., 129, 221.

Gardner, F. F., Milne, D. K., Mezger, P. G. and Wilson, T. L. 1970a, Astr. Ap., 7, 349.

———————— 1970b, Ap. Lett., 6, 87.

Georgelin, Y. P. 1970, Astr. Ap., 7, 322.

Georgelin, Y. P. and Georgelin, Y. M. 1970, Astr. Ap., 6, 349.

Georgelin, Y. M., Georgelin, Y. P. and Roux, S. 1973, Astr. Ap., 25, 337.

Georgelin, Y. M. and Georgelin, Y. P. 1976, Astr. Ap., 49, 57.

Gillespie, A. R., Huggins, P. J., Sollner, T.C.L.G., Phillips, T. G., Gardner, F. F. and Knowles, S. H. 1977, Astr. Ap., 60, 221.

Goldberg, L. 1966, Ap. J., 144, 1225.

———————— 1968, in Interstellar Ionized Hydrogen, ed. Y. Terzian (New York: Benjamin), p. 373.

Goldwire, H. C. 1968, Ap. J. Suppl., 17, 445.

Gordon, M. A. 1974, in Galactic and Extragalactic Radio Astronomy, ed. G. L. Verschuur and K. I. Kellermann (New York: Springer), p. 51.

———————— 1978, Ap. J., 222, 100.

Gordon, M. A. and Cato, T. 1972, Ap. J., 176, 587.

Gordon, M. A., Brown, R. L. and Gottesman, S. T. 1972, Ap. J., 178, 119.

Goss, W. M. and Day, G. A. 1970, Aust. J. Phys. Ap. Suppl., 13, 1.

Goss, W. M. and Shaver, P. A. 1970, Aust. J. Phys. Ap. Suppl., 14, 1.

Goss, W. M., Manchester, R. N. and Robinson, B. J. 1970, Aust. J. Phys., 23, 559.

Goss, W. M., Radhakrishnan, V., Brooks, J. W. and Murray, J. D. 1972, Ap. J. Suppl., 24, 123.

Gottesman, S. T. and Gordon, M. A. 1970, Ap. J., 162, L93.

Greisen, E. W. and Lockman, F. J. 1979, Ap. J. (in press).

Griem, H. R. 1967, Ap. J., 148, 547.

———————— 1974, Spectral Line Broadening by Plasmas (New York: Academic Press).

Gum, C. S., Kerr, F. J. and Westerhout, G. 1960, M.N.R.A.S., 121, 132.

Hart, L. and Pedlar, A. 1976, M.N.R.A.S., 176, 135.

Herbst, W. and Racine, R. 1976, A. J., 81, 840.

Herbst, W. and Assousa, G. E. 1977, Ap. J., 217, 473.

Hill, J. K. 1977, Ap. J., 212, 685.

Hjellming, R. M. and Churchwell, E. 1969, Ap. Lett., 4, 165.

Hjellming, R. M., Andrews, M. H. and Sejnowski, T. J. 1969, Ap. J., 157, 573.

Hoang-Binh, D. 1972, Mem. Soc. Royale des Liege, 6th Ser., Book III, p. 367.

Hoang-Binh, D. and Walmsley, C. M. 1974, Astr. Ap., 35, 49.

Hodge, P. W. 1969, Ap. J., 155, 417.

Hummer, D. G. 1965, Mem. R.A.S., 70, 1.

Israel, F. P. 1976, Astr. Ap., 48, 193.

———————— 1977, Astr. Ap., 59, 27.

Israel, F. P. and van der Kruit, P. C. 1974, Astr. Ap., 32, 363.

Jackson, P. D. and Kerr, F. J. 1971, Ap. J., 168, 29.

———————— 1975, Ap. J., 196, 723.

Johansson, L.E.B., Andersson, C., Goss, W. M. and Winnberg, A. 1977, Astr. Ap. Suppl., 28, 199.

Kardashev, N. S. 1959, Soviet Astr. (AJ), 3, 813.

Kerr, F. J. 1969, Ann. Rev. Astr. Ap., 7, 39.

Kielkopf, J. F. 1973, J. Opt. Soc. Am., 63, 987.

Lada, C. J. and Chaisson, E. J. 1973, Ap. J., 183, 477.

Lasker, B. M. 1966, Ap. J., 146, 471.

Lewis, T. G. and Payne, W. H. 1973, J. Assn. Comp. Mach., 20, 456.

Lin, C. C., Yuan, C. and Shu, F. H. 1969, Ap. J., 155, 721.

Lockman, F. J. 1976, Ap. J., 209, 429.

———————— 1977, A. J., 82, 408.

Lockman, F. and Gordon, M. A. 1973, Ap. J., 182, 25.

Lockman, F. J. and Brown, R. L. 1975, Ap. J., 201, 134.

———————— 1976, Ap. J., 207, 436.

———————— 1978, Ap. J., 222, 153.

Mathews, W. G. 1969, Ap. J., 157, 583.

Matthews, H. E., Pedlar, A. and Davies, R. D. 1973, M.N.R.A.S., 165, 149.

Maza, J. and van den Berg, S. 1976, Ap. J., 204, 519.

Menzel, D. H. 1968, Nature, 218, 756.

Mezger, P. G. 1970, in The Spiral Structure of Our Galaxy, ed. W. Becker and G. Contopoulos (Dordrecht: Reidel), p. 107.

Mezger, P. G. and Henderson, A. P. 1967, Ap. J., 147, 471.

Mezger, P. G. and Ellis, S. A. 1968, Ap. Lett., 1, 159.

Mills, B. Y. 1959, in Paris Symposium on Radio Astronomy, IAU Symposium No. 9, ed. R. N. Bracewell (Stanford: Stanford Univ. Press), p. 431.

Milne, D. K. and Wilson, T. L. 1971, Astr. Ap., 10, 220.

Monnet, G. 1971, Astr. Ap., 12, 379.

Nelson, A. H. 1976, M.N.R.A.S., 177, 265.

Olnon, F. M. 1975, Astr. Ap., 39, 217.

Oort, J. H. 1965, in Galactic Structure, Vol. 5 of Stars and Stellar Systems, ed. A. Blaauw and M. Schmidt (Chicago: Univ. of Chicago Press), p. 455.

Oster, L. 1961, Rev. Mod. Phys., 33, 525.

Palmer, P. 1968, unpublished Ph.D. Thesis, Harvard University.

Panagia, N. 1973, A. J., 78, 929.

Panagia, N. and Felli, M. 1975, Astr. Ap., 39, 1.

Pankonin, V., Thomasson, P. and Barshun, J. 1977, Astr. Ap., 54, 335.

Peach, G. 1972, Ap. Lett., 10, 129.

Pengelly, R. M. and Seaton, M. J. 1964, M.N.R.A.S., 127, 165.

Perrenod, S. C., Shields, G. A. and Chaisson, E. J. 1977, Ap. J., 216, 427.

Pottasch, S. R. 1965, Vistas in Astr., 6, 149.

Pyatunina, T. B. and Soglasnova, V. A. 1973, Soviet Astr. (AJ), 17, 325.

Quiroga, R. 1974, Astr. Space Sci., 27, 323.

Radhakrishnan, V., Goss, W. M., Murray, J. D. and Brooks, J. W. 1972, Ap. J. Suppl., 24, 49.

Reifenstein, E. C., Wilson, T. L., Burke, B. F., Mezger, P. G. and Altenhoff, W. J. 1970, Astr. Ap., 4, 357.

Roberts, W. W. 1972, Ap. J., 173, 259.

Roberts, W. W. and Burton, W. B. 1977, in Topics in Interstellar Matter, ed. H. van Woerden (Dordrecht: Reidel), p. 195.

Rubin, R. H. 1969, Ap. J., 154, 391.

———————— 1970, Astr. Ap., 8, 171.

Rubin, R. H. and Turner, B. E. 1971, Ap. J., 165, 471.

Schmidt, M. 1965, in Stars and Stellar Systems, Vol. 5, ed. A. Blaauw, and M. Schmidt (Chicago: Univ. of Chicago Press), p. 513.

Scoville, N. Z., Solomon, P. M. and Sanders, D. B. 1977, in The Structure and Content of the Galaxy and Galactic Gamma Rays, ed. C. E. Fichtel and F. W. Stecker (Washington: NASA CP-002), p. 151.

Searle, L. 1971, Ap. J., 168, 327.

Seaton, M. J. 1964, M.N.R.A.S., 127, 177.

Shane, W. W. and Bieger-Smith, G. P. 1966, B.A.N., 18, 263.

Shaver, P. A. 1976, Astr. Ap., 47, 49.

Shaver, P. A. and Goss, W. M. 1970, Aust. J. Phys. Astr. Suppl., 14, 133.

Shu, F. H., Milione, V., Gebel, W., Yuan, C., Goldsmith, D. W. and Roberts, W. W. 1972, Ap. J., 173, 557.

Simonson, S. C. and Mader, G. L. 1973, Astr. Ap., 27, 337.

Stecker, F. W. 1977, in The Structure and Content of the Galaxy and Galactic Gamma Rays, ed. C. E. Fichtel and F. W. Stecker (Washington: NASA CP-002), p. 315.

Taylor, J. H. and Manchester, R. N. 1977, Ap. J., 215, 885.

Terzian, Y. and Parrish, A. 1970, Ap. Lett., 5, 261.

Thomas, B. M. and Day, G. A. 1969, Aust. J. Phys. Ap. Suppl., 11, 19.

Tinsley, B. M. 1975, P.A.S.P., 87, 837.

Tully, R. B. 1972, unpublished Ph.D. Thesis, U. Maryland.

Turner, B. E. 1972, Ap. J., 171, 503.

———————— 1979, Astr. Ap. Suppl. (in the press).

Viner, M. R., Clarke, J. N. and Hughes, V. A. 1976, A. J., 81, 512.

Visser, H.C.D. 1978, unpublished Ph.D. Thesis, Univ. Groningen.

Weisheit, J. and Walmsley, C. M. 1977, Astr. Ap., 61, 141.

Wentzel, D. G., Jackson, P. D., Rose, W. K. and Sinha, R. P. 1975, Ap. J., 201, L5.

Westerhout, G. 1958, B.A.N., 14, 215.

Whiteoak, J. B. and Gardner, F. F. 1974, Astr. Ap., 37, 389.

Wielebinski, R., Smith, D. H. and Garzon-Cardenas, X. 1968, Aust. J. Phys., 21, 185.

Wilson, T. L. 1970, unpublished Ph.D. Thesis, Mass. Inst. Tech.

———————— 1972, Astr. Ap., 19, 354.

———————— 1974, Astr. Ap., 31, 83.

Wilson, T. L., Mezger, P. G., Gardner, F. F. and Milne, D. K. 1970, Astr. Ap., 6, 364.

Wilson, T. L. and Altenhoff, W. J. 1972, Astr. Ap., 16, 489.

Wilson, W. J., Schwartz, P. R., Epstein, E. E., Johnson, W. A. Etcheverry, R. D., Mori, T. T., Berry, G. G. and Dyson, H. B. 1974, Ap. J., 191, 357.

Woodward, P. R. 1975, Ap. J., 195, 61.

———————— 1976, Ap. J., 207, 484.

———————— 1978, Ann. Rev. Astr. Ap., 16, 555.

Wright, A. E. and Barlow, M. J. 1975, M.N.R.A.S., 170, 41.

Zuckerman, B. 1973, Ap. J., 183, 863.

APPENDIX A

A PROGRAM TO CALCULATE RECOMBINATION LINES FROM MODEL NEBULAE

All synthetic spectra discussed in this dissertation were calculated using a single computer program. Circular symmetry is implicit in its structure, although this is just a matter of convenience--because the solution to the equation of transfer can be expressed as a sum of isothermal, homogeneous solutions times transfer factors, the calculation of emission emergent from the surface of an arbitrarily constructed model is straightforward.

There are three forms of "gridding" in the program. The most fundamental is the division of a path through a model into elements of length Δs_i within each of which all nebular properties are constant. The second is the calculation of emergent surface brightness temperatures at a finite nz points across the model. The third is an arbitrary, but convenient, choice to treat a nebula as a set of nr concentric shells of thickness Δr_i, within each of which T_e, N_e, the micro- and macroturbulence, etc., are constant. The number of shells can be between one and 51, and $1 \leq nz \leq 301$. When nz = 1 the model is equivalent to a plane-parallel model.

Gridding along the line of sight, in static models, is naturally related to the distance travelled through each shell, although tests are made to insure that the path length through a shell is not so small as to cause precision or underflow problems. In macroturbulent (i.e., expanding) models, the projection of the radial

velocity may change significantly within a shell, so an arbitrary gridding is imposed on each line of sight. Thus, the number of terms in the solution to the equation of transfer along a line of sight through the nebular center ($z = 0$) is $2\underline{nr} - 1$ for static models, and at least twice that for macroturbulent models.

It is obvious that the summation of terms in the solution to the equation of transfer can begin (or end) at any arbitrary point along the line of sight. Thus, although spherical symmetry is implicit in the shell structure of the program, it can evaluate the emission from any section of a sphere bounded by two planes perpendicular to the path from source to observer.

The input to the program is a set of electron and ion densities, shell sizes, Doppler and kinetic temperatures, and macroturbulent velocities, together with quantities that describe the section of a sphere that is to be considered, and its distance from the Sun. The result of a single calculation is a set of brightness temperatures $T_{L+c}(z,x,n,\Delta n,m_a,\text{abundance},Z)$ and $T_c(z,\nu)$, where z is the projected distance from the nebular center in units of the nebular radius R, x is the position on the line profile (in macroturbulent models $x = 0$ is taken to be the mean velocity of gas in the innermost shell), n and Δn specify the transition and its frequency ν, m_a is the atomic mass of the line emitter whose abundance and effective nuclear charge are also specified. The set of brightness temperatures, T_{L+c} and T_c, are then independently convolved with a specified Gaussian function to simulate observation with an antenna beam. The continuum flux

density is calculated from unconvolved continuum brightness temperatures. Except where explicitly noted in the text, the models include the effect of radiation from a 2.7 K blackbody incident on the back of the nebula.

Absorption coefficients were calculated for each shell and then multiplied by the appropriate path length to obtain the optical depth in each element. In macroturbulent models the Voigt profile was evaluated separately for each element along the line of sight. Departure coefficients were taken from Brocklehurst (1970) interpolated to the appropriate T_e and N_e. Line profiles were calculated using Griem's (1974) expression for the broadening factor, and Drayson's (1976) suggestions for the calculation of Voigt profiles.

Maintenance of precision in a complicated program can be a major task. Critical portions of this program (e.g., summations where the value of individual elements could differ by many orders of magnitude) were calculated using 53 bit words, and several models were tested with 109 bit arithmetic. Truncation and round-off errors seem to be less than 1% of any calculated quantity.

Accuracy of the program was checked in several ways. First, the code was written in top-down, structured PL/1 and thus logical errors are unlikely (see, e.g., Dahl et al., 1972). Second, the continuum and the line+continuum brightness temperatures are calculated in parallel statements throughout the program. The accuracy of the continuum brightness temperatures can be checked by comparing the flux density derived from them with the flux density calculated analytically

from the integral of $N_e N_i$ over the volume of the model. In all cases the two flux densities differed by less than 1%, and differences were due mostly to the finite number of paths that were calculated through the models. Also, at both the high and low frequency limits, the continuum brightness temperature along a single line of sight can easily be calculated and compared with model results. Again, the agreement was excellent. These facts imply that the program's handling of brightness temperatures is correct. Finally, results for simple models were compared with hand calculations and previously published results. Again, when allowance is made for different authors' choice of departure coefficients and broadening formulae, the agreement was excellent. Whenever model calculations produced unexpected results (e.g., line narrowing due to masing off the 2.7 K background) the basic validity of the results was checked by hand calculation.

The approximation of an ideal, smooth model by a model divided into isothermal, homogeneous cells usually results in a discontinuity in L(z) where z crosses a shell boundary. However, discontinuities at shell boundaries are almost never visible after antenna beam convolution, even when the beam is small. There can be problems when the nebular structure changes over distances which are less than or of order of the sampling interval. This is seen, for example, near the edge of macroturbulent models, where lines of sight intersect only 2 shells. The shells have different thermodynamic properties, but more importantly, different velocities. In essence, lines of

sight at a nebula's edge are sampling a crude and very differentiated macroturbulent model, and calculated profiles sometimes have an artificial two-peaked structure. Line intensities at these areas are quite small, though, and this problem does not affect our overall conclusions about macroturbulent models, nor does it significantly degrade the overall accuracy of the results. However, it does limit line shape analyses to $z \leq 0.9$ in macroturbulent models. To minimize the effects of "gridding", the number of shells was always kept reasonably high, and nz was always kept quite high; typical calculations used $\gtrsim$ 100 lines of sight from the center to the edge of a model divided into $\gtrsim$ 20 shells.